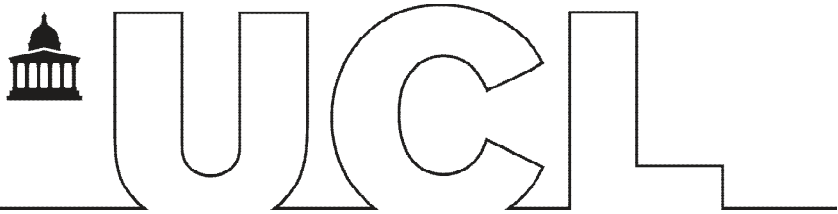

Improving Exciton Dissociation and Charge Transport in Organic Photovoltaic Cells

Marten Tolk

A dissertation submitted for the degree of Doctor of Philosophy

University College London

Department of Physics & Astronomy

2013

I, Marten Tolk, confirm that the work presented in this thesis is my own. Where information has been derived from other sources, I confirm that this has been indicated in the thesis.

Abstract

I have divided this dissertation into three chapters: introduction to organic solar cells, thermo-chemical lithography of a conjugated polymer, and triplet emitters in organic solar cells (OSCs).

The first chapter introduces OSCs giving the background necessary to understand the problem of simultaneous optimisation of exciton dissociation and charge transport.

The second chapter deals with scanning thermo-chemical lithography (SThL) of PPV on indium-tin oxide (ITO) by means of a thermal AFM, i.e. an AFM that has a hot probe scanning across the surface, to ultimately pattern the active layer of an OSC. I investigate the influence of the thermal conductivity of the substrate on the lithography by combining finite element simulations of the heat transfer and experimental results. The model explains the rather substrate-independent feature size observed during experiments and it is found that for the highest resolution features, there exists a small gap of unconverted polymer near the substrate, which is why SThL is possible on high thermal conductivity substrates such as gold.

In the third chapter I report experimental findings regarding the inclusion of triplet emitters in organic photovoltaic cells. The idea is to increase the exciton diffusion length (L) of the primary photoexcitations by converting them into triplet excitons, which are known to have longer lifetimes and hence offer the potential of increased exciton diffusion lengths. Several host systems were chosen, among them P3HT:$PC_{61}BM$, MDMO-PPV:$PC_{61}BM$ and PBTTT:bis-$PC_{61}BM$. As phosphorescent molecules I used Cu-complexes and different Ir-complexes. Results on MDMO-PPV:$PC_{61}BM$ blends and bilayer devices showed a promising increase in the short-circuit current density (J_{SC}) partly supported by an increase in the incident photon to current efficiency peak in the polymer absorption wavelength range. The overall achievability of the idea is critically discussed and a 1D random walk model used to estimate possible improvements of J_{SC} upon increases in L.

Acknowledgments

First and foremost, I would like to thank my supervisors Prof. Franco Cacialli and Dr. Oliver Fenwick for their invaluable assistance, for proofreading this thesis and their willingness to motivate me.

I further wish to express my gratitude to Oliver Fenwick, Francesco Di Stasio, Yong Sig Shin, Gustaf Winroth, Penglei Li and Giovanni Mattia Lazzerini for showing me how to use the various pieces of equipment.

I would also like to thank the chemists who have provided me with some of the materials, Egle Sirtautaite-Sidlauskiene and her supervisor Alan Rowan, and Claudia Bizzarri and her supervisor Luisa De Cola. I am further grateful to Giulia Grancini and Annamaria Petrozza for doing transient absorption measurements on some of my samples and for the following discussions.

I also thank Charlie for, among others, making wonderful food.

I would also like to acknowledge Nico Seidler for our many discussions and his willingness to help fixing equipment in the lab, especially the jinxed evaporator.

I would like to thank Daniel Podobinski for proofreading my thesis.

I would also like to thank the support staff at the UCL Department of Physics & Astronomy for helping with my various requests so quickly and willingly. To the rest of the UCL support staff I can only say that I am very sorry for being a student and an employee at the same time.

For the financial support I thank the Marie Curie Initial Training Network (PITN-CT-2009-238177).

Finally I would like to thank all the people in the lab, my friends and my family for making the PhD time so enjoyable.

Contents

List of Abbreviations and Symbols

$\|f\rangle$	–	final state
$\|i\rangle$	–	initial state
μ	–	mobility
1D, 2D, 3D	–	1-dimensional, 2-dimensional, 3-dimensional
A	–	acceptor
A	–	pre-exponential factor (in the Arrhenius equation) or contact interface between two bodies
ADS077RE	–	bis(2-(9,9-dibutylfluorenyl)-1-isoquinoline(acetylacetonate))
AFM	–	atomic force microscope, atomic force microscopy
BHJ	–	bulk heterojunction
bis-$PC_{61}BM$	–	bisadduct of phenyl-C61-butyric acid methyl ester (PCBM)
c	–	speed of light or specific heat capacity
CB	–	conduction band
CT	–	charge transfer
D	–	donor
d	–	thickness of the semiconductor layer
D	–	diffusivity
d	–	layer thickness
d_r	–	FWHM of the volume inside the conversion boundary subtracted by 2 r_0
d_z	–	The vertical distance (d_z) between B and the conversion
E	–	energy
E_A	–	activation energy
EPIA		European Photovoltaic Industry Association
E_t	–	characteristic energy of the exponential trap distribution
F	–	electrical field
$f_D(\lambda)$	–	donor emission spectrum
FET	–	field effect transistor
FF	–	fill factor
FRET	–	Förster resonance energy transfer
G	–	free energy
h	–	Planck's constant
H'	–	the perturbing Hamiltonian, including the electrostatic interaction of all electrons and nuclei

$H(E)$	–	density of traps at energy E
h_c	–	thermal conductance coefficient
HOMO	–	highest occupied molecular orbital
H_t	–	total trap density
IPCE	–	incident photon to current efficiency
ITO	–	indium tin oxide
J	–	current density or spectral overlap integral
J_0	–	dark saturation current
J_L	–	current density generated by the solar cell
J_{SC} / I_{SC}	–	short-circuit current density / short-circuit current
JV	–	current density - voltage
k	–	thermal conductivity or reaction rate or transition rate or wave-vector
k_B	–	Boltzmann constant
k_D^0	–	decay rate of the excited state in the absence of FRET
k_F	–	Förster resonance energy transfer rate
L	–	exciton diffusion length
LUMO	–	lowest unoccupied molecular orbital
M_{DA}	–	donor/acceptor transfer integral
MDMO-PPV	–	poly[2-methoxy-5-(3',7'-dimethyloctyloxy) -1,4-phenylene vinylene]
n	–	diode ideality factor or refractive index or charge carrier density
N_A	–	Avogadro number
N_{HOMO}	–	the HOMO effective density of states
OLED	–	organic light emitting diode
OSC	–	organic solar cell
P3HT	–	poly(3-hexylthiophene)
PA	–	photoabsorption
PB	–	photobleaching
PBTTT-C_{16}	–	poly(2,5-bis(3-hexadecylthiophen-2-yl)thieno[3,2-b]thiophene)
$PC_{61}BM$	–	[6,6]-phenyl-C_{61}-butryc acid methyl ester, PCBM

PIA	–	photo-induced absorption
PL	–	photoluminescence
P_{light}	–	power of the incoming light
PLQE	–	photoluminescence quantum efficiency
P_{out}	–	maximum output power of a solar cell
PPV	–	poly(*p*-phenylene-vinylene)
q	–	electronic charge
Q	–	heat, energy (in J)
q	–	heat flow density (W/m^2)
Q_0	–	Fluorescence quantum yield of donor in the absence of A
Q_S	–	heat source or heat production (in W/m^3)
r	–	Distance between donor and acceptor
R	–	universal gas constant or thermal resistance (in K/W) or ratio between the number of excitons that reach the fullerene interface over the number of absorbed photons
r_0	–	distance between the centre of the AFM probe and the position where the probe stops touching the polymer layer
R_0	–	distance between donor and acceptor molecule
R_F	–	Förster Radius
R_S	–	series resistance (in the equivalent solar cell circuit)
R_{SH}	–	shunt resistance (in the equivalent solar cell circuit)
SC	–	solar cell
t	–	time or layer thickness
T	–	temperature or transmission
TA		transient absorption
TFT	–	thin film transistor
T_{tip}	–	tip temperature
T_{tip}^{min}	–	substrate dependent minimum tip temperature that assures the polymer sticks to the surface
VB	–	valence band
V_{OC}	–	open-circuit voltage
wt%	–	weight percent
α	–	conversion ratio of converted to initially unconverted molecules

β_C	–	Coulomb integral
β_E	–	exchange integral
γ	–	Langevin recombination constant
$\varepsilon_0 \varepsilon_r$	–	dielectric permittivity.
$\varepsilon_0 \varepsilon_r$	–	dielectric permittivity
$\epsilon_A(\lambda)$	–	acceptor extinction coefficient
η	–	energy conversion efficiency (of a solar cell)
κ^2	–	factor taking into account the relative orientation between two transition dipoles
λ	–	wavelength or reorganisation energy
ν	–	frequency of a photon
ρ	–	mass density or density of states
σ	–	width of the Gaussian distribution of density of states
τ	–	lifetime

List of Figures

List of Tables

1 Introduction

1.1 Why Solar Energy

Harnessing solar energy is unquestionably a very attractive idea. Not only will it provide energy for the next five to six billion years, thus considered “renewable”, but it is also a clean way of producing energy. Considering not just the detrimental effects of carbon dioxide and other greenhouse gases on the environment – which has eventually become a widely accepted fact – but also the political and economic dependencies that are connected with fossil fuels such as oil and gas, cheap, renewable and “independent” energy sources are in greater demand than ever before.

Another attractive aspect of solar energy is that it can produce energy on all different scales, from the humble calculator through off-grid stations in remote areas to big power plants. Furthermore, lots of energy can be generated by simply using space which is already in use: roofs.

Up until now, I mainly talked about electricity generation on a larger scale. In this field, inorganic solar cells dominate by far at the moment. An overview about the different types of solar cells (SCs) will be given in the next section. Here I would like to point out that organic solar cells (OSCs) – the broader topic of this thesis – have the potential to be used in a number of niche markets. Due to their potential lightweight, flexibility, transparency and of course, low cost per watt, they might be used in the future in the following applications:

- Building-integrated photovoltaics: Solar modules as energy source and design elements at the same time
- Emergency blankets or briefcases with solar modules which can be used for notebooks, mobile phones, radios, electronic paper and more
- Electric cars
- SCs integrated in clothes (jackets etc., especially for military) and bags

1.2 Three Generations of Solar Cells

Although the photovoltaic effect was already observed in 1839 by the French physicist A. E. Becquerel, it was not until 1883 when the first SC made out of selenium was built. It took many years for someone (Albert Einstein, 1905) to understand the physics behind this phenomenon and even longer for this idea of light consisting of photons to be accepted in the scientific community. However, the power conversion efficiency of the selenium cell was still quite low, i.e. below 1%.

An accidental discovery at the Bell Laboratories in 1953 revolutionized SC technology after observing that doped silicon is much more efficient than selenium. This was indeed the birth of the first generation of SCs: thick, mono-crystalline, single junction photovoltaic cells made out of silicon. This type of cells is still dominating the market today reaching cell efficiencies up to 24% in production (achieved by SunPower Corp. in 2012[1]) and coming close to their theoretical maximum of 31%[2] or 33.7% (the Shockley-Queisser limit[3]). The most prominent disadvantage of this type of cells is the high material costs of the mono-crystalline silicon rods. As a result of the high ratio of material costs to module costs of around 50% and because mass-production of monocrystalline silicon has already happened and is hence not expected to lead to further cost reductions, it will be difficult to reduce the costs of this type of SCs further in the future.

The second generation, addressing the high production costs, contains inorganic thin-film SCs such as cadmium telluride (CdTe), copper indium gallium selenide (CIGS) as well as amorphous, multi- and micro-crystalline silicon cells. Some companies, e.g. First Solar who produce CdTe cells via roll-to-roll techniques, claim to be able to produce power already below grid parity in California, at around 0.75$/W.[4] Their CdTe cells (modules) have an efficiency of about 17% (14%).[4]

The third generation basically includes the types of SCs that are less developed. Among them are dye-sensitized and polymer SCs, but also tandem and concentrator cells. This thesis deals with polymer SCs which on the one hand have a smaller efficiency (ca. 6% for solution processed cells in the lab in 2007)[5] and 9% at the beginning of 2012[6] compared to other cells (24% for the first generation[1], 17% for CdTe cells and 11% for dye-sensitized cells[7]) but on the other hand offer a huge potential as low-cost alternatives, because mass production techniques such as screen-printing, ink-jet printing and even roll-to-roll printing are applicable. There is another company, Heliatek, which is worth mentioning here, which combines material evaporation with roll-to-roll fabrication and achieved almost 11% efficiency with their organic tandem cells in 2012.[8]

However, another hurdle that needs to be taken in order to industrially apply these cells is their lifetime. The lifetime of polymer SCs is generally reduced upon exposure to oxygen, water and UV-light. Although glass is a formidable sealing material blocking well all of the above mentioned sources of degradation, it cannot always be used due to product requirements (lightweight or flexibility may be required depending on the application).

1.3 Solar Cell Market

As mentioned above the industry is dominated by monocrystalline Si-cells. Especially in Europe the industry has grown strongly in the past years. One reason for the strong growth were governmental incentives, so called feed-in-tariffs (FiTs) which helped the consumer to recuperate some of the investment costs for installed photovoltaic capacity when energy is fed back into the grid. However, incentives are, depending on the country, being more or less slowly reduced and photovoltaics has to become truly cost-competitive. The EPIA,[9] the European Photovoltaic Industry Association, defines competitiveness for photovoltaics as "'dynamic grid parity' - the moment at which, in a particular market segment in a specific country, the present value of the long-term net earnings (considering revenues, savings, cost and deprecation) of the electricity supply from a PV installation is equal to the long-term cost of receiving traditionally produced and supplied power over the grid." Within Europe, this dynamic grid parity is expected for parts of Italy in 2013 and for parts of Germany in 2012. This and the following information in this section 1.3 are taken from the "EPIA's global market outlook for photovoltaics 2016".[9]

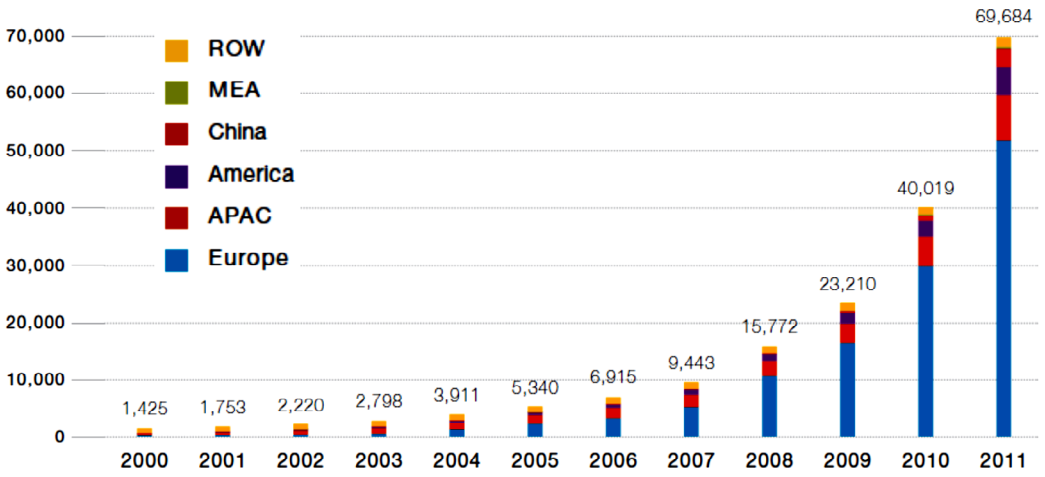

Figure 1-1. Evolution of global cumulative installed photovoltaic capacity between 2000 and 2011 in MW. ROW: Rest of the World, MEA: Middle East and Africa, APAC: Asia Pacific. Figure reprinted with permission from a report by the EPIA.[9]

As we can see from Figure 1-1, most of the currently installed global capacity is located in Europe, and within Europe, Germany and Italy are leading the front. The next few years are difficult to estimate due to changing governmental financial support schemes. In Figure 1-2 two scenarios are shown, a moderate and an (optimistic) policy driven one, visualising the global yearly new installations.

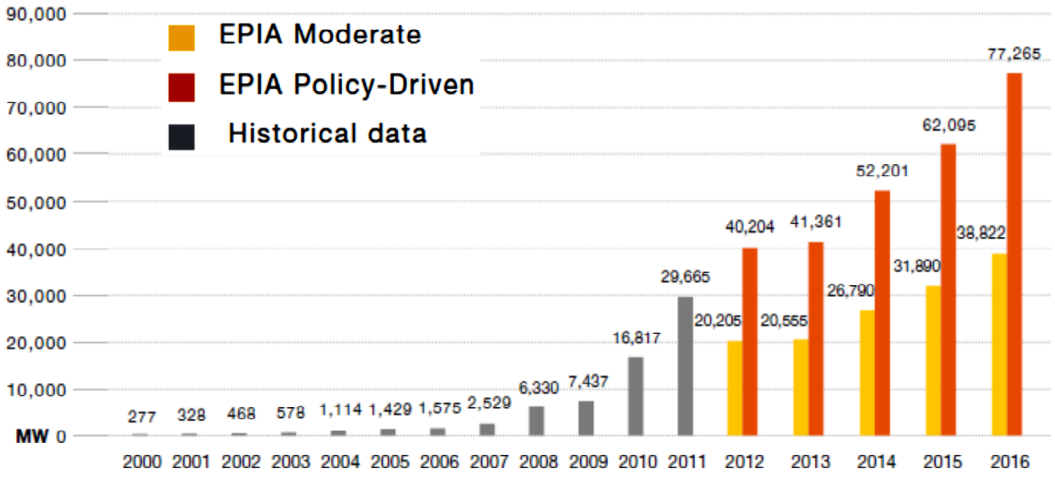

Figure 1-2. Global annual market scenarios of new installations (in MW) until 2016. Two scenarios are presented: the moderate and policy driven scenario. Figure reprinted with permission from a report by the EPIA.[9]

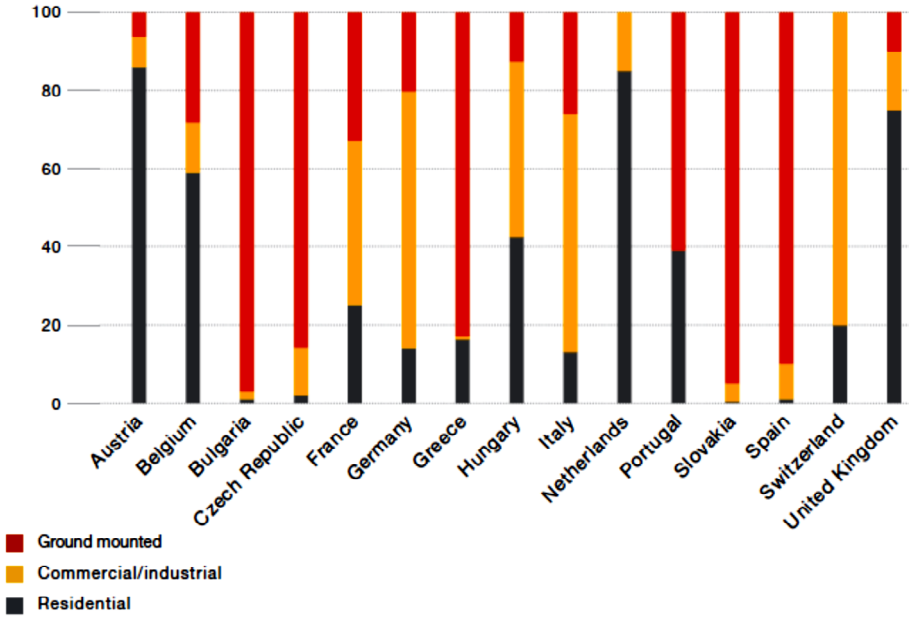

Figure 1-3. European PV cumulative capacity segmentation until 2011 (in %). Figure reprinted with permission from a report by the EPIA.[9]

Figure 1-3 shows the market segmentation of the PV industry. It divides the applications into ground mounted solar panels, commercial and industrial rooftop applications and residential installations. We can see that within Europe, commercial rooftop applications are dominating. It is predicted that this trend towards commercial rooftop applications will continue in the next years.

1.4 Organic Materials in Consumer Products

As far as I am aware, at the time I am writing this thesis (year 2012), conjugated polymers have not penetrated the market. OLEDs are already in wide use, especially smartphone displays (e.g. by Samsung and Sony) and even larger monitors, but they contain conjugated small molecules, not conjugated polymers. Organic transistors have also not yet penetrated the market. Sony demonstrated a flexible OLED display built on organic thin-film transistor (TFT) technology in 2007[10] and a flexible e-reader driven by organic TFTs in 2011,[11] but no product came to market yet.

At this point I would like to note that electronic paper (e-paper, electronic ink) as used in e-readers or pricing labels in retail shops do not contain OLEDs. The circuitry may be driven by organic TFTs as mentioned above but the e-reader itself is not emitting light, only reflecting it in a certain way, which is why it has such a low power consumption.

In the area of polymer photovoltaics, Konarka Technologies was one of the leading companies and produced polymer SCs from 2008. However, they had to file for bankruptcy protection in 2012.

1.5 Physics of Organic Semiconductors

A material is *organic* when its core consists mainly of hydrocarbons, but what makes a material a *semiconductor*? The main difference between conductors, semiconductors and insulators lies in the density of states around the Fermi energy (E_F). Conductors have got free states around E_F so that electrons can gain energy by an applied electrical field. Semiconductors and insulators on the other hand do not have free states around E_F and an electrical field can typically *not* transfer electrons from the valence band (VB) to the conduction band (CB). The band gap energy (E_G), i.e. the difference between the lowest CB energy and the highest VB energy, distinguishes semiconductors (< 3 eV) from insulators (> 3 eV). Note that the value of 3 eV is rather arbitrary as the transition from semiconducting to insulating is smooth and the literature does not give one precise value. For a vanishing band gap the material becomes metallic. In the following I will introduce the physics of organic semiconductors (with occasional comparisons to inorganic semiconductors) and the working principle of organic solar cells.

More background on the photophysics of organic semiconductors is given in section 3.2 on page 81 where issues related to singlet and triplet states, such as the exchange energy, transition rules, and the heavy-atom effect, are discussed.

1.5.1 Introduction to Organic Semiconductors

1.5.1.1 π-Conjugated System

There are two major classes of organic semiconductors: low molecular weight materials and polymers[i]. Both have in common a so called *conjugated π-electron system*.

"A conjugated system is a molecular entity whose structure may be represented as a system of alternating single and multiple bonds. In such a system, *conjugation* is the interaction (overlap) of one p(π)-orbital with another across an intervening σ-bond."[12] Many orbitals can overlap in this manner resulting in one large delocalised π-orbital. This behaviour can be easily explained by the valence bond theory, according to which three of the four valence electrons of a backbone carbon atom are hybridised, giving rise to three sp^2 orbitals. These three sp^2 orbitals form σ-bonds with two other carbon atoms and one hydrogen atom. The remaining valence electron in the p_z-orbital is not bound to another atom and hence free to facilitating electron cloud overlap to adjacent carbon atoms by forming the essential π-bond (see Figure 1-4a). This is visualised in Figure 1-4c for benzene.

[i] The Nobel Prize has been awarded to Alan Heeger, Alan MacDiarmid and Hideki Shirakawa 'for their discovery and development of conductive polymers' in 2000.

The conjugated system can be mainly consisting of double bonds as in polyacetylenes, or mainly of aromatic cycles as in polyfluorenes, or a mixture as in poly phenylene vinylene (chemical structures see Figure 1-5).

Nowadays, conductivities of conjugated polymers are considered "high"[13,14] from about 1 $cm^2 V^{-1} s^{-1}$.

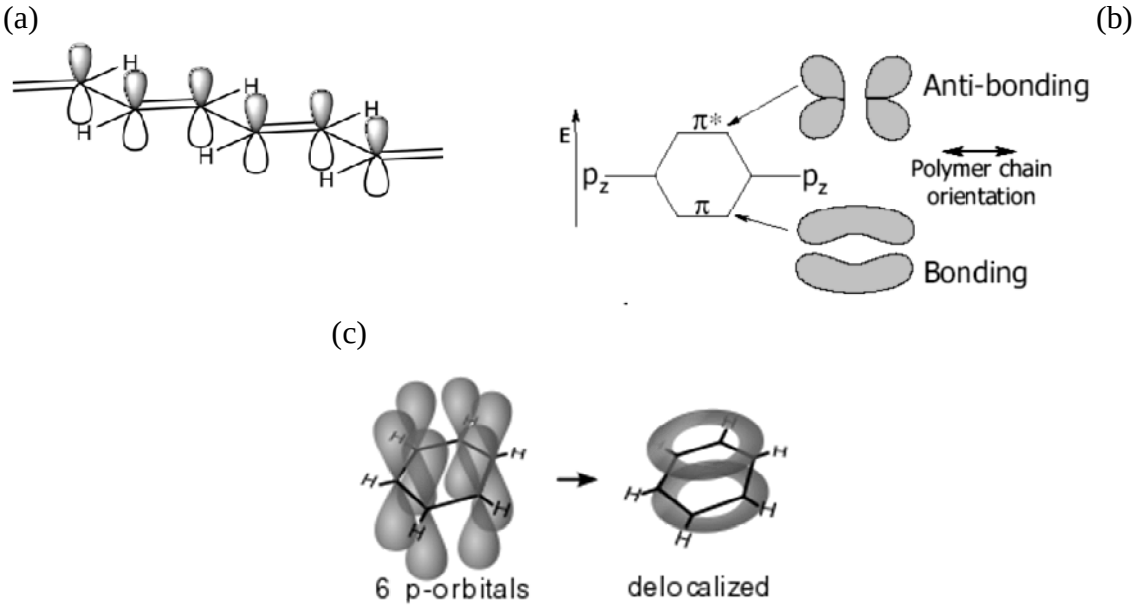

Figure 1-4. (a) Backbone of polyacetylene with p_z-orbitals at each carbon atom. (b) p_z-orbitals can overlap or repulse each other, resulting in bonding π or anti-bonding π*-orbitals. (c) Visualisation of how near p_z-orbitals overlap to create a large delocalised π-orbital.[15] Figure reprinted with permission according to the Creative Commons Attribution-Share Alike 3.0 Unported license. (Note that according to the molecular orbital theory, more than one bonding π -orbital is generated. The rings in (c) is an approximation of the result of the overlap of three bonding π-orbitals).

1.5.1.2 HOMO and LUMO Energy Levels

In organic materials, one rarely deals with bands (a more detailed discussion about why conjugated polymers do not resemble inorganic semiconductors can be found in the literature[16]) and the roles of the VB and CB energies are adopted by the highest occupied molecular orbital (HOMO) and the lowest unoccupied molecular orbital (LUMO) energy levels. The energy necessary for a $\pi - \pi^*$-transition, i.e. the energy gap between the bonding π-orbital (acting as the HOMO) and the anti-bonding π^*-orbital (acting as the LUMO) (Figure 1-4b) is typically in the range of 1.5 eV (e.g. for polyacetylene) to 3 eV, leading to absorption and emission in the visible range.

This energy gap, whose size is one reason why these materials are regarded as "semiconductors", is among others dependent on the degree of conjugation. More precisely, a

larger conjugation length leads to a smaller energy gap (as it can be imagined by thinking of a particle in an infinitely high, one-dimensional box, whose energy levels are known to be proportional to $1/L^2$, where L is the length of the box). This also shows that any kind of defect reducing the conjugation will lead to a blue shift. Possible defects are twisting of the backbone, cis-linkages and chemical defects such photo-oxidation of a backbone carbon atom. We see furthermore that the energy gap can be controlled in a certain degree by controlling the molecular weight of the polymer, i.e. the number of repeating units forming the molecule. (→ band gap engineering).

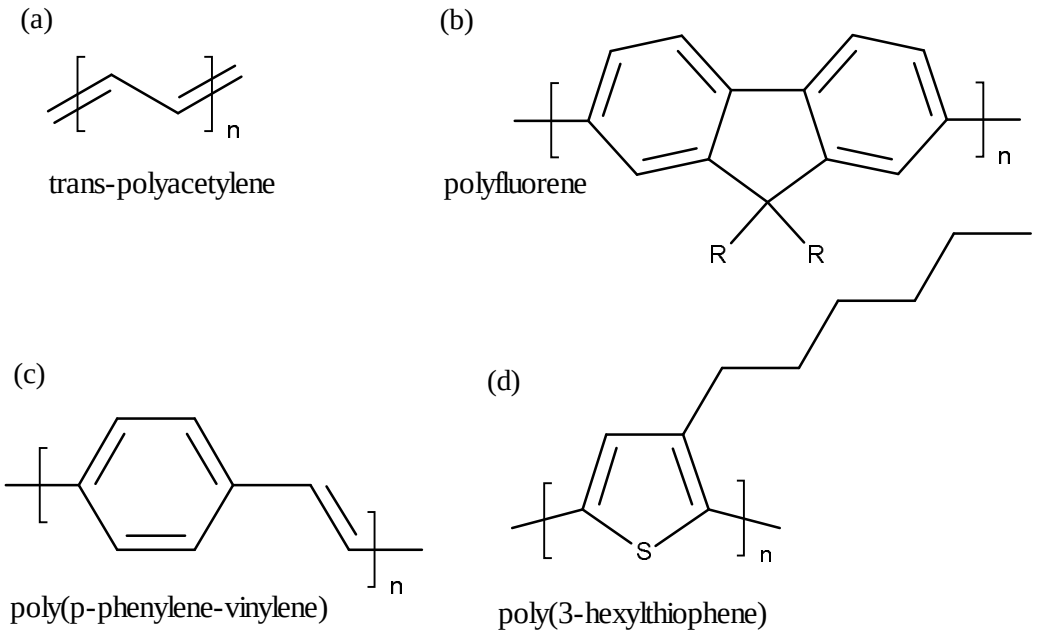

Figure 1-5. Chemical structures of various conjugated polymers. a) Polyacetylene was the first polymer to show a reasonably high conductivity. b) Polyfluorenes have a conjugated system that consists of an aromatic cycle. c) Poly(phenylene vinylene) (PPV), the first polymer used in OLEDs. d) Poly(3-hexylthiophene), the first polymer to give SCs with efficiencies > 3%.

1.5.1.3 Difference Between Molecular Crystals and Amorphous Solids

In the last part of this brief introduction to organic semiconductors I would like to point out main differences between the energy levels of isolated organic molecules, molecular crystals and amorphous solids: Single molecules (excluding long polymers) have discrete energy levels similar to single atoms. If one now introduces a lattice of molecules of the same type, the energy levels need to split up and a band structure arises. In comparison to inorganic semiconductors, however, the bands are quite narrow (less than some kT at room temperature). In disordered organic solids and polymers, the molecular environment will differ considerable leading to a Gaussian density of states[17] and to slightly varying band gaps. Generally one can say that by

increasing the disorder, charge transfer relies more and more on hopping as opposed to band transport. Conjugated polymers usually fall into the category of disordered molecules. Although they might exhibit very strong delocalisation within the molecule, intermolecular charge transport mostly relies very much on hopping.

1.5.2 Introduction to Excitons in Organic Semiconductors

1.5.2.1 Excitons in Inorganic Semiconductors

If a photon of energy $h\nu \geq E_G$ is absorbed by an electron from the VB, this electron will be excited to the CB, leaving behind a positive charge, the hole, in the VB. The electron and the hole now form, at least for a short moment, an exciton, i.e. a bound electron-hole pair. The binding energy of these excitons ('Mott-Wannier-excitons') is smaller than 100 meV and their Coulomb radius, i.e. the average distance between electron and hole, is bigger than the lattice constants. Therefore, these excitons not only have a large diffusion length, but can also be separated rather easily simply by thermal activation at room temperature.

1.5.2.2 Excitons in Organic Semiconductors

Optical excitations in conjugated polymers can be described relatively successfully by excitons. Upon photoabsorption, a geminate electron-hole pair is generated. In contrast to inorganic semiconductors, the average relative permittivity in organic materials is smaller (e.g. 11.68 for Si, 2.25 for polyethylene) so that the excitons ('Frenkel excitons') are relatively strongly coulombically bound with a binding energy of 0.5 to 1 eV[16]. Dissociating these strongly bound excitons is, next to charge collection, the most important critical tasks in organic photovoltaic cells.

The average distance an exciton can move before recombining (radiatively or non-radiatively), i.e. the exciton diffusion length, is typically of the order of 10 nm in conjugated polymers,[18,19] although higher diffusion lengths up to 70 nm have been measured as well.[18,20] It is mainly determined by the Förster radius R_F, which will be explained further in the section 1.5.3.1 on page 36.

The differences between singlet and triplet excitons will be discussed later in chapter 3 on page 81.

1.5.3 Excitation Energy Transfer in Organic Semiconductors

There are three types of energy transfer that are of importance when dealing with excitons. These are trivial energy transfer, Förster Resonance Energy Transfer and Dexter Energy transfer. Trivial transfer is the recombination of the exciton on the donor (D) under emission of a photon and reabsorption of that photon by an acceptor (A). The trivial transfer has a principally infinite range and depends obviously on the overlap of the emission spectrum of D and absorption spectrum of A. This process of reabsorption will not be discussed further. In the following, I will discuss the other types of energy transfer in more detail.

To clarify the notion, I would like to mention that precisely speaking, both, charge and excitation energy transfer actually involve energy transfer. However, the term (excitation) energy transfer is used when charge transfer is excluded.

The different excitation energy transfer mechanisms may be divided into several categories: heterotransfer/homotransfer and radiative/non-radiative transfer.

- A *heterotransfer* is a process by which an excited donor molecule D transfers energy to an acceptor molecule A corresponding to

  $$D^* + A \rightarrow D + A^*.$$

  Therefore this process describes exciton transfer between molecules of different materials.

- Accordingly, a *homotransfer* describes the (repeated) transfer to molecules of the same kind (D = A) and hence also describes energy migration within one material.

- A *radiative* transfer involves a photon as the energy transporting entity, so the process could be written as:

  $$D^* \rightarrow D + h\nu \text{ “followed by” } A + h\nu \rightarrow A^*,$$

  where $h\nu$ is the energy of a photon. This type of energy transfer is also called *trivial energy transfer*.

- A *non-radiative* transfer does not involve a photon and could be illustrated as:

  $$D^* \rightarrow D \text{ “and simultaneously” } A \rightarrow A^*.$$

  The processes falling into this category are the *Förster Resonance Energy Transfer (FRET)* and the *Dexter transfer*.

1.5.3.1 Förster Transfer

Förster Resonance Energy Transfer (FRET) or short Förster transfer is the main type of (intermolecular) energy transfer in conjugated polymers. FRET mainly describes singlet-singlet energy transfer (see transition rules in section 3.2.3 on page 82). It is often approximated as a dipole-dipole interaction between two point dipoles, although this approximation is rarely appropriate considering typical radii of Frenkel excitons of some nanometres (hence approaching the D-A distance).

The transfer rate relies among others on the overlap between the emission spectrum of the donor and the absorption spectrum of the acceptor. Assuming D and A are point dipoles, the FRET rate (k_F) can be calculated[21] as follows:

$$k_{\mathrm{F}} = k_{\mathrm{D}}^{0} \left(\frac{R_{\mathrm{F}}}{r}\right)^{6}, \qquad \text{Eq. 1-1}$$

where

$$R_{\mathrm{F}}^{6} = \frac{9000\, Q_0 \ln(10) \kappa^2 J}{128 \pi^2 n^4 N_{\mathrm{A}}} \qquad \text{Eq. 1-2}$$

and

$$J = \int f_{\mathrm{D}}(\lambda) \varepsilon_{\mathrm{A}}(\lambda) \lambda^4 d\lambda. \qquad \text{Eq. 1-3}$$

k_D^0 is the decay rate of the excited state in the absence of FRET, R_F is the Förster radius, r is the distance between D and A, Q_0 is the fluorescence quantum yield of D in the absence of A, κ^2 is the kappa square factor which takes into account the relative orientation between the two transition dipoles, n is the refractive index of the medium surrounding D and A, N_A is the Avogadro number, J is the spectral overlap integral between the normalised emission spectrum of the donor ($f_D(\lambda)$) and the extinction coefficient of the acceptor ($\varepsilon_A(\lambda)$).

Simply by looking at Eq. 1-1 on its own, it is clear that R_F is the distance between donor D and acceptor A at which the FRET is as efficient as all the other (radiative and non-radiative) decay channels combined, i.e. at which $k_F = k_D^0$. Already at a distance of $2\ R_F$, however, is the FRET rate reduced to $(1/2)^6 \approx 1.6\%$ of k_D^0.

R_F is the average distance an exciton can move, so it gives an estimate of the maximum distance between molecules which still allows exciton migration. (Of course, as one is talking about probabilities, there is no maximum distance in a narrow sense.) Since FRET is the more probable (longer-range compared to Dexter transfer) singlet-singlet transfer route, R_F turns out to be a key parameter for OSCs, as it determines the maximum allowed distance between a

photogenerated exciton and a type II heterojunction that still allows splitting the exciton with a considerable probability.

1.5.3.2 Dexter Transfer

The Dexter transfer can be thought of as an electron exchange via tunnelling, i.e. two molecules exchange an excited electron with an electron of lower energy, most probably in the ground state. As this type of excitation energy transfer requires electron cloud overlap, it is only a short range interaction with an exponentially decreasing rate as a function of the donor-acceptor distance.

The Dexter energy transfer describes the triplet-triplet energy transfer but is also a possible mechanism for singlet-singlet energy transfer (see section 3.2.3 on page 82 regarding the explanation of the transition rules). For the latter process, however, FRET usually dominates due to its longer-ranged nature (efficient up to several nm D-A separations). The transfer rate of the Dexter transfer also relies on the overlap between the donor emission and acceptor absorption spectrum and can be calculated as follows[22]:

$$k_D = K\,J\,e^{\frac{-2r}{L}}, \qquad \text{Eq. 1-4}$$

where *K* is related to the specific orbital interactions, *J* is a spectral overlap integral normalised for the extinction coefficient of the acceptor and *L* is the Van der Waals radius. As already pointed out, FRET dominates in typical conjugated polymers.

Dexter transfer can also be thought of as a simultaneous transport of an electron and a hole with a rate constant equal to a to the product of electron and hole transfer rate as calculated via Marcus theory.[23,24] In Marcus theory the rate constant is due to an ionic term that recognizes the free energy for formation of a transition state and an electronic term proportional to the probability for charge transfer at the transition state.[25] The electron or hole transfer rate (*k*) is given by

$$k = \sqrt{\frac{4\pi^3}{h^2\lambda k_B T}}\,|M_{DA}|^2 \exp\left[-\frac{(\Delta G + \lambda)^2}{4\lambda k_B T}\right], \qquad \text{Eq. 1-5}$$

where λ is the reorganisation energy, T is the temperature, k_B is the Boltzmann constant and M_{DA} is the transfer integral. Therefore, for small changes in G, i.e. $\Delta G \approx 0$, Marcus transfer via an activated complex behaves similar to an Arrhenius barrier of *λ/4*. As the difference in triplet energies of donor and acceptor increases (and assuming $G_D > G_A$, i.e. $\Delta G < 0$), the transfer rate

increases as well until resonance is reached ($-\Delta G = \lambda$). For large differences, however, the transfer rate decreases, leading to the "Marcus inverted region".[25]

1.5.3.3 Heterojunctions

A *heterojunction* is an interface between molecules (or atoms) of different types. As illustrated in Figure 1-6, different types of heterojunctions lead to different processes, i.e. either charge or energy transfer.

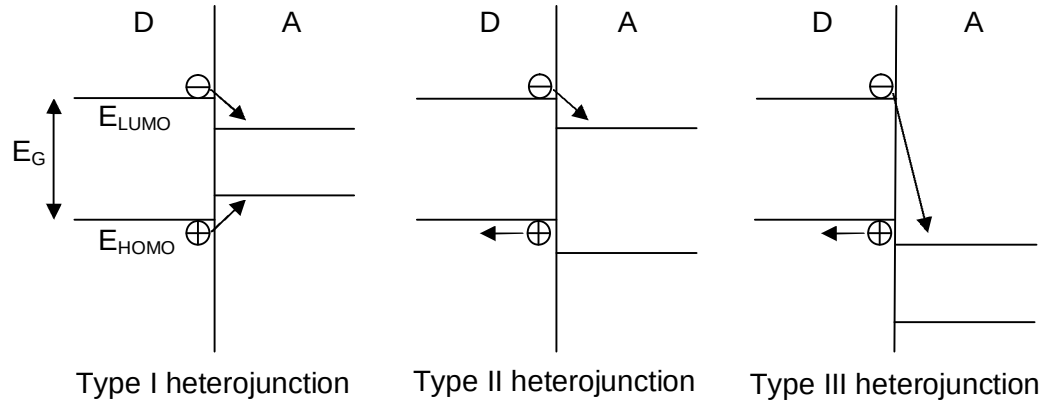

Figure 1-6. Energy diagrams of the three different types of heterojunction between a donor molecule D and an acceptor molecule A. The type II (staggered) heterojunction facilitates charge separation, i.e. the desired process in OSCs. Note that in a type III heterojunction the HOMO and LUMO energy levels would change once materials get in contact. More precisely, considering the isolated energy levels, electrons from just below the HOMO level of the donor could transfer to the LUMO of the acceptor and hence fill it.

In a type I heterojunction, the energy gap of the one material, now referred to as the (electron-) acceptor A, is located completely within the energy gap of the other material, the (electron-) donor D. If one now imagines an exciton on D, one clearly understands that the electron from the LUMO as well as the hole from the HOMO may transfer to A, as this is energetically favourable; hence this kind of interface results in energy transfer. (Whether or not this transfer happens at once or one after another is not of importance at this point. The result is that energy is transferred from D to A).

In a type II heterojunction on the other hand, where the LUMO and the HOMO of the acceptor are deeper (i.e. greater electron affinity and greater ionisation potential), only the electron is likely to be transferred from D to A; hence this type of interface is likely to result in charge

transfer. The same would hold for a type III heterojunction (also called broken heterojunction), but this type of interface usually does not occur when dealing with organic semiconductors. The type II heterojunction is the desired heterojunction for OSCs where the exciton needs to be separated into different charges.

1.5.4 Charge Transport in Organic Semiconductors

In ordered *in*organic semiconductors atoms are covalently bonded and the delocalisation of orbitals is so large that band transport describes charge transport very well. In organic materials, molecules are only weakly bonded by the Van-der-Waals forces, they are often rather disordered (especially long range order) and delocalisation is usually small. Depending on the degree of order, charge carrier transport in organic semiconductors can fall between two extremes: band transport and hopping. In the following I will describe the mobility (μ) in each case. The current density (J) is related to the mobility via

$$J = q\, n\, \mu\, F, \qquad \text{Eq. 1-6}$$

where q is the electronic charge, n is the charge carrier density and F the applied electric field.

1.5.4.1 Band Transport

Band transport is typically observed in ordered, highly purified molecular crystals, fabricated for example by chemical vapour deposition, at not too high temperatures. Because the delocalisation is still relatively weak compared to inorganic semiconductors, the bandwidth is small (typically a few kT at room temperature only), leading to mobilities of 1 to 10 cm²/Vs at room temperature.[26] The mobility (μ) dependence on temperature (T) in ideal band transport can be approximated by

$$\mu \sim T^{-n} \qquad \text{Eq. 1-7}$$

where n = 1…3, depending on the dimensionality of the system. (However, in the presence of traps, significant deviations from this law are observed). Increasing T leads to stronger electron-phonon coupling, hence to increased effective masses and reduced band widths, therefore to a reduced μ.

1.5.4.2 Hopping Transport

Hopping on the other hand is the dominant charge transport process in disordered materials. Although polymers can aggregate and show somewhat increased crystallinity, in most cases, they fall into this category.

Hopping transfer is usually described by Marcus theory whose electron transfer rate was already shown in the section 1.5.3.2 about Dexter transfer according to Eq. 1-5. Note that the hopping rate is hence proportional to a tunnelling term, $|M_{\mathrm{DA}}|^2$, which takes into account the wave function overlap, and an activated hopping term, $\exp[(\Delta G + \lambda)^2/(4\lambda k_{\mathrm{B}}T)]$, which is equivalent to an Arrhenius barrier E_{A} of the height $(\Delta G + \lambda)^2/(4\lambda)$. Furthermore a Poole-Frenkel-like electric-field dependence was found, which means that the hopping rate (and hence μ) is dependent on the electric field in the following form:

$$\mu \propto \exp\left(-\frac{E_A + \sqrt{q^3 F/(\pi\epsilon_0\epsilon)}}{k_{\mathrm{B}}T}\right), \qquad \text{Eq. 1-8}$$

where $\epsilon_0\epsilon$ is the dielectric permittivity. Note that although the Poole-Frenkel mechanism,[27] which treats the effect of F on carriers trapped in Coulomb potential wells in isotropic solids, may not be the 'true' reason for the observed field dependence, Eq. 1-8 is in good agreement with many observations. (Other models such as the charge-dipole[28] model, the Guassian disorder model[29] or the correlated disorder model[30] also result in such a field dependence).

I would like to emphasize that only a very brief overview has been given here and that charge transport modelling in organic semiconductors remains a topic of active research. There is no model available that can describe most organic materials due to a variety of effects such as mobile defect states, unintentional doping, disorder, morphological effects, etc.. Note that electron transport in conjugated polymers is usually substantially weaker than hole transport, probably due to electron traps existing in most materials. A recent study[31] even shows that the same electron trap distribution and density is present in most materials.

1.5.5 Langevin Recombination

Langevin recombination is the main type of non-geminate bimolecular charge recombination occurring in organic materials. Non-geminate (as opposed to geminate) means that it is not dealing with the charges that make up the exciton (i.e. electron-hole pair that may recombine geminately before it is split) but with charges that interact after they were successfully separated. Langevin recombination is derived under the assumption that the limiting process is

that charges come close enough to each other and not the interaction itself. The process is hence dependent on the charge carrier densities and mobilities only.

The Langevin recombination rate (R) can be derived by:[32]

$$R = \gamma\,(n\,p - n_{\mathrm{i}}\,p_{\mathrm{i}}), \qquad \text{Eq. 1-9}$$

where n and p are the electron and hole densities, n_{i} and p_{i} are the intrinsic electron and hole densities (often assumed to be zero) and γ is the Langevin recombination constant:

$$\gamma = \frac{q}{\varepsilon}(\mu_{\mathrm{e}}+\mu_{\mathrm{p}}), \qquad \text{Eq. 1-10}$$

where μ_{e} and μ_{p} are the electron and hole mobilities.

It is noted that the formula above is the simplest form of the Langevin recombination and that adjustments may have to be made to explain experimental results, such as reduced Langevin recombination[33] or two-dimensional Langevin recombination.[34]

Non-geminate bimolecular charge recombination is of tremendous importance in solar cells, influencing the fill factor (*FF*) as well as the open-circuit voltage (V_{OC}) to a large degree. As a general rule, the lower the non-geminate charge recombination, the higher the charge concentration that can be maintained and hence[35] the higher is V_{OC}.

1.5.6 Mode of Operation of Polymer Solar Cells

The processes involved in power generation in polymer photovoltaic devices can be divided into five steps. These are:

(1) Incoupling of a photon
(2) Absorption of this photon and formation of an exciton
(3) Diffusion of this exciton
(4) Dissociation of this exciton into separated charges
(5) Transport and collection of these charges at the electrodes

Polymer photovoltaic devices are typically made out of a sandwich structure, whereas the active layer, i.e. the layer where beneficial photon absorption takes place, is often a blend out of one hole-conducting and one electron-conducting material. Further layers, such as exciton blocking layers at the electrodes, may also be included, but will not be taken into account here.

A simplified band diagram of a single layer solar cell is shown in Figure 1-7.

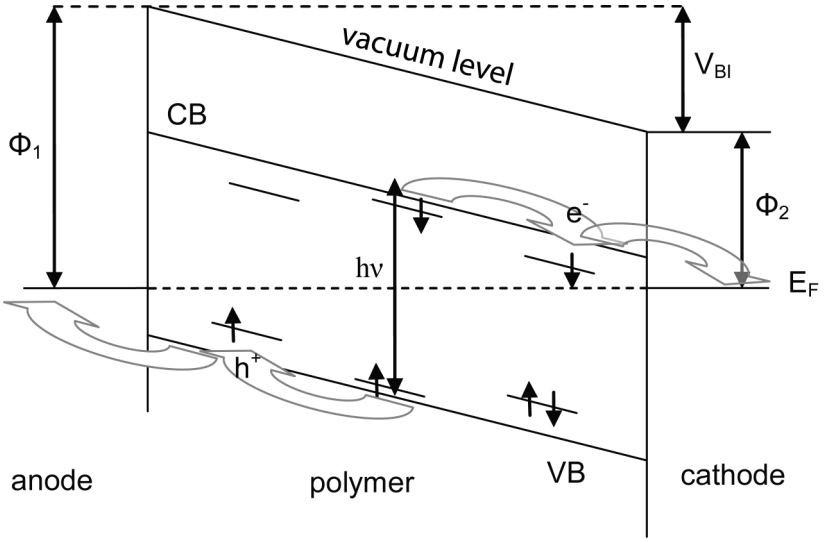

Figure 1-7. Illustration of the mode of operation of a single-layer SC with connected electrodes. The difference in work functions (Φ_1 and Φ_2) of the electrodes (the built-in voltage V_{BI}) cause an electrical field. Assuming there are no free charge carriers within the polymer, the potential is a linear function of the position, i.e. linear band bending results. After absorption of a photon of energy *hv*, an exciton is generated which is split into electron and hole. It is assumed here that no type II heterojunction is needed to split the exciton.

1.5.6.1 Incoupling of a Photon

Light usually comes in through a transparent, conductive oxide such as indium tin oxide (ITO). The higher the refractive index of this material, the higher is the reflection loss at the air-glass interface. Special anti reflection layers (e.g. downward pointing pyramids[36] or one-dimensional gratings[37]) can improve the efficiency by reducing the reflectance or by increasing the optical path and hence the chance of photon absorption.

1.5.6.2 Photon Absorption and Exciton Formation

The aim is to absorb as many photons as possible within the active layer of the SC. The overall light absorption depends on the absorption spectrum (coefficient), thickness and the local electrical field ($|\boldsymbol{E}|^2$) in the active layer. The latter depends not only on the active layer itself, but, due to the micro cavity effect, on the transmission, refractive index and thickness of *each* layer. Also, other optical features such as a patterned electrode or nanoparticles within a layer (which may change the refractive index or lead to plasmon-enhanced absorption) can change the local electrical field.

The absorption spectra of the polymer should as a first approximation match fairly well the solar spectrum to absorb the maximum amount of light. This is achieved by using a small band gap material. On the other hand, a small band gap will limit the open circuit voltage (V_{OC}), so that the HOMO-LUMO gap should ideally be around 1.4 eV. The ideal band gap is discussed in more detail in the section 3.8.3 on page 191. Initially, most polymers lacked absorption in the important red part of the spectrum, so huge efforts have been undertaken to reduce their band gap.[38] However, reducing the band gap too much to perfectly match the solar spectrum is not beneficial because a lowering of the band gap also results in a lowering of the open-circuit voltage (V_{OC}) which is connected to the difference of the LUMO levels of the (electron-) acceptor and the HOMO level of the donor.

$$e\,V_{\mathrm{OC}} = E^{\mathrm{A}}_{\mathrm{LUMO}} - E^{\mathrm{D}}_{\mathrm{HOMO}} - 0.2\ \mathrm{eV} \qquad \text{Eq. 1-11}$$

The value of 0.2 eV is not very precise and depends on the materials and morphology. A visualisation of the dependence of V_{OC} on the energy levels is shown in Figure 3-2 on page 88.

1.5.6.3 Exciton Diffusion

After the exciton has been generated through photoabsorption, it will move through the material, driven by an electrical field due to a difference in work function or due to a chemical potential gradient near heterojunctions. The corresponding transport processes (Förster and Dexter transfer) have already been described in the section about excitation energy transfer.

The exciton (or polaron pair (see page 87)) will move until it is either trapped, dissociated, decayed radiatively (luminescence) or decayed non-radiatively (vibronic or thermal decay). As already mentioned, the exciton diffusion length of conjugated polymers is typically 10 nm.[19]

1.5.6.4 Exciton Dissociation

The dissociation of an exciton, i.e. the splitting of the exciton into a free electron and hole, is the only desirable route for photovoltaic applications. Although it can happen at material inhomogeneities or at electrode-polymer interfaces, exciton dissociation is particularly efficient at type II heterojunctions[39] as described earlier.

1.5.6.5 Charge Transport and Collection at the Electrodes

Upon exciton dissociation, the charges need to find their ways to their respective electrodes. Especially for blends as active layers, the existence of continuous percolation paths is critical.

Even if a charge carrier is close to the respective electrode, it is not certain that it will be able to reach the metal. "The probability associated with all the barrier penetration mechanisms involved at the interfaces towards the metallic surfaces is a function of geometry, topology, and interface formation."[39]

1.5.6.6 Loss Mechanisms

There are loss mechanisms at every step described above.

1. Photon absorption is imperfect due to the nature of the limited absorption in the active layer and due to incoupling losses (light transmission and reflection).
2. Exciton recombination:
    - Excitons may decay to the ground state at any stage of their lifetime.
    - Charge-exciton reactions can deactivate the exciton.
    - Depending on the solar cell, inter-system crossing to a triplet exciton may also present a loss mechanism.
3. Charge recombination or trapping:
    - Electron and hole may mutually recombine with each other just after exciton dissociation ("geminate charge recombination"). Note that in typical polymer-fullerene SCs charge transfer at the type II heterojunction is orders of magnitude faster than exciton decay or charge recombination[30,31] so that geminate charge recombination does not pose a problem in such systems. On the other hand, efficiencies of most polymer-polymer solar cells are indeed reduced by inefficient exciton dissociation.
    - Electron and hole may recombine at a later stage with other free charge carriers ("non-geminate charge recombination"). This bimolecular recombination is usually assumed to be of Langevin-type and increases with mobilities and charge carrier densities.
    - They may also become trapped and act as charge or exciton recombination centres.
4. Charge collection (extraction) at the electrode.

It is noted that electrons or holes may not always perfectly recombine with their respective electrode so that the low surface recombination rate may create a space charge. The space-charge creates an S-shaped JV curve decreasing the solar cell performance.[40,41]

2 Scanning Thermo-Chemical Lithography of a Conjugated Polymer

2.1 Motivation

If we were able to pattern the active layer of OSCs with high resolution and high throughput, we would have a route to reduce the duration of morphology optimizations by a very large degree and improve the SC efficiencies. The reasoning is the following: The high binding energy of the photogenerated Frenkel-excitons requires the use of two materials within the active layer to generate a type II heterojunction where excitons, i.e. bound electron-hole pairs, can be efficiently split into free charge carriers. The problem now is that the exciton diffusion length is of the order of 10 nm for typical conjugated polymers such as PPV,[42] so that the maximum distance from any point in the active layer to an interface should not exceed this quantity to assure efficient exciton dissociation. In order to solve that problem it is common to use the bulk-heterojunction architecture where both materials are simply mixed to create an interdigitated network where the domain size is not much larger than the exciton' diffusion length. This approach, however, is detrimental to charge transport due to island formation and a high degree of non-geminate charge recombination. If an exciton is split at an interface with an island, one of the two carriers will be trapped, never able to reach an electrode to generate current. Instead, the trapped charge on an island may recombine geminately, i.e. with its initial counter charge, or non-geminately, i.e. with another free charge carrier, reducing the efficiency of the SC. Patterning the active layer in a controlled manner as in Figure 2-1 would significantly improve the charge transport while maintaining the good exciton dissociation ability of the common bulk-heterojunction architecture.

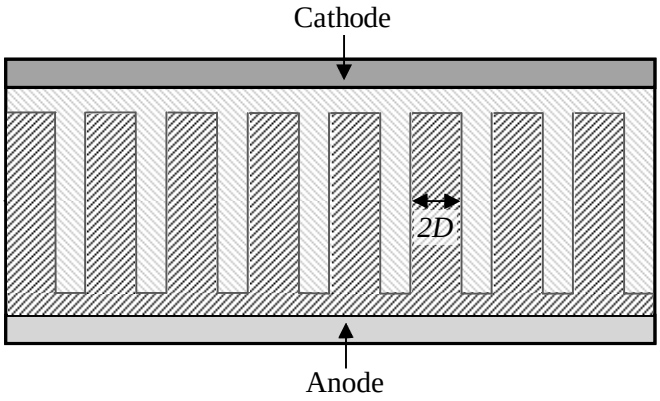

Figure 2-1. Ideal structure of a patterned device with a large heterojunction interface. *D* is the exciton diffusion length of the light absorbing polymer. A typical active layer thickness is ~ 100 nm.

In my experiments I used SThL to convert the poly(p-phenylene vinylene) (PPV) precursor poly(p-xylene tetrahydrothiophenium chloride) (PXT, see Figure 2-4c). PPV is a prototypical conjugated polymer as it is one of the first that has been successfully applied to create organic LEDs[43,44] transistors,[45,46] and photovoltaic cells.[47-49] By choosing a π-conjugated polymer instead of an arbitrary polymer I can show more directly and more convincingly how SThL may be used in the future to produce high efficiency OSCs.

The work described in this thesis is different from the work presented in my MSc thesis. During the MSc project I conducted SThL experiments on ITO whereas within the PhD project I investigated the influence of the thermal conductivity of the underlying substrate via finite element modelling, which was used to simulate the temperature distribution during SThL. Finite element modelling is a numerical method to solve partial differential equations if analytical techniques do not work because either the differential equations themselves or the geometry is too complicated. As the simulations are a means to understand experimental observations, the experimental methods and results will be presented in the next section. Experiments on gold were carried out by other members of the group during the PhD project.

2.2 Background

In this section I will give an overview over various nanolithography techniques including scanning thermo-chemical lithography (SThL) and I will describe how an atomic force microscope (AFM) as well as a thermal AFM works. For a better understanding of the motivation above refer to the section 3.2 on page 81 where a general introduction to π-conjugated polymers and OSCs is presented.

2.2.1 Scanning Thermo-chemical Lithography and other Nanolithography Techniques

Lithography (from the Greek words lithos = 'stone' and graphein = 'write') is a term originally describing a certain printing process, invented around 1800. During lithography, an image is drawn onto a lithography stone with a hydrophobic substance. By covering the surface with a water and ink solution, the ink will stick to the hydrophobic substance (the so called positive image) and the water will be covering the rest, i.e. the negative image. The lithographic stone can then be pressed onto paper.

Nanolithography on the other hand is a much more general term, describing all methods by which structures in the nanometre regime, i.e. ≤ 100 nm, can be fabricated. Nanolithography is of immense importance in today's science and industry. Although it has its most prominent application in nanoelectronics for the fabrication of integrated circuits, there are other areas including the development of nanosensors and other nanoelectromechanical systems (NEMS). The list of nanopatterning techniques is large, including near-field scanning and far-field photolithography; focussed ion beam and electron beam lithography;[50,51] thermal,[52] thermo-mechanical[53,54] and scanning thermo-chemical lithography (SThL); dip-pen lithography; nanoimprinting, hot-embossing and injection moulding lithography, etc. Some of them I will introduce in the following.

2.2.1.1 Other Nanolithography Techniques

Far-field photolithography[55] is the process enabling the mass fabrication of nm-sized transistors in any processor and is hence the most commonly used type of nanolithography in our time. During far-field photolithography, light is travelling through a photomask (also called optical mask or shadow mask) that contains the required geometric pattern. The light is then absorbed by a photoresist which covers the substrate underneath. Depending on the type of photoresist

(positive or negative), the exposed or unexposed areas will be rinsed away in the next step, revealing the surface underneath. At this point one has the choice to either remove substrate material in the now uncovered areas via an etching process or to locally deposit material onto the uncovered surface. Note that in order to create whole integrated circuits, the photolithographic process has to be repeated many times with different photomasks. The advantage of this technique is the high throughput of the optical (parallel) process. The equipment required to produce modern integrated circuits, however, is extremely expensive (hundreds of millions to billions of dollars). As the wavelength of the light used to expose the photoresist determines the maximum possible resolution (→ Abbé diffraction limit), the wavelength in far-field photolithography is becoming ever shorter. Currently deep-UV light is used, but extreme UV or X-ray lithography are candidates for next-generation lithography.

Scanning near-field optical lithography[56-58] (SNOL) is, as the name suggests, a serial technique and hence has a low throughput. SNOL uses an optical fibre with a sharp (~50 nm wide) opening at the end. The so called evanescent wave exiting the fibre interacts with the surface and is not limited to the Abbe diffraction limit (as the wave is not actually diffracted) and resolutions better than the used wavelength can be achieved. SNOL was also used to convert a conjugated polymer creating nanosized structures[59] similar to the work described here.

Electron beam lithography and *focussed ion beam lithography*[51,52] make use of a focussed particle beam that scans across the target surface and locally removes material. As scanning techniques they are naturally slow but obtainable resolutions are extremely good, down to ~5 nm. The optical mask used in far-field photolithography for example is typically made by electron beam lithography.

Nanoimprinting,[60] *hot-embossing*[61] and *injection moulding lithography* all rely on mechanical deformation of a film. They are similar to far-field lithography in a sense that these are parallel and hence high throughput techniques. Very good resolutions down to 10 nm have been achieved suggesting a large potential for a range of applications.

2.2.1.2 Scanning Thermo-chemical Lithography

Scanning thermo-chemical lithography, SThL,[59,62-66] is a versatile nanopatterning technique where a hot probe is scanned across a surface to induce a local chemical reaction in a thin film to generate the desired pattern.

SThL is an interesting technique as it does not suffer from the resolution limitations imposed by the Abbe diffraction limit in conventional far-field photolithography, or from the irradiation

damage caused by e-beam lithography.[67,68] Upscaling the throughput by using an array of hot probes has also been shown,[53] demonstrating that SThL can be used to produce nanoscale prototypes more cheaply and conveniently than other techniques. As an ultimate aim one can think of using SThL to pattern the active layer of SCs.

SThL is a very versatile but rather rarely applied technique. In 2004, thermo-chemical patterning of a photoresist was reported to achieve resolutions in the range of 450-1800 nm.[63] In 2007, another SThL technique based on the conversion of a copolymer from hydrophilic to hydrophobic was shown to result in sub-15 nm resolutions.[64] SThL has also been used to reduce graphene oxide,[65] to create three-dimensional structures within a thin layer of photoresist,[66] and to convert a sacrificial precursor polymer to create structures with sub-30 nm resolutions.[62]

2.2.2 Atomic Force Microscope (AFM)

The atomic force microscope (AFM) was developed by Gerd Binnig, Calvin Quate und Christoph Gerber [69] as a successor of the scanning tunnelling microscope (STM). It relies on a sharp tip being scanned across a surface with very small contact forces. Figure 2-2 shows the working principle of an AFM. The fine tip is connected to a so called cantilever, a small conducting beam than can vibrate and reflect the light coming from the laser. The reflected light is collected by a photodiode which can monitor the position of the laser spot and hence indirectly measure how much the cantilever is bent. The signal can then be used by a feedback system to alter the height of the cantilever. The cantilever is typically moved by piezoelectric crystals to control the vertical and horizontal position very accurately (sub Å resolution).

The two most common modes of operations of an AFM are the contact and tapping mode.

Contact mode

In contact mode the tip is constantly in soft contact with the surface. This is achieved by adjusting the height of the tip via the feedback loop so that the cantilever is always bent by the same amount.

Tapping mode

In tapping mode, the cantilever vibrates at one of its resonance frequencies (typically above 100 kHz). The tip will touch/"tap" the surface once every period and the amplitude of the vibration will be used as the feedback parameter.

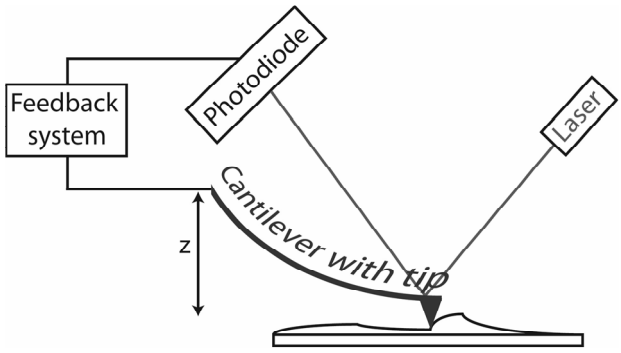

Figure 2-2. Schematic of an atomic force microscope (AFM). The bending of the cantilever is measured by a laser which is being reflected by the cantilever and detected by the photodiode. A feedback system can then adjust the z-coordinate of the cantilever while the probe is scanned across the sample.

2.2.3 Thermal AFM

The term "thermal AFM" will be used in the following to describe the instrument used to pattern the polymer surface. The difference between a thermal AFM and an ordinary AFM is that its tip is a resistive probe with a temperature dependent resistivity.

Such a resistive probe can be applied in two different ways.[70,71] It can either be used passively by providing a temperature dependant resistivity which can be used to obtain a temperature map of the surface, or, as in my experiments, it can be actively heated by applying a voltage across it. The power necessary to achieve a certain temperature (corresponding to a certain electrical resistance of the probe) can be measured to create thermal conductivity maps of the surface.

A thermal AFM is typically used for micro-thermal analysis.[70,71] During micro-thermal analysis, the probe temperature is ramped up and the response (expansion, shrinking) of the substrate/material underneath measured to obtain information about the thermal properties of the material, such as the glass transition temperature.

2.2.3.1 Calibration of the Probe

The temperature of the probe can be calibrated by assuming a linear relationship between the resistance of the probe and its temperature. The necessary reference points can be obtained by recording power–resistance (‘local differential thermal analysis’) and height–resistance (‘local thermo-mechanical analysis’) curves while heating different polymers. Each such curve allows for the determination of two data points:

The room temperature can be clearly related to the point, at which the power starts to increase. The melting temperature T_m or glass transition temperature T_G[ii] on the other hand can be determined from the height-temperature curve[72]: While the temperature increases, the polymer (and substrate underneath) will expand increasing the deflection and hence, the z-feedback being active, the height of the tip. At the transition temperature, however, this effect will be overcompensated by the probe being pushed into the now softening polymer by the force applied to the cantilever, which is determined by the set point of the AFM. Depending on parameters such as the thickness and viscosity of the film, as well as the thermal properties of the underlying substrate, the drop in the slope of the height-resistance curve will be more or less dramatic. The transition temperature is often taken as the temperature at which the slope of the probe height as a function of temperature changes suddenly.[72]

The reference polymers in my experiments are

- poly(caprolactone) (PCL) with T_m = 60 °C,
- polyethylene (PE) with T_m = 120 °C and
- poly(ethylene terephthalate) (PET) with T_G = 262 °C

After measuring each polymer at least three times with a heating rate of 10 °C/s, a linear regression between the probe resistance and the temperature was carried out (see Figure 2-3). Note that although rather large deviations of 30-50 °C between glass transition temperatures measured by local thermo-mechanical analysis and differential scanning calorimetry (DSC) have been reported[73], my calibrations resulted in straight lines between resistance and temperature indicating successful calibrations.

[ii] There is a difference between T_m and T_G of a polymer: T_m is characteristic for the crystalline part of the polymer and is associated with the first order phase transition which involves the latent heat. T_G on the other hand is the second order phase transition, which is connected to the amorphous part of the polymer. T_G is smaller than T_m. In the following I will refer to the term “transition temperature” if I do not want to specify the type of transition.

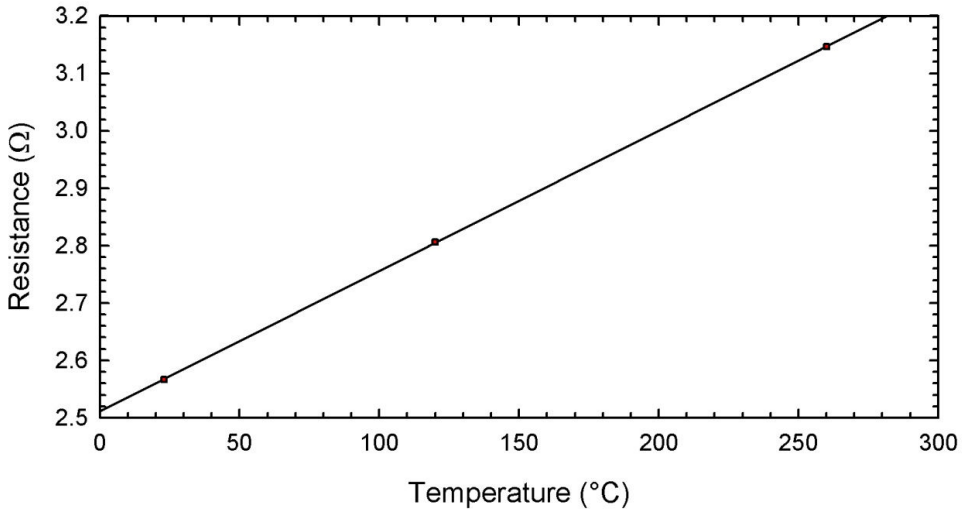

Figure 2-3. Calibration curve after using two reference polymers with transition temperatures at 120 °C (PE) and 262 °C (PET). Image taken from Tolk.[74]

2.3 Experiment

2.3.1 Thermal AFM

The thermal AFM used for my experiments consisted of an AFM (Explorer, Veeco Instruments – Santa Barbara, CA) on which a so-called Wollaston wire probe[75,76] (Bruker) was mounted. This resistive probe consists of a 75 µm diameter silver wire which is etched and bent in the middle to expose a ≈ 5 µm diameter platinum-rhodium (9:1) core (see Figure 2-4a). The thermal AFM allowed temperatures up to 650 °C (a temperature so high that it is commonly used to "clean" the probe, as most organic materials will disintegrate at such high temperatures).

To avoid confusion I will refer to the term “thermal AFM” whenever I am referring to this instrument and “AFM” when I am referring to the Veeco Dimension 3100 that was used to image the final structures. All AFM images presented in this report are tapping mode images whereas the amplitude of the cantilever vibration is used as the feedback variable.

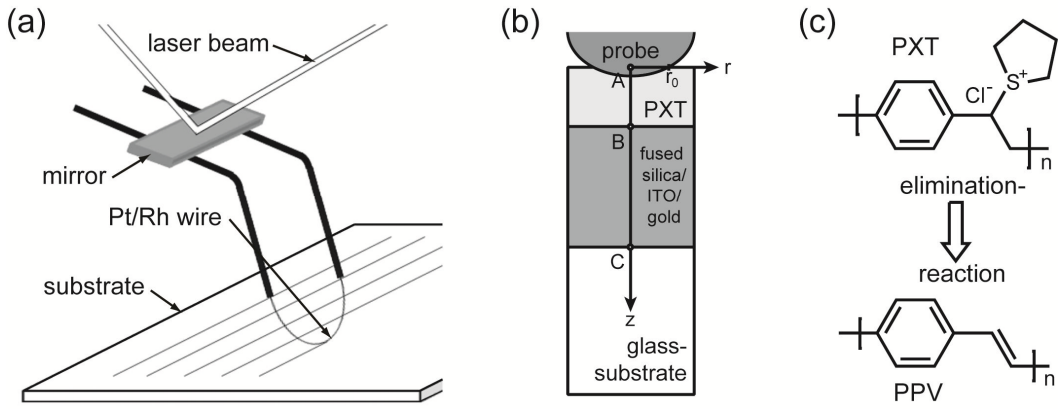

Figure 2-4. (a) Setup of the experiment. The hot Wollaston wire probe is scanning across a sample whose cross-section can be seen in (b). The points A, B and C mark the location of the interfaces along the z-axis (i.e. at r = 0). (c) Chemical structures of PXT and PPV. Image reprinted with permission from Tolk et al.,[77] Copyright (2012) American Institute of Physics.

2.3.2 Method

The main type of substrates used in my experiments are indium-tin oxide (ITO) covered glass substrates. Experiments on fused silica already exist[62] and have only been repeated briefly to assure reproducibility. Finally, the first experiments on gold were carried out by Dr Oliver Fenwick and Sadi Ahmad[iii] to explore a much larger range of substrate thermal conductivities. The thermal conductivity, *k*, of ITO ranges from 3.1 $W\,m^{-1}\,K^{-1}$ for very thin films[78] to bulk

[iii] both members of the CMMP group at UCL, Department of Physics & Astronomy

conductivities[79] of 14 W m^{-1} K^{-1}, which is significantly higher than that of fused silica[80] (k = 1.4 W m^{-1} K^{-1}). The thermal conductivity of gold[81] is 317 W m^{-1} K^{-1}.

The substrates are cleaned in an ultrasonic bath in acetone and isopropanol for 10 minutes each, followed by an oxygen plasma treatment to reduce the surface roughness and improve the adherence of PXT molecules to the partially oxidized ITO surface.

After cleaning the substrate, the PXT solution (0.25 wt% in water, Sigma Aldrich) is spin-coated onto the samples in air resulting in film thicknesses of ≈ 20 nm on spectrosil and ≈ 35 nm on ITO as determined via a Dektak profilometer.

The lithography was done by scanning the hot probe in contact mode across the surface. The contact force has been chosen to be as low as possible to avoid sinking of the probe into the precursor layer but to also ensure reliable contact. A set point of about 3 nA was used, translating into a contact force of 2.3 µN. (This value was determined by Dr Oliver Fenwick by approaching a hard surface without being in feedback to calculate the change of the photodiode signal as the function of deflection and by using the known value of the spring constant of the cantilever.)

During the lithography I kept the scan angle and all feedback parameters constant. The feedback parameters are the set point (photodiode voltage which is proportional to how much the cantilever is bent) and the P, I and D gain of the PID (proportional-integral-derivative) controller. These 'gains' determine how the height of the tip is adjusted with respect to the error-signal, which is the difference between the measured photodiode voltage and the desired photodiode set point. The scan angle needs to be constant because the probe tip is not isotropic. Within one plane, the radius is 2.5 µm, i.e. the actual radius of the platinum-rhodium core wire, and within the other plane, the radius of curvature is determined by how much the wire is actually bent around to form the tip, which is larger than 2.5 µm. The correct scan angle has been used which assures that the 2.5 µm curvature radius is responsible for the feature sizes.

After patterning, the samples are rinsed in methanol to remove any unconverted precursor on the substrate and then baked in a vacuum oven at about 200 °C and < 10^{-3} mbar for at least 2 hours to assure complete conversion into PPV.[82]

2.3.3 Experimental Results and Discussion

Most of the experimental results on ITO are already described in my MSc thesis. I will, however, show the most important images and briefly discuss them before adding the finite element modelling.

Figure 2-5 shows AFM images of PPV structures written at 350 °C and 10 µm/s. The images are taken after the last step, i.e. the post-baking step, and show that straight and reproducible lines can be manufactured.

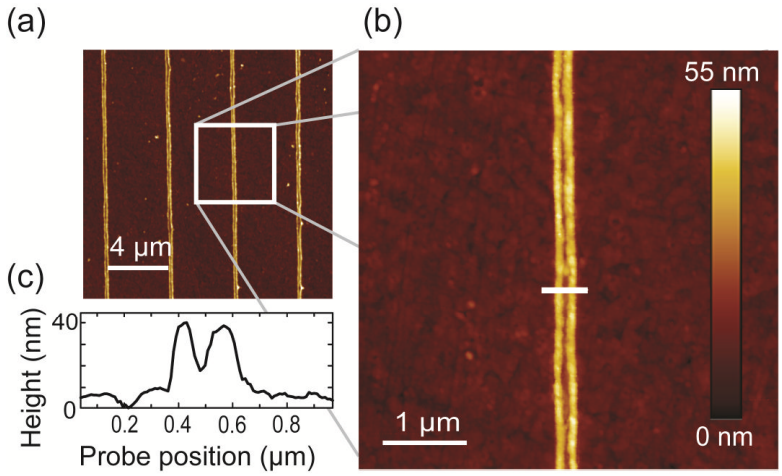

Figure 2-5. The upper images (a) and (b) show micrographs of lines written at 350 °C and 10 µm/s. The line profile across the white line in (b) is illustrated in (c). The initial precursor film was ~ 35 nm thick. Experiment done during the author's MSc project. Figure reprinted with permission from Tolk et al.,[77] Copyright (2012) American Institute of Physics.

Figure 2-6a displays lines profiles taken at constant temperature but different writing speeds. It clearly demonstrates that lower writing speeds lead to taller and wider structures as one would expect from the increase in exposure time of the precursor film to the hot tip. Also important to note is the transition from a single line profile at high writing speeds to a double peaked shape in the regime of lower writing speeds where the viscous flow cannot be neglected. The sudden change of the line profile when decreasing the writing speeds from 10 to 5 µm/s must result from the probe suddenly sinking considerably into the precursor film. Penetration of the probe into the layer can generally result from two processes. First, the viscoelastic behaviour of polymers enabling viscous flow and second, it is known that the precursor will shrink during the elimination reaction[59]. To which degree the precursor shrinks is not clear, especially considering the potentially different behaviour of shrinking purely due to baking in a vacuum oven, for example, and shrinking under mechanical pressure of a hot tip as in our case.

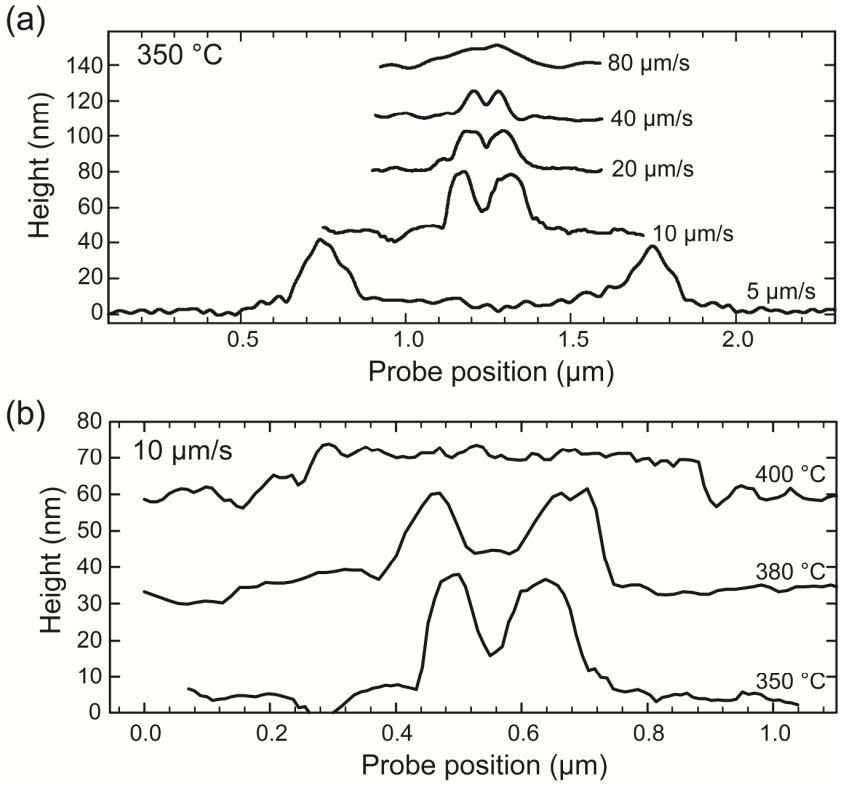

Figure 2-6. Line profiles of structures written at (a) a fixed temperature of 350 °C with a range of scan speeds from 5 to 80 µm/s and (b) a fixed writing speed of 10 µm/s for temperatures of 350, 380 and 400 °C. Experiment done during the author's MSc project.[74] Note that all curves are stacked for clarity.

Figure 2-6b shows line profiles at a fixed writing speed but varying temperature. The lateral centre of each structure is at the same height within the range of temperatures while the height of the peak decreases with increasing temperature. This behaviour is not what is expected simply by assuming a higher conversion ratio and more pronounced viscous flow with higher temperature. The shape is particularly interesting at 400 °C where the typical double peaked shape becomes one wide plateau. I propose two effects which could lead to that behaviour: first, at such a high temperature heat conduction within the film might become considerable, so that surface elements are "pre-hardened" by the incoming probe before actually coming into contact with it, therefore reducing penetration when the probe actually touches the element. (The elasticity modulus of PXT is only 2.1 GPa compared to up to 70 GPa for highly order PPV films prepared by the zone reaction method.[83]) This, however, does not explain why the volume of converted material seems to be larger at lower *T*. Hence I suggest that at 400 °C, enhanced shrinking under pressure of the probe may play a significant role in forming the wide and flat structures. (The local thermal analysis (LTA) performed on PXT[62] showed that the probe sinks into the precursor layer at about 415 °C, which is close to 400 °C.)

I have also tried to optimize the features regarding line density and resolution. Figure 2-7a shows structures that were written at 400 °C and the maximum writing speed that is supported by the thermal AFM of 150 µm/s. At these high speeds especially, the trace and retrace of the probe does not always overlap resulting in these two separated lines with a peak-to-peak gap of 320 nm. Figure 2-7b shows lines with a very high resolution of up to 36 nm (FWHM). We can see that the anchoring of the polymer to the substrate is rather weak resulting in these awry features; instead of straight lines one observes crooked or zigzagged lines. However, we have a first indication that the influence of the thermal conductivity of the underlying substrate on the highest resolution seems negligible as a similar resolution of 37 nm was previously achieved on fused silica on a slightly thicker (40 nm instead of 35 nm) precursor film.[62]

At last I would like to mention that experiments on gold covered silicon oxide substrates (see Figure 2-8) were also carried out. They were done by Sadi Ahmad and Dr Oliver Fenwick. Again, resolutions comparable to those on fused silica and ITO have been achieved. Note that the polymer film thickness on gold was only 20 nm, in contrast to 35 nm on ITO and 40 nm on fused silica, making a direct comparison with ITO and fused silica more difficult. (As the film thickness is reduced, heat from the probe can more easily reach the polymer/interlayer interface and the highest achievable resolution is expected to improve due to the lower necessary tip temperature). Nevertheless, it is actually surprising to see the lithography working on gold as one may expect that most of the heat near the polymer/gold interface is conducted away due to the high thermal conductivity of gold and that, therefore, the converted material does not stick to the interlayer and will be washed away in the following rinsing step. The finite element simulations will give further insight into this issue.

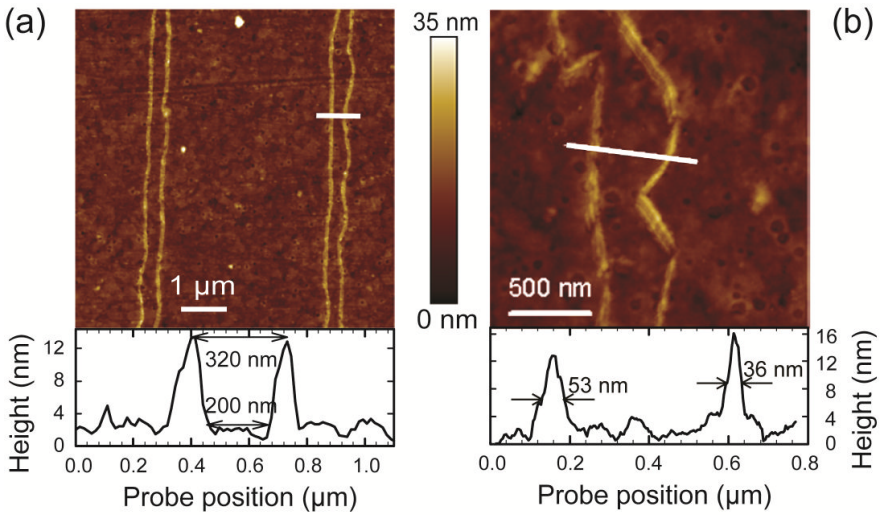

Figure 2-7. (a) Patterning at 400 °C and 150 µm/s and line profile along the white line. (Inset) The line profile is the result of the probe scanning twice across the surface (trace and retrace), leading to a line spacing of 320 nm. (b) Patterning at 380 °C and 20 µm/s resulting in a high resolution of 36 nm, however at the expense of the quality of the lines which are then no longer straight or well-connected. Experiment done during the author's MSc project.[74]

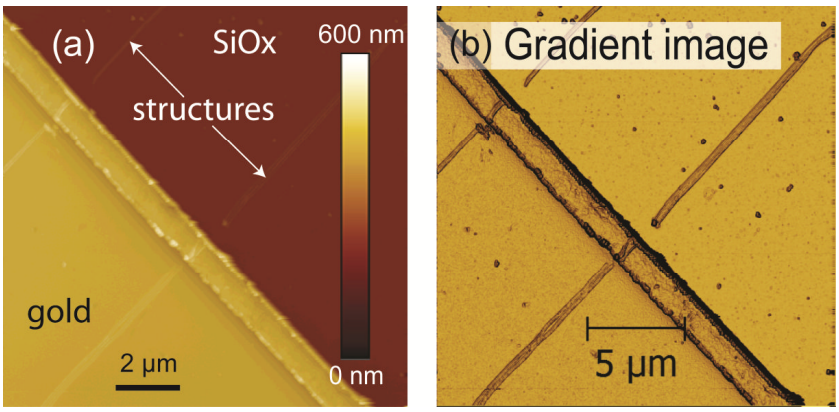

Figure 2-8. AFM images of PPV lines written across a silicon oxide (SiO_2) – gold interface. (a) The upper right area of the image shows the SiO_2 surface whereas the bottom left area shows the ~ 200 nm thick evaporated gold layer. The lines were written at 400 °C at 20 µm/s across the interface and are only hardly visible in the image due to the small height of the features (~ 15 nm) compared to the interface step. (b) Gradient image of (a) for better visualization of the lines. The interruption of the line is an artefact that results from the large radius of curvature along the patterning direction, causing the tip to touch the step before the patterned line reaches it. Figure taken from the supplementary information from Tolk et al..[77]

2.4 Finite Element Modelling

In the previous section we saw that similar resolution could be achieved virtually independent of whether the interlayer was fused silica or ITO. Even using gold we were able to obtain PPV structures sticking to the interlayer. This may be counterintuitive considering the very high thermal conductivity of gold which is expected to result in low temperatures and hence no conversion to PPV near its interface. To understand this apparent independence of the resolution of SThL I use finite element modelling with COMSOL Multiphysics. In the following I will explain the fundamentals of the finite element method (FEM) and then describe the equations used in this particular application.

2.4.1 Theoretical Background

2.4.1.1 Finite Element Modelling

The finite element method (FEM) is used to find numerical solutions in a system of (linear or non-linear) partial differential equations (PDEs). This method is usually used whenever a system of PDEs or a geometry is too complex, in that analytical solutions either cannot be found or it is not feasible to attempt any analytical solving.

During the FEM, continuous domains are divided into subdomains, called elements, creating a so-called mesh. Because the size of the elements can be varied, the FEM is also used whenever the required precision of the solution depends on the specific domain, or when the solution is not smooth. Therefore, element sizes are reduced and hence precision increased in the areas of interest, and mesh-size increased in other regions. In my case for example I am interested in the solution near the probe-precursor contact area and do not require many data points in the bulk of the substrate, where the temperature is expected to be rather constant. This leads to a considerable reduction in computation time. A section of the mesh used in my simulations is shown in Figure 2-9, where one can see large differences in mesh-sizes between the different domains.

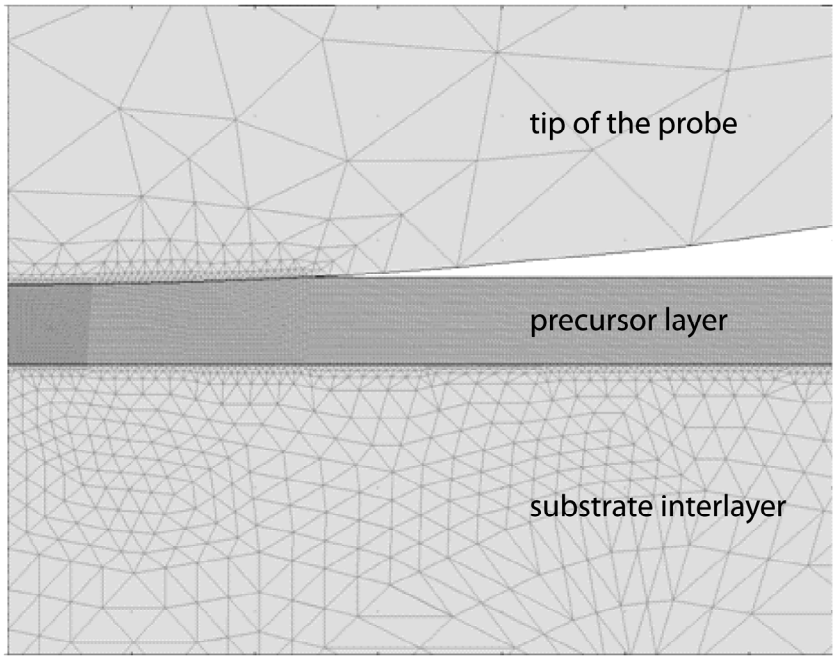

Figure 2-9. Mesh mode view (Comsol Multiphysics) of the geometry used for the simulations. The top part shows the probe touching the polymer layer, whose domains are very small to achieve accurate results in this region. The layer underneath shows the substrate interlayer. The influence of the thermal conductivity of this layer is the focus of the work in section 2. The glass substrate underneath the interlayer is not shown.

2.4.1.2 Means of Heat Transport

Heat can be transported via three mechanisms: conduction, convection and thermal radiation.

Heat conduction or *heat diffusion* is a mechanism by which heat is transferred within one body or between bodies in physical contact with each other. Neighbouring atoms, molecules or electrons are exchanging energy. The basic macroscopic equation governing heat conduction is the heat equation, which will be described in detail in the next section.

During *convection*, heat is transferred from one body to the next due to the flow of the "hot" material itself, i.e. due to mass transport. The transport medium, i.e. the fluid, may be a liquid or a gas. Heat transfer via convection will not be considered in our case.

Thermal radiation transfers heat via the emission and re-absorption of photons. The microscopic cause for thermal radiation is the movement of accelerated charges within atoms. The spectrum of thermal radiation for a black body in thermal equilibrium is simply a function of its temperature and is described by Planck's Law:

$$B_\nu(T) = \frac{2h\nu^3}{c^2}\frac{1}{e^{\frac{h\nu}{k_B T}} - 1} \quad or \quad B_\lambda(T) = \frac{2hc^2}{\lambda^5}\frac{1}{e^{\frac{hc}{\lambda k_B T}} - 1}. \qquad \text{Eq. 2-1}$$

B is the spectral radiance, h is Planck's constant, ν is the frequency of a photon, λ is the wavelength of a photon, k_B is the Boltzmann constant and T is the temperature.

Heat transfer via radiation was found to be negligible during the simulations.

2.4.1.3 Heat Equation

The heat equation governs the heat transfer and temperature evolution in almost any macroscopic material (excluding only quantum gases and other 'exotic' media). I used it to simulate the temporal and spatial evolution of the temperature within the polymer and the substrate. The heat equation is the following parabolic partial differential equation:

$$\rho\, c\, \frac{\partial T}{\partial t} + \nabla(-k\, \nabla T) = Q_S\,, \qquad \text{Eq. 2-2}$$

where ρ is the mass density, c is the specific heat capacity, T is the temperature, t is the time, ∇ is the Nabla operator, k is the thermal conductivity and Q_S is the heat source or heat production (in W/m^3). In thermal equilibrium$\left(\frac{\partial T}{\partial t} = 0\right)$, the heat equation becomes

$$\nabla(-k\, \nabla T) = Q_S\,. \qquad \text{Eq. 2-3}$$

I note that this equation is mathematical identical to the Poisson equation in electrodynamics, only that the electrical potential is replaced by the temperature and the charge density by the heat production. In case of an isotropic medium (where k is a scalar quantity) and without a heat source, Eq. 2-3 becomes

$$\nabla^2 T = 0, \qquad \text{Eq. 2-4}$$

where ∇^2 is the Laplace operator (usually denoted as Δ, but not used here to avoid confusion with the Delta symbol Δ used later). The equation is thus also called Laplace equation. Solutions to the Laplace equation are not trivial in more than one dimension. Solutions to the Laplace equation are called Harmonic functions. They have been thoroughly investigated by mathematicians and will not be discussed here in detail.

2.4.1.4 Thermal Contact Resistance

The thermal contact resistance R_{CR} (in K/W) is a measure of how easily heat can be transferred between two bodies in contact. It is defined as the ratio between the temperature drop (ΔT) at the joint and the heat flow ($\Delta Q/\Delta t$ in W) across the contact interface (of area A):

$$R_{\mathrm{CR}} = \frac{-\Delta T_{\mathrm{joint}}}{\frac{\Delta Q}{\Delta t}}. \qquad \text{Eq. 2-5}$$

If we remove the words "at the joint" and "across the contact interface" in the above definition and consider a body of width Δx, we obtain the definition for a thermal resistance R in general:

$$R = \frac{-\Delta T}{\frac{\Delta Q}{\Delta t}} = \frac{\Delta x}{k\,A}. \qquad \text{Eq. 2-6}$$

In terms of the thermal conductance coefficient (h_c), R_{CR} can be written as

$$R_{\mathrm{CR}} = \frac{1}{h_c\,A}. \qquad \text{Eq. 2-7}$$

In many applications (such as the cooling of a processor in a PC to name just one) the thermal contact resistance between two (solid) bodies is of tremendous importance. No hard surfaces are perfectly smooth, instead they are rough or deformed. As a result, perfect contact between two solid surfaces is impossible. Small air gaps are present which reduce the effective contact area and lead to an additional thermal resistance as the thermal conductivity of air is usually much lower than that of the contacting bodies. If we compare Eq. 2-6 and Eq. 2-7 we see that (as intuitively expected) R_{CR} increases when the "effective thermal conductivity" (k_{air}) of the air-gap decreases or the "effective thickness" ($\Delta x = \Delta t_{\mathrm{air}}$) increases.

Derivation of the formula defining the thermal contact resistance:

According to Fourier's law of heat conduction,

$$\vec{q} = -k\,\nabla T, \qquad \text{Eq. 2-8}$$

the heat flow density ($\vec{q}$ in W/m², i.e. the heat flow per area and time) between two bodies is proportional to the temperature gradient and the proportionality factor is k, the thermal conductivity. (The heat equation given in Eq. 2-3 is actually derived from Fourier's law and the law of energy conservation). In one dimension, Eq. 2-8 becomes

$$q_x = -k\,\frac{dT}{dx}, \qquad \text{Eq. 2-9}$$

which may be rewritten in the integral form:

$$\frac{\Delta Q}{\Delta t} = -k\,A\frac{\Delta T}{\Delta x}, \qquad \text{Eq. 2-10}$$

where $\Delta Q/\Delta t$ is the energy flow per time (in W) and A is the projected area in x-direction. Under the condition of energy conservation one can find for a multilayer structure that

$$\frac{\Delta Q}{\Delta t} = \frac{-A\,\Delta T}{\frac{\Delta x_1}{k_1} + \frac{\Delta x_2}{k_2} + \frac{\Delta x_3}{k_3} + \cdots + \frac{\Delta x_n}{k_n}}, \qquad \text{Eq. 2-11}$$

or in terms of thermal resistances R_i:

$$\frac{\Delta Q}{\Delta t} = \frac{-\Delta T}{R} = \frac{-\Delta T}{R_1 + R_2 + \cdots + R_n}, \qquad \text{Eq. 2-12}$$

If we start from Eq. 2-11 and imagine a three-layer structure composed of two bodies in contact and a thermally resistive layer in their middle (see Figure 2-10), we can replace the term $\Delta x_2/k_2$ by the thermal contact resistivity ($1/h_c$) and obtain

$$\frac{\Delta Q}{\Delta t} = \frac{-A\,\Delta T}{\frac{\Delta x_1}{k_1} + \frac{1}{h_c} + \frac{\Delta x_3}{k_3}}. \qquad \text{Eq. 2-13}$$

Eq. 2-13 can be used to measure R_{CR} via heat flux meters.

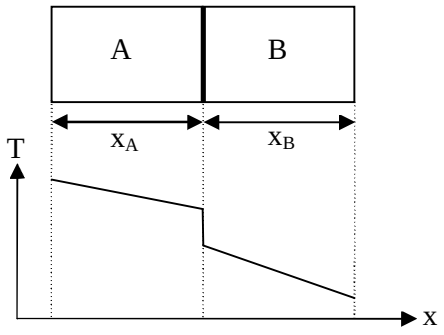

Figure 2-10. Visualisation of the thermal contact resistance between two bodies which leads to a "sudden" drop in temperature at the contact interface. The slopes in the graph for body A and B depend on their thermal conductivities *k*. The higher *k*, the smaller the slope.

2.4.1.5 Arrhenius Equation

The Arrhenius equation is an empirical formula to calculate the reaction rate constant (k) of a thermally driven chemical reaction as

$$k = A\, e^{-\frac{E_a}{RT}}, \qquad \text{Eq. 2-14}$$

where A is the pre-exponential factor, E_a is the activation energy and R is the molar gas constant.

For a reaction from molecule A to molecule B (A→B), let $N_A(t)$ be the number of molecules A as a function of time. Starting with a simple rate equation and reaction rate constant k (Eq. 2-14):

$$\frac{dN_A(t)}{dt} = -k\, N_A(t), \qquad \text{Eq. 2-15}$$

and using the boundary conditions $N_A(0) = N_0$, $N_A(\infty) = 0$ and $N_B(0) = 0$, one finds that the conversion ratio (α), i.e. the ratio between the number of converted molecules (N_B) to initially unconverted molecules (N_0), is as follows:

$$\alpha = \frac{N_B(t)}{N_0} = 1 - \exp(-k\, t) \qquad \text{Eq. 2-16}$$

$$\alpha = 1 - \exp\left(-A\, e^{\frac{-E_a}{R\,T}}\, t\right). \qquad \text{Eq. 2-17}$$

The Arrhenius equation (Eq. 2-17) is also known to describe the conversion from PXT to PPV[84] and the values for the activation energy (E_a) and the pre-exponential factor (A) can be taken from the literature[84] (128 kJ/mol and 1019/min, respectively). Figure 2-11 shows the Arrhenius equation for PXT to get an impression about the timescales involved. At ~130 °C one needs 1 s to convert the polymer while at 350 °C, 10^{-6} s is enough to completely convert the polymer. Considering for example a relatively high writing speed of 100 µm/s and a contact length of only 10 nm, one obtains an exposure time for polymers at the top surface of 10^{-4} s, which is two orders of magnitude longer than what would be needed to convert the polymer to nearly 100%. This shows us that we will have in all cases a complete conversion at the top of the film where the hot probe touches the polymer. However, this information is not enough because if only the top layer was converted, the film could still be washed away in the rinsing step. Therefore one needs to investigate the temperature distribution within the film.

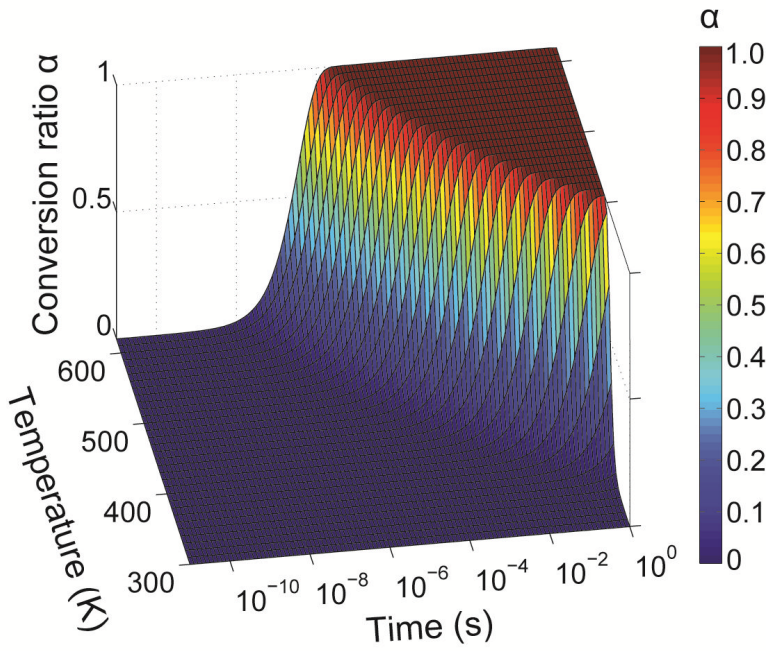

Figure 2-11. Conversion ratio (α) of PXT as a function of temperature and exposure time. Figure taken from the supplementary information from Tolk et al..[77]

2.4.1.6 Geometry and Material Properties in the Model

2.4.1.6.1 Geometry

In the following I assumed the effective radius of curvature to be 2.5 µm, i.e. the nominal radius of the Wollaston wire, a tip penetration of 3 nm (leading to a contact width of 245 nm) and a temperature of 350 °C. The penetration depth of 3 nm has been chosen following measurements on the tip penetration of a hot probe on PXT before rinsing.[62] Regarding the substrate, I followed the geometry of the ITO substrates, i.e. I assumed a 1.5 mm thick quartz substrate with a 150 nm layer of ITO and a 35 nm PXT layer on top (see Figure 2-4b). To compare with the other substrates (fused silica and gold) I simply exchanged the ITO layer with the respective other material. This 150 nm thick layer of fused silica, ITO or gold will be termed "interlayer" in the following.

2.4.1.6.2 Material Properties

Within the model I used the following physical parameters:

- for fused silica and glass: k = 1.4 W m^{-1} K^{-1}, ρ = 2203 kg/m^3, c = 703 J kg^{-1} K^{-1};
- for ITO: k = 8.7 W m^{-1} K^{-1}, ρ = 7100 kg/m^3, c = 380 J kg^{-1} K^{-1};

- for gold: k = 317 W m^{-1} K^{-1}, ρ = 19300 kg/m^3, c = 129 J kg^{-1} K^{-1}.
- Because the values for PXT are not well known, as a an approximation we took the values of the well characterized polymer poly(methyl methacrylate) (PMMA) that is often used in e-beam lithography:[50,51] k = 0.19 W m^{-1} K^{-1}, ρ = 1190 kg/m^3, c = 1420 J kg^{-1} K^{-1}. Note that the value of k for the polymer is likely to be overestimated. A justification for the value is given in section 2.4.3.1 on page 70.

2.4.2 Results

Figure 2-12a shows the temperature development at point B, i.e. at the polymer-interlayer interface. We see that depending on the underlying interlayer, the steady state temperature at point B is different, varying from about 142 °C for fused silica to 57 °C for ITO down to basically room temperature (23 K) in case of gold. The trend is easily explained by the fact that a substrate with higher heat conduction will more quickly transport energy away from point B. Considering again the exposure time of > 10^{-4} s derived above, we see that we can in very good approximation assume that the polymer is in thermal equilibrium during the exposure time. From here on, only steady state distributions are considered.

Figure 2-12b shows the cross section of T along the z-axis. The curve starts at point A at the probe-polymer interface with T_{tip} (350 °C). Up to point B, i.e. within the polymer, the temperature gradient is in good approximation constant and strongly dependent on k. The reason for the constant temperature gradient is that the heat transport is rather one-dimensional in that region, because the probe-polymer contact width is about 245 nm, whereas the polymer layer is only 35 nm thick. The heat equation (Eq. 2-4) then becomes $\partial^2 T/\partial z^2 = 0$ and hence describes a constant temperature gradient. Figure 2-12c illustrates the conversion ratio along the *z-axis* that follows from the temperature distribution in Figure 2-12b. We see that α drops from 95 % to 5 % within a layer of $\Delta z \sim 5$ nm independent of k. To quantify the location of the conversion boundary I arbitrarily define the conversion boundary as the surface where α = 50 %. (As the conversion boundary is so sharp, the precise value is not crucial). The vertical distance (d_z) between B and the conversion boundary is 2.7, 11.0 and 13.2 nm for fused silica, ITO and gold, respectively, in the case of the 350 °C hot tip assumed here. In Figure 2-12d, d_z is plotted as a function of T_{tip} ranging from 200 to 450 °C. If we assume that d_z is the parameter that indicates whether or not a structure will stick to the surface, we can determine the substrate dependent minimum tip temperature (T_{tip}^{min}) from Figure 2-12d. (The red vertical line marks d_z = 11.7 nm, a value that will be explained later).

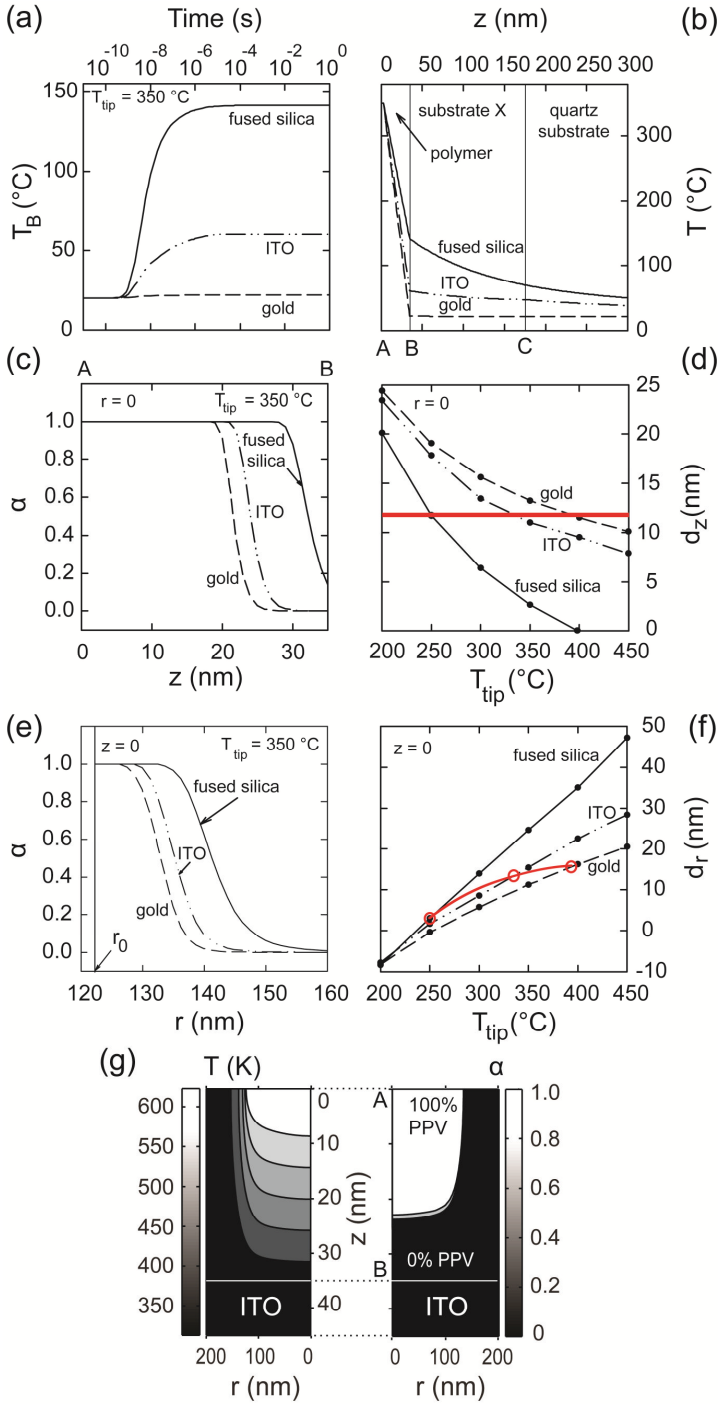

Figure 2-12. Finite element modelling. (a) Simulated time development of T at $r = 0$ at the polymer-substrate interface (point B). (b) Simulated temperature distribution along the z-axis at steady state. The curve starts at $z = 0$ (point A) with $T_{tip} =$ 350 °C. Up to $z = 35$ nm (point B), i.e. within the polymer, the temperature gradient is in good approximation constant. (c) Conversion ratio (α) of the polymer along the z-axis from A to B. (d) Vertical distance (d_z) of the conversion boundary from the substrate for different T_{tip}. The red line marks an estimate of the largest possible d_z (d_z^{max}) which still ensure that the structure will not be washed away during the rinsing step. (e) Plot of α along the air-polymer interface. (f) Plot of d_r = FWHM - 2 r_0 for different T_{tip}. The red circles indicate the expected smallest d_r which follow from $d_z = d_z^{max} = 11.7$ nm for the different substrates. (g) Surface plots of T and α in both spatial dimensions in case of an ITO substrate and a 350 °C hot tip. Image reprinted with permission from Tolk et al.,[77] Copyright (2012) American Institute of Physics.

In Figure 2-12e I plotted the conversion ratio along the air-polymer interface. The conversion ratio (α) drops from 95 % to 5 % within a layer of $\Delta r \sim 10$ nm (for gold) to 16 nm (for fused silica). I define d_r as the FWHM of the volume inside the conversion boundary subtracted by $2\,r_0$. d_r will serve as an indicator for the expected minimum feature size as the probe contact width becomes zero. It is plotted as a function of T_{tip} in Figure 2-12f. The red circles indicate d_r at the minimum tip temperature (T_{tip}^{min}) which we obtained above from $d_z = 11.7$ nm. Figure 2-12g illustrates the temperature and conversion ratio in both spatial dimensions to get a better impression of the shape of the converted volume.

2.4.3 Discussion

From the temporal evolution in Figure 2-12a we learned about the µs-timescale of the heat transfer which allowed the assumption that the polymer is in thermal equilibrium during the whole exposure time. This not only greatly reduces the computation time but we also learn that the specific heat capacity (c) and mass density (ρ) of the substrate, which are present only in the time dependent (but not time independent) heat equation, should not influence the process unless they are so high that the thermal equilibrium is only reached after a time comparable to the exposure time. Therefore it is sensible to concentrate solely on the thermal conductivity k of the materials. The fact that B is approximately at room temperature in the case of gold means that a further increase in k will not change the curve significantly anymore. Hence gold can be considered as a limit case representing k-values from $\sim k_{gold}$ to ∞.

2.4.3.1 Adhesion to the Substrate

In Figure 2-12c we could see that the vertical distance (d_z) between the interface (point B) and the conversion boundary is 2.7, 11.0 and 13.2 nm for fused silica, ITO and gold, respectively. Considering that we have achieved successful lithography for ITO and gold, we can deduce that d_z can be considerably > 0 without the converted polymer being rinsed away during development. (The author is aware of the fact that a higher thermal conductivity of the polymer itself increases the heat flow and would lead to a smaller d_z. However, conjugated polymers are known for their low thermal conductivities and the chosen value of 0.19 $W\,m^{-1}\,K^{-1}$ for the precursor is slightly larger than reported values for undoped and unstretched conjugated polymers such as polyanaline,[85] polythiophenes[86] and other PPV derivatives.[87] In order for the conversion boundary to touch the ITO-substrate, the thermal conductivity of the polymer would have to be increased by a factor of ~ 5.) This is in contrast to experiments done on the PPV

precursor by scanning near-field optical lithography (SNOL), where a good agreement was found when one assumes that the UV-dose at point B determines the resolution.[59]

I investigated the existence of a $d_z > 0$ further to find the maximum d_z which ensures that the structure sticks to the surface (d_z^{max}). To this end, I plotted d_z as a function of T_{tip} in Figure 2-12d. If we consider the smallest necessary tip temperature (T_{tip}^{min}) of 250 °C on fused silica for a writing speed of 20 µm/s and a similar film thickness,[62] we obtain d_z^{max} = 11.7 nm (red line in Figure 2-12d). The intersection of this line with the ITO curve gives T_{tip}^{min} = 335 °C, which is in fairly good agreement with the experimental observation that 300 °C was a too low temperature for writing speeds as low as 10 µm/s and that we could find very faint structures written at 350 °C at up to 80 µm/s. Assuming the same parameters, the model predicts that T_{tip}^{min} ~ 393 °C for gold.

2.4.3.1.1 Effect of Film Thickness on Feature Adhesion

The effect of film thickness on feature adhesion has not been the focus of this work. General trends, however, are that a higher film thickness than used here requires a larger T_{tip} to obtain the necessary d_z^{max}. This will in turn increase the lateral heat spread and therefore increase the minimum feature size. For too large film thicknesses, this can cause problems due to the degradation of the used precursor at too high T_{tip}. Reducing the film thickness will result in a smaller necessary T_{tip} as the polymer is the most thermally resistive material compared to the interlayer or the substrate. This leads to less heat spread and hence to a better final resolution. For the studies here I deliberately chose a larger film thickness of 35 nm because although film thicknesses ≤ 10 nm would be ideal to reach highest resolutions, they become very limited in their applications.

2.4.3.1.2 Factors Facilitating Feature Adhesion

We have seen above that combining simulations and experiments, we obtained a d_z^{max} = 11.7 nm. Therefore we have to consider factors facilitating feature adhesion. Such factors are a) the interlayer surface roughness, b) entanglement between polymer chains in the converted and unconverted region and c) electrostatic interaction of the precursor polymers with the ITO interlayer.

a) A surface roughness in the range of a few nm can already give a sizable contribution to the reduction of the "effective d_z" because non-conformal coverage of the rough surface (so as

to form a flat top surface, as it is commonly observed) would result in a spatially non-uniform film thickness, with local minima a few nm smaller than the thickness assumed in the model. Furthermore, it is conceivable that the precursor polymer chains would more easily get entangled and adsorbed due to the nanocavities offered by the rough surface.

b) Another effect that the model is not taking into account is the entanglement of the polymer chains between the converted and unconverted regions. While it might be argued that this should be of the order of the polymer gyration radius (3-4 nm for some soluble PPVs, which should provide a reasonable model for PXT),[62] one cannot rule out a value a few nanometres larger than that (up to an extreme value of ≈ 10 nm for a fully elongated strand).[62] This higher value could be the result of the shrinking of the precursor polymer during conversion[82] (due to the elimination of the tetrahydrothiophenium group). This volume reduction may lead to significant straightening and uncoiling near the converted regions and hence may affect the true value of d_z.

c) Additionally I note that a monolayer of PXT can be electrostatically bound to the ITO surface which has been treated by an oxygen plasma. The oxygen plasma leads to the formation of a dipole layer on ITO via the oxidation of surface Sn^{IV}–OH to surface Sn^{IV}–O.[88,89] PXT acts as a polyelectrolyte in water where the chains are positively charged and compensated by Cl^- counterions, and the positively charged chains can adhere to Sn^{IV}–O surface groups.

   As a final point I note that conversion of PXT to PPV releases HCl,[90] which has been proposed to etch metallic or ITO substrates with formation of the related salts. Diffusion of HCl downwards may enable HCl to reach the interlayer. These salts may locally increase surface roughness or introduce polar interactions that would aid adhesion of the features.

None of these effects question the finite value of d_z, but instead confirm that the predicted $d_z > 0$ actually captures an important aspect of the physics of this process, and ultimately also explain why we can anchor nanopatterns on gold despite its very low surface temperature ($T_B \approx$ room temperature). With this in mind we can look at the implications that the scenario of adhesion in the $d_z > 0$ regime has for the ultimate performance of SThL on a range of substrates.

2.4.3.2 Minimum Feature Size

In Figure 2-12e we see that the lateral distance from r_0 to the conversion boundary is 10.4, 12.8 and 18.9 nm for gold, ITO and fused silica, respectively. Hence a higher k actually leads to a smaller conversion radius at the polymer-interlayer interface under the condition that T_{tip} remains constant. d_r was defined as FWHM – 2 r_0 and may be thought of as an approximation of the FWHM as the contact width (2 r_0) goes to zero. d_r will serve as the indicator for the

expected minimum feature size (f), which could be estimated by $f = d_r + w_0$, where w_0 is the "true" contact width.

The question now remains if the need for a higher T_{tip} at a higher k will overcompensate the improvement of the resolution that we would expect if we kept T_{tip} constant. To examine this further I plotted d_r as a function of T_{tip} in Figure 2-12f. The red circles indicate the smallest necessary tip temperatures T_{tip}^{min} (which we obtained from $d_z^{max} = 11.7$ nm) with the corresponding substrate dependent d_r^{min}. We would therefore predict that the resolution will deteriorate slightly upon changing to a higher thermal conductivity substrate. Quantitatively, f is expected to increase with respect to fused silica by 10.3 and 12.6 nm for ITO and gold, respectively, in case of a 35 nm precursor layer. Experimentally we found an optimum FWHM of 37 nm on a 40 nm thick precursor film on fused silica and 36 nm on a 35 nm thick precursor film on ITO. The deterioration of the resolution is therefore less than predicted by the model, even considering the 5 nm thicker film on fused silica.

In Figure 2-12g I illustrate the distribution of T and α in both spatial dimensions in the case of an ITO covered glass substrate. T decays linearly in the z- and exponentially in r-direction resulting in α dropping from 95 % to 5 % within a layer of $\Delta z \sim 5$ nm or $\Delta r \sim 10$ to 16 nm along the axes. This is a sharp change of α compared for example to SNOL.[57,91] Figure 2-12g also shows another aspect that was neglected up until now, which is that the overall shape of the converted volume calculated by the modelling differs from the observed line shapes in the sense that the calculated shape is wider near the surface and narrower near the film, whereas experimentally we see the opposite. This apparent collapse of the converted polymer is an effect which was also observed and modelled for SNOL.[92]

At this point I note that the thermal conductivity of a thin film is usually smaller than that of the same material in the bulk. For 200 nm gold films, k may be reduced by a factor of about 0.5 compared to the bulk value,[81] which, according to this model, results in changes of d_z of less than 0.1 nm and changes in d_r of no more than 0.2 nm for T_{tip} between 250 and 450°C.

It is clear that the model cannot be expected to quantitatively reproduce the full spectrum of experimental results. There are too many effects that have not been considered, most importantly

a) the writing speed dependent penetration depth and hence contact width that is caused by the viscoelasticity of the polymer, and
b) the observed difference between pre-rinse indentation width and post-rinse feature size.[62]

c) It is also not clear how the shrinking of the polymer during conversion (due to the elimination of the thiophene group as described earlier) influences the structure during the writing process.

Note that the effect of postbaking on the other hand has been investigated for PPV structures[59,62] and it was shown[62] that whereas the height of the features written by SThL shrinks by about 30%, the width (FWHM) is almost unchanged.

2.4.3.3 Influence of Thermal Contact Resistance

I further investigated the influence of a thermal contact resistance at the various interfaces (substrate/interlayer, polymer/interlayer and probe/polymer) to test the robustness of the results. To that end, I changed the boundary condition at the interfaces from 'continuity' to 'thin thermally resistive layer' with the thermal conductivity of air (k_{air}) and thickness t_{air}. By doing that, a finite R_{CR} effectively originates from an infinitely thin layer leading to a sharp drop in T at the interface. The advantage of this technique is not only its simplicity, it also preserves the original meanings of d_z and d_r as the geometry does not change.

k_{air} is set to the function given by the Comsol material library: $k_{air} = (-2.2758 \cdot 10^{-3} + (T/K) \cdot 1.1548 \cdot 10^{-4} + (T/K)^2 \cdot (-7.90253) \cdot 10^{-8} + (T/K)^3 \cdot 4.11703 \cdot 10^{-11} + (T/K)^4 \cdot (-7.4386) \cdot 10^{-15})$ W m^{-1} K^{-1}.

In Figure 2-13, I plotted d_z and d_r as a function of t_{air} for T_{tip} = 350 °C. We find that an imperfect contact between the interlayer and the underlying glass substrate (see Figure 2-13a) has no influence as long as the effective air-gap is thinner than ~20 nm. Note that fused silica substrates do not feature a substrate/interlayer interface as the material is the same for substrate and interlayer. Nevertheless, for the sake of completion the additional R_{CR} was modelled also in this case.

A thin air-layer between polymer and interlayer (see Figure 2-13b) has a similar influence on d_z as a thin air-layer between glass and interlayer, but its influence on d_r is larger. Note, however, that one expects the effective air-gap to be small for all interlayers because first, surface roughnesses are in the nm range and second, the precursor polymer (PXT) solution is a liquid during its deposition (via spin-coating) and is hence expected to effectively fill any gaps.

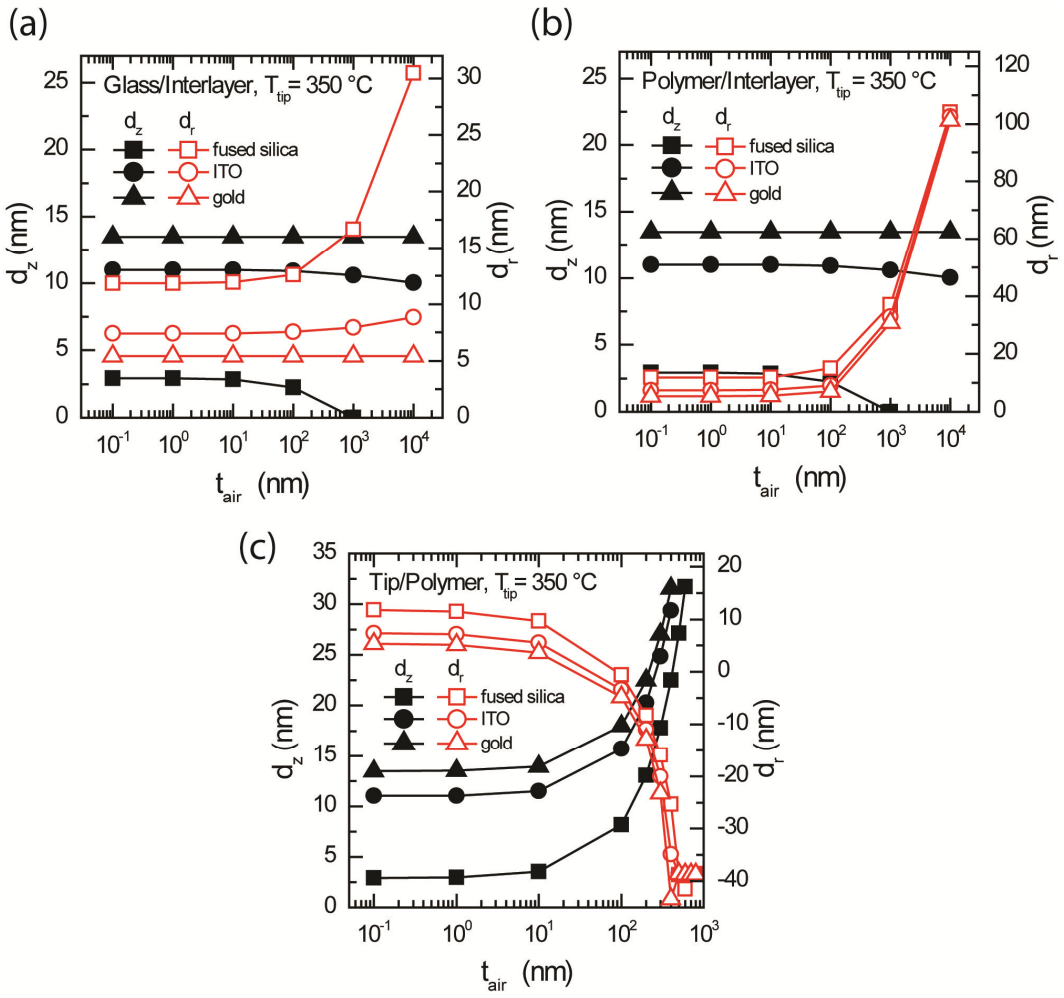

Figure 2-13. Diagrams showing the influence of the addition of an air-layer between (a) the glass/interlayer interface, (b) the polymer/interlayer interface, and (c) the tip/polymer interface for a tip temperature (T_{tip}) of 350 °C. Values of d_z (black, filled symbols) and values of d_r (red, open symbols) are given as a function of the thickness of the thin thermally resistive air-layer (t_{air}). Figure taken from the supplementary information from Tolk et al..[77]

The strongest influence was found to be caused by an imperfect contact between the tip of the probe and the polymer (see Figure 2-13c). However, the influence is still relatively small. For an air-gap of for example 10 nm, an already overestimated value due to the good contact between tip and polymer achieved by the AFM feedback mechanism, d_z only changes up to 1 nm and d_r changes up to 3 nm. At t_{air} larger than ~ 300 nm (an obviously unrealistically large value), the probe cannot convert material inside the polymer film anymore so that d_z approaches 32 nm, i.e. the polymer film thickness (35 nm) subtracted by the probe penetration depth (3 nm at r = 0). At this point, d_r approaches an interlayer-independent value of -39 nm.

2.4.3.4 Influence of Contact Width

Another uncertainty in the model is the assumed contact width between the tip of the probe and the polymer ($2\ r_0$). The uncertainty stems from the several effects, such as

- the writing-speed dependent penetration depth and hence contact width,
- the observed reduction in feature size upon development,[62] and
- lateral shrinking during the post-baking step.[62]

Most of the modelling is done with a penetration depth of 3 nm and hence a contact width of 245 nm, which seems an overestimation of $2\ r_0$ for the smallest, observed features.

The effect of reducing the contact width ($2\ r_0$) on d_z and d_r is shown in Figure 2-14a for a 350 °C hot probe. Upon reducing $2\ r_0$, the temperature at any point will be reduced at thermal equilibrium because there is less heat-flow available. This then of course leads to an increase of d_z and a reduction of d_r. We also see that at very small contact widths (smaller than the polymer film thickness, here 35 nm), lateral heat diffusion starts to dominate and d_z becomes almost independent of the type of interlayer.

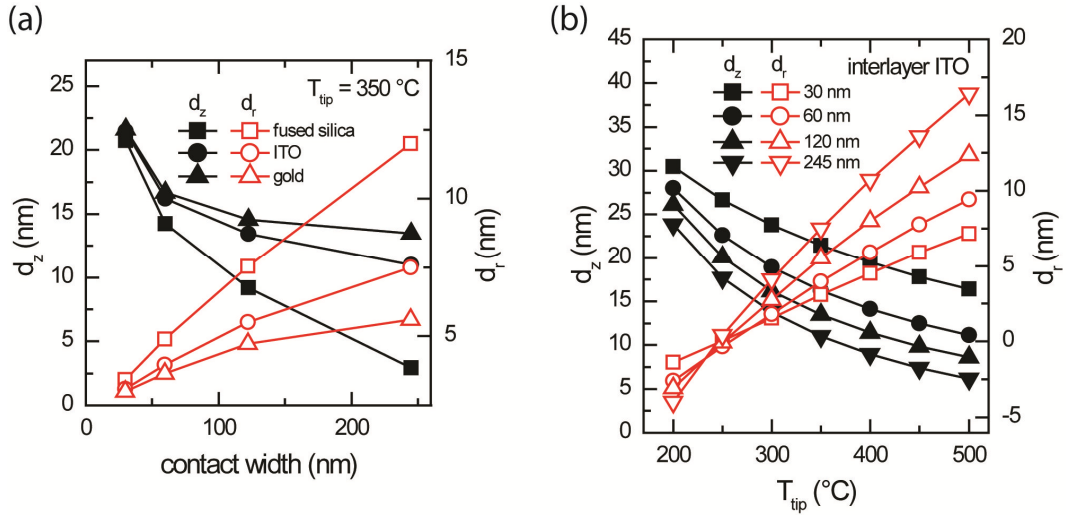

Figure 2-14. (a) d_z and d_r as a function of the probe-polymer contact width for a constant tip-temperature (T_{tip}) of 350 °C. (b) d_z and d_r as a function of T_{tip} for different contact widths (30, 60, 120 and 245 nm) in case of indium-tin oxide (ITO) as the interlayer. Figure taken from the supplementary information from Tolk et al..[77]

The effect of the tip temperature (T_{tip}) on d_z and d_r for different contact widths in case of ITO as the interlayer is shown in Figure 2-14b. We see again that d_z grows for smaller contact widths, further supporting the notion that one would expect a region of unconverted polymer near the interlayer.

2.5 Summary and Outlook

In summary, I have shown that SThL of a PPV precursor is possible on a range of substrates covering thermal conductivities from that of fused silica (k = 1.4 W m^{-1} K^{-1}) to that of gold (k = 317 W m^{-1} K^{-1}). I conducted experiments on ITO which is the most common transparent electrode used today in organic devices such as organic LEDs, transistors and solar cells. The shapes of structures written on ITO were qualitatively similar with the exception observable at high temperatures (≥ 400 °C) where new effects lead to very wide and flat structures. I achieved a maximum resolution (FWHM) of 36 nm on a ~35 nm thick precursor film on ITO which is almost identical to the published resolution of 37 nm on a 40 nm precursor film on fused silica.[62] First experiments on gold have shown similar resolutions showing that the highest resolutions seem to be rather independent of the thermal conductivity of the underlying substrate.

Finite element simulations indicate that the converted volume can be several nm away from the substrate without the features losing the ability to stick to the substrate during development. This allowed gap of unconverted polymer is the reason why SThL can also work on very high thermal conductivity substrates such as gold. I have given several effects that may lead to such a $d_z > 0$: interlayer surface roughness, polymer chain entanglement and electrostatic interaction of the ITO with the interlayer, especially ITO.

The model further predicts that the lateral resolution is expected to deteriorate only slightly upon increasing k due to the rising substrate dependent minimum probe temperature. The difference of the FWHM between fused silica and gold is predicted to be only 12 nm (for the standard geometry).

The combined experimental and modelling work shows that SThL is a versatile technique that can achieve nanoscale resolutions on a wide range of substrates to be used in a range of applications such as data-storage[53,54] and general photoresist patterning.[93] One should not forget that the requirements for the polymer to be converted may not be as high, because there are various thermally activated cross-linkers (with reasonably low conversion temperatures) that can be added to the functional polymer; the crosslinking material could then be patterned and, similar to my approach, result in local insolubility. In order to achieve very high resolutions, a high stiffness (large elasticity modulus) is desired to avoid sinking of the probe into the polymer layer.

On another note, the fact that a considerably higher temperature was necessary on ITO compared to fused silica points away from the hypothesis that a catalyst may be formed at the precursor-substrate interface promoting the conversion of the PPV precursor.[94]

Going back to the idea of using SThL to produce high efficiency solar cells, we are indeed very close to the optimal feature size of about 20 nm (2x the exciton diffusion length for typical conjugated polymers). One should not forget that for my experiment rather huge Wollaston wire probes were used with a radius of curvature of 2.5 µm. State-of-the-art resistive probes made out of Si have a radius of curvature of ~ 5 nm (e.g. probes from Anasys Instruments – CA, USA), i.e. three orders of magnitude smaller. The application of such fine probes is likely to result in much smaller structures with higher line densities without the occurrence of re-flattening already partially converted structures. It would also result in lesser requirements regarding the stiffness of the polymer as probe penetration would be less detrimental to the final resolution. In the future one could also try to cool the substrate to avoid overall conversion of the polymer layer, an effect that becomes non-negligible at very high line densities. Of course a single probe would never be used to actually pattern the active layer of a solar cell due to the very low throughput. However, we will see how fast technology advances and if or when we may see arrays of a million AFM tips; arrays of 32x32 = 1024 AFM tips have already been produced in 2002.[95]

3 Triplet Emitters in Organic Solar Cells

3.1 Motivation

In organic light emitting diodes (OLEDs), the idea of using phosphorescent emitters is rather evident: Because general spin statistics states that only 25% of the generated excitons are singlets[96] and 75% are triplets, and because triplet excitons do not decay radiatively in a fluorescent host due to the forbidden intersystem crossing (ISC), the inclusion of a material that allows light emission from a triplet state is a means to improve the external quantum efficiency potentially by a factor of 4.

In organic photovoltaic cells on the other hand, the idea of using triplet emitters is not much explored despite two advantages of generating predominantly triplet excitons instead of singlet excitons: The first advantage is that triplet excitons have been frequently reported to have larger diffusion lengths than singlet exciton[97,98] due to their longer lifetime. The second advantage is that direct back-electron transfer (i.e. geminate recombination) on a fluorescent host from the triplet charge-transfer (CT) state to the (singlet) ground state is spin-forbidden.

In the following I will present some more background regarding triplet excitons, inter-system crossing and other phenomena so that the two advantages mentioned above can be better understood. I will then show possible methods to achieve a higher ratio of triplet excitons in the active layer of SCs in section 3.2.9.3 on page 91.

3.2 Theoretical Background

In this section I will complement the background given in section 1.5 on page 31 by giving further information on singlet and triplet excitons and related phenomena such as the importance of spin-orbit coupling for intersystem-crossing and the heavy-atom effect. I will also deduce the transition rules for energy transfer from Fermi's Golden rule and I will mention a few trends of important properties in conjugated polymers such as the magnitude of the exchange energy or the relation between the charge-transfer energy and the effective band gap and the open-circuit voltage. After the basics are understood I will explain the advantages and disadvantages of triplet excitons in OSCs and I will explain two approaches attempted in this work to increase the ratio of triplet excitons.

3.2.1 Singlet and Triplet Excitons

A singlet state is a state with a spin-multiplicity ($2S + 1$) of 1 and a triplet state is a state with a spin-multiplicity of 3. Here S is the total spin-quantum number of the state. The electron and the hole of an exciton can be thought of having a spin $s = ½$. Therefore, by applying general quantum mechanical angular momentum algebra, the overall spin S of an exciton can either be $S = 0$ (½ - ½) or $S = 1$ (½ + ½), giving rise to a singlet ($2S + 1 = 1$) or triplet ($2S + 1 = 3$) state, respectively.

The ground state (S_0) is always a singlet state with paired electron spins because Pauli's Exclusion Principle forbids two electrons with the same spin to occupy the same (lowest energy) orbital. For higher lying states (S_n and T_n with $n > 1$), both singlet and triplet states are possible. Triplet states are always slightly stronger bound than singlet states with the energy difference being the quantum mechanical *exchange energy* (see page 86). What is important to know at this point is that optical transitions from any excited triplet state to the singlet ground state (or vice versa) are ‘forbidden’ without any *spin-orbit coupling* (see page 87). Forbidden means that in the dipole approximation the matrix element for this transition is zero, i.e. the transition is impossible. Due to the forbidden transition, triplet excitons have a longer lifetime than singlet excitons, which can lead to greater diffusion lengths.

3.2.2 Triplet-Triplet Annihilation

Excited states can interact with each other. Singlet states may for example interact with each other to create a higher lying singlet state, they may interact with charges leading to charge

separation, a singlet state may split into two triplet states if the triplet level is low enough (singlet fission) etc.. Also triplet states may interact with each other. One important mechanism that plays a huge role in phosphorescent OLEDs is triplet-triplet annihilation (TTA). It is also proposed as a way of improving SCs by harvesting lower energy photons. As the term suggests, two triplet excitons annihilate each other during TTA. TTA could be treated as a special case of Dexter energy transfer, during which both donor (D) and acceptor (A) are in an excited state before the energy transfer:

- $^3D^* + {}^3A^* \rightarrow {}^1D + {}^3A^*$

3.2.3 Transition Rules

In the following I will deduce the transition rules governing Förster and Dexter transfer. The transition rules are deduced from Fermi's Golden Rule, which calculates the transition rates $k_{\mathrm{i}\rightarrow\mathrm{f}}$ from an initial state $|i\rangle$ to a continuum of final state $|f\rangle$ as

$$k_{\mathrm{i}\rightarrow\mathrm{f}} = \frac{2\pi}{\hbar}|\langle f|H'|i\rangle|^2\,\rho_{\mathrm{f}}\,, \qquad \text{Eq. 3-1}$$

where H' is the perturbing Hamiltonian and ρ_{f} is the density of final states. In our case, H' includes the electrostatic interaction of all electrons and nuclei.

Due the Pauli principle for electrons, the overall wave functions ψ must always be antisymmetric due to electron exchange and hence satisfy $\psi(1,2) = -\psi(2,1)$, where '1' and '2' indicate electron 1 and electron 2. If we now rewrite the initial and final states (ψ_{i} and ψ_{f}) as proper antisymmetric wave functions using the donor and acceptor wave functions ($\psi_{\mathrm{D,D^*}}$ and $\psi_{\mathrm{A,A^*}}$), we find that

$$\beta = \langle\psi_{\mathrm{f}}|H'|\psi_{\mathrm{i}}\rangle \qquad \text{Eq. 3-2}$$

$$= \left\langle \frac{1}{\sqrt{2}}[\psi_{\mathrm{D}}(1)\psi_{\mathrm{A^*}}(2) - \psi_{\mathrm{D}}(2)\psi_{\mathrm{A^*}}(1)] \middle| H' \middle| \frac{1}{\sqrt{2}}[\psi_{\mathrm{D^*}}(1)\psi_{\mathrm{A}}(2) - \psi_{\mathrm{D^*}}(2)\psi_{\mathrm{A}}(1)] \right\rangle \qquad \text{Eq. 3-3}$$

$$= \beta_{\mathrm{C}} - \beta_{\mathrm{E}}\,, \text{where} \qquad \text{Eq. 3-4}$$

$$\beta_{\mathrm{C}} = \int\int \psi_{\mathrm{D^*}}(1)\psi_{\mathrm{A}}(2)\; H'\; \psi_{\mathrm{D}}(1)\psi_{\mathrm{A^*}}(2) d\tau_1 d\tau_2 \qquad \text{Eq. 3-5}$$

is the Coulomb integral and

$$\beta_E = \int\int \psi_{D^*}(1)\psi_A(2)\, H'\, \psi_D(2)\psi_{A^*}(1)d\tau_1 d\tau_2 \qquad \text{Eq. 3-6}$$

is the exchange integral.

The integration in the last two equations happens over all coordinates (τ), i.e. over the spatial coordinates ($r = \{x, y, z\}$) and the spin (ω).

The integral

- β_C indicates the probability for Förster transfer and
- β_E indicates the probability for Dexter transfer.

The wave functions ψ above contain not only the spatial parts $\phi(x, y, z)$ but also the spin wave functions $\sigma(\omega)$. We may therefore split $\psi(i)$ for electron *i* into

$$\psi(i) = \phi(x_i, y_i, z_i)\, \sigma(\omega_i)\ . \qquad \text{Eq. 3-7}$$

Note that the spin of an electron (or hole) *i* is either

- up: $\sigma(\omega_i) = \alpha(\omega_i)$, or
- down: $\sigma(\omega_i) = \beta(\omega_i)$

and that the spin functions are orthogonal:

$$\int \alpha(\omega_i)\alpha(\omega_i)d\omega_i = \int \beta(\omega_i)\beta(\omega_i)d\omega_i = 1 \qquad \text{Eq. 3-8}$$

$$\int \alpha(\omega_i)\beta(\omega_i)d\omega_i = \int \beta(\omega_i)\alpha(\omega_i)d\omega_i = 0 \qquad \text{Eq. 3-9}$$

Note that we can use here the spin of the single electrons (± ½ as opposed the overall spin on donor/acceptor, which is either 0 (singlet) or 1 (triplet)) as we are only concerned with the "active" orbitals.

We may now rewrite the Coulomb and exchange integrals:

$$\begin{aligned} \beta_C &= \int\int \psi_{D^*}(1)\psi_A(2)\, H'\, \psi_D(1)\psi_{A^*}(2)d\tau_1 d\tau_2 \\ &= \int\int \phi_{D^*}(1)\phi_A(2)\, H'\, \phi_D(1)\phi_{A^*}(2)dr_1 dr_2 \ * \\ &\quad * \int \sigma_{D^*}(\omega_1)\sigma_D(\omega_1)d\omega_1 \int \sigma_A(\omega_2)\sigma_{A^*}(\omega_2)d\omega_2 \end{aligned} \qquad \text{Eq. 3-10}$$

$$\begin{aligned}\beta_E &= \int\int \psi_{D^*}(1)\psi_A(2)\, H'\, \psi_D(2)\psi_{A^*}(1)dt_1dt_2 \\ &= \int\int \phi_{D^*}(1)\phi_{A^*}(1)\, H'\, \phi_D(2)\phi_A(2)dr_1dr_2 \; * \\ &* \int \sigma_{D^*}(\omega_1)\sigma_{A^*}(\omega_1)d\omega_1 \int \sigma_D(\omega_2)\sigma_A(\omega_2)d\omega_2\end{aligned} \qquad \text{Eq. 3-11}$$

We are now ready to find the transition rules by considering the orthogonality of the spin functions.

3.2.3.1 Transition Rules for Förster Transfer

Förster transfer may happen if the Coulomb integral (β_C) does not vanish. If we look at the second term in β_C in Eq. 3-10, we see that it must be ensured that $\int \sigma_{D^*}(\omega_1)\sigma_D(\omega_1)d\omega_1 \neq 0$ and $\int \sigma_A(\omega_2)\sigma_{A^*}(\omega_2)d\omega_2 \neq 0$. According to Eq. 3-8 and Eq. 3-9 we find the following rule:

During Förster transfer, both, the donor and the acceptor, must each conserve their spin.

As a result the following transitions are allowed:

a) $^1D^* + {}^1A \rightarrow {}^1D + {}^1A^*$
   This is the singlet-singlet transition.

b) ($^1D^* + {}^3A \rightarrow {}^1D + {}^3A^*$)
   Note that this singlet to triplet transition requires A to be in a triplet state before the energy transfer takes place. In almost all cases the (ground state), however, A will be in a singlet state (see transition (e)) and hence this is a rather theoretical transition.

The following transitions are forbidden:

c) $^3D^* + {}^1A \rightarrow {}^1D + {}^1A^*$
   This triplet to singlet transition is *forbidden* according to the transition rule for FRET stated above. However, this transition may still be observed because $^3D^*$ has a long lifetime and although the FRET rate is very low, it may still be larger than the relaxation rate from $^3D^* \rightarrow {}^1D$. This process may actually be very efficient if the donor is phosphorescent.[99]

d) $^1D^* + {}^1A \rightarrow {}^1D + {}^3A^*$

e) $^3D^* + {}^1A \rightarrow {}^1D + {}^3A^*$

This is the triplet to triplet transition.

3.2.3.2 Transition Rules for Dexter Transfer

Dexter transfer may happen if the exchange integral (β_E) does not vanish. If we look at the second term in β_E in Eq. 3-11, we see that it must be ensured that $\int \sigma_{D^*}(\omega_1)\sigma_{A^*}(\omega_1)d\omega_1 \neq 0$ and $\int \sigma_D(\omega_2)\sigma_A(\omega_2)d\omega_2 \neq 0$. Applying again the spin orthogonalities, we find that the spin of the ground state of the acceptor before transfer and the donor after transfer must be the same and the spin of the excited state of donor before transfer and acceptor after transfer must be the same. As a consequence, the overall spin of the donor-acceptor pair must be conserved. We may hence imagine the Dexter transfer as an electron exchange process between the ground states and the excited states, during which

the spin of the exchanged electrons must be conserved.

In order to find the allowed transitions, one needs to picture the spins of the participating electrons in the HOMO and LUMO orbitals of donor and acceptor (see for example Figure 3-1). The following transitions are allowed:

f) $^3D^* + {}^1A \rightarrow {}^1D + {}^3A^*$ (same as (e))

The triplet to triplet transition can only be provided by Dexter transfer.

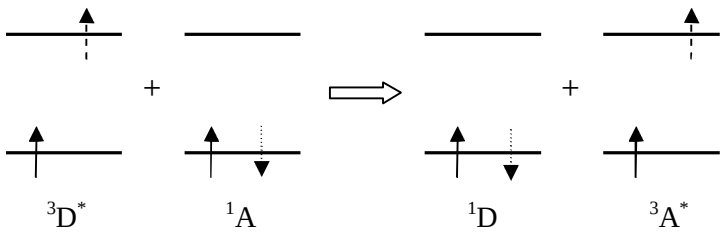

Figure 3-1. Visualisation of spins for the transition $^3D^* + {}^1A \rightarrow {}^1D + {}^3A^*$

g) $^1D^* + {}^1A \rightarrow {}^1D + {}^1A^*$ (same as (a))

Although this singlet to singlet transition is allowed, Förster transfer usually dominates this transition due to its longer-ranged nature.

3.2.3.3 Wigner's Spin Conservation Rule

Wigner's spin conservation rule[100] states that the overall spin of a system must be conserved. It covers any energy transfer process (Förster and Dexter transfer). Note that Wigner's spin conservation rule is fulfilled with the transition rules obtained above, and is specified by additional restrictions for Förster transfer (conservation of the donor spin and acceptor spin) and Dexter transfer (conservation of the spin of the exchanged electrons).

3.2.4 Exchange Energy

As mentioned above, the exchange energy is the difference between singlet and triplet excitons. It fundamentally stems from quantum mechanics, or more precisely the Pauli principle, where it is shown that for indistinguishable particles, the overall wave function must be either symmetric (bosons) or anti-symmetric (fermions, e.g. electrons) upon the exchange of those particles, leading to a new term in the expectation value of the energy. A requirement for exchange energy is therefore an orbital overlap of the participating particles.

The singlet-triplet energy splitting on the same molecule can be considerable with values around 0.7 eV (for polymers[101]) whereas *charge transfer states*, where electron and hole are located on different molecules, usually do not.

3.2.5 Charge Transfer State

A charge-transfer (CT) complex is an association of two or more molecules (typically a donor and an acceptor molecule), or of different parts of one very large molecule, in which a fraction of electronic charge is transferred between the molecular entities. The resulting electrostatic attraction provides a stabilizing force for the molecular complex.

Within the field of polymer SCs, the charge transfer state (CT state) is of great importance. The CT state is the state that is occupied after an exciton reaches the type II heterojunction, leading to an interfacial charge pair residing at the polymer/fullerene interface, and before the CT-state dissociates to obtain two separate (free) charges.[102] CT states are basically non-radiative exciplexes, i.e. excited states where the electrons and holes are located on different molecules, but with a high probability to lead to charge separation. The energy of the CT state is lower than the energy gap on either material but higher than the energy of the system with completely

separated (free) charges. Note that despite the energy of the charge-separated state being lower, there is an activation barrier that must be crossed first due to the Coulomb attraction.

The precise process of how the Coulomb attraction in a CT state is overcome to create long-range charge separation is currently under discussion. One theory is that charge separation happens efficiently if the electronically excited CT state forms largely delocalised band states which can overlap with the HOMO/LUMO orbitals of the donor/acceptor.[103]

The CT state gives the maximum possible open circuit voltage ($e\,V_{OC} \leq E_{CT}$). Typical values for the difference between the CT state and the energy-gap and for the difference between $e\,V_{OC}$ and E_{CT} in conjugated polymers are given in section 3.2.8.

3.2.6 Polarons and Polaron Pairs

A polaron is a charged quasiparticle that is accompanied by a polarisation field that disturbs the surrounding molecules in a way that lowers its energy. In the context of organic semiconductors, this means that polarons are charges that occupy energy levels within the band gap, i.e. either slightly below the lowest unoccupied molecular orbital (LUMO) or slightly above the highest unoccupied molecular orbital (HOMO).

Both, excitons and polaron-pairs are in a way coulombically bound electron-hole pairs, but the binding energy in polaron-pairs is lower and they are more spatially separated.

3.2.7 Spin-orbit Coupling, Intersystem Crossing and the External Heavy-Atom Effect

Spin-orbit coupling is the quantum mechanically explained phenomenon where electron spin interacts with angular momentum. A basic rule is that the higher the spin-orbit coupling, the higher the probability of *intersystem crossing* (ISC), i.e. the chance of a triplet state converting into a singlet state (or vice versa). To achieve efficient ISC, it is not only good to have many unpaired electrons as in paramagnetic materials, but the geometry plays a huge role. Certain symmetries can completely negate any spin-orbit coupling, which is why ISC is often enhanced at defect sites where the symmetry of the crystal lattice is broken.

Heavy metal atoms usually show high spin-orbit coupling (→ *heavy atom effect*) which is why complexes with Pd (atomic number $Z = 46$), Ir ($Z = 77$) and Pt ($Z = 78$) are so successfully used in triplet emitting materials. However, also lighter atoms such as S ($Z = 16$), which is part of

the thiophene group, show considerable coupling constants and hence allow ISC to occur to some degree.

An open theoretical question is the range of the *external* (or 'remote') *heavy-atom effect*. The phenomenon of the "collisional perturbation of spin-orbit coupling and the mechanism of fluorescence quenching" was described by Kasha in 1952.[104] There he assumed that the degree of ISC from the singlet to the triplet state of the perturbed molecule depends on the degree of penetration of the π-electron into the electric field of the nucleus of the perturbing atom and the strength of the electric field. The former requires orbital overlap and the latter is increased by a high atomic number.

However, "a more complex *indirect* interaction is required to describe the RHAE (remote heavy atom effect)-enhanced intersystem crossing rate. It is unambiguously established that the covalent through-bond framework alone fails to describe the trends in the RHAE effect either at the rate constant level […] or at the matrix element level […] Hence, this indirect coupling must involve dominant noncovalent contributions as well."[105]

It was later shown in a number of papers[105-107] that the heavy-atom effect seems to be efficient over a longer distance, for example when the chromophore and the heavy atom are separated by two C-C σ-bonds[106] or even by three amino acid residues.[107] Mathematical descriptions can be found in the literature.[105,108,109] The main finding from these descriptions is that the efficiency of the heavy-atom effect also depends on a resonance-energy term.

3.2.8 Trends of Energy Levels and other Properties in Conjugated Polymers

There are a few interesting trends connected with the energy levels of the singlet and triplet states that have been reported in the literature. First of all, spin-orbit coupling is considered weak in general for conjugated polymers, especially when one is taking into account the high non-radiative decay rate of the triplet state.[110] This is why phosphorescence in conjugated polymers is usually very hard to detect and cooling is necessary to reduce the non-radiative decay rate.

It was also found that the energy gap law could be applied to the T_1-S_0 transition in conjugated polymers, which means that the lower the energy difference between T_1 and S_0, the higher the non-radiative decay rate of this transition.[110]

The exchange energy itself was studied in more detail and it was found that for a number of different conjugated polymers, the exchange energy was rather constant around 0.7 eV.[101] It is

widely accepted that the lower the energy difference between a singlet and its closest triplet state, the higher the ISC rate.[111]

Studies[112] on a large number of polymers have shown some important trends regarding the charge transfer state energy E_{CT} (see Figure 3-2):

- $E_{CT} - |E_{HOMO}(D) - E_{LUMO}(A)| = 0.3$ eV. E_{CT} is the energy of the charge-transfer state.
- $E_{CT} - e\,V_{OC} = 0.5$ eV.
- The CT state needs to be at least 0.1 eV below the S_1 state in order to achieve photo-induced electron transfer (PET).
- If the T_1 state is more than 0.1 eV below the CT state, the triplet state will be occupied heavily in favour of the CT state.

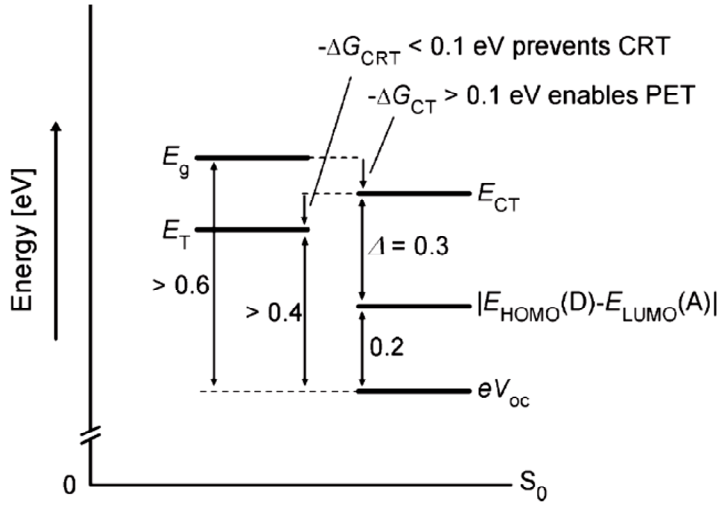

Figure 3-2. Relation of the energy of the CT state with respect to the donor band gap E_g, $e\,V_{OC}$, and $|E_{HOMO}(D) - E_{LUMO}(A)|$. E_g is the donor band gap $|E_{HOMO}(D) - E_{LUMO}(D)|$, CT means charge transfer and CRT means charge recombination to the triplet. Further explanations are in the text. Image reprinted with permission from Veldman et al.,[112] Copyright (2009) WILEY-VCH Verlag GmbH & Co. KGaA, Weinheim.

3.2.9 Generating Triplet Exciton in Polymer Solar Cells – Advantages, Disadvantages and Methods

3.2.9.1 Advantages of Converting Singlet to Triplet Excitons

In the motivation section of this chapter I talked about the advantages of generating triplet excitons, which exhibit the potentially longer diffusion lengths and the reduced geminate recombination. Now that the background has been given, I will elaborate on them:

Triplet excitons have been reported to have larger diffusion lengths than singlet excitons.[97,98] This is because in a fluorescent host with little intersystem crossing, any generated triplet has a strongly forbidden radiative decay, which leads to a strong increase of the lifetime (τ) compared to singlet excitons (up to ms[113] for triplets compared to ns for singlets). Even considering that the Dexter transfer, which governs the triplet-triplet energy transfer, is not as efficient as the Förster transfer, which dominates the singlet-singlet energy transfer, triplets often have larger exciton diffusion lengths (µm ranges for triplet excitons conjugated polymer have been reported[98,113] compared to ~ 10 nm commonly found for singlet excitons). The connection between lifetime and diffusion length (L) is given by the diffusivity (D):

$$L = \sqrt{D\,\tau}. \qquad \text{Eq. 3-12}$$

D is determined by the efficiency of the energy transfer mechanism and by the degree of conjugation (if the exciton is delocalised over a larger area of the molecule, naturally the effective diffusion length is increased). As the effective conjugation length is the same for singlet and triplet excitons, the difference in D for singlets and triplets will be determined by the difference between the efficiency of the Förster- and Dexter transfer.

Assuming we created more triplets and they had a larger diffusion length, we could create SCs with larger domains than typical for bulk-heterojunction SCs and hence improve the charge transport while maintaining the good exciton dissociation ability of morphologies with smaller domains. As a limiting case, even highly efficient bilayer cells can be envisaged if the average exciton diffusion length approaches typical film thicknesses (~ 100 nm).

The second advantage of triplet excitons is illustrated in Figure 1 of Guo et al..[114] We imagine that the spin-orbit coupling is generally low within our material but that we managed to generate a triplet exciton. After the triplet exciton ($^3D^*$) reaches the interface, it transfers an electron to the acceptor leading to a charge transfer (CT) state ($^3[D^{+*}, A^{-*}]$). Now the CT state can either dissociate into free separated charges (which is the desired process), or undergo intersystem crossing (ISC) into a singlet excited state, from where it could recombine or generate free charges. The main difference compared to singlet excitons is that direct back electron transfer, i.e. geminate recombination, of the triplet CT state is spin-forbidden.[115] This is an important aspect as it has been shown that at least for polymer/polymer SCs, geminate recombination is a key loss mechanism.[116-118] In polymer-fullerene SCs geminate recombination occurs as well, but it is less clear if geminate recombination[119-121] or bimolecular recombination[122-124] dominates.

3.2.9.2 Disadvantages of Converting Singlet to Triplet Excitons

In the following I will discuss the potential disadvantages of increasing the ratio of triplet excitons.

First, due to the energy difference between singlet and triplet excitons (the exchange energy), more energy of the initially absorbed photon is lost. If the triplet level on the donor is still above (higher in energy) the CT level, no problem arises, but if the triplet level is below the CT level, the CT state will not be sufficiently occupied and hence charge separation will not occur and the power conversion efficiency of the SC will deteriorate. (Note that the CT state should be virtually identical for singlet and triplet CT states for the same donor-acceptor system due to the low exchange energy of CT states). This loss in photon energy due to singlet-to-triplet conversion is mainly a problem if one aims for "ultimate" performances as the ultimate SC will have a CT state just (~ 0.1 eV) below the singlet level on the donor to use the maximum of the photon's energy but while assuring quick transfer of the singlet exciton to the CT state. In such a configuration, an ISC to the triplet state will result in the triplet level being below the CT level.

Furthermore, it is not clear whether the exciton diffusion length of triplet excitons is indeed much larger than for singlet excitons. The problem is that despite the undoubtedly longer life time of triplets, the diffusivity is sometimes so much reduced that the diffusion length is not improved.[25]

Another aspect to keep in mind is that, assuming one does have increased spin-orbit coupling and hence increased ISC ($S_1 \rightarrow T_1$) in the host, this would not only increase the number of triplet excitons, but it would also increase the ISC rate from the triplet state (T_1) to the ground state (S_0), i.e. it would reduce the triplet exciton's lifetime and diffusion length. However, to which degree this would happen is not clear as rates vary over many orders of magnitudes depending on which transition one is looking at. As an example, highly efficient triplet emitters such as $Ir(ppy)_3$ have an ISC rate[125] from $S_1 \rightarrow T_1$ below $(100\ fs)^{-1}$, yet the radiative transitions from the triplet to the singlet ground states are in the µs range, and hence still three orders of magnitude larger than on purely fluorescent materials.

3.2.9.3 Methods of Converting Singlet to Triplet Excitons

In order to convert singlet to triplet excitons in the SC's active layer, two methods can be envisaged.

1. One idea is to convert the singlets from the host via transferring them to the guest, where they are converted into triplet excitons due to the strong intersystem-crossing (ISC) rate, with subsequent back-triplet-exciton-transfer to the host.[126,127] This approach puts strong constraints on the energy levels of the material (see Figure 3-3a). One effect that helps to achieve such an energy level configuration is that phosphorescent guests with high spin-orbit coupling usually have rather small exchange energies ($E(S_1) - E(T_1)$). Note that the first step may happen either via Förster transfer or via charge transfer of electron and hole from the host to the guest.

2. The other approach relies on the magnetic moment of the phosphorescent guest molecule to induce sufficient spin-orbit coupling in the host polymer so that the ISC rate is increased directly on the host without the need of exciton transfer between host and guest (see Figure 3-3b). (This approach is similar to adding directly heavy metal atoms to the donor polymer or to the blend. The problem, however, is that these atoms often aggregate together). As mentioned earlier, the range of the external heavy-atom effect is not completely clear. However, there are claims[128,129] that this approach can work in OSCs.

Both approaches have been used in this work.

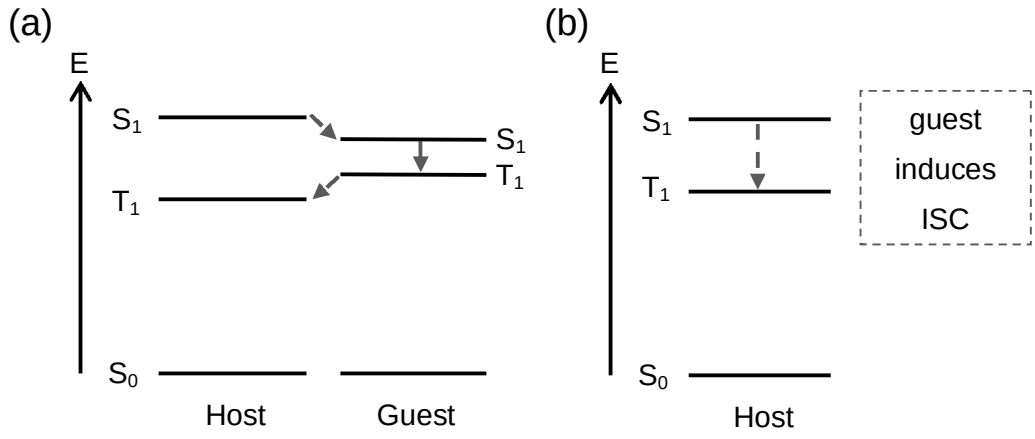

Figure 3-3. Possible strategies to increase the number of triplet excitons. (a) Exciton energy diagram illustrating the intersystem crossing (ISC) on the guest. (b) Direct ISC on the host, induced by the guest.

3.3 Characterisation Techniques

Aside from measurements of the absorption by an absorption spectrometer, the thickness via a profilometer and the photoluminescence (PL) via a time correlated single photon counter (TSCPC), the most important SC specific measurement techniques are determining the IV curve and the incident photon to current efficiency (IPCE) spectrum. Other important methods are those that observe the morphology of the active layer. Although not the focus of this study, the morphology of the active layer greatly alters the performance of a SC, especially in a bulk heterojunction architecture: the phase separation, domain sizes and crystallization influence exciton dissociation and charge transport. Techniques that are able to help in uncovering the morphology are, among others, atomic force microscopy (AFM), transmission electron microscopy (TEM), confocal microscopy, micro-Raman spectroscopy, as well as scattering techniques such as X-ray diffraction. To determine the mobility, I fabricated field-effect transistors (FETs) of blends of the materials.

3.3.1 JV Characteristics

The IV curve (or JV curve, where I is the current, J is the current density and V is the voltage) of a SC is measured under certain standard conditions. These are a photon flux of 1000 W/m^2, a temperature of 25 °C and an AM1.5 illumination. The air-mass coefficient (AM) of 1.5 corresponds to a solar zenith angle of 48.2 ° which has been chosen to represent roughly the yearly average at mid-latitudes. The measurements were done in rough vacuum (10^{-2} mbar) under a class AAA solar simulator from Oriel which uses a Xenon lamp and a special filter to generate the necessary spectrum.

The most important parameter which can be determined by obtaining the IV curve is the energy (or power) conversion efficiency η:

$$\eta = \frac{P_{\mathrm{out}}}{P_{\mathrm{light}}} = \frac{(I\,V)_{\mathrm{max}}}{P_{\mathrm{light}}} = \frac{\mathrm{FF}\,I_{\mathrm{SC}}\,V_{\mathrm{OC}}}{P_{\mathrm{light}}}. \qquad \text{Eq. 3-13}$$

P_{out} and P_{light} are the maximum output power and the incoming light power, I_{SC} is the short-circuit current, V_{OC} is the open-circuit voltage and FF is the fill factor. The meanings of I_{SC}, V_{OC} and $(I\,V)_{max}$ are shown in Figure 3-4. The FF, as it can be deduced from above, can be expressed as

$$FF = \frac{(I\,V)_{\mathrm{max}}}{I_{\mathrm{SC}}\,V_{\mathrm{OC}}} \qquad \text{Eq. 3-14}$$

and can be interpreted as a measure of how rectangular the characteristic is in the 2nd quadrant. Within the framework of the equivalent circuit for a SC (see Figure 3-5), the FF is strongly influenced by the parasitic series and shunt resistance (R_S and R_{SH}). The series resistance (ideally zero) is mainly increased by contact resistances and low mobilities within the solar cell. A shunt resistance (ideally infinite) is decreased due to conduction through filaments or defect states. Note that processes such as an electric field dependent exciton dissociation or charge carrier recombination will also look like the introduction of a parasitic resistance. The formula for the JV characteristics according to the equivalent SC circuit is

$$J = J_L - J_0 \exp\left[\frac{e}{nkT}(V - J\,R_\mathrm{S})\right] + \frac{J\,R_\mathrm{S} - V}{R_\mathrm{SH}}, \qquad \text{Eq. 3-15}$$

where J_L is the current generated by the SC, J_0 is the dark saturation current, n is the diode ideality factor, k is the Boltzmann constant and T is the temperature. From the formula above we can understand the influence of a series and shunt resistance on the JV characteristics:

- Increasing R_S will at first reduce the slope at high voltages (near V_OC). Increasing R_S by large amounts will also reduce J_SC.
- Decreasing R_{SH} by small amounts will at first increase the slope near $V = 0$. Decreasing it further will also reduce V_OC. Drastically reducing R_SH will even reduce J_SC.

From a molecular point of view, the FF is influenced by how easily a charge can be extracted from the active layer. This again is influenced by many factors such as the morphology,[130] the interface between the electrodes and the active layer,[130,131] the mobility and the non-geminate recombination of the free charge carriers.[132]

The origin of V_OC is not completely clear. In single layer devices, V_OC can be estimated by the difference of the electrode work function according to the metal-insulator-metal (MIM) model.[133] In bilayer heterojunctions, this is still true although a build-up of charge at the heterojunction has to be taken into account as well.[134] In bulk-heterojunction devices on the other hand, V_OC depend strongly on the energy levels of the participating materials if the contacts are ohmic. An upper limit for V_OC is the difference between the LUMO energy of the electron acceptor and the HOMO energy of the electron donor. For non-ohmic contacts, the work-function difference is a good indicator again for V_OC.[135]

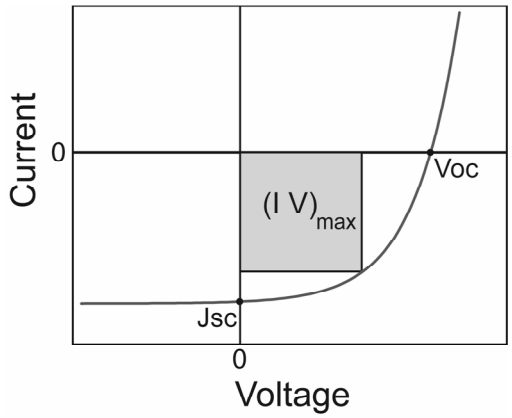

Figure 3-4. Typical IV curve of a photovoltaic cell. The adopted convention is to show the important part in the 2nd quadrant. The grey rectangle shows the product of I and V at the maximum power point. The more the rectangle fills the area above the curve in the 2 nd quadrant, the higher is the FF. Also shown are the short-circuit current (J_{SC}), i.e. the current at zero voltage, and the open-circuit voltage (V_{OC}), i.e. the voltage at zero current.

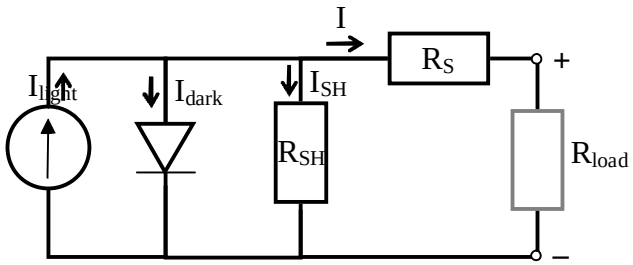

Figure 3-5. Equivalent circuit of a SC including the series resistance (R_S) and shunt resistance (R_{SH}).

3.3.2 IPCE Spectrum

The IPCE spectrum stands for the

- incident photon to current efficiency spectrum, sometimes also referred to as
- incident photon conversion efficiency spectrum, or
- incident photon to current conversion efficiency spectrum, or
- EQE (external quantum efficiency) spectrum.

The IPCE gives the number of charges that run through the external circuit as a function of wavelength.

$$IPCE = \frac{N_{\text{charge}}}{N_{\text{photon}}} = \frac{1240\ I_{\text{SC}}}{(\lambda/\text{nm})\ P_{\text{in}}}, \qquad \text{Eq. 3-16}$$

where I_{SC} is the short-circuit current, λ is the wavelength and P_{in} is the power of the incoming (monochromatic) photons. Note that an IPCE of 100 % means that every photon generates both, an electron and a hole, within the active layer and that both charge carriers reach their respective electrodes.

The IPCE spectra in this work were measured at room temperature in rough vacuum using a home-built apparatus containing a Xenon lamp and a monochromator from Bentham.

3.3.3 Mobility

The mobility (μ) of a material is a measure of how easily charges are transported in a material. The drift velocity (v_d) is related to the mobility and the applied electrical field (E): $v_d = \mu E$. The mobilities are different for electron and holes in a semiconductor and are (at least in the area of inorganic semiconductors) often connected to the effective mass of the charge carrier which is again influenced by the band diagram ($E(k)$, where k is the wave-vector). The mobility is not to be confused with the conductivity, which is a quantity that is also influenced by the number of charges taking part in the conduction.

The mobilities were determined by fabricating field-effect transistors (FETs), whose structures are shown in Figure 3-6. The FETs have a bottom contact architecture where gold is evaporated onto a Si/SiO_x wafer to define drain and source. The first step is to spin-coat hexamethyldisilazane, HDMS, onto the substrate (mainly to improve the adhesion of the active layer). The active layer is then spin-coated on top and contacted with a probe station in a glove box. The mobility was extracted by applying a drain voltage that drives the transistor in saturation regime (for a range of gate voltages) and taking the trans-characteristics, i.e. the drain-source current (I_{DS}) as a function of the gate voltage (V_{GS}). The slope of the square root of I_{DS} is then proportional to the square root of the mobility:

$$I_{DS} = \frac{W}{2L}\,\mu\, C\,(V_{GS} - V_0)^2\,, \qquad \text{Eq. 3-17}$$

where W is the width of the channel, L its length, C the capacitance per area and V_0 the zero-voltage which can also be calculated by fitting a linear function to the square root of I_{DS}. and measuring its intercept with $I_{DS} = 0$.

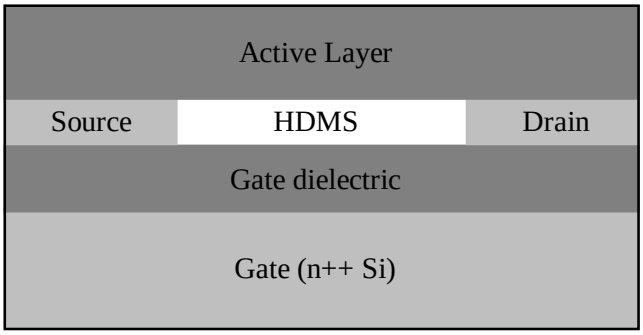

Figure 3-6. Structure of field-effect transistors (FETs) used to determine charge carrier mobilities. The substrates are bought from the Faunhofer Institut Photonische Mikrosysteme, Dresden, Germany. It is a bottom gate structure, where the 675 ± 40 µm thick gate consists of heavily doped Si and the gate dielectric is the 230 ± 10 nm SiO_x layer on top. Source and drain contacts consist of a 30 nm gold layer with a 10 nm high work function adhesion layer (ITO). There are 16 transistors on one substrate. They all have the same width of 10 mm but have variable lengths of 2.5, 5, 10 and 20 µm (4 transistors each). The active layer in my experiments was a blend consisting of a P3HT, $PC_{61}BM$ and the triplet emitter E. Contact with the source and drain electrodes is facilitated simply via pushing with a wire through the active layer onto the electrodes.

3.3.4 Modelling and Interpretation of Current-Voltage Characteristics

In the context of organic electronics, models for

- ohmic current,
- space-charge-limited current (SCLC) and
- SCLC with an exponential trap distribution

are often applied.[136-138]

Ohmic current can be described by

$$J = q\, n\, \mu\, \frac{V}{d}\,, \qquad \text{Eq. 3-18}$$

where q is the electronic charge, V is the applied voltage, d the thickness of the active layer and μ the mobility. Ohmic current is often observed at low bias voltages, where injection is inefficient and the number of charges inside the device lead to a negligible space charge.

3.3.4.1 Space-Charge-Limited Current Model

The *SCLC model* assumes that carriers are injected ohmically (i.e. without an injection barrier) and that the bottleneck of charge transport is the build-up of a space charge inside the device. In the absence of traps, this leads to the well-known Mott-Gurney law[139]:

$$J = \frac{9}{8} q\, \mu\, \epsilon_0\, \epsilon_r\, \frac{V^2}{d^3}, \qquad \text{Eq. 3-19}$$

where $\varepsilon_0 \varepsilon_r$ is the dielectric permittivity.

3.3.4.2 Space-Charge-Limited Current Model Including Traps

If we assume an exponential distribution of traps which decreases with distance from the HOMO, such as

$$H(E) = \frac{H_t}{E_t} \exp\left(\frac{E_{HOMO} - E}{E_t}\right), \qquad \text{Eq. 3-20}$$

where $H(E)$ is the density of traps at energy E, H_t is the total trap density (obtained by integrating $H(E)$ over E) and E_t is the characteristic energy of the trap distribution, the resulting current turns out to be a high power function of the voltage. More precisely, assuming the overall trap density is much larger than the number of free carriers, that carrier diffusion is negligible and that all the HOMO states are located at E_{HOMO}, the model predicts for one carrier dominated transport:[140,141]

$$J = K\, \frac{V^{m+1}}{d^{2m+1}} \qquad \text{Eq. 3-21}$$

where $m = \frac{E_t}{kT}$ and

$$K = q^{1-m}\, \mu\, N_{HOMO}\, \frac{(2m+1)^{m+1}}{(m+1)^{2m+1}} \left(\frac{\epsilon_0\, \epsilon_r\, m}{H_t}\right)^m, \qquad \text{Eq. 3-22}$$

where N_{HOMO} is the HOMO effective density of states and H_t is the total trap density. The trap degeneracy is assumed to be 1.

According to the SCLC model, one would actually expect

- ohmic behaviour in the low current bias regime (where the field generated by the few injected carriers is negligible compared to the applied electrical field),
- trap-limited SCLC for higher applied bias and
- trap-free SCLC current for high bias voltages where all traps are filled and the number of free charge carriers is considerably larger than the number of traps.

3.3.4.3 Device Simulation - Influence of Doping, Mobility and Traps and the JV Curves

The above presented space-charge-limited current gives a good idea of the general shape of current-voltage (JV) characteristics taken in the dark. However, also when confronted with JV curves obtained under illumination, one may want to distinguish effects such as doping, mobility and traps, or at least predict the qualitative influence of each of them.

Due to the lack of knowledge of the precise morphology, and the difficulty in applying it even if known, *macroscopic* device simulations are typically done to investigate the influences of these macroscopic device parameters.

3.3.4.3.1 Influence of Doping on Solar Cell Performance

Schafferhans et al.[142] for example investigated the influence of hole doping and charge carrier mobility on the SC performance. They used a macroscopic model that relies on the Poisson equation, the continuity and drift-diffusion equation in one dimension, and a Langevin-type bimolecular non-geminate recombination. The charge generation by light was assumed to create free polarons (assuming 100% exciton dissociation into free charges) and the electron and hole mobility was set to equal values and independent of the electrical field.

They found (see Figure 3-7a and b) that a stronger doping would mainly lead to a decreasing J_{SC}, because the increased number of free charge carriers would lead to a less strong internal electrical field and hence increase the transit time which leads to an increasing recombination. Due to the increased recombination, the fill-factor is also expected to drop, but to a lesser degree than J_{SC}. V_{OC} on the other hand is predicted to be virtually constant upon doping.

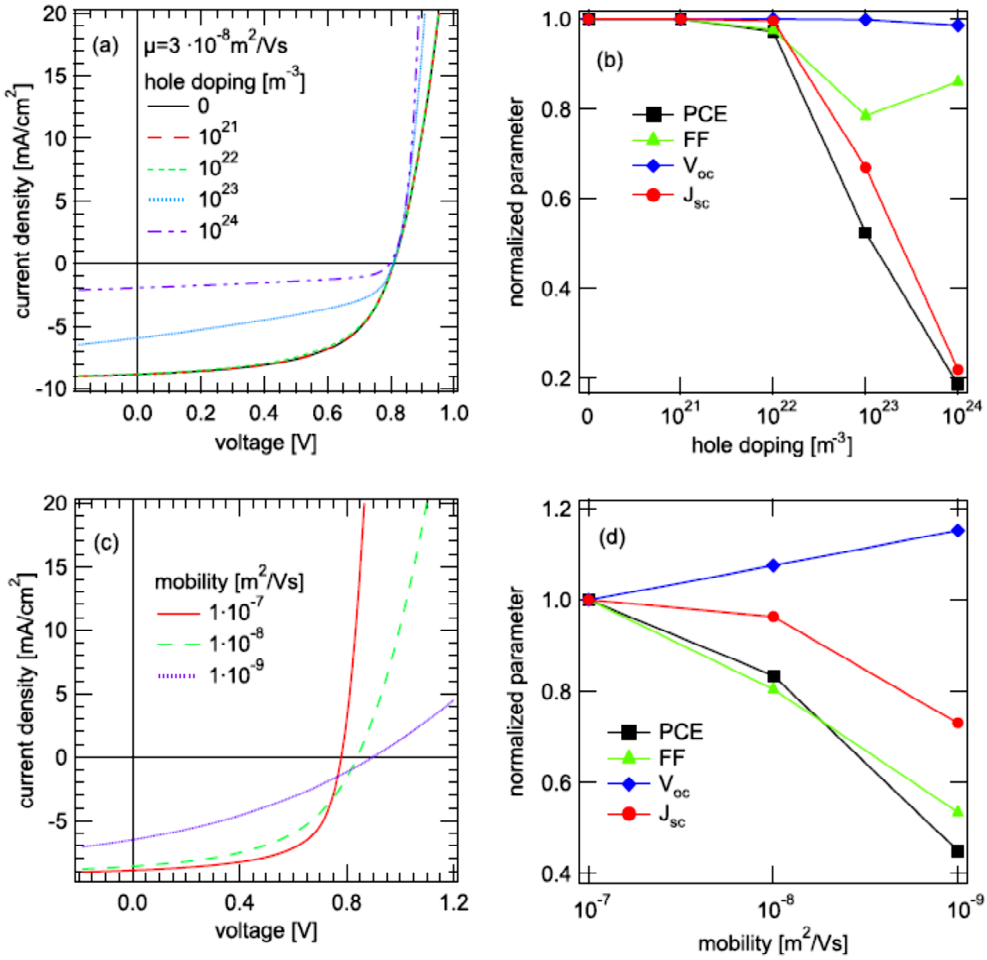

Figure 3-7. Simulated JV-curves for different levels of (a) hole doping and (c) mobility. (b) and (d) show the corresponding normalised values of the power conversion efficiency (PCE), *FF*, V_{OC} and J_{SC}. Figure reprinted with permission from Schafferhans et al.,[142] Copyright (2010) Elsevier.

3.3.4.3.2 Influence of Mobility

The influence of mobility on device performance (see Figure 3-7c and d) has also been in investigated by Mandoc et al.[143] and Deibel et al.,[144] where a macroscopic device model similar to that of Schafferhans et al. was used. (Deibel et al. further considered a field dependent polaron pair dissociation and a reduced Langevin recombination rate).

A high mobility is expected to lead to a high polaron pair dissociation (typically *not* a bottle-neck for polymer-fullerene SCs, but for polymer-polymer SCs) and a high charge extraction and hence to a high J_{SC}. On the other hand, the very efficient charge extraction at high mobilities leads to low charge carrier concentrations and hence to a small V_{OC}. As a result of the counteracting effects of charge extraction and charge (polaron) recombination, the FF as a

function of mobility was shown[144] to have a maximum at about 10^{-6}-10^{-4} m^2 V^{-1} s^{-1} (see Figure 3-8).

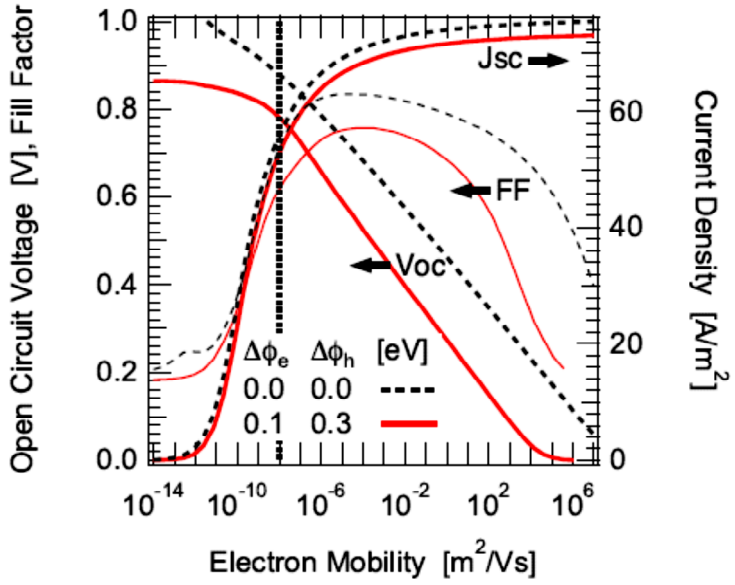

Figure 3-8. Simulated influence of the electron mobility on V_{OC}, *FF* and J_{SC} for two sets of injection barriers (solid red and black dashed lines). Image reprinted with permission from Deibel et al.,[144] Copyright (2008) WILEY-VCH Verlag GmbH & Co. KGaA, Weinheim.

3.3.4.3.3 Influence of Traps

Traps will have a strong influence on non-geminate charge recombination. Whereas without traps, only free charges recombine, in the presence of traps one also has to consider the recombination between a trapped charge (that is being released in the process) and a free charge or between two trapped charges. Note that trap states may also just be 'intrinsic' states originating from the tail of the HOMO or LUMO density of states (see e.g. Figure 5a in Blakesley et al..[145]). Because of the latter, the effect of the addition of traps is somewhat similar to the increase of energetic disorder (see Figure 4b of Blakesley et al..[145]). Increasing the number of traps or the energetic disorder will[146] reduce J_{SC}, *FF* and V_{OC}.[145] Especially for energetic disorder, there seems to be a threshold above which J_{SC} and *FF* are decreasing very strongly. Note that V_{OC} is rather unaffected even by large values of σ which is the parameter describing the spread of the Gaussian distribution of the density of states.

3.3.5 Time-Correlated-Single-Photon-Counting

A Time-Correlated-Single-Photon-Counter (TCSPC) can be used to measure the PL spectrum and the lifetime of any emitting species.

Within a TCSPC, the luminescent sample is excited by a pulsed laser. The laser pulses and any photons emitted by the sample can be measured by a very sensitive photon-detector as a function of time. The details of how the pulses and the start of the measurement are synchronised are not relevant to the discussion below.

By measuring the temporal evolution of the number of emitted photons one can get information about the emitting species, for example how many different species are involved in the PL, and what are their individual lifetimes. The lifetimes then indicates whether one is likely to deal with e.g. singlet excitons, singlet exciplexes or triplet excitons, etc..

3.3.5.1 Signal in Case of One Species

Let us assume a species (an excited state) A is emitting light according to

$$\frac{dN(t)}{dt} = N(t) \cdot k\,, \qquad \text{Eq. 3-23}$$

where k is the overall decay rate and $N(t)$ the number of molecules in the excited state A. We further assume here that the sample is excited at exactly $t = 0$. This assumption is reasonable for lifetimes much larger than the width (full width at half maximum) of the instrument response function, which is the temporal signal measured when only the laser light is detected and hence depends on the laser pulse width and the detector. For a very quickly decaying signal, however, the measured signal has to be deconvolved with the instrument response function. Note that the number of collected photons ($n(t)$) is proportional to the number of excited molecules ($N(t)$), i.e. $n(t) = c_1\, N(t)$, where the proportionality constant c_1 is determined by a number of factors such as the radiative decay rate of the species A, the geometry of the setup, the quantum efficiency of the photon-detector used in the TCSPC, or the occurrence of reabsorption of the emitted photon.

The overall decay rate k includes the radiative (k^{rad}) and any non-radiative (k_i^{nr}) decay mechanisms:

$$k = \; k^{\mathrm{rad}} + \sum_i k_i^{\mathrm{nr}}\,. \qquad \text{Eq. 3-24}$$

Solving Eq. 3-23 yields a mono-exponential decay signal:

$$N(t) = N_0 \cdot e^{-kt} + b \quad \text{or} \quad N(t) = N_0 \cdot e^{-\frac{t}{\tau}}, \qquad \text{Eq. 3-25}$$

where N_0 is the number of excited molecules immediately after excitation (i.e. at $t = 0$), τ is the lifetime ($\tau = 1/k$) and b is a constant resulting from the background noise. We will assume $b = 0$ in the following.

If we take the natural logarithm of $N(t)$ we obtain

$$\ln\big(N(t)\big) = \ln(N_0) - \frac{1}{\tau}\, t\,. \qquad \text{Eq. 3-26}$$

We hence see that in the simplest case of a single emitting species following Eq. 3-23, $\ln\big(N(t)\big)$ follows a linear function whose slope (m) is a measure of the decay rate ($m = -k = -1/\tau$).

3.3.5.2 Signal in Case of Multiple Emitting Species

Let us now assume that a number of species (N_S) are emitting light in the wavelength range where the signal ($N(t)$) is collected. Eq. 3-23 then becomes

$$\frac{dN(t)}{dt} = \sum_j^{N_S} N_j(t) \cdot k_j\,, \qquad \text{Eq. 3-27}$$

where k_j is the overall decay rate of the species j and $N_j(t)$ the number of molecules in the excited state j. Solving Eq. 3-27 we now obtain a multi-exponential decay signal:

$$N(t) = \sum_j^{N_S} N_j^0 \cdot \exp\big(-k_j \cdot t\big), \qquad \text{Eq. 3-28}$$

or, after taking the natural logarithm:

$$\ln\big(N(t)\big) = \ln\left(\sum_j^{N_S} N_j^0 \cdot \exp\,(-k_j \cdot t)\right). \qquad \text{Eq. 3-29}$$

The above equations (Eq. 3-28 or Eq. 3-29) can be used to fit the decay curves to obtain the missing parameters N_j^0 and k_j. Note, however, that fitting such curves is a challenge as it is often not clear from the curves how many different species are contributing to the signal. This is why it is usually advised to keep the number of species N_S during the fitting as small as possible.

For a general introduction to lifetime measurements and a discussion of various decay models refer to the literature.[21]

3.3.6 Photoluminescence Quantum Efficiency Measurements

The photoluminescence quantum efficiency (PLQE) is the ratio between the number of emitted photons (N_{Em}) to absorbed photons (N_{Abs}).

$$\mathrm{PLQE} = \frac{N_{\mathrm{Em}}}{N_{\mathrm{Abs}}}, \qquad \text{Eq. 3-30}$$

The PLQE is not only important for LEDs, where it gives the highest possible internal quantum efficiency, but also for SCs. In a polymer SC, the dissociation of excitons into free charge carriers at a type II heterojunction is one of many loss mechanisms, and a high PLQE would indicate that this process is inefficient. A high PLQE for a BHJ SC therefore indicates that either the domains of the absorbing material are too big for excitons to diffuse to the heterojunction, or that exciton splitting at the interface is not efficient.

In the following I will describe how the PLQE of solid films can be measured. The technique used for this work is described by de Mello et al..[147] It relies on taking the following luminescence signals of all light (laser and PL) exiting the integrating sphere (see Figure 3-9):

- measurement without sample in the dark, i.e. without laser, to correct all measurements for background noise
- measurement of the signal with laser, without sample ("NO"-signal)
- measurement of the signal with laser and with sample, whereas the laser does *not* hit the sample surface *directly* ("OFF"-signal)
- measurement of the signal with laser and with sample, whereas the laser beam hits the sample surface *directly* ("ON"-signal)

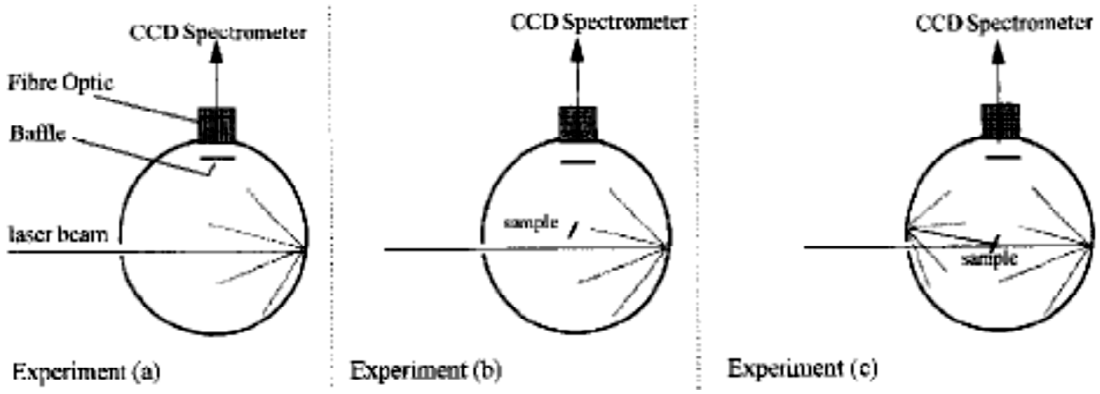

Figure 3-9. Illustration of the measurements necessary to determine the PLQE of solid films. (a) Taking the spectrum without sample. (b) Taking the spectrum with the sample inside the sphere, without illuminating the sample directly. (c) Taking the spectrum with the laser light hitting the sample directly. Image reprinted with permission from de Mello et al.,[147] Copyright (1997) WILEY-VCH Verlag GmbH & Co. KGaA, Weinheim.

In the following we will use *P* for the PL signal and *L* for the laser signal. *A* is the fraction of laser light (directly hitting the sample) absorbed by the sample and *r* is the fraction of reflected laser light (by the sphere) that is absorbed by the sample. We obtain the following equations for the case that the laser light does not hit the sample directly:

$$\begin{aligned} L_{\mathrm{OFF}} &= L_{\mathrm{NO}} \cdot (1 - r), \\ P_{\mathrm{OFF}} &= \mathrm{PLQE} \cdot L_{\mathrm{NO}} \cdot r, \end{aligned} \qquad \text{Eq. 3-31}$$

and the following equations in the case where the laser light does hit the sample directly:

$$\begin{aligned} L_{\mathrm{ON}} &= L_{\mathrm{NO}} \cdot (1 - r) \cdot (1 - A) = L_{\mathrm{OFF}} \cdot (1 - A), \\ P_{\mathrm{ON}} &= \mathrm{PLQE} \cdot L_{\mathrm{NO}} \cdot A + (1 - A) \cdot P_{\mathrm{OFF}}\,. \end{aligned} \qquad \text{Eq. 3-32}$$

Rewriting the last equation results in the final expression:

$$\mathrm{PLQE} = \frac{P_{\mathrm{ON}} - (1 - A) P_{\mathrm{OFF}}}{L_{\mathrm{NO}} \cdot A} = \frac{P_{\mathrm{ON}} - \frac{L_{\mathrm{ON}}}{L_{\mathrm{OFF}}} P_{\mathrm{OFF}}}{L_{\mathrm{NO}} \cdot \left(1 - \frac{L_{\mathrm{ON}}}{L_{\mathrm{OFF}}}\right)}. \qquad \text{Eq. 3-33}$$

3.4 P3HT:$PC_{61}BM$ blends with Cu-complexes

3.4.1 Materials

The host blend is a P3HT:$PC_{61}BM$ blend, which is possibly the most investigated material system so far in the area of polymer-fullerene SCs. The high efficiency of the P3HT:$PC_{61}BM$ bulk heterojunction system is assigned to several properties, such as the ultrafast exciton splitting in about 100 fs,[148] the high mobility of P3HT[149] and a favourable morphology.[150]

As triplet emitters I used Cu-complexes (see Figure 3-10) which were synthesized by Claudia Bizarri from the University in Münster, Germany. The advantage of using Cu instead of other heavier metal atoms is that Cu is cheaper due to its higher abundance, and it is more environmentally friendly. What makes Cu potentially a non-optimal choice for triplet emitting materials is the relatively low atomic number of 29 and an average mass of 63.5 u. This is because generally, the heavier the atom the higher the improvement of the ISC rate. Another very positive aspect of these compounds is that they are readily soluble in organic solvents such as chlorobenzene, which is often a problem with phosphorescent emitters, such as *fac*-Tris[2-phenylpyridinato-C_2,N]iridium(III) ($Ir(ppy)_3$). The electronic configuration of Cu in its oxidative state +1 is $d^{10}s^1$. The filled d-orbital leads to a symmetrical charge distribution and a tetrahedral configuration. In the excited state, the metal centre is formally oxidized from +1 to +2, which leads to a flattening of the tetrahedron.[151,152]

There were several Cu-complexes available (see Table 3-1) and I decided to use those that are not charged (and compensated by a counter ion) to avoid any unnecessary complications such as ion-movement and additional charge/exciton and charge/polaron-pair reactions with the counter-ions. The molecules “D” and “E”, which were mainly used for this study, are shown in Figure 3-10. The energy levels are shown in Figure 3-11. One of the ligands, bis[2-(diphenylphosphino)phenyl]ether (DPEPhos), occurs in all the molecules, whereas the other ligand differs. An interesting feature of these compounds is that the DPEPhos ligand is known to prevent exciplex formation between a tetrahedral complex and solvent molecules. Nevertheless, the PL efficiency in solution is still lower than in film due to solvent-induced exciplex quenching.[153,154] Due to the small differences in the molecular structures and their energy levels, it is not obvious which would be the best material as the guest. The potential mechanism to increase the number of triplet excitons relies on the second approach, i.e. increasing the ISC rate directly on the host due to the proximity of the guest molecules.

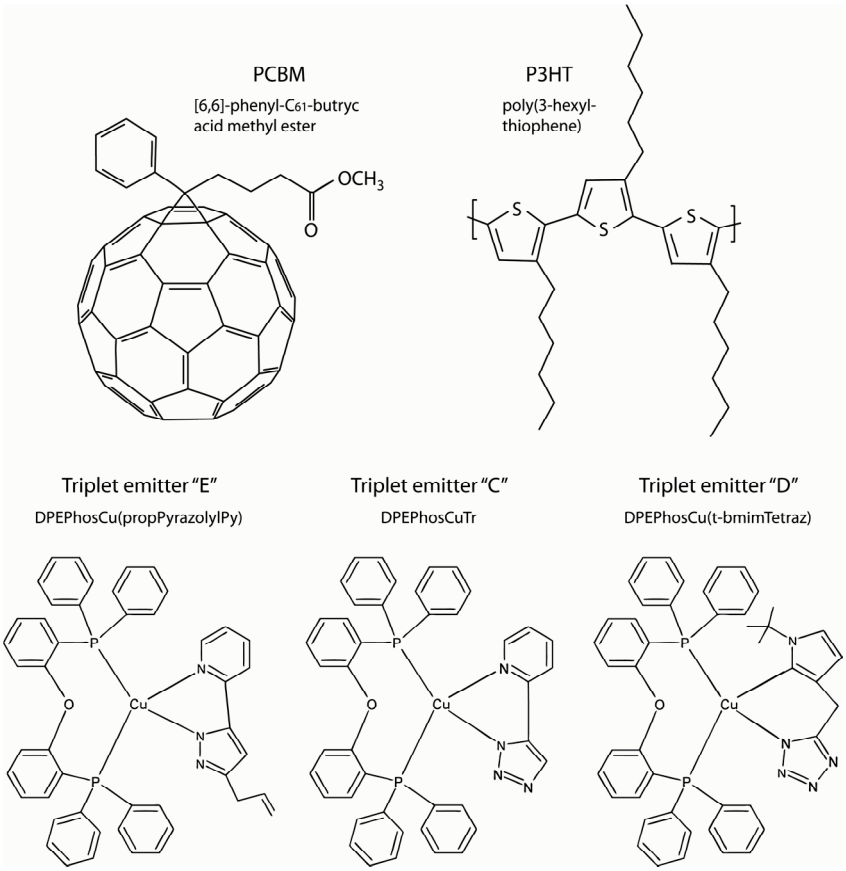

Figure 3-10. Chemical structures of the used materials.

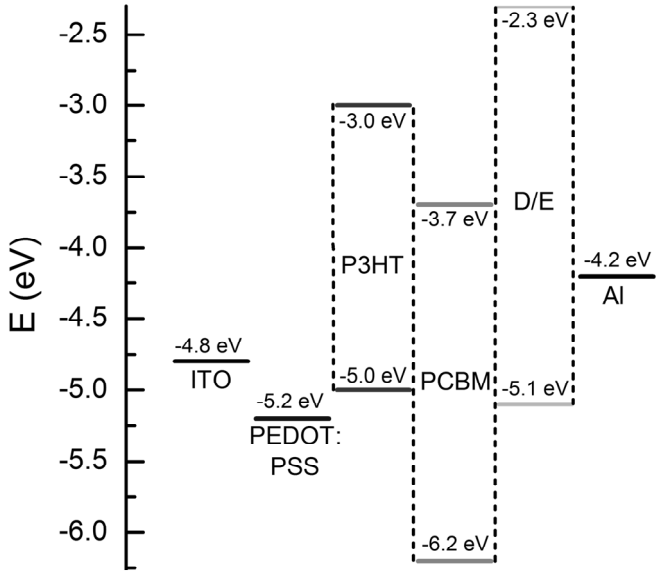

Figure 3-11. HOMO and LUMO levels of the materials. The HOMO and LUMO levels of the triplet materials were determined by cyclic voltammetry (see Table 3-1). The LUMO level was not available for the triplet emitter "C". The values for $PC_{61}BM$ are taken from Chu et al.[155] and the values for P3HT are averaged from various references.[129,156,157]

Table 3-1. Photophysical properties of the available Cu-complexes, measured by Claudia Bizzarri from the University of Münster, Germany. λ_{em} is the wavelength where the photoluminescence has a maximum. Φ is the photoluminescence quantum efficiency and τ is the lifetime of the state measured at the respective λ_{em}.

	Solution[a]				***Thin film***		
Compound	λ_{em} (nm)	***HOMO*** (eV)	***LUMO*** (eV)	Φ	λ_{em} (nm)	Φ	τ
C	527	-5.16 (-5.6)^{UPS}	--	--	520 [b]	% [b]	--
D	549	-5.132 (-5.3)^{UPS}	-2.35	0.45% (dmf)	490 [b] 463 [d]	4% [b] 2% [c]	--
E	563	-5.11	-2.28	0.42% (dmf)	535 [b] 508 [d]	5% [b] 22% [c] 33.5% [d]	5.7 µs (6.2%) [d] 21.1 µs (93.8%) [d]

[a]photophysics measured in dry and freshly distilled DCM; quantum yield measured in specified different solvents; electrochemistry in dry DMF. HOMO-LUMO values are calculated from potential values; UPS values are specified
[b]neat film;
[c] 5% in PMMA;
[d]10% in PMMA;

3.4.2 Triplet states on P3HT

The host material in my study was chosen to be poly(3-hexylthiophene), P3HT, which for many years has been the high efficiency benchmark new SCs were tested against. Together with phenyl-C_{61}-butyric acid methyl ester, $PC_{61}BM$, it has been reported to show efficiencies of over 6 %,[158] although it is generally accepted within the community that 3.5 % is a more routinely achievable value.[159]

We first need to study in some detail with what kind of photo-excited states we are dealing with in a P3HT:$PC_{61}BM$ blend. As the absorption is mainly achieved by P3HT due to the better overlap with the solar spectrum, we are mainly interested in excitons formed on P3HT. Although the situation is often simplified by assuming that singlet excitons are generated and travelling along the conjugated polymer domains, the situation can be more complicated. There is for example the possibility of intersystem crossing (ISC) to triplet excitons or the generation of polaron pairs and more or less localized polarons.

Starting with oligothiophenes, it was reported that they primarily form triplet excitons after photo-excitation.[160] These triplet excitons are considered to result from ISC from the photo-excited singlet state due to the non-negligible spin-orbit coupling constant of sulphur[160] of 184 cm^{-1}. The behaviour of P3HT in solution was measured, finding a fluorescent lifetime of 500 ps,

an ISC rate constant of $k_{ISC} = (1.2\ ns)^{-1}$, an intrinsic lifetime of the singlet excitons of 2 ns and a non-radiative decay rate[161] of $k_{nr} = (1.5\ ns)^{-1}$. P3HT films of different regioregularities have been investigated.[162,163] In regio*random* P3HT it was found that intrachain excitons are the primary photoexcitations in the ps-time domain. There is considerable ISC leading to long-lived triplet excitons. A small fraction of the singlet excitons also separated into polaron pairs and later into isolated, long-lived intrachain polarons. The situation for regio*regular* P3HT is different. The primary photoexcitations are singlet excitons delocalised among neighbouring lamellae layers leading to a larger interchain component which also reduces phosphorescence. The singlet excitons have a much lower ISC rate than in the regiorandom case so that long-lived triplet excitons are not observed. The singlet excitons instead rather dissociate into polaron pairs which later separate into isolated polarons which are delocalized as well among adjacent lamellae layers and have small relaxation energies. The differences of properties between P3HTs of different regioregularities are shown in Table 3-2.

Table 3-2. Summary of comparison between regiorandom and regioregular P3HT.[162,163]

	regiorandom P3HT	**regioregular P3HT**
primary photoexcitations	intrachain excitons	delocalised excitons
inter-system crossing (ISC)	considerable ISC	much lower ISC
existence of long-lived triplet excitons	yes	no
final excitations	singlet excitons → polaron pairs → isolated, long-lived intrachain polarons	singlet excitons → polaron pairs → isolated, delocalised polarons

Therefore one may expect both delocalized polarons within the lamellae structure and the other excited species such as intrachain polarons and triplets in the amorphous part. The distinctive behaviour in a blend of regioregular P3HT and $PC_{61}BM$ was recently investigated by Grancini et al..[164] In the amorphous P3HT phase, the singlet excitons do not dissociate and do not generate charges, whereas in the crystallized P3HT phase, a CT state was observed and the decay fitted with a biexponential decay with $\tau_1 = 8$ ps and $\tau_2 > 500$ ps. The border region between the P3HT crystal phase and the $PC_{61}BM$ crystal phase showed an even longer-lived CT state which showed a decay with $\tau_1 = 12$ ps and $\tau_2 > 1$ ns. (The generation of this CT state is very efficient as the dissociation of the photo-excited states near the interface has been shown to occur with nearly 100 % efficiency. Hwang et al.[148] for example have reported a very fast (< 120 fs) charge separation to the initial CT state which is followed by a transfer of the mobile

polarons to the bicontinuous polymer/ $PC_{61}BM$ network.) The relative longevity of this CT state is a reason for the undesirable geminate recombination.

Hence we see that if the P3HT is actually sufficiently crystallized within the domain, triplet excitons should not form and it may be useful to increase the ratio of triplets excitons to improve not only the exciton diffusion length but also to lower the geminate recombination as explained in section 3.2.9.1 on page 89.

The polaron lifetime was measured within in a P3HT:$PC_{61}BM$ bulk heterojunction to be 300-400 ns by Li et al.[165] Another technique called impedance spectroscopy gave charge carrier lifetimes within the ms domain.[166]

3.4.3 Device Fabrication

In this section I will describe in detail the fabrication process for the photovoltaic cells. The various layers are shown in Figure 3-12.

Before depositing the first layer onto the indium-tin oxide (ITO) covered glass substrates (purchased from UQG Ltd., Cambridge, UK), they were cleaned with acetone and isopropanol in an ultrasonic batch for 10 min each. Then the substrates were treated by an oxygen plasma to improve its properties, in particular to improve its work function and to create a surface charge that benefits the deposition of the next layer, poly(3,4-ethylenedioxythiophene): poly(styrenesulfonate) (PEDOT:PSS, high conductivity version purchased from Sigma Aldrich as a 1.3 wt% dispersion in water). The time between oxygen plasma and spin coating of PEDOT:PSS was less than 3 min.[167] The 80 ± 15 nm thick PEDOT:PSS layer was baked at 140 °C for 10 min inside a nitrogen filled glove box to remove any remaining water. The components for the active layer (P3HT and $PC_{61}BM$, both purchased from Sigma Aldrich) were separately dissolved in chlorobenzene at a concentration of 2 wt% (except of the triplet emitter which was further diluted to improve the accuracy of the guest content) before mixing them. The thickness of the active layer was about 135 ± 15 nm. The different heat treatments are discussed later. The >150 nm thick aluminium layer was deposited by a thermal evaporator under a pressure below $6 \cdot 10^{-6}$ mbar.

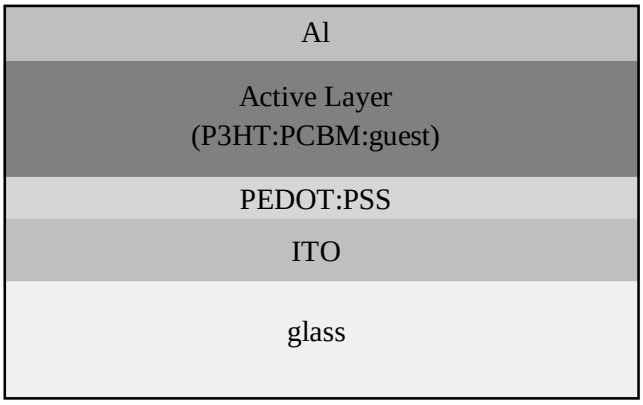

Figure 3-12. Sandwich structure of photovoltaic devices. The anode is indium-tin oxide (ITO), which is a transparent conductive oxide. The following PEDOT:PSS (Poly(3,4-ethylenedioxythiophene): poly(styrenesulfonate)) layer serves as a hole extraction layer. The active layer consists of a P3HT:PC_{61}BM:guest blend. Aluminium was used as the cathode.

3.4.4 Addition of the Phosphorescent Guests

3.4.4.1 Performance of Triplet Emitter E

I started my experiments with the triplet emitter E using a recipe which works well for standard P3HT:PC_{61}BM SCs. This recipe includes using chlorobenzene as a solvent and using a post-evaporation baking of 140 °C for 10 min. To get a feeling for reasonable guest concentrations, I started with varying the guest content from 0 to 25 wt% (with respect to the mass of P3HT+ PC_{61}BM).

The result was that the performance of the SCs dropped considerably, with all devices above 1 wt% guest concentration not working at all, more precisely showing short circuit characteristics. I further found that short-circuits occurred mainly for the baked devices with more than 1 wt% guest concentration.

The JV-curves of devices with the triplet emitter E for guest concentrations up to 1 % are shown in Figure 3-13 and the respective short-circuit current densities (J_{SC}), open-circuit voltages (V_{OC}), fill-factors *(FF*) and energy conversion efficiencies (η or power conversion efficiency, *PCE*) are shown in Figure 3-14. Devices marked as baked were annealed after evaporation at 140 °C for 10 min and cooled down slowly (leaving them on unheated parts of the hot plate as opposed to putting them onto a metal block for rapid cooling. Slower cooling (as opposed to fast cooling) may improve the crystallization and improve the phase separation.

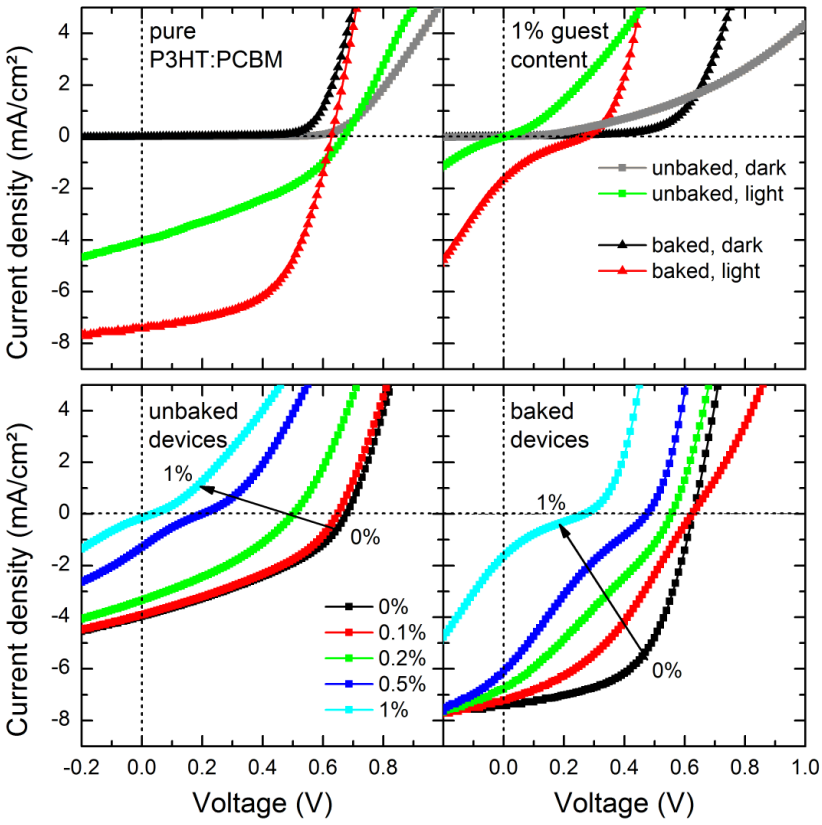

Figure 3-13. JV-curves for devices with the compound E**.** In the first 2 Figures (a) and (b) one can see JV curves for both, dark and illuminated devices, for devices only containing the pure P3HT:$PC_{61}BM$ blend as the active layer (a) as well as active layers with 1 % guest concentration (b). Figure (c) and (d) show the JV curves for the different guest concentrations used for the unbaked (c) and baked (d) devices. More explanations in the text.

The undoped devices worked roughly as expected. With J_{SC} = 4.2 mA/cm², V_{OC} = 0.66 V and *FF* = 37 %, I obtained an efficiency of η = 1.0 % for the unbaked devices. Baking improved considerably J_{SC} (7.4 mA/cm²) and *FF* (54 %), resulting in η = 2.5 %. I would like to mention here that the performance of unbaked devices of pure P3HT:$PC_{61}BM$ blends varies considerably from batch to batch. A possible reason is that small differences in the temperature of the glove box and the solution, the solvent atmosphere and the spin coating change considerably the morphology of the unannealed devices. After baking, however, the different batches "converge" in their performance towards the same point, demonstrating the importance of the annealing process as a means to control the morphology and to reduce batch to batch variability.

Upon increasing the triplet content, basically all parameters decrease in a monotonic fashion. We also see that the JV curves gain an s-shape. In the literature, such a shape was attributed to various effects: surface dipoles,[168] a reduced surface recombination rate,[40] charge traps[168,169] and imbalanced mobilities.[170] The incident photon to current efficiency (IPCE) is shown in Figure

3-15. Upon baking, a more pronounced shoulder is observable at ~ 610 nm (consistent with improved crystallization), but no clear trend can be seen in connection with the triplet content.

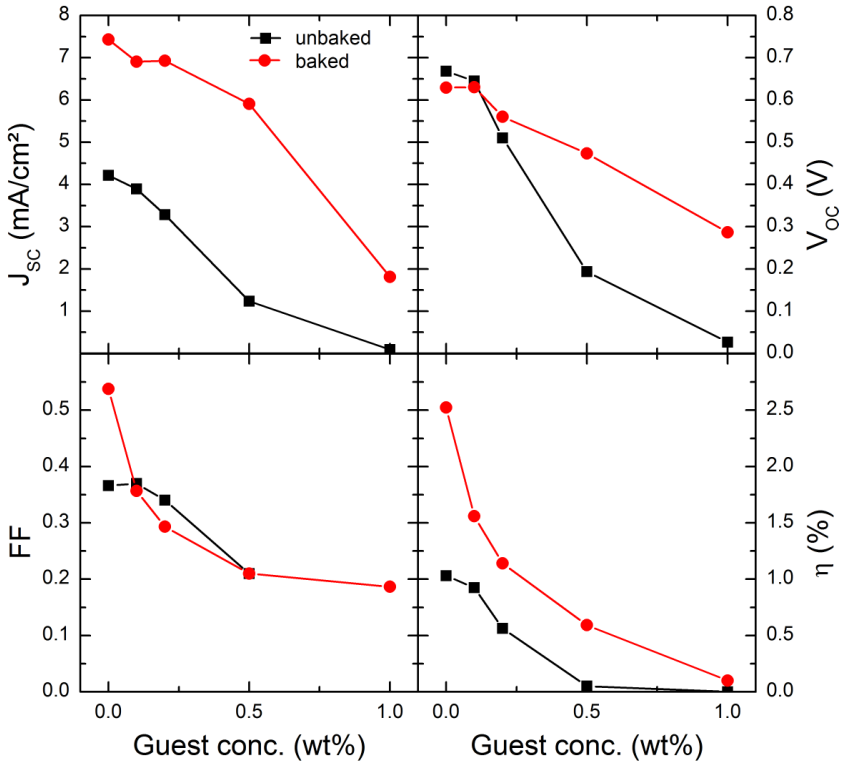

Figure 3-14. SC parameters with the triplet emitter E. Both, unbaked (black) and baked devices (red) are shown.

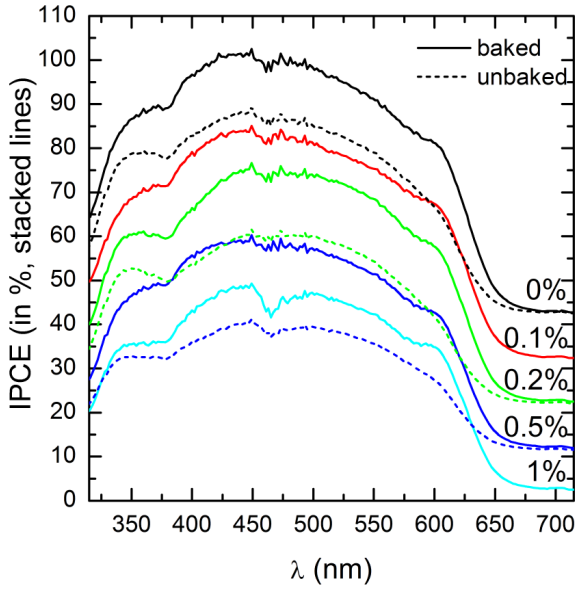

Figure 3-15. IPCE spectra of unbaked and baked devices of batch 4 with the triplet emitter E, stacked for clarity. The only significant difference between the unbaked and baked devices (besides the maximum of each curve) is the shoulder at about 610 nm which only appears for the baked devices. No clear trend is apparent with rising the guest ratio.

An interesting aspect of these devices is that despite a J_{SC} of near zero at high guest concentrations, the short-circuited devices showed considerable photoconductivity, i.e. the current increases considerably at voltages > 0 for illuminated devices compared to devices in the dark. I will come back to this point later.

3.4.4.2 Performance of Triplet Emitter D

Due to the low performance of the triplet emitter E, other Cu-complexes were tried. Whereas triplet emitter C showed disappointing results as well (see Appendix on page 202), compound D (chemical structures were shown in Figure 3-10d) was found to affect the performance much less than triplet emitter E and C. The JV curves of first devices are shown in Figure 3-16. I found that increasing the stirring time from about 1 hour for the separated solutions and > 30 min for the mixed solution to overnight stirring and > 4 h, respectively, improved the device characteristics in a sense that the degradation upon inserting the guest was reduced. This can be seen by comparing the bottom diagrams of Figure 3-16 and Figure 3-17. The JV-curves in the latter are only marginally influenced by the guest. The SC parameters for devices with short and long stirring are compared in Figure 3-18.

For the less stirred and baked devices, one can see a maximum of the efficiency at a guest concentration of 0.2 wt%. This, however, results mainly from the unexpectedly low FF of the pure P3HT:$PC_{61}BM$ blend of only 40 %. The graphs also show that the unbaked devices (black curves) were generally more “immune” against triplet doping for both batches. Another noteworthy feature is the high V_{OC} for the less stirred, unbaked devices (~ 0.65 V) compared to the long stirred, unbaked devices (~ 0.50 V). Upon baking, however, V_{OC} tends to converge to the same value (~ 0.59 V). This is a phenomenon mentioned earlier. The author believes that little changes in the temperature of the glove box and the solution or when the solution has last been heated considerably influences the morphology of the active layer. Heating the film will then lead to a rather similar morphology fairly independent of the initial morphology.

The IPCE spectra are not shown because similar to compound E, no clear trend can be seen, except decreasing values with decreasing J_{SC}.

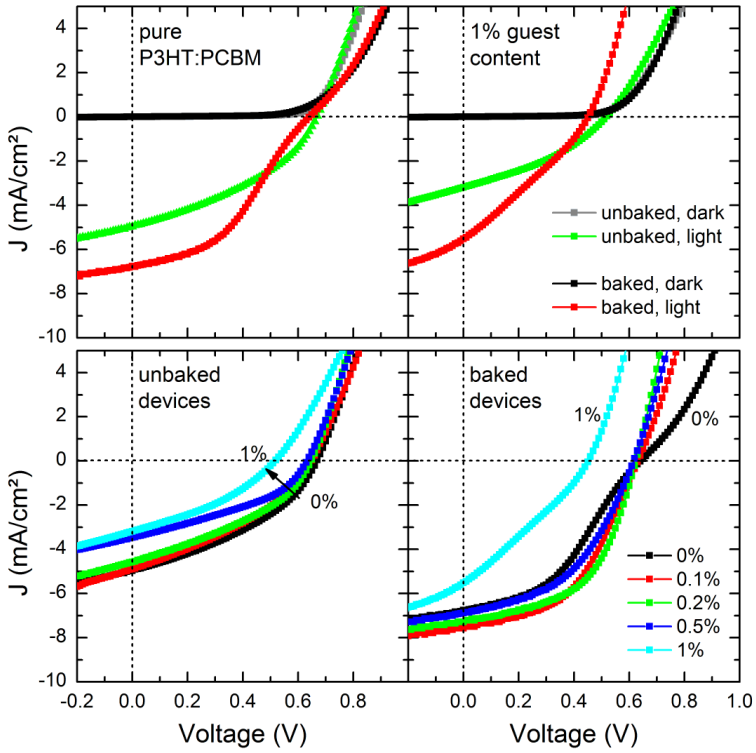

Figure 3-16. JV-curves of devices with compound D. (batch with short stirred solutions).

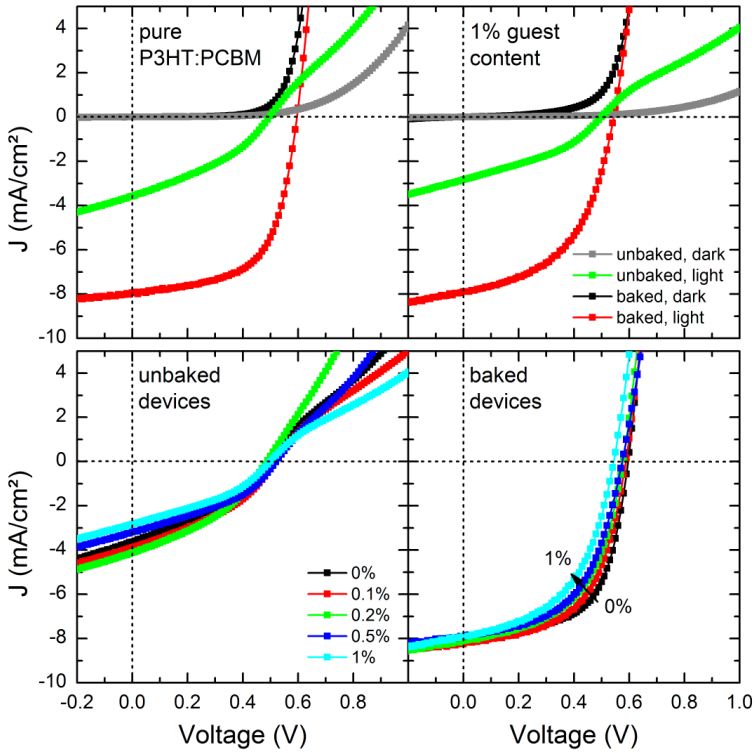

Figure 3-17. JV curves of devices with compound D (batch with long stirred solutions).

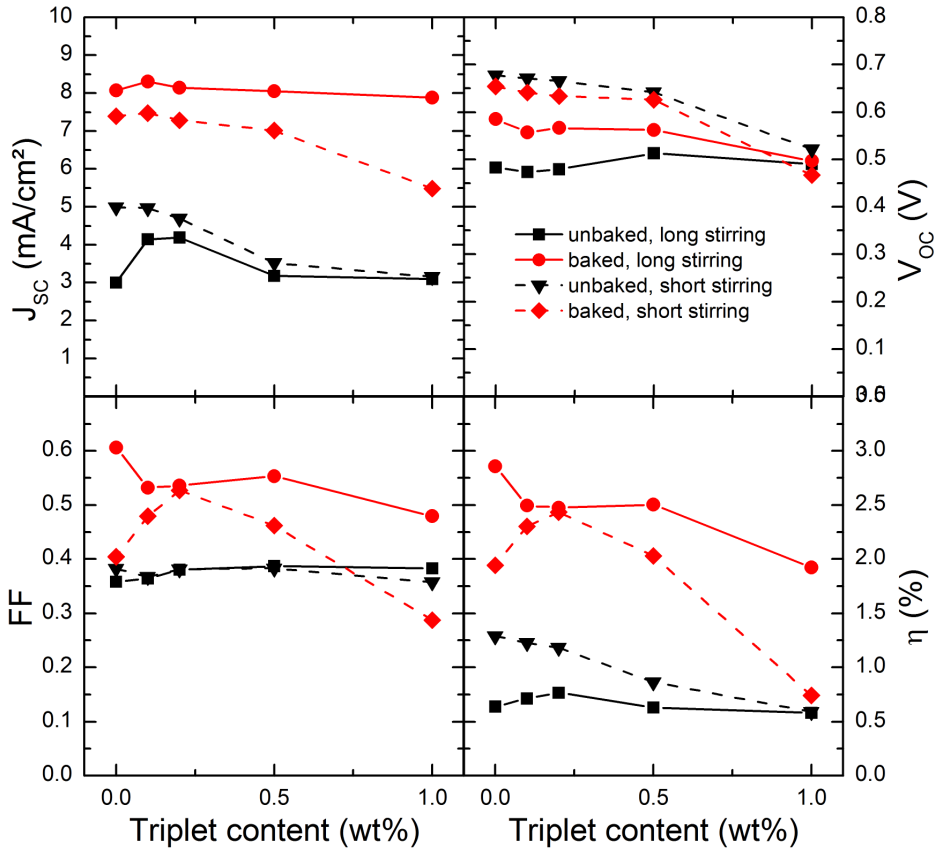

Figure 3-18. Comparison of SC parameters between long (solid lines) and short stirred (dashed lines) devices with triplet emitter D. Unbaked (black lines) and baked devices (red lines) are shown.

3.4.4.3 Triplet emitter D with Different Morphology

It is well documented that the annealed P3HT:$PC_{61}BM$ layer as fabricated above ("standard" procedure resulting in high efficiency devices) has a highly optimized morphology[150] with relatively small domains to achieve efficient exciton dissociation and charge separation. Under the hypothesis that more triplets with large diffusion lengths are formed upon inserting the triplet emitter, slightly larger domain sizes should not negatively affect the performance, or said in a different way, if the domain sizes are larger than they are for the singlet-optimized morphology, the pure blend should suffer a higher loss in performance than the blend with the triplet emitter.

To achieve a morphology with larger domains, I annealed the blend before evaporation instead of afterwards and I increased the annealing temperature by 10 °C to 150 °C. The reasons for the change in morphology is that first of all, a higher temperature will lead to a higher diffusion rate of the blend components and hence to more phase separation, and second, in case of the post-evaporation baking, the cathode constricts the movement of the active layer components. On a

larger scale, pre-baking at 140 and 150 °C lead to large $PC_{61}BM$ clusters that are about 400 nm high and have a diameter of 7-9 µm (see Figure 3-19). The identification of the large clusters as $PC_{61}BM$ domains has been done by other groups.[171,172] In Figure 3-20 the surface morphology of the differently treated active layers are shown, where it was zoomed-in into the non-elevated areas, i.e. those that do not consist purely of $PC_{61}BM$. (Note that it is not easily possible to lift-off the evaporated cathode so that the morphology after post-baking is not well known, but expected to show less phase separation). For the pure P3HT:$PC_{61}BM$ blend, the typical domain size (given here in full width of half maximum (FWHM)) increased from about 50 to 60 nm upon changing the annealing temperature. Interestingly, the inclusion of 1 % of the triplet emitter led to a reduction of the domain size by about 20 nm in both cases. The domain sizes of the at 140 °C annealed devices with 0 % triplet emitter (~ 50 nm) is hence very similar to the domain sizes (~ 40 nm) of the at 150 °C annealed devices with 1 % triplet emitter (Figure 23a and d). Considering the same domain sizes and the much worse performance of the latter devices, which will be shown below, a pure morphological effect of the triplet emitter on the device performance can be ruled out.

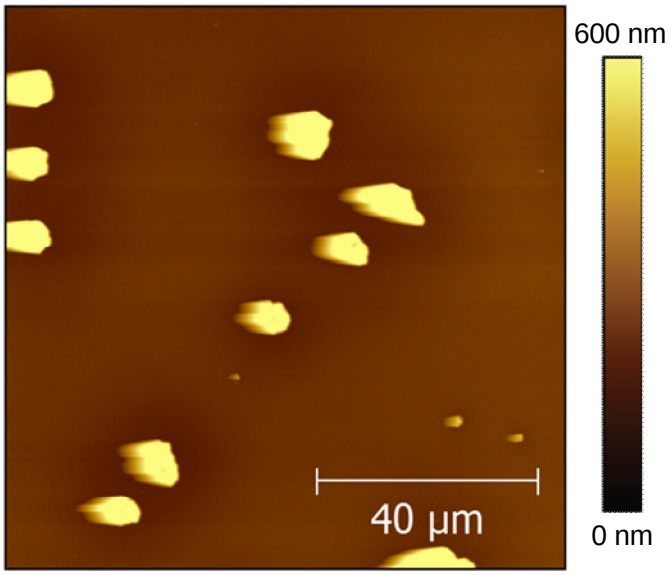

Figure 3-19. AFM images of a P3HT:$PC_{61}BM$ blend, baked before evaporation at 150 °C for 10 min. The elevated structures ($PC_{61}BM$ clusters) are ~ 400 nm high and have a diameter of 7-9 µm. On the same scale the morphology of a device baked before evaporation at 140 °C looks very similar (not shown).

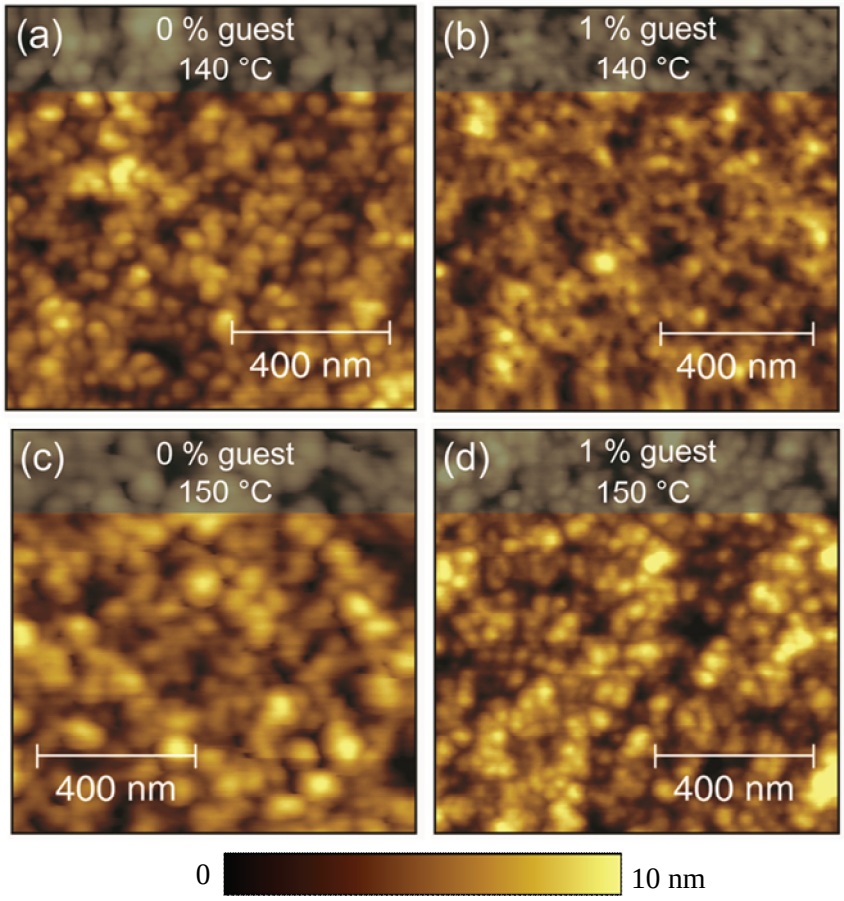

Figure 3-20. AFM images of active layers spin-coated onto spectrosil substrates. The description of the active layer can be seen at the top of each image. The surface roughnesses are 1.62 nm, 1.56 nm, 1.66 nm and 1.68 nm going from (a) to (d). The typical domain diameters (FWHM) are ~ 50 nm, ~ 30 nm, ~ 60 nm and ~ 40 nm.

The JV curves and corresponding parameters are illustrated in Figure 3-21 and Figure 3-22. To ease the comparison, the parameters of the pre-evaporation baked devices have been included in Figure 3-22. The first observation is that the pre-evaporation baked pure P3HT:$PC_{61}BM$ blend performed worse than the post-evaporation baked one. The strong decrease in energy conversion efficiency stems mainly from the loss of V_{OC}, which dropped from 0.59 V to 0.36 V. The lower performance is expected due to the large µm-sized $PC_{61}BM$ clusters and generally larger domain sizes. Another very interesting aspect is that V_{OC} is virtually independent of the guest content, whereas J_{SC} is reduced considerably upon increasing the guest content. Note that the stable V_{OC} is a feature that was only observed for triplet emitter D.

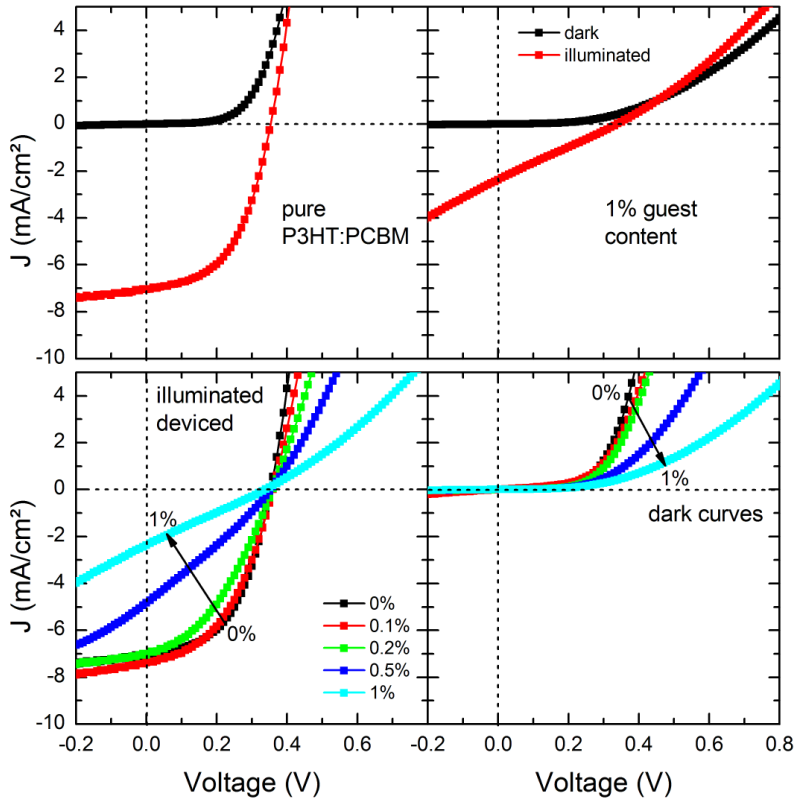

Figure 3-21. JV curves of devices with compound D, which were annealed before evaporation at 150 °C for 10 min.

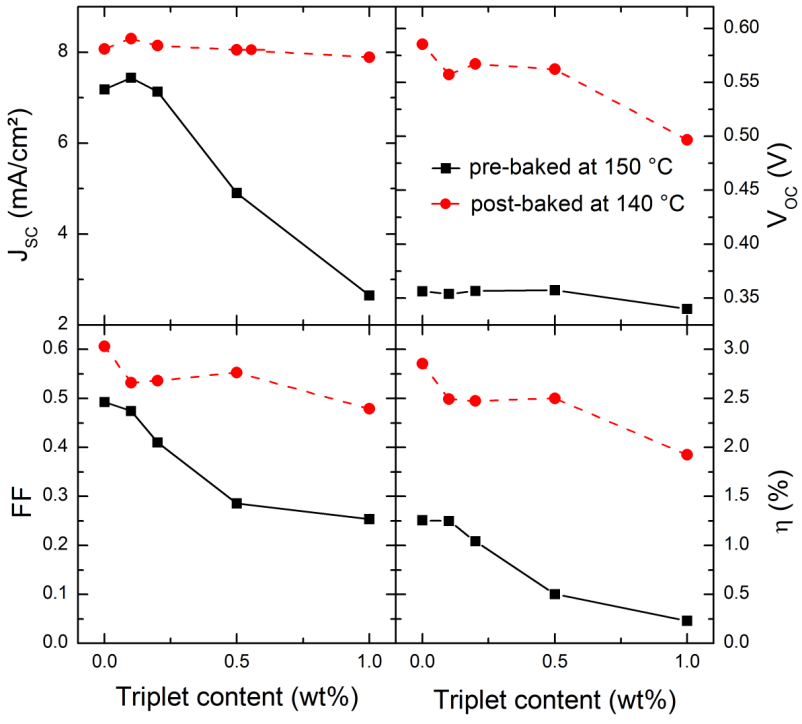

Figure 3-22. SC parameters of devices with triplet D. Compared are post-evaporation baked devices with pre-evaporation baked devices.

3.4.5 Causes of the Performance Drop

At this point I would like to summarize some important information gathered so far.

a) From the AFM images we have seen that the inclusion of the triplet emitter leads to smaller domains. This is already a potential reason for a decrease in the performance, because smaller domains generally worsen the charge extraction due to smaller crystallized domains reducing the mobility and due to the larger likelihood of islands which will trap charges by themselves and increase the rate of non-geminate recombination. This would directly lead to a smaller I_{SC} and *FF* which has been observed in almost all devices. However, I have also shown that the changing domain size alone cannot account for the strong reduction in performance. Note that smaller domains often improve J_{SC} due to more efficient exciton harvesting/dissociation.

b) Another observation was that extensive stirring improves the stability of the devices which contain the triplet emitter. Assuming longer stirring helps separate the molecules and avoids aggregation, this means that larger aggregates of the triplet emitter are worse for the device performance than smaller, better distributed ones. The reason for that is not understood, as, assuming the guest is a trap for example, more isolated, less aggregated guest molecules should influence the device much more than few large aggregates. A hypothesis is that the aggregation of the guest leads to different energy levels which may improve the hole transfer/trapping rate to the guest molecule, or that aggregates can become so large that a continuous (conductive) pathway on the guest from electrode to electrode exists.

c) The observed s-shape observed in the JV curves of solar cells that contain the triplet emitter E may be caused by several effects (reduced surface recombination, reduced charge carrier mobility, addition of traps for one type of charge carriers, or the creation of a dipole at one of the interfaces).

d) I have also mentioned the considerable photoconductivity observed for the seemingly short-circuited devices at relatively high concentrations of the compound E. The reasons for such a diminished performance while exhibiting photoconductivity means that either excitons on P3HT are already trapped before reaching an interface with $PC_{61}BM$ (and then liberated by the incoming photons), or, more likely, a part of the photogenerated charges is trapped on the guest molecules (and then liberated by the incoming photons).

Looking at the energy diagrams with the results measured by Charlotte Fléchon (see Figure 3-23), it is indeed possible that the guest molecules act as hole traps, for both, holes coming from P3HT and $PC_{61}BM$.[iv]

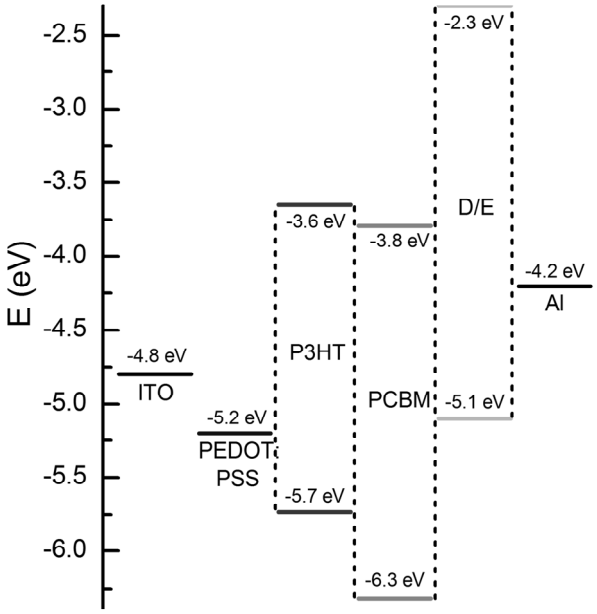

Figure 3-23. HOMO/LUMO energy levels with values for P3HT and $PC_{61}BM$ measured by Charlotte Fléchon. The surprising result is the much lower lying HOMO level of P3HT compared to literature values (see Figure 3-11) which enables hole transfer from P3HT to the guest.

Therefore I did mobility measurements (as described in the characterization techniques section) by fabricating FETs. The active layer in the transistors were P3HT:$PC_{61}BM$ blends with the triplet emitter E. Mobilities were extracted from the transfer characteristics in the saturation regime and the result can be seen in Figure 3-24. Some data points, such as those for the hole mobility of the baked devices, are missing due to devices not showing the necessary output characteristics (see appendix on page 203) to extract the mobility, i.e. when the other type of charge carrier is completely dominating. The data show two important features. First of all, the electron mobility is fairly independent of the guest concentration and close to the reported value of $2 \cdot 10^{-3}$ $cm^2 V^{-1} s^{-1}$ in a P3HT:$PC_{61}BM$ blend.[166] The other is that at least for the unbaked devices, the hole mobility decreases by two orders of magnitude upon inserting 1% of the guest. Note that an increased number of traps will increase the number of scattering centres and hence reduce the mobility (→ Matthiessen's rule). The measured mobilities are hence an indication that the guest molecules may act as hole traps and the decreasing performance is due to the large

[iv] I would like to mention at this point that some literature values for the energy levels of P3HT differ considerably from our measured values. According to Peet, J. et al., Applied Physics Letters 93, 163306 (2008) for example, the LUMO and HOMO values are 3.1 and 4.9 eV, respectively. These energy levels would not have led to hole trapping from the P3HT to the guest.

number of hole traps and the decreasing hole mobility. Note that the guest may also simply disturb the P3HT lattice and therefore reduce the hole mobility. However, the shift of the threshold voltage in the transfer characteristic at negative gate voltages also (see appendix page 203) also points towards an increase of hole traps for increasing guest content.

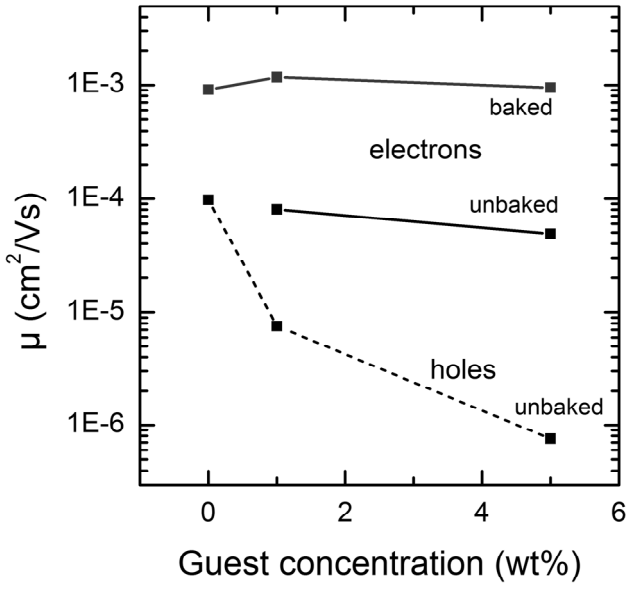

Figure 3-24. Electron (solid lines) and hole mobilities (dashed line) for FETs made with compound E in the active layer. The mobilities were measured at room temperature in a nitrogen atmosphere. If values are not shown, this is due to output-characteristics not showing the necessary behaviour to extract the mobility from the respective transfer-characteristic.

Another noteworthy observation is the increased electron mobility upon baking. This could have two reasons. First, baking leads to larger phase separation and to larger crystallized $PC_{61}BM$ domains, and second, $PC_{61}BM$ may diffuse preferentially towards the channel and may therefore lead to a higher $PC_{61}BM$ concentration in the channel. As $PC_{61}BM$ is a much better electron conductor than P3HT, this would improve the electron mobility in the FET.

3.4.6 Calculation of the Trap Density

Figure 3-25 shows the dark JV-curve of a SC device without the inclusion of triplet emitters, i.e. with the pure P3HT:$PC_{61}BM$ blend as the active layer. The curve shows an ohmic behaviour from 0–0.2 V (red dashed line) and changes into a power law function at ~ 0.3 V in agreement with Eq. 3-17. The exponent (c) in the fitted power law ($J = J_0 + b \cdot V^c$) is 5.1. We could use this information to determine the characteristic energy E_t of the trap distribution if we assume that

such an exponential trap distribution is indeed present and that only one type of charge carrier dominates the current.

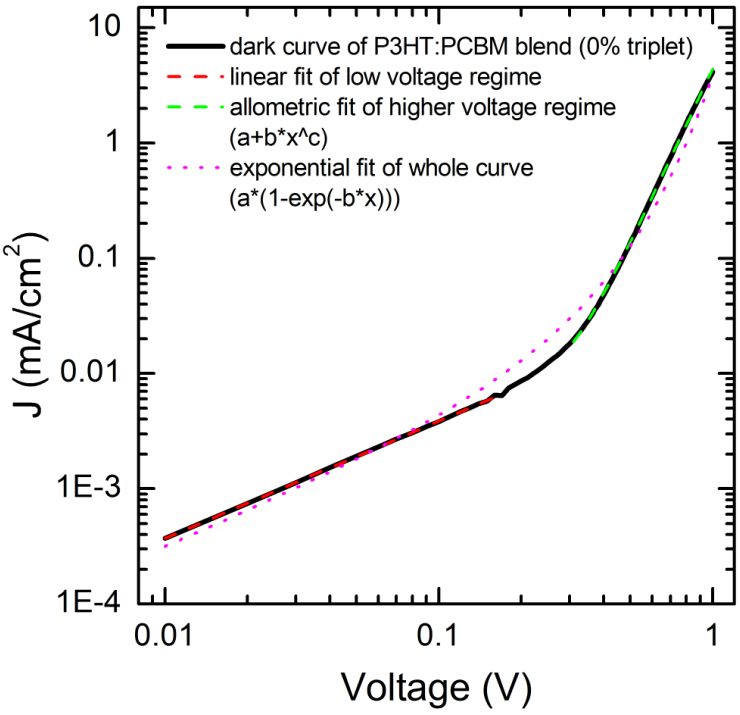

Figure 3-25. Dark JV-curve of a pure P3HT:$PC_{61}BM$ SC. Different fits have been applied. One can see the linear (ohmic) regime at lower voltages (fitted with dashed red line) and the trap filling regime at higher voltages (fitted with dashed green line).

The question remains as to whether the latter condition is indeed fulfilled, i.e. if only one charge carrier dominates the current. From the FET mobility measurements of the pure P3HT:$PC_{61}BM$ blend we saw that at least for the baked transistors, the electron mobility of $PC_{61}BM$ was higher than the hole mobility of P3HT. However, such a result has to be treated with caution. Not only is it well known that in most organic semiconductors the hole mobility is much larger than the electron mobility,[31] but it has been frequently reported that the mobility cannot simply be assumed to be independent of the type of device due to several reasons: (a) The electrical field in LEDs or SCs is much larger than in transistors, (b) the polymer and fullerene domains may be concentrated in different regions depending on the device, (c) The direction of the charge transport is different in FETs and SCs and (d) some studies on bilayer P3HT/ $PC_{61}BM$ SCs suggest that the electron mobility of $PC_{61}BM$ is the efficiency limiting factor[173] and that the most important effect of baking is to increase the electron mobility in $PC_{61}BM$ due to the formation of larger crystallised aggregates. This indicates that electron transport is rather the bottle neck in the blend instead of hole transport. In fact, during my experiments I observed a

strong dependence of the dark current on the inclusion of the triplet emitter, which, together with the assumption that the holes are trapped on the guest, is consistent with the notion that electrons are *not* dominating the dark current in the applied voltage regime as it may be deduced from the FET mobility measurements. (However, it may also be possible that electrons are the dominating type of charge carriers, but that hole trapping leads to a strong reduction in conductivity due to electron-trap interactions). Note that the injection barriers according to Figure 3-23 do not give a clear indication regarding which carrier can be expected to dominate the device at low voltages. For the sake of calculating the number of traps, we assume for now that the majority of the trap-influenced SCLC results indeed from hole conduction in P3HT.

The traps in a P3HT:$PC_{61}BM$ blend have been investigated by Schafferhans et al.[142] during degradation experiments. In Figure 3-26 the trap distribution as measured from thermally stimulated current (TSC) measurements is illustrated, showing two trap distributions, T1 and T2, in P3HT and a third one, T3, in the blend. Shallow traps, i.e. those that can be easily activated, act as dopants. T3 has a too high activation energy and will not dope the system while T1 and T2 can both dope the system with holes. Another example of trap concentration measurements in P3HT:$PC_{61}BM$ blends is shown in Figure 3-27.

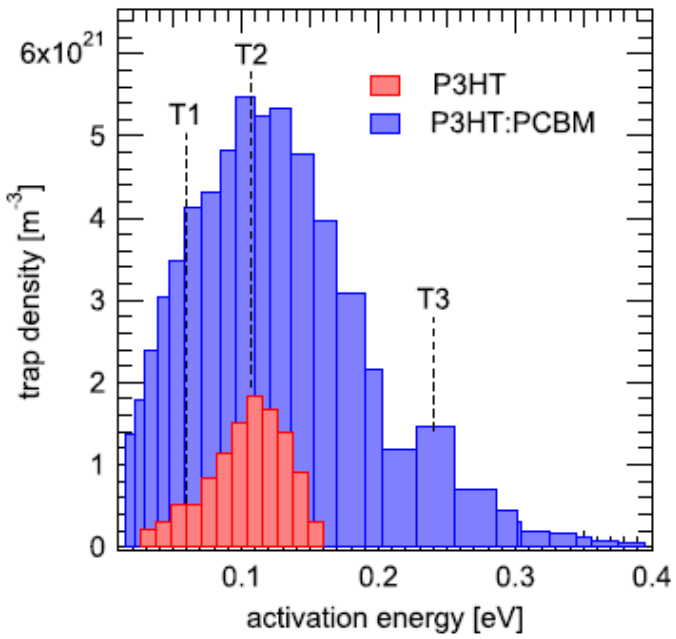

Figure 3-26. Trap density in P3HT and P3HT:$PC_{61}BM$ blends as obtained by TSC (thermally stimulated current) measurements. P3HT shows two trap distributions, T1 and T2, which both contribute to the blend. A third trap distribution, T3, is seen in the blend. Image reprinted with permission from Schafferhans et al.,[142] Copyright (2010) Elsevier.

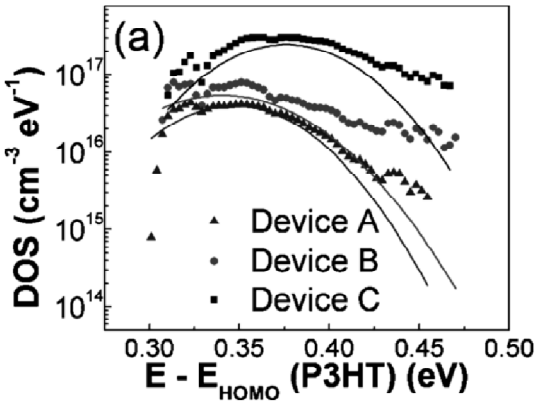

Figure 3-27. Trap density in P3HT:$PC_{61}BM$ blends for devices grown with different growth rates determined by $C(V)$ and $C(f)$ measurements according to Nalwa et al.,[174] Copyright (2011) American Institute of Physics. The higher the growth the more traps are present. Note that the traps are deeper than in Figure 3-26.

Going back to using the exponent of the fit (c) of 5.1 (for the pure P3HT:$PC_{61}BM$ blend) to determine the characteristic energy of the trap distribution (E_t), we obtain $m = 4.1$, hence $E_t = 4.1$ kT = 0.10 eV at room temperature. This results in an exponential distribution of trap states that decays to 1/e of its initial value (at the HOMO) after moving 0.10 eV inside the band gap. In Figure 3-28 I used the exponent and prefactor of the dark currents of the prebaked devices with compound D to calculate the total trap density (H_t) for the actual guest concentrations used. The inset shows the trap density as a function of (E - E_{HOMO}) for a guest concentration of 0 %, i.e. the pure P3HT:$PC_{61}BM$ blend. For the calculation I assumed the following values: $\varepsilon_r = 2$, $N_{HOMO} = 1 \cdot 10^{25}$ m^{-3} (typical values[142] are between 10^{24} and 10^{26} m^{-3}), $d = 150$ nm, $T = 293$ K and a mobility interpolated from Figure 3-24. The calculated H_t for the pure blend ($2 \cdot 10^{22}$ m^{-3}) is double the published value of pure P3HT[175] ($1 \cdot 10^{22}$ m^{-3}). As expected, my calculations show a linear increase of H_t upon adding more guest molecules.

Looking at the absolute value of guest molecules in the device (of the order of 1 wt%), one would expect an even stronger (negative) influence of the guest on the current. It is possible, however, that due to aggregation of the guest molecules, the effective number of traps is much lower than the number of guest molecules.

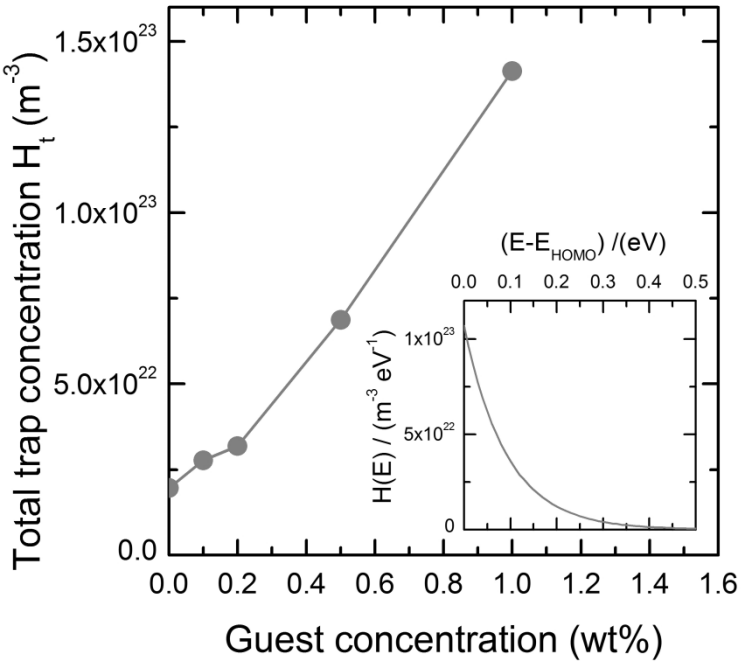

Figure 3-28. Calculated total guest concentration H_t as a function of the guest concentration actually used for the devices. Devices were prebaked and the guest is compound D. The inset shows the energetic distribution calculated from the fitted curve for a guest concentration of 0 wt%.

3.4.7 Further Considerations

3.4.7.1 Possibility of Doping

The influence of doping on the solar cell performance was described in section 3.3.4.3.1 on page 99. It is in good agreement with the pre-baked devices with compound D (see Figure 3-21 on page 119), where V_{OC} was unaffected while the FF decreased to some degree and J_{SC} dropped heavily upon adding the guest.

However, I would like to stress again that it is *not* obvious how the triplet emitter can act as a dopant. Defect states can serve as dopants, but only if they provide electrons near below the host's LUMO or holes near above the host's HOMO, i.e. the defect states must provide charge carriers which can be promoted easily to the host via little excitation energy (or energetic disorder as in the case of disordered organic materials). If we look at the energy levels, we see that the HOMO of the triplet emitter is more than 1 eV away from the HOMO of the P3HT and even further away from the HOMO and LUMO of $PC_{61}BM$, which means that no doping is expected unless defect states with different energy levels are generated which can easily donate holes or electrons.

The effect of doping was mentioned nevertheless, because it is not just in agreement with the pre-baked devices with compound D, but it could also give an explanation for another observation: The so far unexplained short-circuit characteristics at high (≥ 5 %) guest concentrations of the triplet emitter E may be explained by extremely high doping creating a degenerate semiconductor with near metallic behaviour. Interestingly, Arkhipov et al.[176] suggested that while low doping can reduce the mobility, high doping can increase the mobility because the density of ionized dopants will create a smoother potential landscape for the charge carriers.

3.4.7.2 Mobility and Traps

In section 3.3.4.3.2 on page 100 the influence of mobility on the SC parameters was shown. The performance parameters in the above experiments indeed behaved in accordance with a reduced mobility, with exception of V_{OC}, which never increased upon adding the guest. It either remained rather constant, such as for triplet emitter D with pre-baking, or, as in all other experiments, it decreased. This hence indicates that another effect is contributing to the reduction of V_{OC}.

Traps may explain this "non-increasing" V_{OC}. As it was shown in section 3.3.4.3.3 on page 101, an increased number of traps will reduce all parameters, i.e. J_{SC}, *FF* and also V_{OC}. To which degree mobility and traps contribute to the change of the parameters is not clear. However, together they are in qualitative agreement with the observed changes of the SC parameters.

3.4.7.3 S-shaped JV-curves

In a number of devices, such as the devices with compound E and the long stirred, unbaked devices with compound D, S-shaped JV-characteristics could be observed. Wagenpfahl et al.[40] showed that S-shaped JV-curves can be caused by defect states at the electrodes leading to a build of a space-charge if the majority surface recombination rate is reduced. This may suggest that it is possible that the triplet emitter accumulates preferentially at the electrode and the storage of trapped holes may lead to the space-charge. However, according to the simulations, the occurrence of the S-shape should be accompanied by a decrease in V_{OC}, which was not observed for the unbaked devices with materials D, but was observed with the compound E. Another question is why the S-shape could not be observed after baking the long stirred devices with compound D, because if the triplet emitter preferentially accumulates near an electrode,

baking would probably rather help diffusing to the desired location and is hence expected to increase the effect.

3.4.8 Energy Level Configurations that Avoid Charge Trapping

I would like to go back once more to the problem of charge trapping. According to the HOMO/LUMO values which are available from the literature, for example 4.9 eV[177] for the HOMO of P3HT, the HOMO of the triplet emitters (~ 5.1-5.2 eV) would have actually been lower than the HOMO of P3HT, hence I did not expect hole trapping from P3HT when I started the experiments. According to *later* measurements done by Charlotte Fléchon[v], whose results were used in Figure 3-11, charge trapping towards P3HT would have been expected. However, charge trapping seems to be a more fundamental problem of the approach tried in this work, i.e. the inclusion of a third compound in a donor-acceptor blend such as P3HT:$PC_{61}BM$. The reason for this will be discussed in the following. To go through the various possible processes, I will be discussing first what one would expect without exciton transfer (i.e. considering only the HOMO and LUMO levels), then what could happen if such transfer is allowed. Unless mentioned otherwise, I will consider that excitons are generated on both, donor and acceptor (but not on the guest), but that free charges/polarons are not generated on the pure donor or acceptor, respectively.

3.4.8.1 First Case, Assuming No Exciton Transfer to the Guest

I have illustrated all possible relative HOMO and LUMO configurations in Figure 3-29. We see that configurations (c), (d), (g), (h) and (j) will always lead to charge trapping on the guest for charges coming from either the donor or the acceptor and are therefore undesirable in all circumstances.

If we ignore the possibility of exciton transfer to the guest and only consider the HOMO and LUMO levels, there will always be charge trapping on the guest of at least one type of carrier unless its LUMO is higher than the LUMOs of both host materials and its HOMO is lower than the HOMOs of both host materials (see Figure 3-29a). This means that the band-gap of the triplet emitter must be at least |LUMO(donor) - HOMO(acceptor)| to avoid any charges getting transferred to the guest. Obtaining such energy levels for the guest is difficult when the acceptor has a HOMO as low as that of the popular acceptor material $PC_{61}BM$ (6.3 eV).

[v] PhD student in the CMMP group at the Department of Physics & Astronomy, UCL, from 2009.

The requirement can be relaxed to some extend within a double-layer architecture where donor and acceptor are separated. By including the guest only into the donor for example, one does not need to care anymore about the HOMO level of the acceptor (if one accepts slight problems at the donor/acceptor interface where charge trapping could still occur). As a result, the configuration 'b' shown in Figure 3-29 is acceptable in a double-layer device. All the other thinkable situations 'c' – 'j' shown in Figure 3-29 could always lead to at least one type of charge carrier being transferred from the donor or acceptor to the guest and are therefore not ideal.

Under the assumption that excitons are only split at the donor/acceptor interface, (so that in the first step, holes will always be on the donor and electrons on the acceptor,) there are a few more arrangements than just 'a' that would not lead to charge trapping. These are the configurations 'b', 'e' and 'f'.

3.4.8.2 Second Case, Considering Exciton Transfer to the Guest

If (singlet) exciton transfer from the host materials to the guest is considered as well and assumed to be more efficient than exciton dissociation at a type II heterojunction, most arrangements could in the first step lead to energy transfer from the host to the guest, subject to the singlet level of the host lying higher than on the guest. I would like to mention at this point that relaxation energies for excitons (difference between HOMO-LUMO gap and exciton energy) may differ considerably between excitons on different materials. Therefore one cannot simply deduce from the band-gap where the singlet level lies.

Once the exciton is on the guest, it is either

- trapped on the guest (until it recombines), or
- transferred further to the third material if it is in proximity and the exciton levels fit, or
- converted into a triplet state, from where it may go back to the host if the host's triplet energy is lower (as in Figure 34k), or
- exciton dissociation at a type II heterojunction occurs. This will then lead to charge trapping unless the third component is also in proximity to rescue the trapped charge, either with an exciton level lower than the occupied CT state or with a matching HOMO/ LUMO level.

This means that if energy transfer occurs from the host to the guest, we must either achieve the approach in Figure 34k or the guest must be located at the interface to the other host component.

In order for singlet exciton transfer to occur from the host to the guest, the absorption spectrum of the guest needs to overlap with the emission spectrum of the host (this is true for all types of exciton energy transfer). Assuming a rather material-independent energy difference between band gap (correlated with absorption) and singlet exciton (correlated with emission), in order to achieve energy transfer to the guest, the guest should have a smaller band gap than the host components, which is in contrast to the ideal situations (regarding charge trapping) 'a' or 'b' ('b' only ideal if a bilayer is considered with guests only in the donor).

Therefore, if we do not use arrangement 'a' or 'b', we rely either on

- avoiding energy transfer from the host to the guest, also no exciplex (CT state) formation; or
- an efficient S_1 (host) → S_1 (guest) → T_1 (guest) → T_1 (host) conversion process; or
- a morphology where the guest is only situated at the interface between donor and acceptor, allowing arrangements 'a', 'b', 'e' and 'f'. (This would mean that we do *not* efficiently increase the diffusion lengths of excitons rendering the inclusion of the guest rather useless).

Despite the demand of perfectly fitting energy levels and the need for very efficient energy transfer (S_1 (host) → S_1 (guest) → T_1 (guest) → T_1 (host)), the approach of Figure 3-29k was claimed to be achieved[126] by using arrangement 'e', where the HOMO and LUMO level of the guest are in between the respective levels of the donor (MDMO-PPV, poly[2-methoxy-5-(3',7'-dimethyloctyloxy) -1,4-phenylene vinylene]) and acceptor ($PC_{61}BM$). There is also another publication[177] where arrangement 'e' was used. The guest was a small molecule for near-infrared absorption and the donor a P3HT:$PC_{71}BM$ blend. The improvement of efficiency in this case was not attributed to triplet harvesting, but to the improved absorption spectrum better matching the solar spectrum. No decrease of performance was observed up to 10 wt% of the guest (independent of whether the devices have been baked or not). The fact that the absorption of light through the small band gap molecule generated additional IPCE means that this guest must have been mainly situated at the donor/acceptor interface and rarely within a pure donor or acceptor domain (even before baking), an interesting point that has not been mentioned by the authors.

3.4.8.3 Conclusion on Possible Energy Level Configurations

In conclusion, I have shown that, unless aiming for the approach in Figure 3-29k, the arrangement ‘a’ is ideal, because it avoids charge trapping as well as exciplex formation in any case. Unfortunately, ‘a’ is rather hard to realise if the host has a material with a high LUMO or low HOMO (such as $PC_{61}BM$). If one is dealing with a double-layer and only injects the guest into the donor for example, the requirements are lowered to further allow ‘b’.

As discussed above, the guest may not even mix with the host and only occur at domain interfaces, so that ‘b’, ‘e’ and ‘f’ are also feasible. However, if there is no intermixing of the guest with the host, the phosphorescent complex can obviously not create many triplets on the host, so the original idea of the inclusion of a triplet emitter to generate more triplet excitons to improve the exciton diffusion length will not work in those cases.

The configurations ‘b’, ‘e’ and ‘f’ are possible if energy transfer and CT state formation between host and guest can be avoided (not including the approach in Figure 3-29k, which relies on energy transfer to the guest) and if no excitons are split within donor or acceptor domains alone. However, I have discussed in section 3.4.2 that in the case of P3HT, exciton/polaron dissociation may already occur within the polymer. Such behaviour would result in a stronger constraint on the LUMO level, forbidding the configurations ‘e’ and ‘f’.

To summarize once more, apart from when following the approach in Figure 3-29k, we see that the possible energy level configurations of the blend components depend on whether or not energy transfer to the guest, exciton splitting at the host/guest interface, and exciton dissociation within the donor or acceptor domains can be successfully avoided. If the answer is *no* to only one of these points, performance losses can be expected for all configurations but ‘a’.

3.4.9 Conclusion

I have added phosphorescent guests (a Cu-complex) to blends of P3HT and $PC_{61}BM$ to try to improve the ratio of triplet over singlet excitons via the second approach, i.e. via increasing the ISC directly on the P3HT due to the proximity of the guest molecule. Upon increasing the guest concentration, basically all SC parameters were decreasing. The positive effect of long (overnight) stirring has been established. Upon investigating the mobilities by fabricating FETs, I came to the hypothesis that the guest molecules act as hole traps. After measurements of the energy levels of our materials via cyclic voltammetry we found that the HOMO level of the guest was indeed higher than the HOMO level of P3HT, which means that hole trapping is a

likely explanation for the deteriorating device performances. More precise estimations of the number of traps as a function of the guest content have been presented.

The strong negative influence of the guest on charge transport overshadowed any potential increase in triplet content. In the following, different material systems have been used.

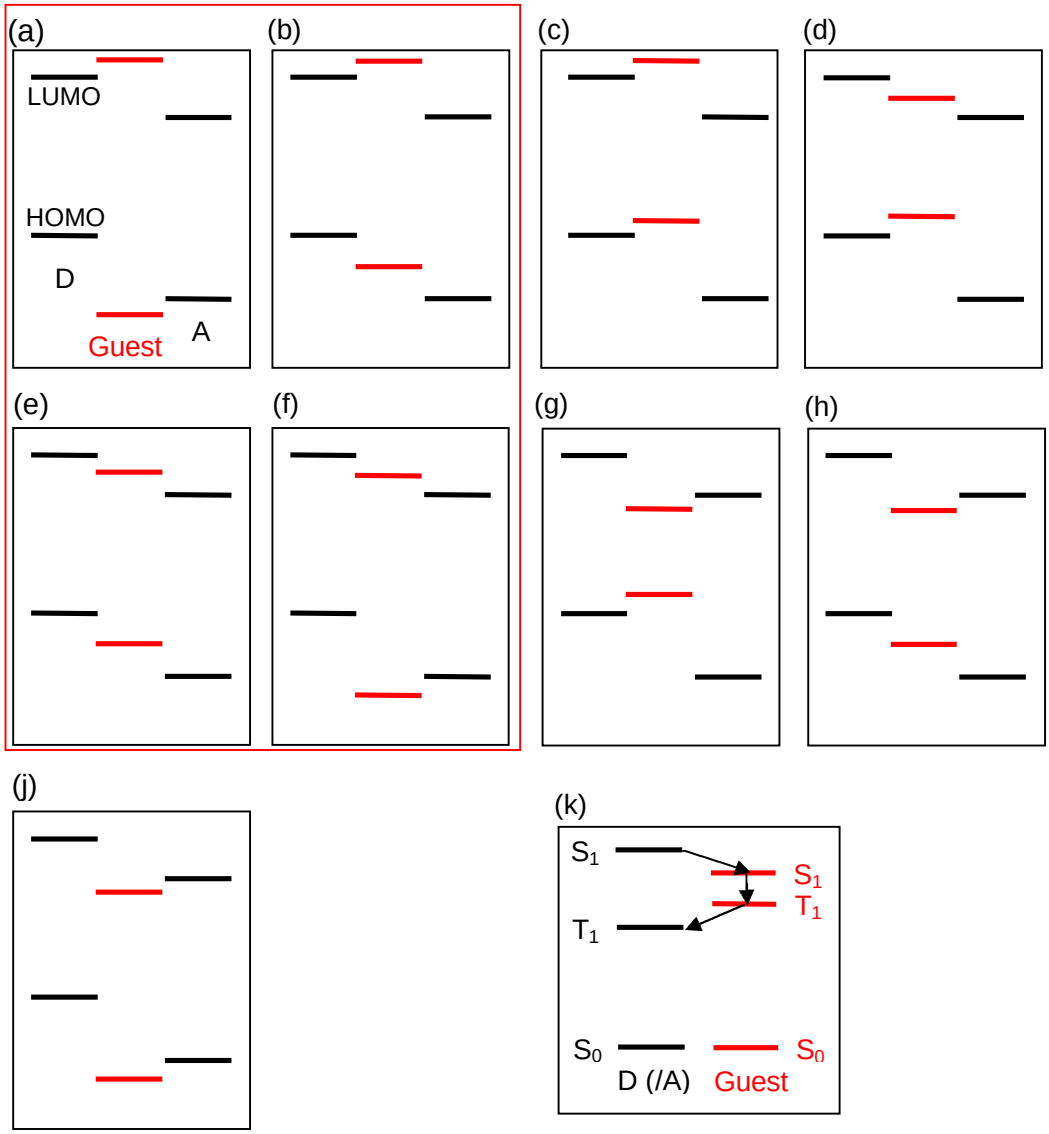

Figure 3-29. (a)–(i) Illustration of all possible relative positions of HOMO and LUMO levels of donor (D), acceptor (A) and guest. Configurations (c), (d), (g), (h) and (j) will always lead to charge trapping on the donor and are therefore undesirable in all circumstances. More explanation in the text. (k) Desired arrangement of singlet and triplet energy levels to convert singlets on the donor (or acceptor) via intersystem crossing on the guest.

3.5 MDMO-PPV:$PC_{61}BM$ blends with Ir-complex

In the following I investigate the influence of adding the phosphorescent guest bis(2-(9,9-dibutylfluorenyl)-1-isoquinoline(acetylacetonate)) (ADS077RE) into a polymer-fullerene SC consisting of poly[2-methoxy-5-(3',7'-dimethyloctyloxy) -1,4-phenylene vinylene] (MDMO-PPV) and phenyl-C61-butyric acid methyl ester ($PC_{61}BM$) on the SC performance.

This material system has been carefully chosen in order to provide the right energy level configuration for the first approach (see section 3.2.9.3 on page 91), which relies on Förster transfer from the host to the guest, followed by ISC on the guest and back energy (Dexter) transfer from the guest to the host. Note also that the donor polymer is rather amorphous in pristine form, so that the addition of guest molecules should influence charge transport less strong than in a crystalline donor material that is disturbed by the guest.

3.5.1 Materials

The donor polymer is MDMO-PPV (purchased from Sigma-Aldrich), the acceptor fullerene derivate is $PC_{61}BM$ (purchased from Sigma-Aldrich) and the phosphorescent emitter is the Ir-complex ADS077RE (purchased from ADS). The chemical structures of these materials are shown in Figure 3-30.

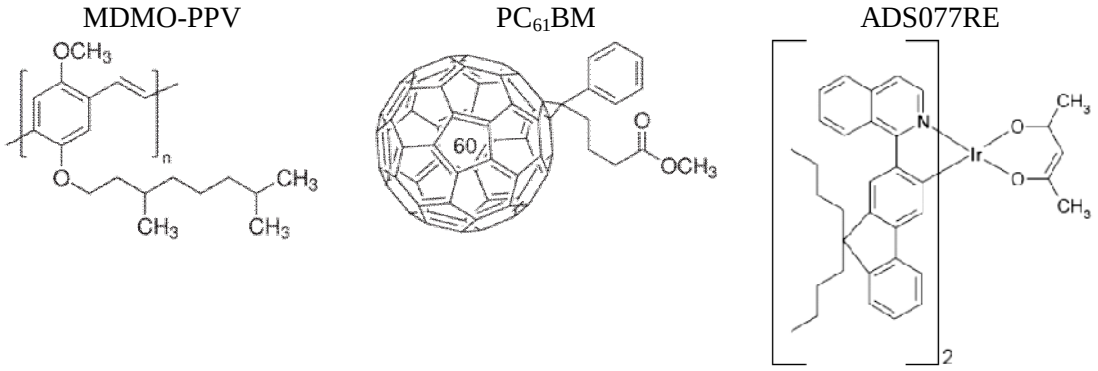

Figure 3-30. Chemical structures of MDMO-PPV, $PC_{61}BM$ and the Ir-complex ADS077RE.

3.5.1.1 HOMO-LUMO Energy Levels

The HOMO and LUMO energy levels of our materials and of P3HT are shown in Figure 3-31. For MDMO-PPV, two values are given for both, the HOMO and the LUMO level; the dashed lines correspond to literature values[126,178] and the solid lines to measurements by our group[vi]. According to the classification scheme on page 132, we are dealing here with configuration 'c' or 'e', depending on which HOMO measurements to use. If the literature value for the HOMO of MDMO-PPV (5.3 eV) is to be trusted, we are dealing with configuration 'e', which is acceptable if most of the excitons are generated in the donor polymer or when one is using a bilayer where the guest is only mixed with the donor. If the measurement by our group (5.65 eV) is to be trusted, then we have configuration 'c', presenting the problem of hole trapping for holes not only originating from $PC_{61}BM$, but also from MDMO-PPV.

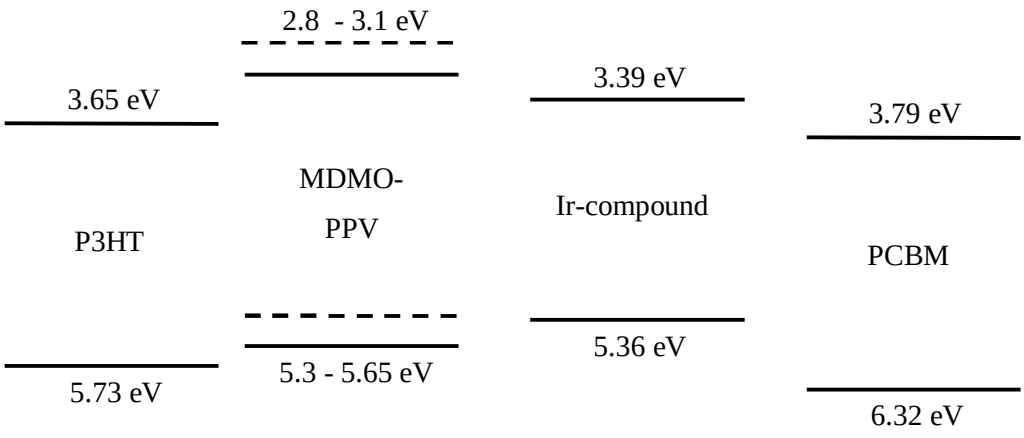

Figure 3-31. HOMO and LUMO levels of the used materials according to measurements by Charlotte Fléchon. The dashed lines for MDMO-PPV correspond to values taken from the literature.[126,178] The exact MDMO-PPV HOMO level distribution may be crucial to determine if charge trapping can be expected from MDMO-PPV to the Ir-complex.

3.5.1.2 Singlet and Triplet Levels

To achieve Förster or Dexter transfer one relies on a spectral overlap between absorption and emission of the respective (fluorescence/phosphorescence, host/guest) spectra. The overlap between the host emission spectrum and the guest absorption spectrum, as well as the estimated singlet and triplet levels are shown in Figure 3-32. The green area indicates the wavelength region in which the polymer emission and guest absorption spectrum overlap. The overlap is essentially between the singlet emission of the donor and the lowest-lying singlet metal-to-

[vi] measurements performed by Charlotte Fléchon in the UCL Department of Chemistry in the group of Darren J. Caruana

ligand charge-transfer (MLCT) state of the guest (see Figure 3-33). Note that depending on the precise HOMO values, it may also be possible that electron and hole are transferred onto the guest, effectively resulting in the desired energy transfer.

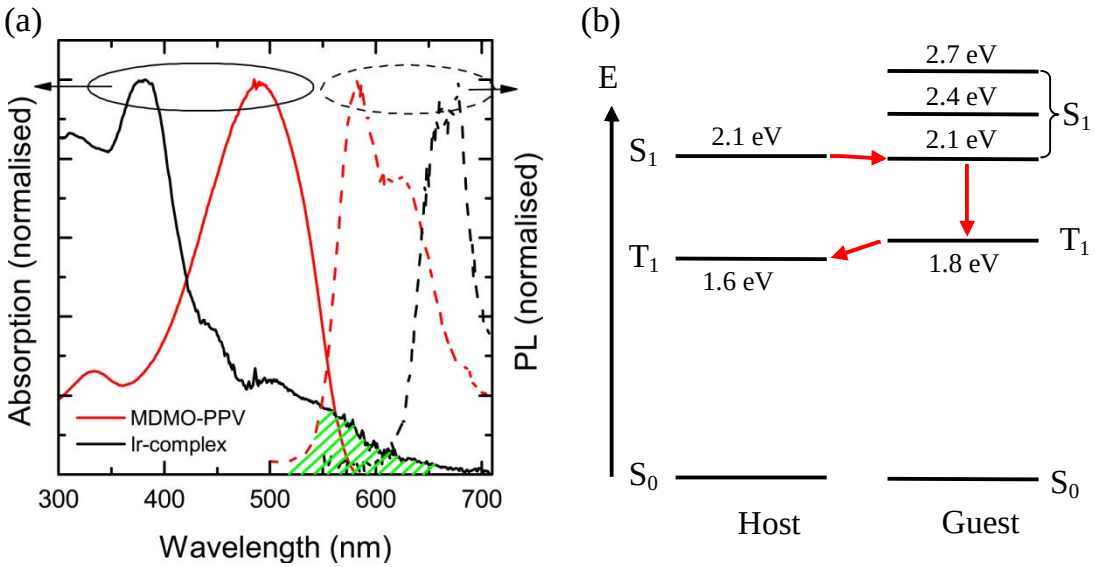

Figure 3-32. (a) Absorption and emission spectra of the donor polymer and the Ir-complex in solid state. The green area indicates in which wavelength range a significant Förster transfer from the host to the guest is possible. (b) Exciton energies of the participating materials. The host is MDMO-PPV and the guest is the Iridium compound ADS077RE. The singlet energy levels of the guest are taken from fittings of Gaussians to the absorption spectrum[179] (see Figure 3-33). The triplet level of the guest corresponds to the photoluminescence peak wavelength (675 nm).

The singlet level of MDMO-PPV (2.1 eV) as well as the triplet level of the Ir-complex (1.8 eV) are obtained by using the wavelength of maximum emission of the corresponding compound (580 nm and 675 nm, respectively). The triplet level of MDMO-PPV[126] (1.6 eV) and the singlet levels of the Ir-complex[179] (see Figure 3-33) are taken from the literature. Note that the triplet level for MDMO-PPV may be overestimated as, according to an assumed exchange energy of 0.7 eV[101] or according to Offermans et al.,[180] the triplet level may lie around 1.4 or 1.3 eV. In any case, it is lower than the triplet level on the guest, hence allowing Dexter energy transfer. The triplet level of $PC_{61}BM$ is around 1.5 eV[114] and triplet transfer to $PC_{61}BM$ may hence be possible depending on the precise energy levels. If the triplet level on $PC_{61}BM$ is lower than the CT level, exciton dissociation at the donor/acceptor interface may be hindered (similar to a too low triplet level on the donor polymer), as the CT level may not be significantly populated in such a scenario. The author is not aware of publications concerning exciton dissociation at a type II heterojunctions from the triplet state on $PC_{61}BM$.

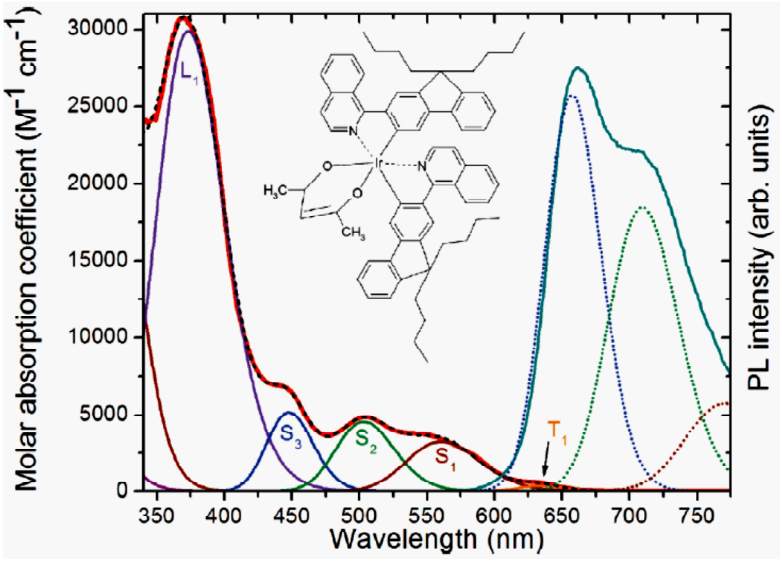

Figure 3-33. Absorption and Emission of the Ir-complex showing the contributions of the ligand centred L_1 state, three singlet metal-ligand charge-transfer (MLCT) states and a triplet MLCT state. The emission on the right is phosphorescent. Image reprinted with permission from Hedley et al.,[179] Copyright (2010) American Chemical Society.

3.5.1.3 Charge Transfer State Energy

To make sure that triplet excitons can still be split at the D/A interface, the CT state needs to lie below the T_1 level of the donor (1.6 eV). According to section 3.2.8 or Figure 3-2 on page 89, the energy of the CT-state (E_{CT}) can be estimated by either considering V_{OC} or $|E_{HOMO}(D) - E_{LUMO}(A)|$.

- According to $E_{CT} = e\,V_{OC} + 0.5$ eV one obtains $E_{CT} = 0.8$ eV + 0.5 eV = 1.3 eV.
- According to $E_{CT} = |E_{HOMO}(D) - E_{LUMO}(A)| + 0.3$ eV one obtains
  - $E_{CT} = 5.3$ eV – 3.7 eV + 0.3 eV = 1.9 eV if the literature values for MDMO-PPV and $PC_{61}BM$ are used, or
  - $E_{CT} = 5.65$ eV – 3.79 eV + 0.3 eV = 2.16 eV if the measurements by our group[vii] for MDMO-PPV and $PC_{61}BM$ are used.

The above calculations give considerably different estimates of the CT-state energy. Calculating E_{CT} via V_{OC} results in a desirable situation where the CT state (1.3 eV) is expected to lie below 1.6 eV. Calculating E_{CT} via the effective band-gap on the other hand results in a situation where E_{CT} (1.9 - 2.2 eV) is expected to be larger than 1.6 eV, hence resulting in a configuration where charge separation via the CT state may not be efficient.

[vii] by Charlotte Fléchon

3.5.2 Device Fabrication

Blends and bilayer SCs were fabricated with materials presented in this section. Bilayer devices offer the advantage of a better controlled morphology and, most importantly for the work here, a possibly fullerene free layer of donor polymer. In order to create bilayers, several approaches were attempted, among them the use of a bad solvent, evaporation of an electron conducting layer on top of the donor layer, and the application of a crosslinker. The first two approaches are shown in the appendix in section 4.1 on page 198. The use of the crosslinker was successful and will be described in the following.

3.5.2.1 Crosslinker FPA

This approach to achieve bilayers relies on crosslinking the first layer (donor) so that it becomes insoluble in the solvent used for the second layer (acceptor). The crosslinker used is bis(fluorinated phenyl azide) (FPA, synthesised by the group of Peter Ho, Singapore, chemical structure shown in Figure 3-34a).[181] The proposed working principle for the crosslinker is shown in Figure 3-34b. The crosslinker generates a singlet nitrene upon photoabsorption, which is so reactive that it can be inserted into alkyl chains for example. FPA has been shown to crosslink various different conjugated molecules whilst not reacting with the polymer and absorbing at a very low wavelength of ~ 250 nm, a spectral region where many polymers are transparent. Also, FPA shows little exciton and carrier trapping in many polymer matrices.[181] FPA was found to have no influence on the PLQE of MDMO-PPV films.

The fabrication procedure for bilayers was as follows: The crosslinker solution (in toluene) was added to the polymer (MDMO-PPV) solution (in chlorobenzene) and the first layer was spin coated as normal. Then the substrate was baked at 75 °C for 20 min to distribute the crosslinker within the blend. The layer was then irradiated with UV light (250 nm UV LED, UVTOP® from Sensor Electronic Technology) at a distance of 10 cm for 10 min. (Two samples were irradiated simultaneously). Afterwards, the layer was spin rinsed two times with chlorobenzene at 5000 rpm to remove any non-crosslinked polymer.

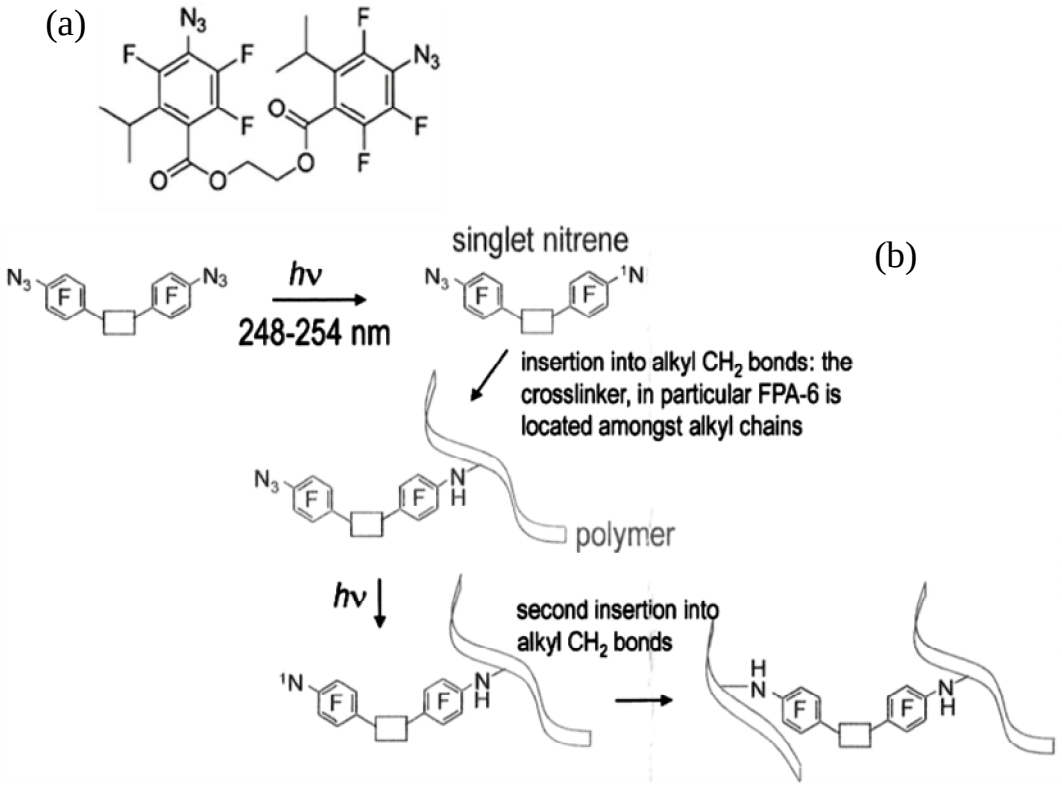

Figure 3-34. (a) Chemical structure of the crosslinker molecule FPA. (b) Crosslinking mechanism of FPA. Photoabsorption leads to the production of very reactive singlet nitrene, which may react with an alkyl chain.(Figure courtesy of Prof. Peter Ho, Singapore).

The film retention for crosslinked materials generally depends on the crosslinker concentration and the molecular weight of the material to be crosslinked. The molecular weight of MDMO-PPV is rather low (23 k) so that a rather high concentration of the crosslinker FPA must be used. As the absorbance (A) is proportional to the thickness (t) of the material the light has to travel through and the absorption coefficient (α), i.e. $A = \alpha\, t$, the film retention ratio (t_{after}/t_{before}) can be determined as the ratio of the absorbance after and before spin rinsing in a good solvent (see Table 3-3).

One can see from Table 3-3 that 10 wt% is a good crosslinker concentration if one intends to crosslink most (~90%) of the material. Interestingly, even without UV-exposure, ~84% of the material is retained on the substrate for a 10 wt% crosslinker concentration. A possible explanation for that observation may be that the heating step prior to the UV-exposure already crosslinks the material.

Table 3-3. Film retention determination via absorption peak measurements. The crosslinker concentration, the MDMO-PPV film thickness and the guest concentration have been varied. Also, the film retention without the UV exposure step has been measured.

Crosslinker concentration	Spin-speed donor layer	Guest concentration	UV exposure?	Retention ratio
1 wt%	1800 rpm	0.0 wt%	yes	73.4% 65.1%
3 wt%	1800 rpm	0.0 wt%	yes	79.1% 77.1%
10 wt%	4000 rpm	0.0 wt%	no	86.3%
10 wt%	4000 rpm	0.5 wt%	yes	92.0%
10 wt%	4000 rpm	2.5 wt%	no	82.8%

3.5.2.2 Final Device Fabrication Procedure

In the following, devices have been fabricated as follows:

The indium-tin oxide (ITO) substrates (purchased from UQG Ltd., Cambridge, UK) were ultrasonicated in acetone and isopropanol for 10 min each before exposing them to an oxygen plasma. A 62 ± 5 nm layer of high-conductivity PEDOT:PSS (purchased from Sigma-Aldrich) was spin-coated under air onto the devices. After annealing the PEDOT:PSS for 10 min at 140 °C the active layers were spin-coated under nitrogen atmosphere, achieving a 74 ± 9 nm thick layer as measured via a Dektak profilometer. MDMO-PPV:$PC_{61}BM$ blends were prepared in toluene.

For bilayer devices, the MDMO-PPV and $PC_{61}BM$ (both purchased from Sigma Aldrich) were dissolved in chlorobenzene. MDMO-PPV was mixed with 10 wt% of FPA. After spin coating the MDMO-PPV:FPA blend, the substrate is annealed at 75 °C for 20 min and exposed to UV-light (250 nm LED). Before $PC_{61}BM$ is deposited, the layer is spin-rinsed twice with chlorobenzene at 5000 rpm to remove any residual non-crosslinked polymer. For the bilayer devices which include the triplet emitter, the MDMO-PPV layer was 56 ± 10 nm and the $PC_{61}BM$ layer ~ 32 nm thick, as measured via a Dektak profilometer.

The cathode consists of a ≥ 150 nm thick Aluminium layer evaporated at pressures below 10^{-5} mbar.

3.5.3 Thickness Optimisation For Bilayer Devices

3.5.3.1 Dark JV Characteristics

Before using the phosphorescent emitter the behaviour of the pure bilayer needs to be examined and the optimum thicknesses of the respective layers found. It is often useful to investigate the JV curves of devices not only under illumination, but also in darkness, because removing the light means blocking out effects of exciton diffusion and dissociation and one can solely focus on charge transport including charge injection/extraction.

Figure 3-35 shows the JV curves of dark bilayer devices with different MDMO-PPV thicknesses (spin-speeds indicated by the colour) and different $PC_{61}BM$ thicknesses (spin-speeds indicated by the line style). From the dark JV-curves it is clear that upon reducing the film thickness of the MDMO-PPV layer, the slope of the curve at higher voltages is strongly increased. This slope gives an indication of the series resistance R_S (if one thinks of the SC as a diode with a shunt and series resistance as explained in section 3.3.1 on page 93). Changing the $PC_{61}BM$ spin-speed on the other hand does not result in a clear trend. We therefore find that for thicknesses of the donor layer ≥ 56 nm (corresponding to the spin-speed of 4000 rpm), the MDMO-PPV layer presents the bottle-neck with regards to charge transport in these devices.

We hence find that the optimum spin-speed for MDMO-PPV seems to be 4000 rpm from a charge transport point of view.

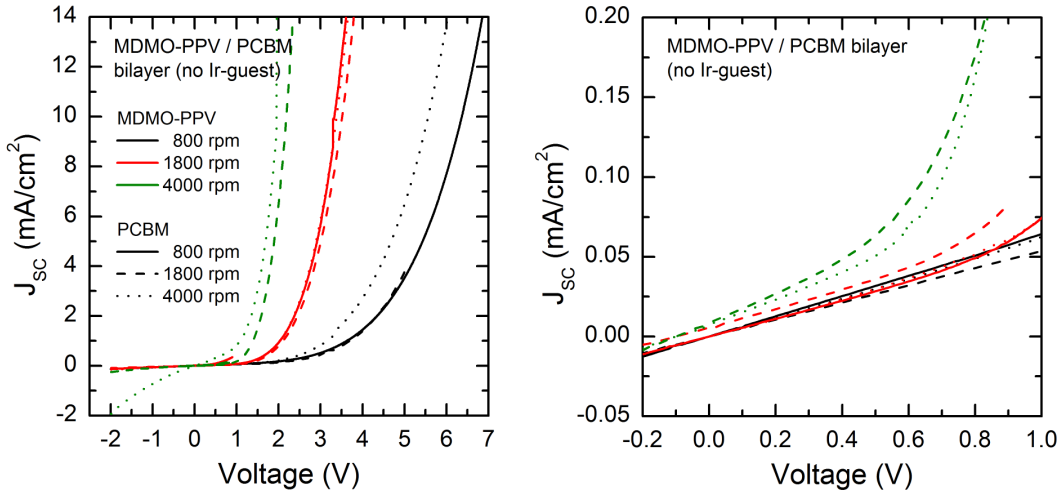

Figure 3-35. (a) Dark JV curve of bilayer devices with different thicknesses of MDMO-PPV and $PC_{61}BM$. (b) Zoom-in into the low bias regime. The thickness of the donor layer is illustrated by the colour (black, red, green) of the curves whereas the thickness of the acceptor layer is illustrated by the line style (solid, dashed, dotted).

3.5.3.2 Illuminated JV Characteristics

The JV curves of bilayer devices under illumination and the respective performance parameters are illustrated in Figure 3-36 and Figure 3-37.

We see that J_{SC} (black squares in Figure 3-37) is improved for higher spin-speeds, which means that the reduction of light absorption at higher speeds, which by itself would result in a lower J_{SC}, is overcompensated by the improvement in charge transport for thinner donor layers. The hole mobility on MDMO-PPV is hence the bottleneck in these devices.

However, not only does J_{SC} increase, but also does V_{OC} and to a very small extend the FF upon increasing the spin-speed. More precisely, we see that V_{OC} is purely a function of the polymer thickness and independent of the acceptor thickness.

Similarly to the increase in J_{SC}, the FF can "normally" be expected to increase upon reducing R_S. However, the increase in FF was small, from 25% for a spin-speed of 800 rpm up to 28% for a spin-speed of 4000 rpm. Note that all curves show a very linear behaviour between $V = 0$ and $V = V_{OC}$, which mathematically leads to a FF of 25%. The linear behaviour suggests that there may be a problem of charge injection, but knowing that a BHJ architecture with the same materials works very well, this cause seems unlikely.

If we look at the influence of varying the $PC_{61}BM$ spin-speed, we only find an influence on J_{SC}. We see that within devices with the same MDMO-PPV film thicknesses, increasing the spin-speed from 1800 to 4000 rpm significantly reduces J_{SC}. (Changing the spin speed for $PC_{61}BM$ from 800 to 1800 rpm does not show a large effect). The reason for that cannot be explained under the assumption of a perfect bilayer, because reducing the thickness of $PC_{61}BM$ should not reduce exciton dissociation or negatively influence electron transport. Looking at AFM images of bilayer devices (see Figure 3-41), we see an imperfect coverage of the donor layer with $PC_{61}BM$. Therefore, increasing the spin-speed from 1800 to 4000 rpm possibly led to a larger surface of the donor layer that was not covered by $PC_{61}BM$, hence reducing J_{SC}.

As a result of the thickness optimisation, we find an optimum donor layer of ~56 nm and an optimum $PC_{61}BM$ layer of ~32 nm. Note that increasing the exciton diffusion length in a bilayer (i.e. the further aim of this work) should alter the optimum donor thickness towards larger values. However, the problem with hole transport arising for larger MDMO-PPV thicknesses would compensate any improvement in exciton dissociation rates. Considering exciton diffusion lengths in MDMO-PPV of about 6 ± 1 nm,[182] the optimum MDMO-PPV film thickness should be even smaller than 56 nm. Therefore, an increase in the exciton diffusion length should improve J_{SC} even for the rather thin donor layer of 56 nm thickness.

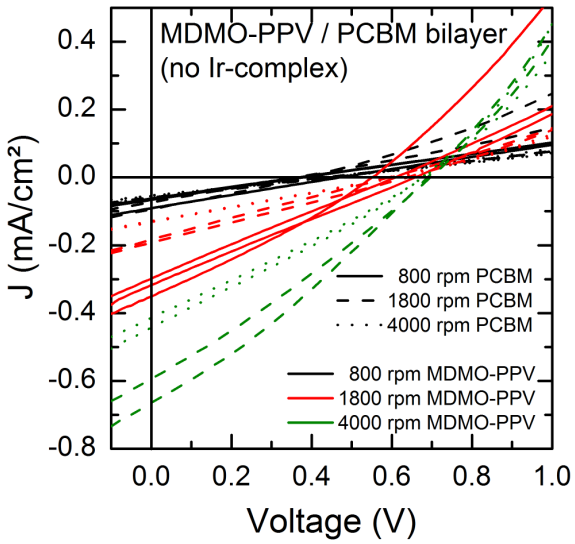

Figure 3-36. JV-curves of illuminated bilayer cells with different thicknesses of MDMO-PPV and $PC_{61}BM$. The thickness of the polymer layer is illustrated by the colour of the curves whereas the thickness of the acceptor layer is illustrated by the line style (solid, dashed, dotted).

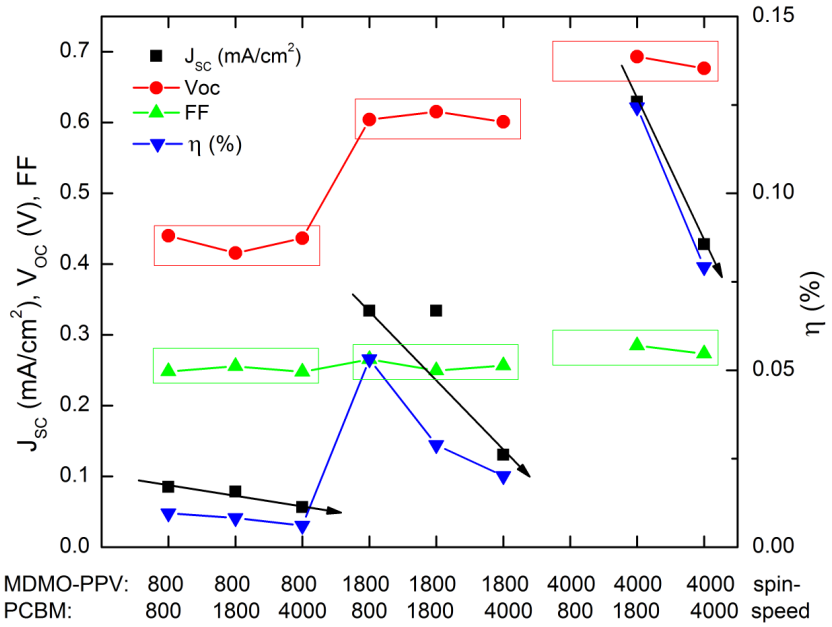

Figure 3-37. Performance parameters for MDMO-PPV/ $PC_{61}BM$ bilayer cells without the Ir-compound as a function of spin-speeds of the layers. η is the power conversion efficiency.

Note that there is a way of determining the exciton diffusion length by preparing bilayers of the donor polymer and a quenching layer ($PC_{61}BM$). This method relies on varying the thickness of the donor layer to maximise J_{SC}. The thickness at maximum J_{SC} can then be related to the exciton diffusion length (in first approximation, this thickness equals the exciton diffusion

length). However, the problems with hole transport at larger donor film thickness does not allow us to perform this investigation. Also, this method relies heavily on obtaining perfectly separated donor and acceptor layers with a sharp interface (→ problem of $PC_{61}BM$ diffusion and intercalation) and a well controlled film thickness (→ spin coating of films below ~30 nm is rather unreliable).

3.5.4 Addition of the Phosphorescent Guest

3.5.4.1 Results for Blend Devices

As the idea of this work is to increase the exciton diffusion length in the donor polymer, when fabricating blend devices, one should aim for a morphology where the materials are not completely intercalated and/or making larger domains than ideal for the reference cell (without a phosphorescent guest). Knowing that an additional baking step typically changes the degree of phase separation, I measured the SC performance of reference blend devices with different annealing temperatures.

From Figure 3-38a one can see a maximum of the photovoltaic efficiency at 70 °C, where all parameters but J_{SC} were maximized. J_{SC} was maximized at 80 °C. The SC performance has then been measured as a function of guest content for the optimum annealing temperature of 70 °C (Figure 3-38b) and at 90 °C (Figure 3-38c), i.e. at an annealing temperature that is expected to lead to less intercalation and larger domains.

We see that at 70 °C there is a negligible (3%) increase in J_{SC}, but a significant increase in V_{OC} (11%) and *FF* (16%) upon adding 1 wt% of the guest. Increasing the guest content to 3 wt% increases *FF* further but reverts V_{OC} back to the reference cell value. At 90 °C on the other hand, we observe an increase in all three parameters upon adding 1% of the triplet emitter. Increasing the number of guest molecules further is detrimental for the performance. The improvement of the overall energy conversion efficiency (η) at 1 wt% guest content for the devices pre-annealed at 90 °C (70 °C) amounts to 59%, (31), of which about 11% (3%) is coming from J_{SC}, 9% (11%) from V_{OC}, and 26% (16%) from *FF*. Absolute values of the solar cell parameters are given in Table 3-4.

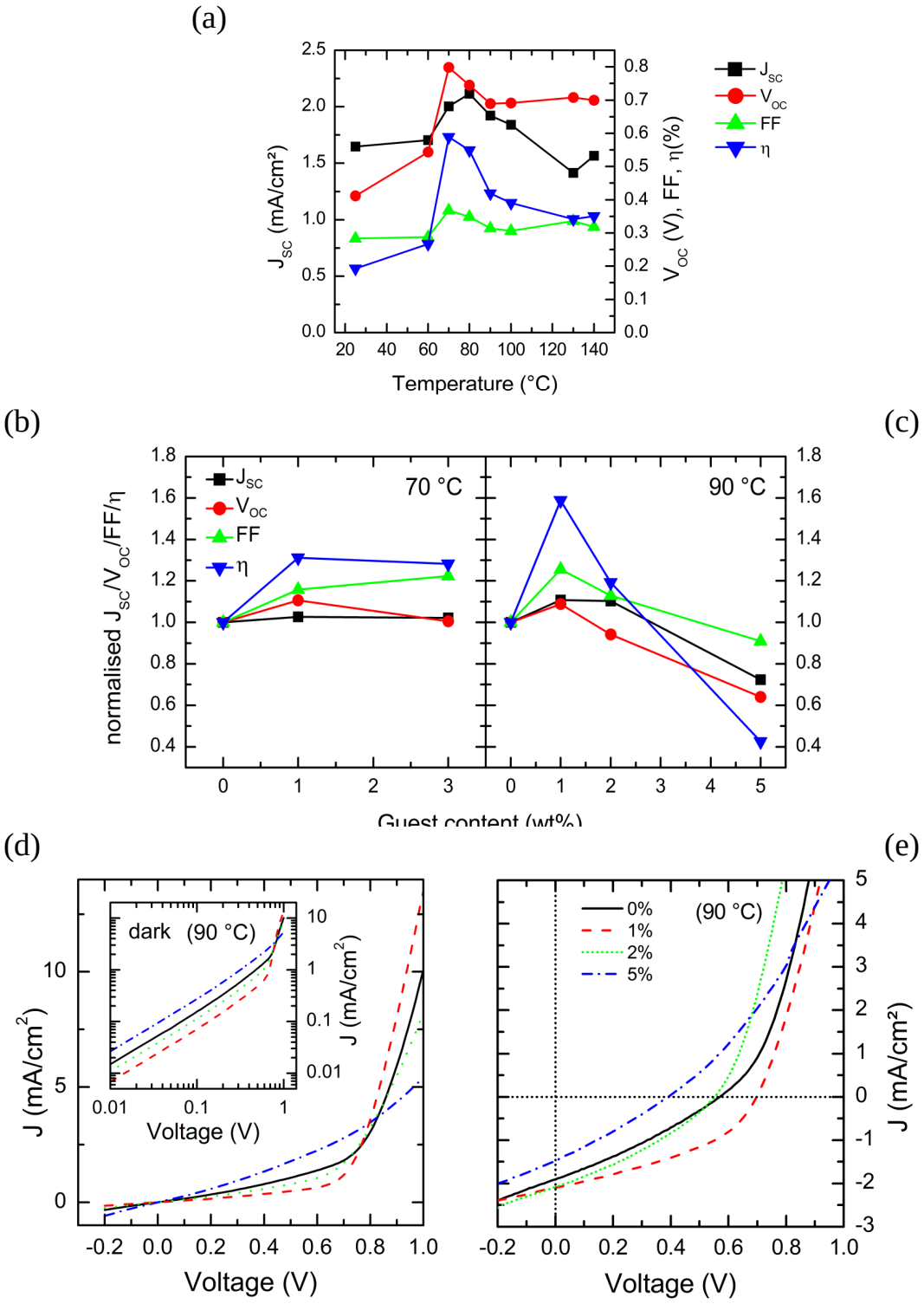

Figure 3-38. (a) MDMO-PPV:$PC_{61}BM$ blend devices annealed at different temperatures. (a) The optimum temperature of 70 °C and (b) a higher than optimum temperature of 90 °C was then used to study the effect adding different amounts of the triplet emitter ADS077RE. J_{SC} is indicated by black squares, V_{OC} by red circles, *FF* by green upwards pointing triangles and the power conversion efficiency η by blue downwards pointing triangles. (d) and (e) show the dark and illuminated JV curves for different amounts of guest content for blend devices annealed 90 °C.

Table 3-4. Absolute values of J_{SC}, V_{OC}, *FF* and η for devices prebaked at 70 °C and 90 °C.

triplet content (wt%)	J_{sc} (mA/cm²)	V_{oc} (V)	*FF*	η (%)
70 °C prebaked				
0	2.26	0.56	0.30	0.39
1	2.32	0.62	0.35	0.51
3	2.31	0.57	0.37	0.50
90 °C prebaked				
0	1.86	0.58	0.30	0.32
1	2.07	0.63	0.37	0.51
2	2.06	0.54	0.33	0.38
5	1.35	0.37	0.27	0.14

AFM images of blends of MDMO-PPV with $PC_{61}BM$ (1:4 weight ratio) in toluene are shown in Figure 3-39, where one can see a morphology dominated by $PC_{61}BM$ clusters. These $PC_{61}BM$ clusters also appear without annealing the blend to 90 °C. The clusters have a diameter of approx. 200-400 nm. More precisely, I find an increase of the mean diameter (of 'equivalent discs') of the $PC_{61}BM$ grains of about 23% upon annealing the blend at 90 °C (from 226 nm to 278 nm) and a smaller additional increase of 15% after adding 5 wt% of the Ir-compound to the blend.

Blends of the same material in chlorobenzene resulted in smaller clusters with diameters of approx. 120-200 nm (results not shown). The blend is known to show mixing on a smaller scale in chlorobenzene as compared to toluene. As more phase separation is desired to test the influence of the triplet emitter on the exciton diffusion length, toluene was the chosen solvent for the blends.

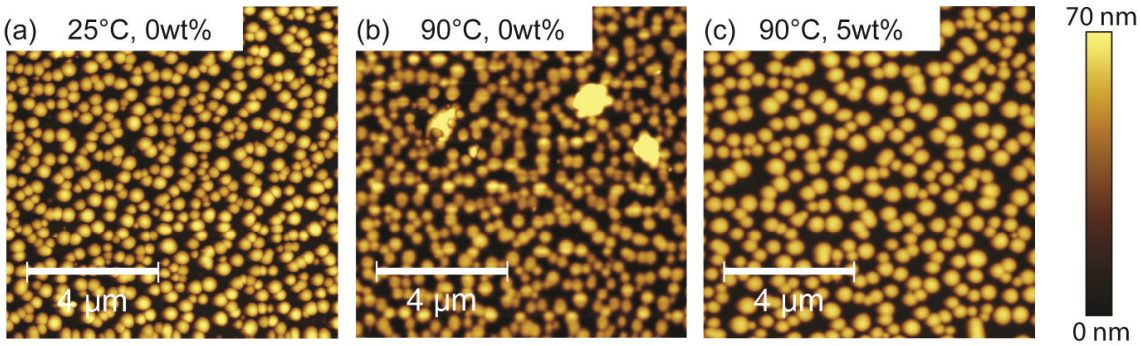

Figure 3-39. Tapping mode AFM images of blends spin coated from toluene. (a) unannealed blend without the triplet emitter, (b) annealed blend without the triplet emitter and (c) annealed blend with 5 wt% of the triplet emitter. All blends where prepared on spectrosil without any oxygen plasma or deposition of PEDOT:PSS. Vertical scale bars indicate 4 µm.

3.5.4.2 Results for Bilayer Devices

I then fabricated bilayer devices with the same materials and measured the performance as a function of guest content. As mentioned already, bilayers offer the advantage of a better controlled morphology where domains of phases of the pure donor polymer are more likely to exist.

Figure 3-40a shows JV-curves in the dark, presenting a slightly reduced current at higher voltages upon adding the Ir-compound. In Figure 3-40b I then show average JV-curves for illuminated devices as a function of guest concentration. The corresponding performance parameters are illustrated in Figure 3-40c, where we can see that J_{SC} is the only parameter that increases upon adding the guest. The incident photon to current efficiency (IPCE) spectra (see Figure 3-40d) show more clearly where the increase in current originates. Interestingly we see a reduction in the part of the current that is generated due to light absorption by $PC_{61}BM$ (peak at around 350 nm), but a clear increase in the current generated due to absorption by the donor polymer (which has its absorption maximum at 490 nm).

I also investigated the bilayer morphology via AFM. No difference can be seen in the AFM images between bilayers where the donor film contains the Ir-compound (not shown) and those which do not (Figure 3-41a). The AFM image reveals an interesting looking surface with petal-like features. It is the impression/interpretation of the author, that what one sees there is a discontinuous $PC_{61}BM$ layer. The centre between different adjacent petals is aggregated $PC_{61}BM$ and the petals itself is "missing $PC_{61}BM$". The step between a petal and the outer environment is approx. 30 nm high, which is in good agreement with the $PC_{61}BM$ film thickness (32 nm as measured with a Dektak profilometer). Also interesting is the small $PC_{61}BM$ cluster in the middle of each petal.

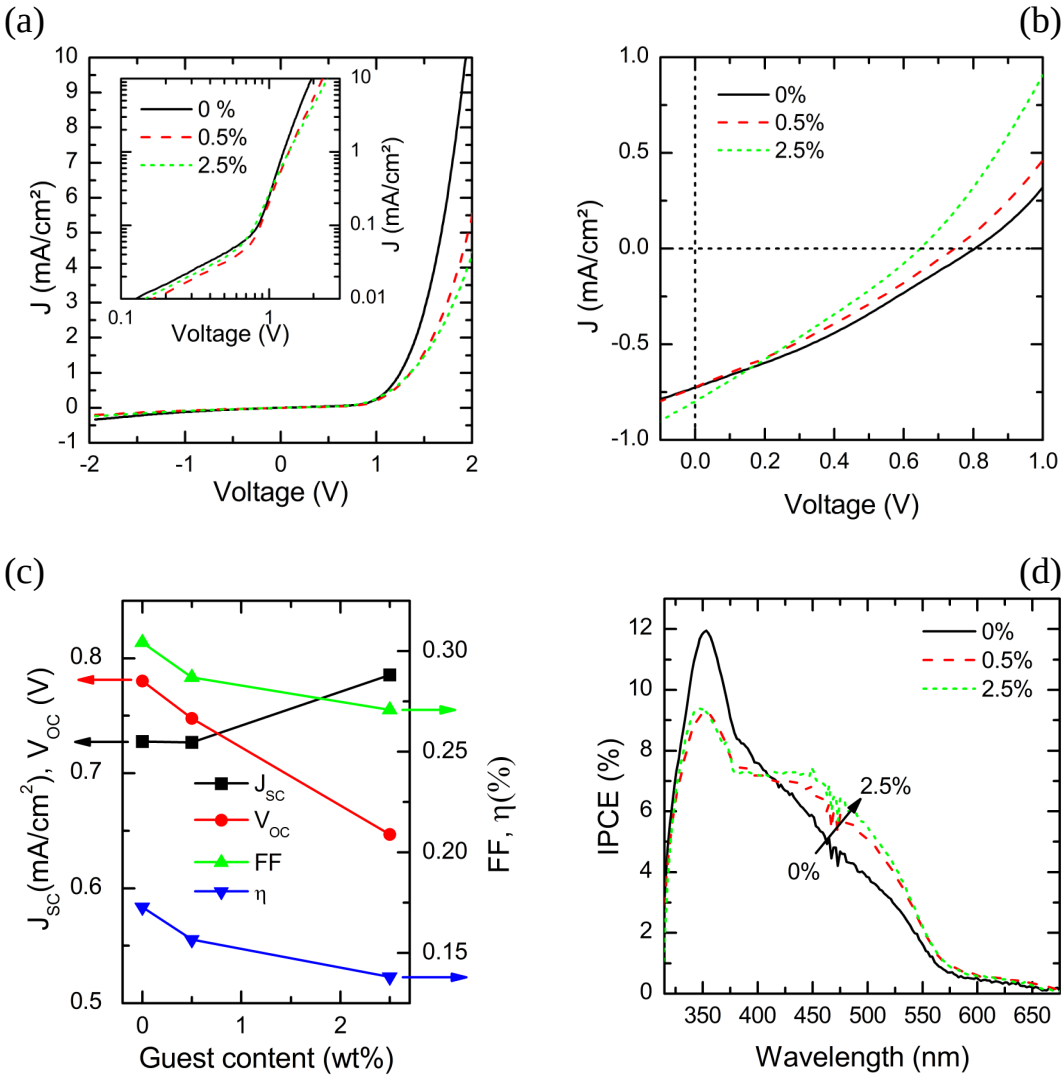

Figure 3-40. **Bilayer devices**. (a) JV curves of devices in the dark. (b) JV curves of illuminated devices. (c) Summary of performance parameters. (d) IPCE spectra demonstrating an increase in signal originating from donor absorption.

Upon baking at 140 °C one can see (Figure 3-41b and c) that the former rather smooth and continuous $PC_{61}BM$ layer is now aggregated into small clusters with diameters of around 400 nm. Interestingly this is similar to the domain sizes of $PC_{61}BM$ clusters in *blends* made out of toluene. I hence suggest that intercalated domains are formed upon annealing. As we try to avoid intercalation, bilayer devices were not annealed at any point.

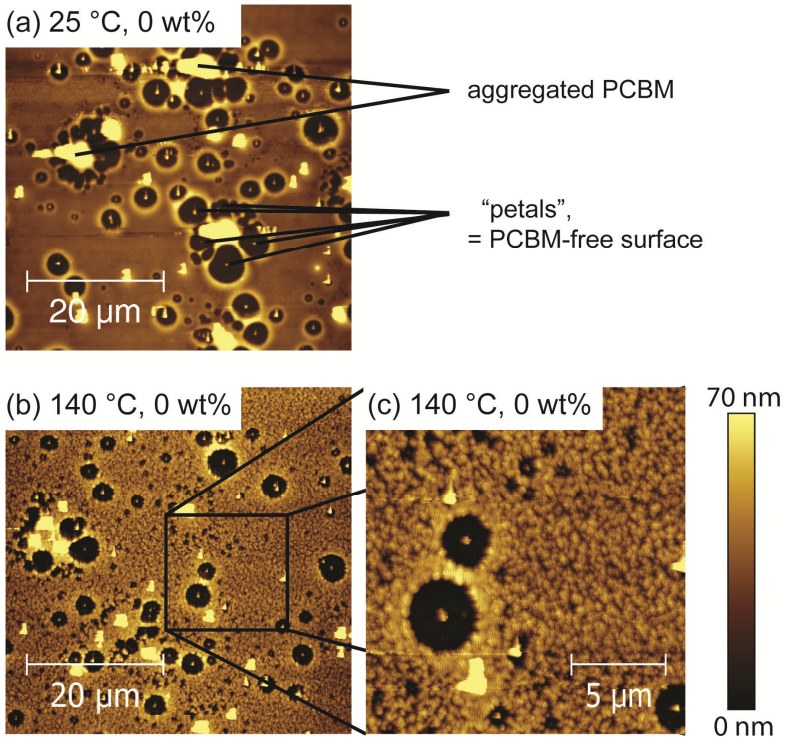

Figure 3-41. AFM images of bilayers without triplet emitter showing "petal"-like structures. (a) before annealing, (b) after annealing at 140 °C for 10 min. (c) amplified image of (b). One can see how the previously smooth surface shows considerable clustering upon baking. Bilayers were deposited on spectrosil substrates. Individual layers were spin coated from solutions in CB (with small amounts of toluene in the donor solution due to the addition of the crosslinker solution).

3.5.5 Transient Absorption

In order to gain further insight into processes such as Förster and Dexter transfer and the occurrence of triplet excitons in the donor polymer upon addition of the guest, transient absorption (TA) measurements were carried out by Giulia Grancini at the Milano Istituto Italiano di Tecnologia in the Center for Nanoscience and Technology, Milano, Italy, in the group of Annamaria Petrozza, who also helped interpreting the results. They also provided the figures which I adapted to a small degree. The measurements give further insight into processes such as Förster and Dexter transfer and the occurrence of triplet excitons in the donor polymer upon addition of the guest.

3.5.5.1 Experimental Setup

3.5.5.1.1 Nanosecond Transient Absorption (TA) Measurements

Nanosecond transient absorption (TA) measurements were carried out with a LP920 laser flash spectrometer (Edinburgh Instruments). It is based on a standard "pump-probe" set-up where the sample is excited by a ns laser pulse (pump) and the time evolution of the differential absorption changes induced by the pump is monitored by a second weak probe generated by a CW light source. The pump pulses are provided by a nanosecond tuneable OPOLett-355II laser. The probe light is provided by a pulsed Xenon arc lamp. The sample was kept at a 45° angle to the excitation beam. The beams are focused on the sample ensuring the spatial overlap. The transmitted probe signal is spectrally filtered by a monochromator and detected. Two different detection systems are used: a cooled ICCD camera which enables the detection of the entire spectral range from 350 nm to 850 nm at once and a set of photomultipliers (with both VIS and near-IR detection window from 400 nm to 2000 nm) enabling us to collect the single-wavelength kinetic with higher sensitivity. The signal is finally recorded by a TDS 3032C digital signal analyzer. From the transmission change upon photo-excitation, the variation in the absorption is thus derived as a function of pump-probe delay τ and wavelength λ as:

$$\Delta O.D.(\tau,\lambda) = \log\left(\frac{I_{\text{probe}}}{I_{\text{trans}}(\tau,\lambda)}\right) \qquad \text{Eq. 3-34}$$

where I_{probe} is the intensity of the transmitted probe signal with excitation off and I_{trans} is the transmitted intensity after laser excitation. Alternatively, the normalised differential transmission is shown:

$$\frac{\Delta T}{T}(\tau,\lambda) = \frac{T^{\text{on}}_{\text{pump}} - T^{\text{off}}_{\text{pump}}}{T^{\text{off}}_{\text{pump}}}. \qquad \text{Eq. 3-35}$$

The system has sensitivity of $5\text{x}10^{-4}$ and a time resolution of 7 ns for the VIS photomultiplier, and around 70 ns for the IR detector.

3.5.5.1.2 Femtosecond Transient Absorption (TA) Measurements

Femtosecond TA measurements were taken by a setup driven by a 1 KHz repetition rate pulse at λ = 780 nm with 150 fs pulse width, coming from a regeneratively amplified mode locked Ti:sapphire laser (Clark-MXR Model CPA-1). A fraction of this beam is used as the excitation pulse at 390 nm wavelength due to second harmonic generation in a non linear crystal. Another small fraction of the laser light is focused into a 2 mm thick sapphire plate to generate a stable single-filament white-light supercontinuum, which serves as a probe pulse, spanning in

wavelength from 400 to 1000 nm. The pump and probe beams are spatially and temporally overlapped on the sample, controlling the time delay by a motorised slit. The minimum detectable signal is $\Delta T/T \sim 10^{-4}$. The system has a ~ 150 fs temporal resolution. The pump beam energy density used in the experiment is kept deliberately low (10-50 nJ, 300 μm beam size). All the measurements were taken with the samples in a vacuum chamber to prevent any influence from oxygen or sample degradation.

3.5.5.2 Nanosecond TA measurements

3.5.5.2.1 MDMO-PPV and MDMO-PPV + Ir-complex

First the excitation was tuned to 500 nm, i.e. the absorption peak of MDMO-PPV. Figure 3-42 shows the comparison of the transient absorption (TA) spectra integrated in the first 100 ns using the ICCD detection. The pure MDMO-PPV shows a broad photo bleaching (PB) feature (negative $\Delta O.D.$) in fair accordance with its absorption spectrum. We see two peaks, at around 500 nm and at the shorter wavelength side. At the red side of the spectrum (see also Figure 3-43a), a slightly positive signal appears due to the tail of the Triplet $T_1 \rightarrow T_n$ absorption band of the MDMO-PPV peaking around 900 nm.[183]

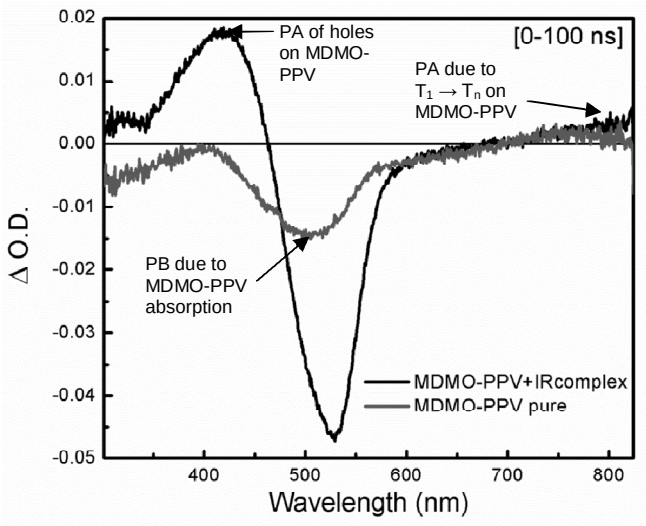

Figure 3-42. Comparison of the TA spectra in the visible region for pure MDMO-PPV (grey) and for the MDMO-PPV + Ir-complex (black) integrated in the first 100 ns temporal window. Figure courtesy of Giulia Grancini, Center for Nano Science and Technology@PoliMi, Istituto Italiano di Tecnologia.

The TA spectrum of the MDMO-PPV with the Ir-complex shows again the PB and the photo-induced absorption (PA) due to triplet absorption and a new positive band peaking at 400 nm

appears. This band can be assigned to polaron photo-induced absorption (hole in the MDMO-PPV), as it is also observed when the MDMO-PPV is blended with $PC_{61}BM$. This demonstrates that an electron transfer occurs between the MDMO-PPV and the Ir-complex, as suggested by the dashed energy level scheme in Figure 3-31 on page 134.

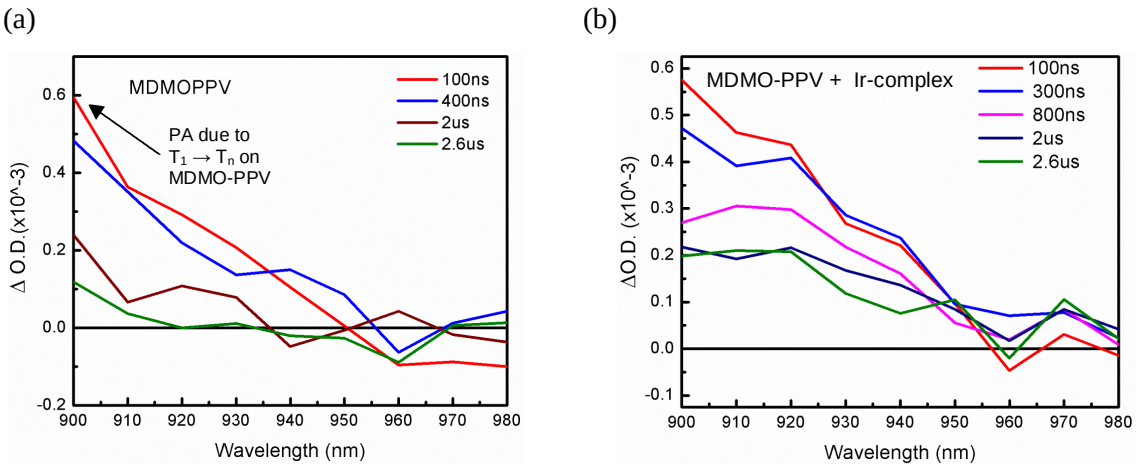

Figure 3-43. TA spectra in the near IR region for (a) the pure MDMO-PPV sample and (b) for MDMO-PPV + 2.5% Ir-complex. Every scan is integrated over 100 ns. Note that the instrument sensitivity is around $2x10^{-4}$, so the data in the red edge are within the noise.

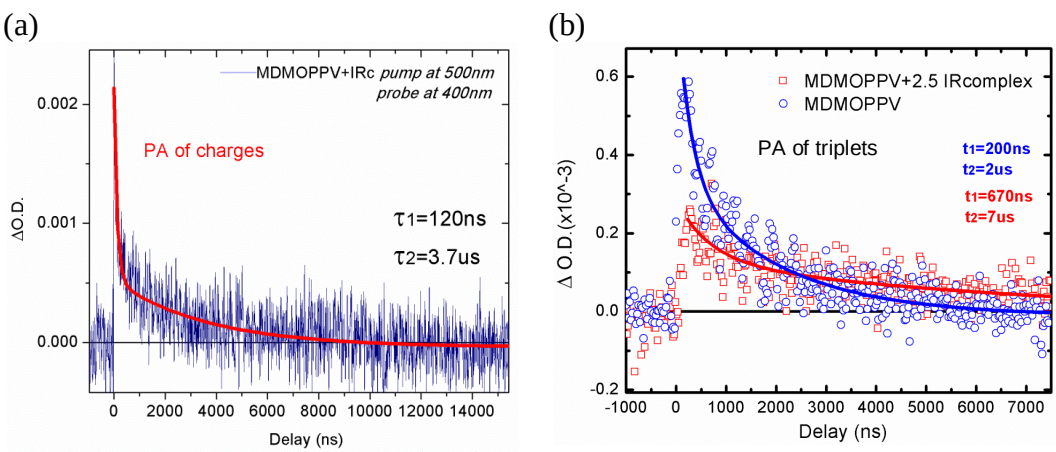

Figure 3-44. (a) Dynamics at 400 nm probe wavelength of the MDMO-PPV + Ir-complex. (b) TA dynamic for the MDMO-PPV + 2.5% Ir-complex at a 920 nm probe wavelength upon 500 nm excitation in the first 10 µs time window. Figures courtesy of Giulia Grancini, Center for Nano Science and Technology@PoliMi, Istituto Italiano di Tecnologia.

On the other hand one should notice that the TA spectra of the MDMO-PPV + 2.5% Ir-complex still shows the PA band around 900 nm. However, it exhibits a different decay, with a very long-living component, as also demonstrated by the dynamics in Figure 3-44b.

Upon exciting at 500 nm one mainly pumps the MDMO-PPV, however, also the Ir-complex is excited. Two possible routes may be opened. When the MDMO-PPV is excited, a fast charge-transfer channel is opened at the interface with the Ir-complex, as the PA band due to holes in

the MDMO-PPV reveals. This suggests that an interfacial CT state (or possibly polaron pair) is formed and is a preferential channel upon S_1 excitation. However, the CT has a lifetime of a few microseconds, whereas the triplet band has a much longer one, indicating that another state may feed the triplet of the MDMO-PPV. At 500 nm the Ir-complex is also excited. Upon fast ISC a triplet-triplet Dexter transfer can occur in the longer timescale from the Ir-complex to the MDMO-PPV, thus explaining the longer triplet lifetime. Note that the triplet lifetime in the Ir-complex alone still needs to be measured to better confirm this, and that according to a rough calculation ($E_{CT} \sim |E_{HOMO}^{polymer} - E_{LUMO}^{guest}| = 5.3eV - 3.39eV = 1.91$ eV, and polymer triplet level at $E(T_1) \sim 1.6$ eV), the interfacial CT state between the MDMO-PPV and Ir-complex is at a higher energy than the polymer T_1 state, thus the CT state can also recombine into the T_1 state. Note that the lower lying T_1 state is also in agreement with the observation that within the polymer:guest blend, the time decay of charges is faster (3.7 µs) than that of the T_1 state on the polymer (7 µs).

3.5.5.2.2 Addition of $PC_{61}BM$ to the Blends

The spectrum of the blend in the range between 350 and 800 nm (Figure 3-45a) shows the PB of the MDMO-PPV and the positive band at 400 nm due to PA of charges in the MDMO-PPV upon electron transfer at the interface with the fullerene. No feature of PA of charges are present in the 700 nm region (as observed with ultrafast TA), maybe due to a very small signal. No PA feature in the 920 nm region is observed, indicating that the triplet pathway is quenched by the opening of a charge transfer path at the interface with the $PC_{61}BM$ (as also reported in the literature[112]). In particular we observe in Figure 3-45b a broad negative feature peaking at 1000 nm that has been previously assigned[184] to a radiative charge transfer recombination at the polymer:fullerene interface.

Indeed, it has been suggested[112] that the triplet of the polymer lies above the CT state formed at the MDMO-PPV:$PC_{61}BM$ interface, thus it can recombine to the emissive CT state. Note that with the fs TA one can see that the band at around 800 to 900 nm is quenched in the first 400 ps. If assigned to $T_1 \rightarrow T_n$ PA, already existing in the ps time regime, it is possibly feeding the emissive CT state (see later discussion).

When the Ir-complex is added to the blend in the spectral range between 350 and 800 nm (Figure 3-45c), a similar scenario is detected. The PB and the PA band due to charges at shorter wavelength side is again observed. In this case, however, a very small triplet population might be present upon excitation of the Ir-complex and triplet-triplet energy transfer.

After 100 ns in the NIR region (900 to 1200 nm, see Figure 3-45d) the spectrum is similar to the one of the MDMO-PPV:$PC_{61}BM$, one can still observe the stimulated emission (SE) from the interfacial CT state as the main pathway of recombination. However, a closer look at the dynamics at 910 nm (in Figure 3-46) shows that there is a fast initial positive signal that can be assigned to the $T_1 \rightarrow T_n$ PA of the MDMO-PPV that is then quenched by the formation of the emissive band of the interfacial CT state that is very long lived (still there at 100 µs). This may indicate that the triplet excitations "indirectly" generated in the polymer contribute to the CT state at the polymer/fullerene interface. Note that triplet states cannot be populated by ISC upon excitation of the S_1 state of the polymer as charge transfer would be favoured.

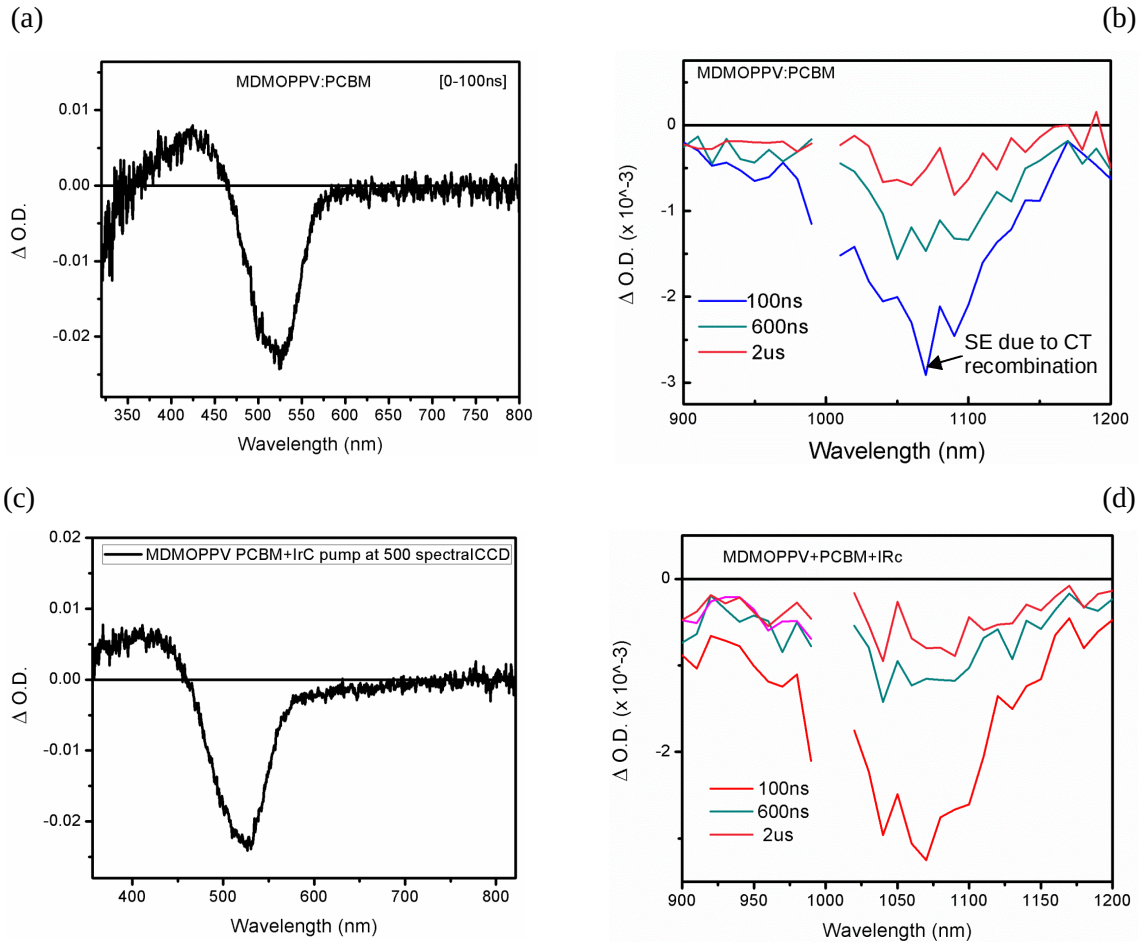

Figure 3-45. TA spectra in the visible (a) and near IR region (b) for the MDMO-PPV:$PC_{61}BM$ blend and for MDMO-PPV:$PC_{61}BM$ + 2.5% Ir-complex (c and d). The TA spectra at the shorter wavelengths (a and c) were recorded with the ICCD from 0 to 100 ns after excitation. Figures courtesy of Giulia Grancini, Center for Nano Science and Technology@PoliMi, Istituto Italiano di Tecnologia.

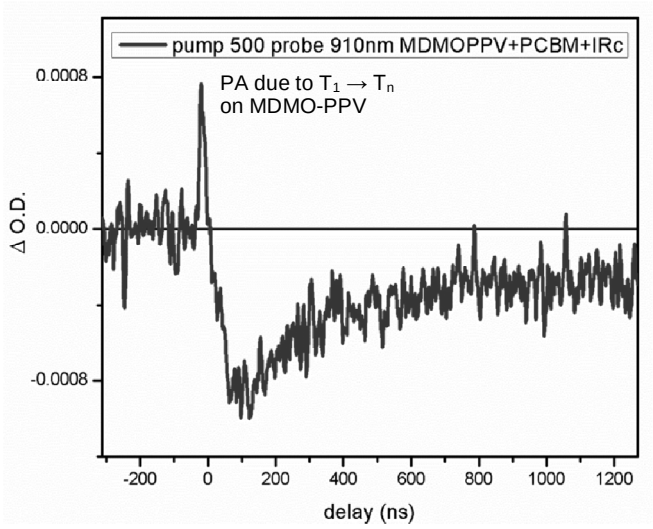

Figure 3-46. TA dynamics at 910 nm for the MDMO-PPV:PCBM + 2.5% Ir-complex, probing the triplet PA on the polymer. A positive signal is observed that may then be quenched by the formation of a CT state with $PC_{61}BM$. Figure courtesy of Giulia Grancini, Center for Nano Science and Technology@PoliMi, Istituto Italiano di Tecnologia.

3.5.5.3 Femtosecond TA Measurements

The results of the fs TA experiments are shown in Figure 3-47. We observe:

- the PB of the MDMO-PPV around 500 nm, and
- a broad singlet PA band in the NIR region peaking around 980 nm decaying during the first hundreds of picoseconds. The residual band around 800 to 900 nm can be due to PA of triplets.

The two spectra are quite similar, however, it is noted that at around 800 nm one can observe for the MDMO-PPV:Ir-complex system a slightly longer lived dynamics (see Figure 3-48), maybe due to longer lived triplet species, in agreement with the ns data.

In the NIR (see Figure 3-49) we can observe the MDMO-PPV singlet absorption peaking at 950 nm. One may note that in presence of the Ir-complex there is a stronger contribution around 800 to 850 nm. A possible initial absorption of triplets may be considered; the triplets quickly recombine feeding the emissive CT state.

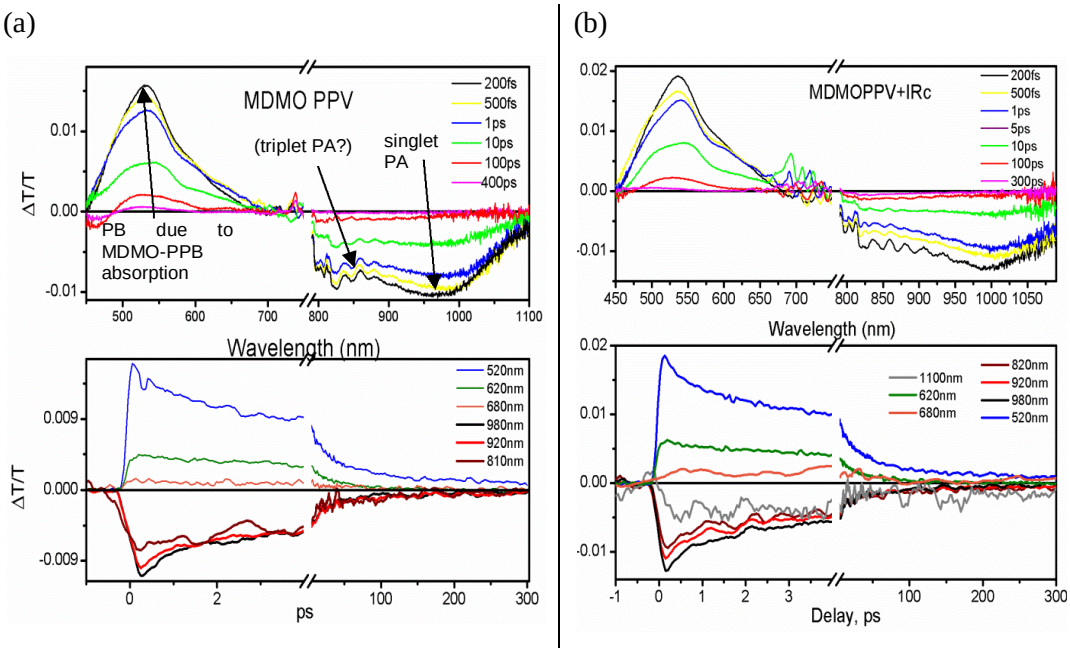

Figure 3-47. TA spectra and time decay in the visible and near IR region for MDMO-PPV (a) and MDMO-PPV + 2.5% Ir-complex (b). Note that now we measure the differential transmission. Figures courtesy of Giulia Grancini, Center for Nano Science and Technology@PoliMi, Istituto Italiano di Tecnologia.

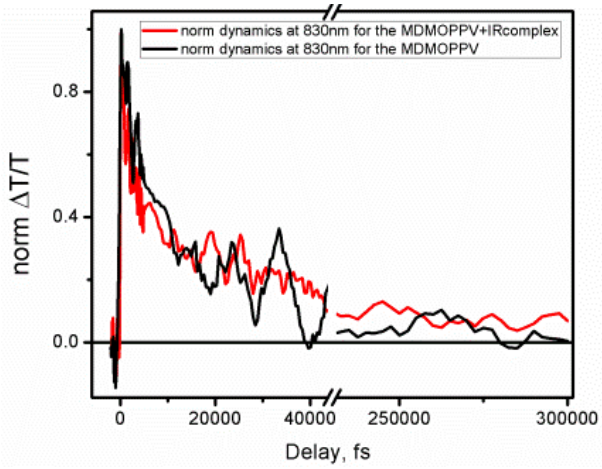

Figure 3-48. Normalised differential transmission time decay at 830 nm for MDMO-PPV and MDMO-PPV + Ir-complex. Figure courtesy of Giulia Grancini, Center for Nano Science and Technology@PoliMi, Istituto Italiano di Tecnologia.

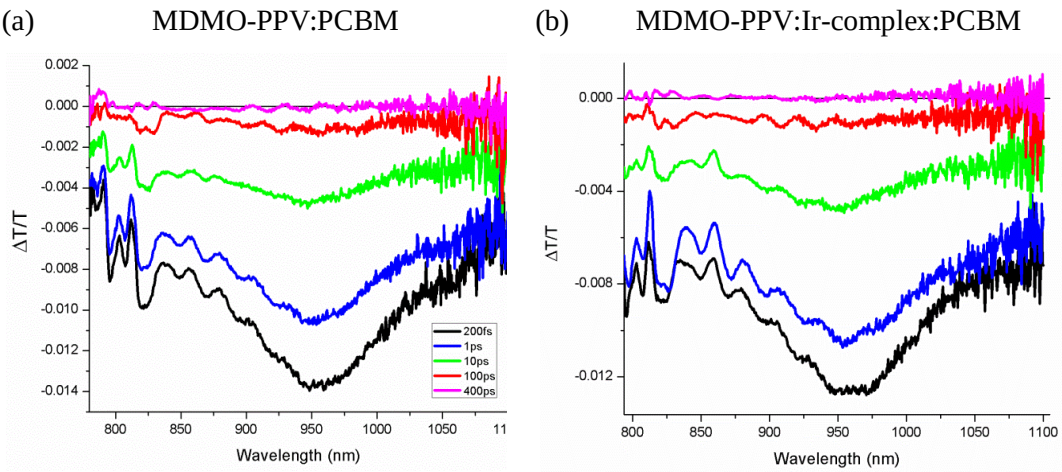

Figure 3-49. TA spectra in the NIR region for (a) MDMO-PPV + $PC_{61}BM$ and (b) MDMO-PPV + 2.5% Ir-complex + $PC_{61}BM$, probing the PA signal due to singlet absorption. Figures courtesy of Giulia Grancini, Center for Nano Science and Technology@PoliMi, Istituto Italiano di Tecnologia.

3.5.5.4 Conclusion of TA Measurements

The main results from the photo-induced absorption experiments are the following: First, the TA measurements indicate that triplet transfer occurs from the guest to the donor. Also, the TA measurements suggests the occurrence of holes on MDMO-PPV upon adding the guest, meaning that upon photoabsorption, exciton dissociation occurs at the polymer/guest interface leading to electron transfer to the guest. Note that the desired route was either charge transfer of both electron and hole, or Förster transfer from the donor to the Ir-complex.

It is also observed that the T_1 state of the donor seems to be positioned below the CT state between MDMO-PPV and the Ir-complex, and that the CT state between the polymer and the fullerene is below the T_1 state of the polymer, hence providing a mechanism for charge separation from the triplet state. The results of the TA experiments are summarised in Figure 3-50.

Note that Förster transfer from the donor to the guest cannot be excluded because by exciting the polymer at 500 nm, one also excites the Ir-complex. It is hence difficult to disentangle from fs TA measurements whether the dynamics of the Ir-complex are due to its excitation or to ultrafast energy transfer from the polymer. However, no clear rise of the PB of the Ir-complex, which should proof the Förster transfer, was observed.

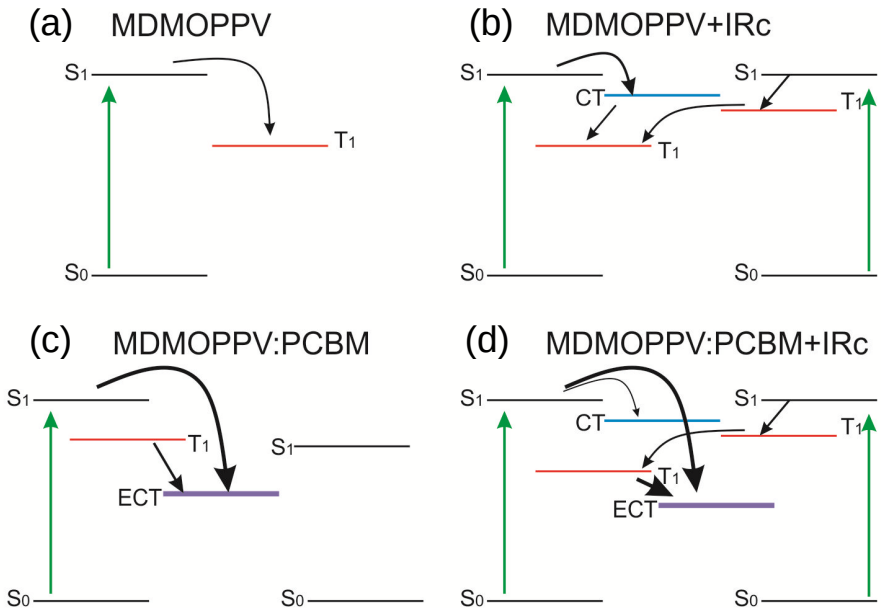

Figure 3-50. Possible pathways observed via TA experiments. IRc stands for Ir-complex. (a) ISC ($S_1 \rightarrow T_1$) in MDMO-PPV. (b) The Ir-complex was also directly excited leading to a T_1 state on the complex, which is then feeding the T_1 state on MDMO-PPV. A CT state is formed at the interface between the polymer and the metal complex leading to charge separation. A part of the CT states transitions into the T_1 state on the polymer. (c) Charge transfer occurring at the interface with $PC_{61}BM$. (d) In the ternary blend the charge separation at the polymer:$PC_{61}BM$ interface is the dominant mechanism. However, feeding of the polymer T_1 state is still observed. Figure courtesy of Giulia Grancini, Center for Nano Science and Technology@PoliMi, Istituto Italiano di Tecnologia.

3.5.6 Discussion

We have so far established that the addition of the triplet emitter to the SC's active layer led to an improvement of J_{SC} for overannealed blend devices and for bilayer devices. Also, in the latter case, we found that the increase in J_{SC} stems from an increase in the number of excitons harvested by the polymer. These results are hence consistent with an increase in the exciton diffusion length.

In the following we will consider the effect of intercalation of polymer and fullerene and try to understand in more detail the different influence of the guest on blend and bilayer devices.

3.5.6.1 Intercalation

3.5.6.1.1 What is Fullerene Intercalation

An aspect of polymer-fullerene SCs which was not discussed in this work so far is (fullerene) intercalation. *Intercalation* is the interdigitation of fullerenes with a polymer, whereas the fullerene fits into the gaps between the polymer side-chains (see for example Figure 3-51). The following information about intercalation is mainly taken from Mayer et al..[185]

Whether a fullerene intercalates or not depends on the size of the fullerene and the free volume between the polymer side chains. As one can imagine, intercalation strongly affects exciton dissociation, recombination and charge transport. It explains among others

- why PL is completely quenched in some polymer-fullerene systems (in those where intercalation occurs),
- why large-scale phase separation occurs in some polymer:fullerene blend ratios while thermodynamically stable mixing on the molecular scale occurs for others, and
- why the hole mobility of MDMO-PPV increases by over two orders of magnitude when blended with $PC_{61}BM$.[186]

It is interesting to note that the optimum polymer:fullerene blend contains much more $PC_{61}BM$ (about 1:4 weight ratio) when intercalation occurs as opposed to when it does not (about 1:1). This is because in a 1:1 ratio, effectively all of the fullerenes will be interdigitated with polymers. Without further fullerenes, no continuous electron pathway can be achieved (see Figure 3-52). Note that the above ratios are weight ratios, not number ratios. Assuming roughly the same densities for polymers and fullerenes, this means that roughly the same volume of donor and acceptor is needed for non-intercalating blends. If we look at the number ratio of intercalating blends, i.e. the number ratio of donor repeating units to acceptor molecules, one finds for example for MDMO-PPV and $PC_{61}BM$ with molecular weights of 288.42 and 910.88 g mol^{-1} that a 1:4 donor:acceptor weight ratio translates into a 1:1.3 number ratio. This means that at such a "high" fullerene concentration, one has enough fullerenes to fill all donor side chain gaps, with some extra fullerene molecules left to help electron conduction.

The first material system in this chapter, i.e. P3HT:$PC_{61}BM$, does not intercalate[185] whereas the material system in this section, i.e. MDMO-PPV:$PC_{61}BM$, does seem to intercalate in non-annealed blends (see next section).

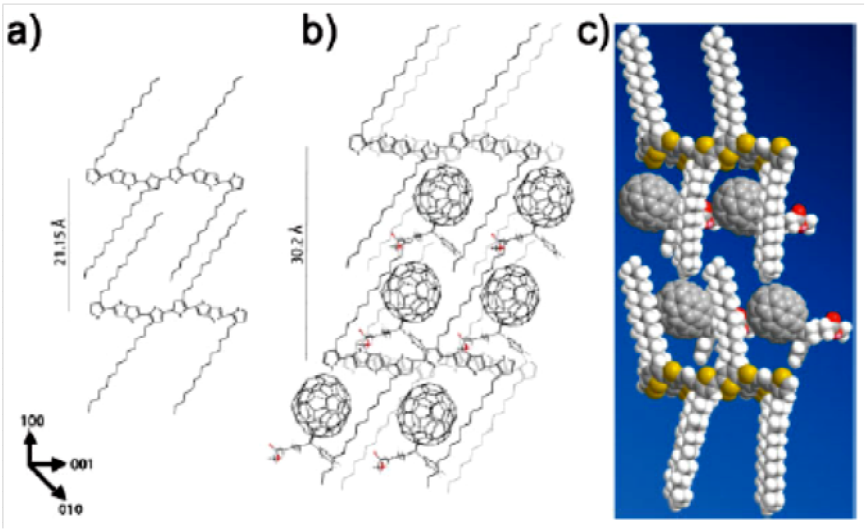

Figure 3-51. Intercalation of PBTTT (poly(2,5-bis(3-tetradecylthiophen2-yl)thieno[3,2-b]thiophene) with $PC_{71}BM$ (phenyl-c71-butyric acid methyl ester). Image reprinted with permission from Mayer et al.,[185] Copyright (2009) WILEY-VCH Verlag GmbH & Co. KGaA, Weinheim.

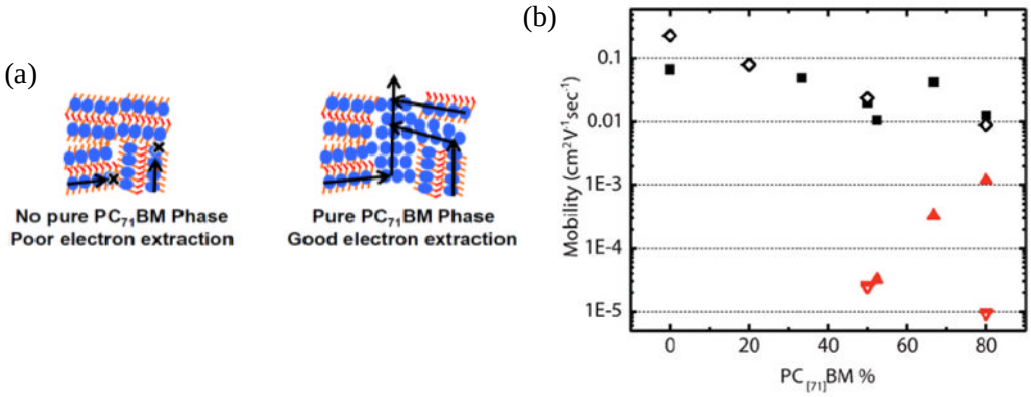

Figure 3-52. Effect of intercalation on charge transport for a PBTTT:$PC_{71}BM$ blend. (a) Due to intercalation a higher fullerene ratio is needed to facilitate electron transport. (b) The electron mobility goes up to measureable values from 50% fullerene concentration (*not* weight %). Points in black are hole mobilities, points in red electron mobilities. Image reprinted with permission from Mayer et al.,[185] Copyright (2009) WILEY-VCH Verlag GmbH & Co. KGaA, Weinheim.

3.5.6.1.2 Literature on MDMO-PPV:$PC_{61}BM$ Blends

There is a lot of evidence that blends of MDMO-PPV:$PC_{61}BM$ intercalate. If we look for example at Figure 3-53a, we see that charge generation is ultrafast, in the region of ~100 fs. Furthermore, let us look at the SEM images[187] in Figure 3-53b. There one can see that the type of tiny domains formed in a 1:1 blend of MDMO-PPV:$PC_{61}BM$ is also found in a 1:4 ratio whereas here they are surrounding the big $PC_{61}BM$ clusters. We can understand this under the assumption of intercalation, where the small spheres in the 1:1 blend are domains of intercalated

bimolecular crystals. At higher fullerene loading, pure $PC_{61}BM$ clusters form which are surrounded by the intercalated bimolecular crystals, exactly what is expected for intercalated blends. Another indicator for intercalation, the optimum fullerene ratio for SCs of 1:4, is fulfilled.

Despite the evidence that intercalation occurs in a non-annealed MDMO-PPV:$PC_{61}BM$ blend, it is not clear what happens in annealed blends. According to Cates et al.,[186] there is strong evidence that phase separation occurs even in 1:1 donor:acceptor blends (a weight ratio at which there are about three times more repeating units than $PC_{61}BM$ molecules) if they are annealed. An AFM image of a 1:1 blend annealed at 130 °C is shown in Figure 3-54. Also, the annealed blends showed incomplete PL quenching,[186] which is a strong sign for incomplete intercalation (at least for good acceptor materials such as $PC_{61}BM$).

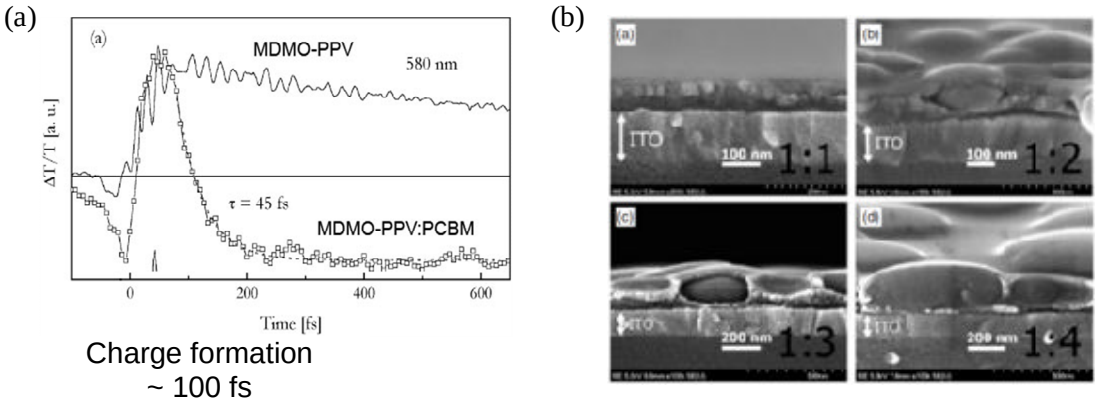

Figure 3-53. Evidence that $PC_{61}BM$ 'usually' intercalates with MDMO-PPV. (a) Ultrafast charge formation after ~100 fs. Images reprinted (adapted) from Brabec et al.,[188] Copyright (2001) Elsevier. (b) SEM images of MDMO-PPV:$PC_{61}BM$ blends cast from toluene. The spheres (20-30 nm in diameter) which can be seen for a 1:1 ratio are surrounding the larger discs for blends with a higher fullerene ratio. Image reprinted from Hoppe et al.,[187] Copyright (2004) WILEY-VCH Verlag GmbH & Co. KGaA, Weinheim.

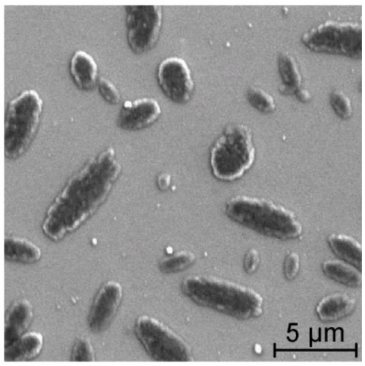

Figure 3-54. AFM image of an annealed (130 °C, 1 h) 1:1 MDMO-PPV:$PC_{61}BM$ blend showing clear phase separation. Figure reprinted with permission from Cates et al.,[186] Copyright (2010) American Chemical Society.

3.5.6.1.3 Impact of Intercalation on this Work

Complete intercalation of donor and acceptor renders the idea of increasing the exciton diffusion length (by converting singlet to triplet excitons) useless as intercalation implies the presence of acceptor molecules less than a nanometre away from where the exciton was generated. It hence comes down to the question of how mixed/intercalated the polymer is with $PC_{61}BM$. As mentioned above, MDMO-PPV showed PL if the blend is annealed at the correct temperature[186] meaning that there must exist somewhat purer donor domains in which the excitons cannot diffuse far enough to an interface with $PC_{61}BM$. If most of the donor molecules are distributed in these donor-rich domains, the improvement of excitons diffusion length via triplet excitons would be beneficial (of course under the assumption that triplet excitons are efficiently split at donor-acceptor interfaces).

Note that despite potential intercalation in a 1:1 MDMO-PPV:$PC_{61}BM$ blend, Rand et al[126] claimed that, similar to the approach attempted here, an increase of the number of triplet excitons, due to the addition of a phosphorescent guest, led to an increased J_{SC}.

Another question to be answered is how perfect the fabricated bilayers are with respect to flatness of the interface and the avoiding of interdiffusion. The crosslinker FPA was shown to crosslink quite well the donor polymer in terms of film retention upon spin rinsing in a good solvent (chlorobenzene), with over 90% of the material remaining if 10 wt% of the crosslinker was added. However, it is not clear how much $PC_{61}BM$ can diffuse and intercalate with crosslinked MDMO-PPV. A first step to answering this question may be to find out how many crosslinker molecules (N(FPA)) there are for each donor repeating unit (N(RU)). In the following, I estimate this ratio, where M is the molecular mass, u the unified atomic mass unit, N is the number of molecules and r is the weight ratio of the crosslinker (10 %).

$$\frac{N(\mathrm{FPA})}{N(\mathrm{RU})} = \frac{\frac{m(\mathrm{FPA})}{M(\mathrm{FPA})}}{\frac{m(\mathrm{PPV})}{M(\mathrm{RU})}} = r \cdot \frac{M(\mathrm{RU})}{M(\mathrm{FPA})} = 10\% \cdot \frac{247u}{304u} \approx 0.081 \qquad \text{Eq. 3-36}$$

From this calculation we find that for each repeating unit, there are 0.081 crosslinker molecules, or vice versa, for each crosslinker molecule, there are about 12 repeating units. A crosslinker molecule will take up space between two side chains (of two repeating units) and may block $PC_{61}BM$ molecules in that region. Hence roughly every 6th side chain will be attached to a crosslinker molecule. This short analysis shows that there will be many repeating units which do

not have a crosslinker molecule attached to them, potentially allowing $PC_{61}BM$ molecules to take up the position in between side chains.

On the other hand, maybe it is sufficient to stiffen the polymer chains in order to hinder $PC_{61}BM$ diffusion into the space between the side chains.

3.5.6.1.4 PLQE Measurements

Under the assumption that the exciton diffusion length is very small and that the number of excitons lost due to non-radiative decays is independent of the guest, the easiest way of getting an idea of intercalation may be via PLQE (photoluminescence quantum efficiency) experiments. The higher the PLQE of a donor:acceptor blend, the more excitons cannot reach the interface (or reach the interface and do not separate, but that can be ruled out for this well-known material system) and the lower is the degree of intercalation. Also, whether or not energy transfer occurs from MDMO-PPV to the guest can be indicated by PLQE measurements, which are shown in Table 3-5.

We see that the PLQE of a pure MDMO-PPV layer was 17%. (The PLQE of a very similar polymer, poly[2-methoxy-5-(2-ethylhexyloxy)-1,4-phenylenevinylene][1], MEH-PPV, was found[187,188] to be between 10 and 24%.[189,190] Adding the phosphorescent guest reduced the PLQE further to about 4%, which could either mean

i. a type II heterojunction is in place and separating the charges (or at least populate a CT state between MDMO-PPV and the guest), or
ii. energy transfer occurs from the donor to the guest, or
iii. the guest increases the non-radiative decay rate of excitons on the donor.

(i) Looking at the HOMO/LUMO levels (on page 134), it may be possible that electrons transfer to the guest while holes remain on the polymer. The electron transfer from MDMO-PPV to the guest may explain the existent, but small, influence of the guest on charge transport in fabricated SCs. This hypothesis is further supported by the transient absorption spectroscopy presented in section 3.5.5 on page 148.

(ii) Due to the lack of PL from the guest we can deduce that if energy is transferred from the polymer to the guest (the desired mechanism), most of the excitons must have been back transferred to the polymer triplet state.

Table 3-5. Photoluminescence quantum efficiency (PLQE) measurements in solid films at room temperature in air with a laser excitation at 412 nm. If not mentioned otherwise, samples are irradiated from the material side (as opposed to from the glass side). Films were spin coated from chlorobenzene (CB) or toluene.

Film composition	PLQE
MDMO-PPV from toluene	17%
MDMO-PPV from toluene, 5% Ir compound	4.2%
pure MDMO-PPV + FPA (from CB)	11%
after development next day (day 3) (75 °C for 10 min, UV 10 min, spin rinsing 2x)	9.5%
bilayer MDMO-PPV + FPA + $PC_{61}BM$ from CB	0.1%
bilayer MDMO-PPV + FPA + $PC_{61}BM$ from CB, 5% Ir compound	0.3%
bilayer MDMO-PPV + FPA + $PC_{61}BM$ from CB, annealing at 140 °C for 10 min	0.1%
bilayer MDMO-PPV + FPA + $PC_{61}BM$ from CB, 5% Ir compound, annealing at 140 °C for 10 min,	0.2%
bilayer MDMO-PPV + FPA + $PC_{61}BM$ from CB on PEDOT/ITO	0.3%
bilayer MDMO-PPV + FPA + $PC_{61}BM$ from CB on PEDOT/ITO, irradiated from glass side	0.6%
1:4 blend from toluene	0
after annealing at 140 °C for 10 min (day 3)	~0
1:4 blend from toluene, 5% Ir compound	0
after annealing at 140 °C for 10 min (day 3)	0
1:4 blend from toluene, 90 °C for 10 min	0
1:4 blend from toluene, 90 °C for 10 min, 5% Ir compound	0
1:4 blend from CB	~0
1:4 blend from CB, 5% Ir compound	0
1:1 blend from toluene, unbaked	0.4%
after annealing at 90 °C	0.6%
after annealing at 130 °C	1.1%
2:1 blend from toluene, unbaked	0.4%
after annealing at 90 °C	0.5%
after annealing at 130 °C	0.7%

The bilayers show measurable PLQEs, but they are surprisingly low and did not exceed 0.3% when the laser beam entered the sample from the material side. This is rather surprising, even considering that the laser light will be partially absorbed by $PC_{61}BM$ before it reaches the MDMO-PPV. The AFM images of these films are shown in Figure 3-39 on page 145. The donor layers are 56 ± 10 nm thick and one would expect incomplete PL quenching due to the singlet exciton diffusion length of less than 10 nm.[182] Also, the AFM images suggest that the MDMO-PPV layer is only partially covered with $PC_{61}BM$, with apparently $PC_{61}BM$ -free regions in form of "petals". However, even in these petals, the MDMO-PPV may be interdigitated with $PC_{61}BM$.

For a laser beam entering the bilayer sample from the ITO side, a PLQE of 0.6% was measured. Interdiffusion of $PC_{61}BM$ into the MDMO-PPV layer can explain this difference in PLQE when we assume the Beer-Lambert absorption law and a rather fullerene free donor layer close to the glass side. The PLQE obtained via the beam entering the sample from the glass side is of course more closely related to the device performance as the solar simulator light also irradiates the sample from this direction.

3.5.6.1.5 Intercalation vs. Phase Separation in Blends

As we saw in Figure 3-38a, there is an optimum temperature of 70 °C for the (1:4) polymer-fullerene devices. The loss of performance above that temperature may be attributed to a reduction of intercalation and an increasing ratio of pure polymer domains. It was already mentioned that the effective mean diameter of the $PC_{61}BM$ cluster increased by about 23% by annealing the substrate to 90 °C.

Therefore, let us now try to answer the following question: Assuming 100% of the polymer is intercalated prior to annealing at a certain weight ratio of PCBM c_1, what would be the maximum increase of the $PC_{61}BM$ cluster diameter if complete phase separation occurred upon annealing at the concentration c_2 used in these experiments?

Let us start by assuming that at 67 wt% $PC_{61}BM$, 100% of the polymer is intercalated. This is a lower boundary according to Cates et al..[186] (Using the molecular weights mentioned earlier and a number ratio of 1:1, one obtains 100% intercalation at 76 wt% of $PC_{61}BM$). The 67 wt% correspond to a donor:acceptor weight ratio of 1:2. In my devices, a 1:4 ratio was used, so that the mass of clustered PCBM equals the mass of intercalated PCBM at room temperature (assuming 100% intercalation). That means if complete phase separation occurred upon annealing, the volume of those PCBM clusters would increase by a factor of 2. A volume

increase of 2 corresponds to an increase in radius or diameter of $2^{1/3} = 1.26$ for a perfect sphere. This means that assuming $PC_{61}BM$ clusters are perfect spheres, a more than 26% increase in mean effective grain radius/diameter upon annealing is not possible. For flat cylinders of constant height, the maximum possible increase of the mean effective grain radius/diameter is 41%.

Our measured increase of 23% upon annealing hence indicates that considerable amount of $PC_{61}BM$ becomes "deintercalated" (i.e. phase separated from the donor) upon baking the blend at ~90 °C. Note that the measured PLQEs of ~0% do not support this approximation.

3.5.6.2 Influence of the Guest on J_{SC} and IPCE spectra

3.5.6.2.1 Blend Devices

Within the BHJ SCs we only saw (see Figure 3-38) an increase in J_{SC} upon adding the guest for blends annealed at a rather high temperature of 90 °C and not for 70 °C, which was the optimum temperature for the reference cell (without guest content). This result is as expected under the hypothesis that we improved the exciton diffusion length: As the morphology of a blend annealed at 70 °C is optimized for singlet excitons, an increase in exciton diffusion length can be small or even negligible, whereas at 90 °C we expect less intercalation and instead the occurrence of pure or at least purer polymer domains which could indeed benefit from an increase in the exciton diffusion length.

However, the IPCE spectra (not shown) do not show a clear increase in the range of the MDMO-PPV absorption, which means that the IPCE originating from PCBM was also increased upon addition of the triplet emitter or that the increase in performance is the result of other factors, such as charge transport, charge recombination and morphology.

Furthermore, we observed an increase of the domain size of the $PC_{61}BM$ clusters for the blend devices annealed at 90 °C of about 15% upon adding 5 wt% of the guest, indicating that adding the guest promotes phase separation. As at 90 °C one is well beyond the optimum temperature of 70 °C for guest-free devices, further phase separation is expected to affect the devices negatively, in particular it is expected to reduce J_{SC} due to the reduction of donor/acceptor interfacial area and to the decrease of the hole mobility in the non-intercalated donor regions. The occurrence of larger clusters at high guest concentrations may hence explain the reduction of J_{SC} if the increase in exciton diffusion length cannot compensate the above effects. Also, if electron transfer from the donor to the guest, as observed via TA measurements, is indeed quite

efficient, electrons are likely to be trapped on the guest unless the $PC_{61}BM$ molecules are in close proximity.

3.5.6.2.2 Bilayer Devices

Regarding bilayer devices, we saw from the JV curves in the dark (see Figure 3-40a) a small negative influence of the guest on charge transport. Nevertheless, as expected from an increase in the exciton diffusion length and a subsequently higher ratio of dissociated excitons, J_{SC} was improved upon adding the guest.

The IPCE spectra are also in agreement with an increase of the exciton diffusion length in the polymer layer as they show an increase of the photocurrent in the range of the MDMO-PPV absorption (at ~450 nm). Note that although the photocurrent peak stemming from the $PC_{61}BM$ absorption is reduced, J_{SC} is increased because high values near the MDMO-PPV absorption are more important than those near the $PC_{61}BM$ absorption due to the stronger solar irradiance at higher wavelengths.

A question remaining is why the IPCE peak of $PC_{61}BM$ was reduced upon adding the guest. Several effects can to be considered:

a) The Ir-complex creates a type-II heterojunction with $PC_{61}BM$. Excitons generated on $PC_{61}BM$ may hence dissociate at the guest interface with the result of a trapped hole on the guest. This trapped hole can then only be released upon light absorption or when the guest is located at the interface with MDMO-PPV. As the triplet emitter was added to the polymer layer, one can assume the latter is indeed the case, i.e. that the guest will almost always find a polymer chain in close proximity. This effect should hence be negligible.
b) Another possible explanation would be the influence of the triplet emitter on charge transport. We have seen in Figure 3-40a that the triplet reduces the dark current. A reduction in hole conductivity would reduce the IPCE spectrum equally over the whole wavelength range and could, together with the increase of the MDMO-PPV IPCE peak, explain the spectrum.
c) It is noted that the reduction of the $PC_{61}BM$ IPCE peak cannot be solely explained by detrimental light absorption in this range via the small number of guest molecules. Light scattering at guest molecules, however, may add to the effect of direct light absorption and play a role. (No quantitative investigation was attempted as it is not clear how and where the guest molecules aggregate).

Also noteworthy, a similar trend in the SC behaviour to that observed in bilayers can be observed if the devices are not exposed to UV-light (see Figure 3-55). Therefore one may also suggest that the Ir-compound deactivates the crosslinker to some degree. In the following I will go into more detail regarding this hypothesis: When spin coating the polymer layer with a spin-speed of 4000 rpm, omitting the UV-exposure step lead to an approximately 8% thinner film as measured via absorption spectroscopy. Due to the spin-rinsing step we expect a slightly more porous film as more donor material is being washed away. Also, the missing crosslinking may allow more efficient intercalation. Hence we expect a larger donor-acceptor interface and a higher J_{SC} for such devices. Indeed, J_{SC} more than doubled if the UV exposure step was omitted and the main contribution stems from the MDMO-PPV layer as deduced from the corresponding IPCE curves. Also, a reduction in V_{OC} and a considerable reduction in the differential resistance at $V = 0$ (i.e. approximately the shunt-resistance under the framework of the equivalent SC circuit) was observed, which may be the result of increased non-geminate recombination due to the interpenetrating materials.

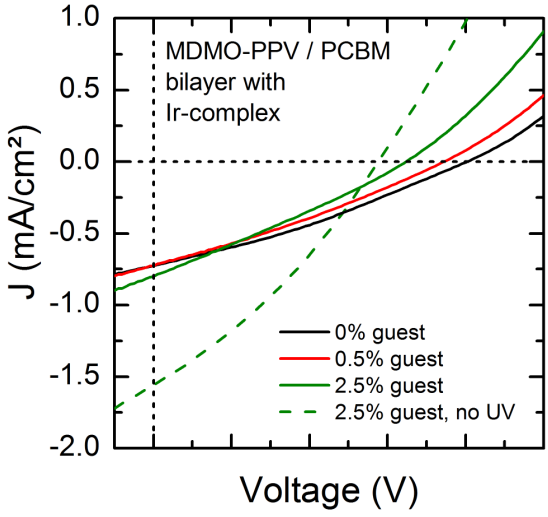

Figure 3-55. JV curve of devices under illumination. Compared are devices of different guest concentrations (black, red and green solid lines) with devices with 2.5% guest concentration where the UV-exposure step was omitted (green dashed line). The spin-speed for polymer and fullerene was 4000 and 1800 rpm, respectively.

3.5.6.3 Influence of the Guest on V_{OC} and FF

Using the same host materials and electrodes, changes in V_{OC} and *FF* upon addition of the triplet emitter are mainly determined by changes in the mobility, the field-dependence of exciton dissociation and non-geminate charge carrier recombination, which in turn depend on a variety of parameters such as the mobility, doping and density of the charge carriers (which in turn partly depend on the morphology). Interestingly, whereas there existed a doping load (1 wt%)

where V_{OC} and *FF* were improved for BHJ devices, no such region could be found in case of bilayer devices. Therefore we need to consider the different influences the guest may have on exciton dissociation and non-geminate charge recombination for the different device architectures. Such differences are for example:

a) For (ideal-) bilayer devices, bimolecular non-geminate charge recombination does not exist due to the separation of electrons and holes in the device architecture.

   Therefore, an increase in non-geminate charge recombination, as e.g. deduced from the reduced V_{OC} and *FF*, can only occur if the bilayer is not perfect, i.e. when $PC_{61}BM$ diffused into the donor layer. This means that either the bilayer is not perfect to start with and the guest acts as charge recombination centres, or the bilayer becomes less perfect due to guest. I noted earlier that the increase of J_{SC} and the MDMO-PPV IPCE peak may be the result of the guest somehow reducing the effectiveness of the crosslinker. This process would also explain the influence of the guest on V_{OC} and *FF*.

b) Exciton dissociation may be improved in bilayer devices due to a potential drop at the interface.[191]

   Although it was claimed for MDMO-PPV:$PC_{61}BM$ BHJ SCs that there is a considerable field dependence of exciton dissociation and that the ratio of dissociating bound electron-hole pairs is about 60% at room temperature,[121] it was later actually measured that electron-transfer from MDMO-PPV to $PC_{61}BM$ is ultrafast and that it is not an efficiency limiting factor in such devices,[192] essentially in agreement with an intercalated system. We may therefore assume that exciton dissociation is ideal for blend devices, especially those annealed below 70 °C, but may be worsened in bilayer devices upon adding the guest. As V_{OC} and *FF* decreased in bilayer devices, exciton dissociation may have worsened indeed upon addition of the guest. Kelvin probe measurements may give further evidence if a change of dipole at the interface occurs or not.

c) Traps

   HOMO/LUMO measurements (Figure 3-31) indicated a potential hole trapping on the Ir-guest. According to measurements by our group, the HOMO of the guest is about 0.3 eV above that of MDMO-PPV, and according to Rand et al.,[126] the HOMO is identical within the uncertainty of the measurements. Hence it was unclear whether the guest may act as a charge trap within the donor polymer or not. The TA measurements gave further evidence that upon photoabsorption on the polymer, electrons are transferred to the guest. The guest acting as a trap may explain why devices generally degrade at guest concentrations higher than ~5 wt%.

As shown in section 3.3.4.2 on page 98, upon the addition of trap states, the first part of the previously trap-free space-charge-limited dark current[139] is then replaced by a trap-filling regime,[139-141] in which the current increases according to a power law with an exponent larger than two. If traps are already present, and more traps with a different distribution are added, the exponent should change. A small change in the exponent (seen as the slope in the log(*J*)-log(*V*)) is indeed observed in the dark current (Figure 3-40a). Note that the slope decreased upon addition of the guest, suggesting that the new traps have a lower characteristic energy than those which were already present without the guest.

d) Mobility

The charge carrier mobility may be influenced by the guest due to charge trapping, intercalation, or by changing domain sizes of donor and acceptor.

We have seen for the blend devices an increase of the $PC_{61}BM$ cluster size upon adding the triplet emitter, indicating enhanced phase separation. This may actually lead to a reduced mobility as intercalated donor regions do show improved hole mobility compared to pure donor regions. A reduced mobility in blend devices would explain the increase in V_{OC} at 1 wt% guest concentration (as higher charge densities due to slower extraction times increase V_{OC}[158,162,163]) but not the increase in *FF*. Note that the dark JV curves (Figure 3-38e) do not indicate a reduction in mobility, which would be seen as a smaller increase in current in the trap-filling or space-charge-limited current regime.

In the bilayer devices we see a reduction of the dark current (Figure 3-40a) consistent with a reduced hole mobility. Note that although in ideal-bilayer devices, non-geminate bimolecular charge recombination should be negligible as mentioned in (a), this does not change the fact that a lower mobility is expected to reduce charge carrier extraction and hence increase V_{OC}. The observed reduction of V_{OC} must hence have other causes. As we found charge transfer from the donor to the guest, we create both type of charge carriers within the donor material, which is then expected to lead to bimolecular charge recombination and hence to a lower V_{OC}.

3.5.7 Conclusion

It was shown that, in agreement with an increased exciton diffusion length in the donor polymer, the addition of the optimum concentration of the phosphorescent guest led to:

(1) an improved J_{SC} for bilayer devices,

(2) an improved J_{SC} for blend devices annealed above the optimum temperature, and
(3) an increased photocurrent in bilayer devices stemming from improved exciton harvesting in the polymer layer as shown by IPCE curves.

After a longer discussion of the possible influences of the guest on blend and bilayer devices, I reach the following conclusion:

(1) As followed from TA measurements, the guest acts as a trap by inducing electron transfer from the polymer to the guest upon photo-excitation. Note that this process does not seem to be very efficient as blend devices only deteriorate at rather high guest concentrations of ~5 wt%.
(2) Defect states and traps are expected to reduce the mobility which was indeed observed for bilayer devices upon the addition of the guest. Despite a reduction in mobility, V_{OC} did not increase in these devices as may be expected according to macroscopic device simulations. The reason is likely to be that the occurrence of electron traps leads to increased charge recombination, which reduces V_{OC} and hence counteracts the effect of the mobility reduction on V_{OC}.
(3) Note that in blend devices, where most guest molecules may have $PC_{61}BM$ molecules in close proximity, the guest molecules would act less as traps because the trapped electron would be transferred further to $PC_{61}BM$. This explains why, for moderate guest concentrations (1 wt%), it was possible to improve all parameters (J_{SC}, V_{OC} and *FF*) in annealed blend devices, leading to an overall improvement of almost 60% for annealing at 90 °C.
(4) The task of estimating the influence of the guest on specific solar cell parameters is a difficult one as a multitude of effects need to be considered:
    - The guest molecules act as electron traps in the absence of $PC_{61}BM$ in close proximity. These traps change dark and light curves differently as electrons are not usually present in the hole conducting polymer in the dark.
    - The mobility is influenced by traps and by the degree of intercalation. The latter depends on the degree of phase separation (→ annealing) or on how perfect the bilayer interface is.
    - The guest may improve the exciton diffusion length by increasing the number of long-living triplet excitons. How much these triplet excitons can improve J_{SC} depends on the triplet exciton diffusion length, the degree of phase separation and on how much the guest reduces the mobility and hence the current.

- V_{OC} and *FF* are functions of all those effects. They are influenced by any effect that changes charge transport or bimolecular charge recombination.

To summarise again, the results of this section demonstrate that the addition of phosphorescent guests to the active layer of organic photovoltaic cells can lead to improved device performance below a certain threshold, above where the guest's negative influences on charge transport or bimolecular recombination overwhelm the increase in exciton diffusion length. The approach presented here may overcome the limitations on domain sizes and the need for intercalation in OSCs.

3.6 P3HT:$PC_{61}BM$ Solar Cells with Ir-Complex Attached to P3HT

3.6.1 Motivation

Considering many of the requirements mentioned above, using triplet emitters as dopants in a donor-acceptor blend may not be the optimum system due to possibility of guest aggregation and the difficult energy level line-up. Instead, it may be better if the donor material itself showed strong inter-system crossing. To this end I have used modified P3HT derivatives containing Ir-complexes, synthesised by Egle Sirtautaite-Sidlauskiene at the University of Nijmegen, Netherlands, in the group of Alan Rowan.

3.6.2 Materials

Two materials containing an Ir-complex were used. A random copolymer containing thiophene monomers and Ir-bearing polythiophene monomers in a 1:1 ratio (Figure 3-56a), and P3HT end-capped by the same Ir-complex (Figure 3-56b).

Note that the Ir-complex is absorbing so far in the blue that no Förster transfer from any of the P3HT polymers to the Ir-complex can be expected. More precisely, the main absorption peak of the Ir-complex in the visible is at 380 nm with a last very small peak at 490 nm. The end-capped P3HT and the P3HT copolymer both present a photoluminescence (PL) peak at around 650 nm, with the onset of the PL at 550 nm, if measured in solid state.

3.6.3 Results and Discussion

The results of baked (solid lines) and unbaked (dashed lines) devices are presented in Figure 3-57. All materials show very low currents compared to the commercial regioregular ADS P3HT (P3HT from American Dye Source Inc., ADS, Canada) demonstrating problems with the mobility. Note that a reduction in mobility is indeed expected as the custom made P3HT polymers are not regioregular and have lower molecular weights. The molecular weights of the copolymer precursor and copolymer are 34k and 50k, respectively. The molecular weight of the end-capped precursor polymer and end-capped polymer are only 3k and 4k, respectively. The absorption spectra in (d) also demonstrate the difference in crystallinity compared to the commercial regioregular P3HT, which is much more red-shifted and has a vibronic shoulder at about 600 nm. That is why comparisons can only be made between the polymer and its respective precursor.

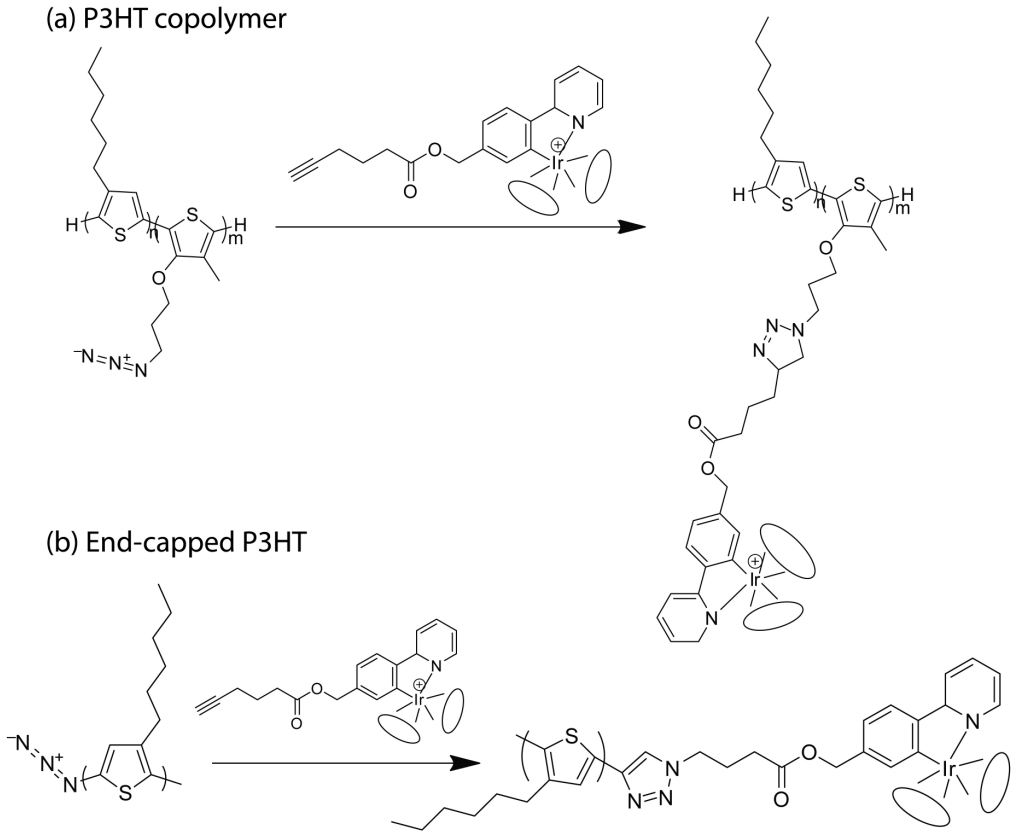

Figure 3-56. Chemical structures of precursor and final product of the P3HT copolymer (a) and end-capped P3HT (b). The n:m ratio of the copolymer is 1:1.

Looking at the illuminated JV curves in (b), we find that the end-capped precursor device performance deteriorates upon addition of the Ir-complex, most likely as a result of the Ir-complex disturbing the crystal structure. For the P3HT copolymer, however, we see that adding the Ir-complex improves both J_{SC} and V_{OC}. Note that for the same processing conditions, the film thickness of the final copolymer precursor was lower than that of the final copolymer, which certainly explains some of the improvement in J_{SC} and V_{OC}.

Also, PLQE measurements of the materials are presented in Table 3-6. As we already know, an improved PL quenching is a necessary (but not sufficient) criterion to establish whether the Ir-complex actually enhances ISC on the donor or induces energy transfer to the Ir-complex. It was found that the addition of the Ir-complex did not quench the end-capped polymer, but quenched the copolymer.

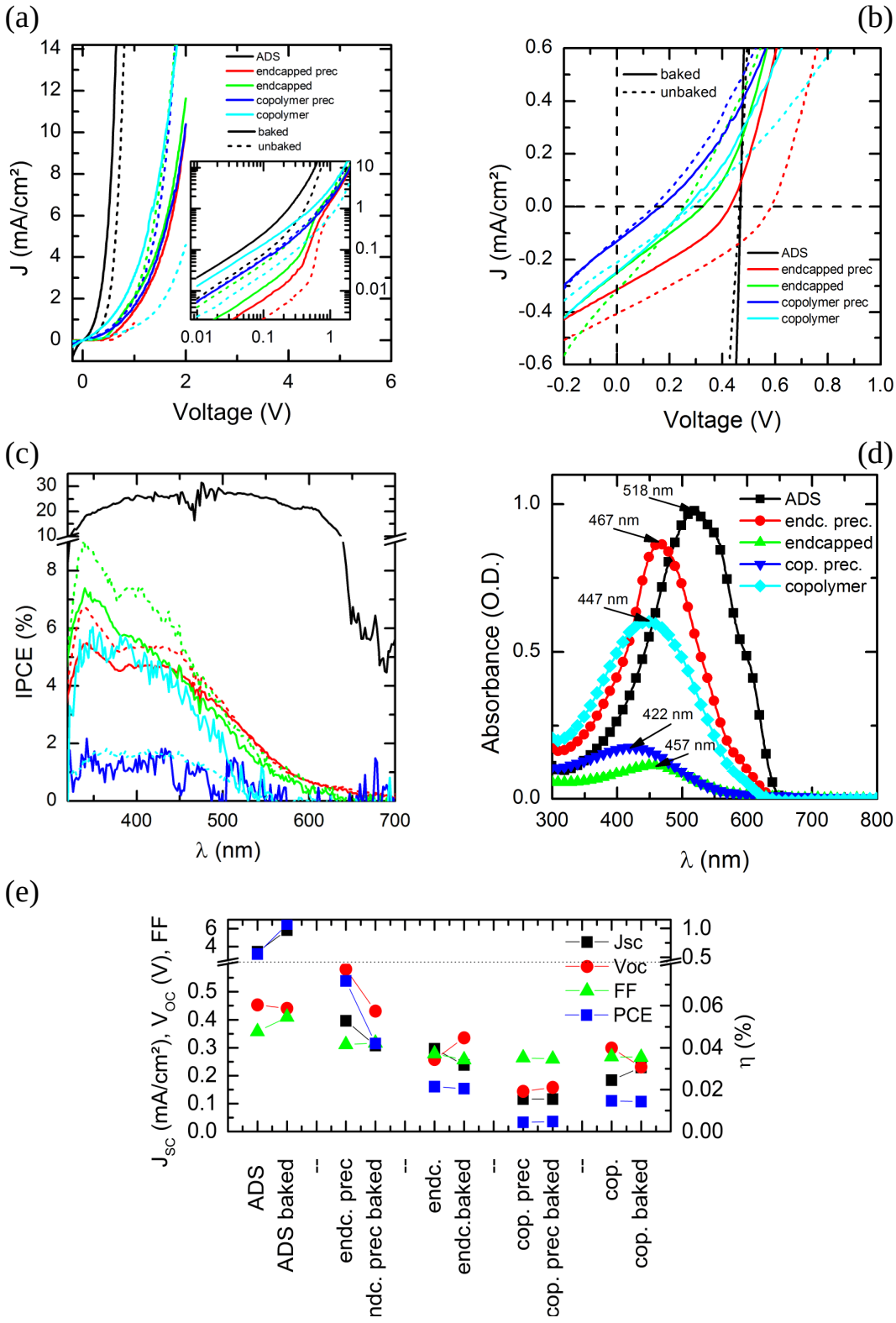

Figure 3-57. Results of solar cells characteristics and absorbance measurements of P3HT polymers containing Ir-compounds attached to the backbone. JV characteristics of devices in the dark (a) and under illumination (b). The inset in (a) shows the same graph in log-log. IPCE spectra (c) and absorbance (in solid state at room temperature for films on fused silica substrates) (d) are also shown. (e) shows the solar cell parameters for the various materials.

Table 3-6. Photoluminescence quantum efficiencies (PLQEs) of the materials

sample	Annealing	PLQE (%)
ADS-P3HT	unbaked	2.8
ADS-P3HT	baked	3.7
Endcapped Prec	unbaked	7.7
Endcapped Prec	baked	7.7
Endcapped	unbaked	9.9
Endcapped	baked	10.6
Copolymer Prec	unbaked	23.9
Copolymer Prec	baked	26.6
Copolymer	unbaked	3.2
Copolymer	baked	12.7

3.6.4 Outlook

As the copolymer shows PL quenching and some promising improvement of its characteristics upon addition of the Ir-complex, the next step would be to establish whether the phosphorescent guest indeed increases the number of triplet excitons in the blend. TA measurements are hence the next step to investigate the materials further. Note that more materials needs to be synthesized in order to continue with this work.

3.7 PBTTT:bis-PC61BM

3.7.1 Motivation

Polymer-fullerene intercalation is very likely to nullify any increase of the number of triplet excitons due to ultrafast exciton dissociation in the intercalated regions. Therefore we need to find a system that does not intercalate, such as PBTTT:bis-$PC_{61}BM$. In the following a possible donor:acceptor blend is investigated as a candidate for the addition of a phosphorescent guest. Note that no guest was added to the host blend.

3.7.2 Materials

Poly(2,5-bis(3-hexadecylthiophen-2-yl)thieno[3,2-b]thiophene) (PBTTT-C16 or PBTTT, from Merck) is a conjugated polymer that became popular due to its very high hole mobility in FETs.[45] PBTTT furthermore offers the advantage of a very strongly temperature dependent solubility so bilayers can be more easily fabricated.

In order to avoid intercalation of the fullerene with PBTTT, bis-$PC_{61}PM$, i.e. the bisadduct of phenyl-C61-butyric acid methyl ester (from Solenne BV, Netherlands), was used. Due to the two side groups, this molecule is too big to fit into between the side chains of PBTTT. The absence of intercalation of this donor:acceptor system was shown by Rance et al.[193] and for PBTTT with bis-$PC_{71}BM$ it was shown by Cates et al..[194] As a triplet emitter, the same Ir-compound as in section 3.5, i.e. ADS077RE (see Figure 3-30), may be used.

According the HOMO and LUMO levels (see Figure 3-59) we are dealing with configuration 'e' (using the scheme in Figure 3-29 on page 132). This configuration is reasonable if energy transfer and CT state formation between host and guest are avoided and if no excitons are split within donor or acceptor domains alone. Note that by estimating the singlet energy levels of PBTTT and ADS077RE, one finds that Förster transfer will not be efficient. The singlet level of PBTTT is around 1.7 eV according to its emission peak at 740 nm and the singlet level of ADS077RE is around 2.1-2.7 eV. By using this triplet emitter one would hence rely on a heavy atom effect improving ISC from S_1 to T_1 on the polymer. By using the triplet emitter *fac*-tris(2-phenylpyridine)iridium, $Ir(ppy)_3$, one may avoid electron trapping from the polymer, but the singlet level is still too high to allow efficient Förster transfer.

(a) (b)

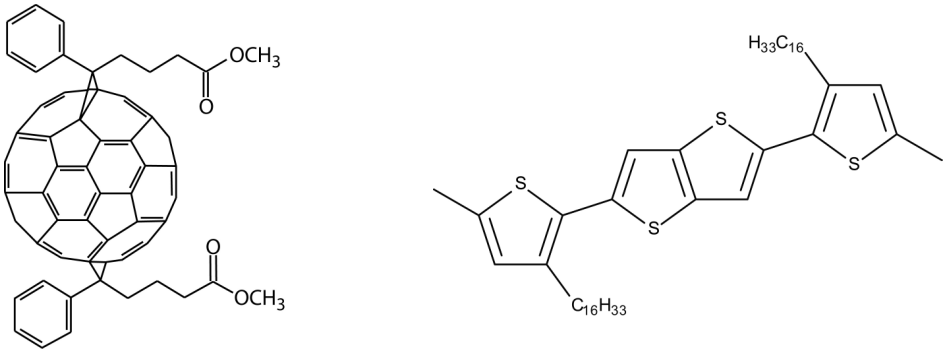

Figure 3-58. Chemical structures of the materials used in this study. (a) bis-$PC_{61}BM$ and (b) PBTTT-C_{16}.

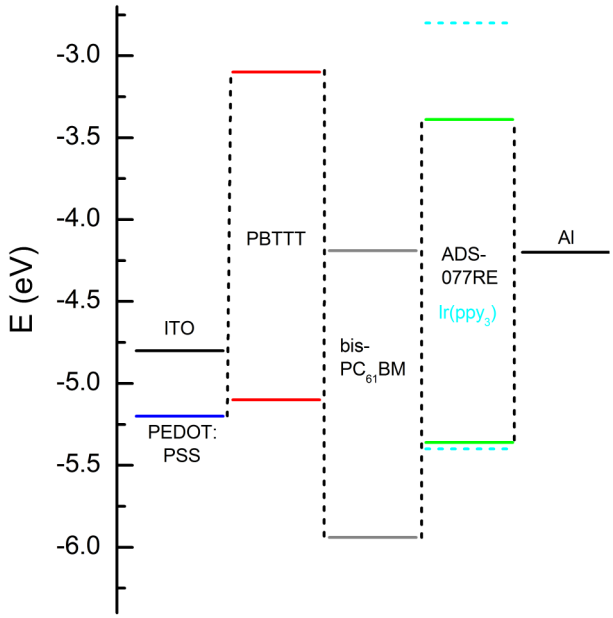

Figure 3-59. Work functions and HOMO/LUMO levels of the materials. E_{HOMO}(PBTTT) = 5.1 eV,[45] E_{HOMO}(ADS077RE) = 5.36 eV, E_{HOMO}(bis-$PC_{61}BM$) = 5.94 eV,[195] E_{HOMO}(Ir(ppy_3)) = 5.4 eV[129], E_{LUMO}(PBTTT) = 3.1 eV,[196] E_{LUMO}(ADS077RE) = 3.39 eV, E_{LUMO}(bis-$PC_{61}BM$) = 4.19 eV,[195] E_{LUMO}(Ir(ppy_3)) = 2.8 eV.[129]

3.7.3 Device Fabrication

Cleaning procedures, spin coating parameters and baking of PEDOT:PSS and the cathode evaporation remain the same as in the previous section (see page 139). Prior to spin coating the active layer, the solutions were kept warm by stirring them on a hot plate at 80 °C. The blend solution has a 1:1 donor:acceptor ratio (which should be close to the optimum for non-intercalating materials)[185], and a concentration of 20 mg/ml in ortho-dichlorobenzene (or 1,2-dichlorobenzene). The spin coating parameters and the annealing procedure were varied to optimize the device performance.

3.7.4 Results and Discussion

3.7.4.1 Optimisation of Blend Devices without a Triplet Emitter.

3.7.4.1.1 "Normal" Annealing Treatment

The "normal" annealing process consists of baking the samples (after cathode evaporation) on a hot plate and cooling them relatively fast by taking the samples from the hotplate and putting them on a metal block.

The results for devices annealed at different temperatures (T) according to the above procedure are shown in Figure 3-60. From the dark JV curves in Figure 3-60a we see that increasing T results in smaller slopes around 0.8 V indicating a reduction in mobility. In Figure 3-60b and d we observe that annealing resulted in a very clear trend in V_{OC}, where V_{OC} steadily increases with temperature. The behaviour of J_{SC} and FF is more complicated and suggests a complex influence of the annealing on domain sizes, charge transport and charge recombination.

Also, slow cooling at 180 °C was found to improve device performance considerably. To investigate the influence of slow film growth further, slow drying and slow cooling was used in the next set of experiments to further optimize the devices.

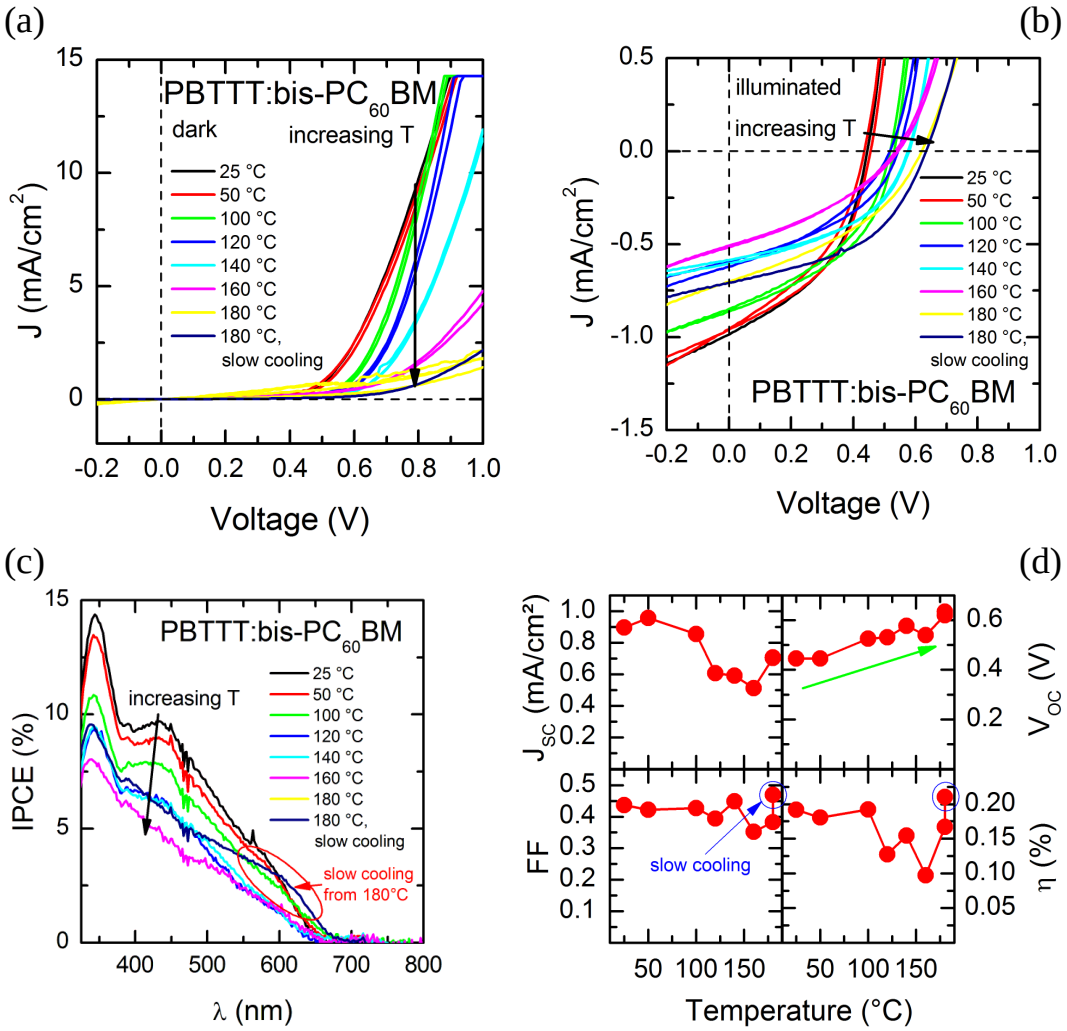

Figure 3-60. (a) Influence of the temperature on the dark JV curve. (b) Influence of the temperature on the illuminated devices. (c) Incident photon to current efficiency (IPCE) spectra for the different temperatures. (b) SC parameters as a function of temperature. PCE is the power conversion efficiency. Slow cooling was used for 180 °C as well which improved the devices considerably.

3.7.4.1.2 Slow Drying and Slow Cooling

The "slow drying" (sd) procedure consists of using 0.1 ml of solvent for each 12x12 mm substrate (which is relatively much) and spin coating the active layer for only 20 s, so that the film will still be wet after spin coating. The bottom and edges of the substrates are quickly dried with tissue and the substrates are put at room temperature under a Petri dish for at least 10 min (until the colour of the film considerably changes indicating that the film is dry). The "slow cooling" (sc) procedure means that after annealing for 10 min at the given temperature, the hot plate is switched off and the substrate left on the hotplate until the hotplate itself is cooled down, which took > 10 min or > 15 min for temperatures of the hot plate > 140 °C.

As we can see from Figure 3-61, using slow cooling and slow drying increased the device performance to some degree. Interestingly, the complicated trend of J_{SC} and *FF* could be reproduced (see Figure 3-61d, the grey squares indicate the parameters for the normal temperature treatment and the red circles indicate the ones for slow dried (sd) and slow cooled devices (sc)), showing that it was indeed not the result of device-to-device variation. Also, upon increasing *T* the smaller slope of the JV curves are observed again, and more importantly, so is the clear linear increase in V_{OC}.

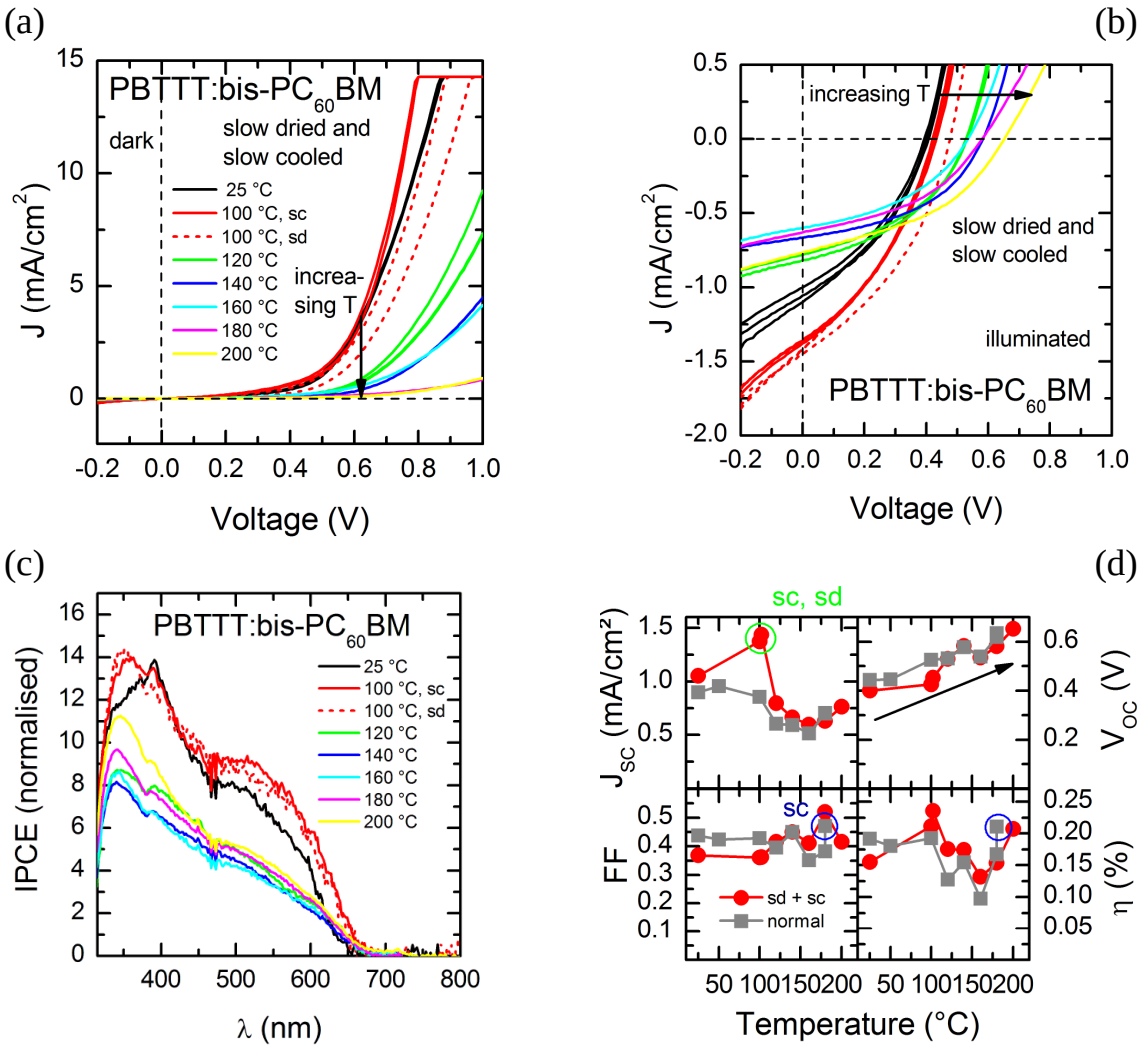

Figure 3-61. SC performance with slow dried and slow cooled devices. Meaning of the diagrams identical to those in the Figure 3-60 above. Note that for heating at 100 °C, devices were either slow cooled (sc) or slow dried (sd).

3.7.4.1.3 Overnight Drying and Spin-Coating Parameters from Literature

As device performance is still rather low, the literature treatment[194,197] (resulting in > 2 % power conversion efficiencies with PBTTT:bis-$PC_{71}BM$ blends) was attempted. This treatment includes spin coating at a lower speed (600 rpm) and for a longer time (60 s), and slow drying

of the samples over night under a Petri dish. The results are shown in Table 3-7 and we find that the previous procedure (sd and sc) resulted in more efficient devices. Efficiencies are still rather low, also due to the use of bis-$PC_{61}BM$ instead of bis-$PC_{71}BM$ (as in the literature[194]).

Table 3-7. SC performance of devices fabricated with "own" procedure (800 rpm, 60 s) and the literature procedure (600 rpm, 20 s, overnight drying under Petri dish). The first column indicates whether annealing happened before or after evaporation.

	Procedure		J_{SC} (mA/cm²)	V_{OC} (V)	**FF**	**PCE** (%)
anneal.	spin c.	Temp.				
before	600 rpm, 60s	90 °C	0.89	0.42	0.42	0.154
before	800 rpm, 20s	90 °C	0.95	0.43	0.40	0.165
after	600 rpm, 60s	100 °C	0.94	0.22	0.27	0.055
after	800 rpm, 20s	100 °C	1.18	0.36	0.33	0.143
before	600 rpm, 60s	100 °C	0.66	0.37	0.34	0.082
after	800 rpm, 20s	220 °C	0.23	0.42	0.19	0.019
after	800 rpm, 20s	240 °C	0.04	0.21	0.18	0.001

3.7.4.1.4 Morphology

It was found that slow drying and *not* slow cooling is responsible for the growth of very large (bis-$PC_{61}BM$) clusters (see camera images in Figure 3-62). Note that although the "spots" in Figure 3-62 look like indentations, this is only an optical illusion; they are in fact "hills" or clusters likely due to the formation of fullerene clusters.

In Figure 3-63 we see AFM images of slow dried and slow cooled devices. Especially looking at the 5x5 µm images (Figure 3-63b), one can see fascinating morphology changes basically at every temperature step (20 °C intervals). An increase in phase separation is apparent, yet the morphology changes are more complex than that. A deep analysis of the morphology may explain the changes in V_{OC}, J_{SC} and *FF* observed in the corresponding devices.

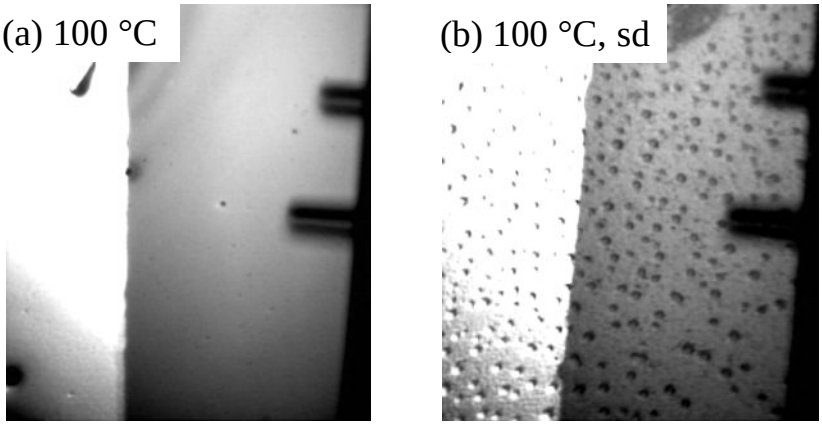

Figure 3-62. Video snapshots of PBTTT:bis-$PC_{61}BM$ devices. (a) no slow cooling and no slow drying. (b) slow dried blend, resulting in large clusters. The bright left area on each image shows the evaporated cathode. The darker area on the right side shows the surface of the active layer. The small dark shadows on the right show two AFM cantilevers which are close to the surface creating a reflection on the surface.

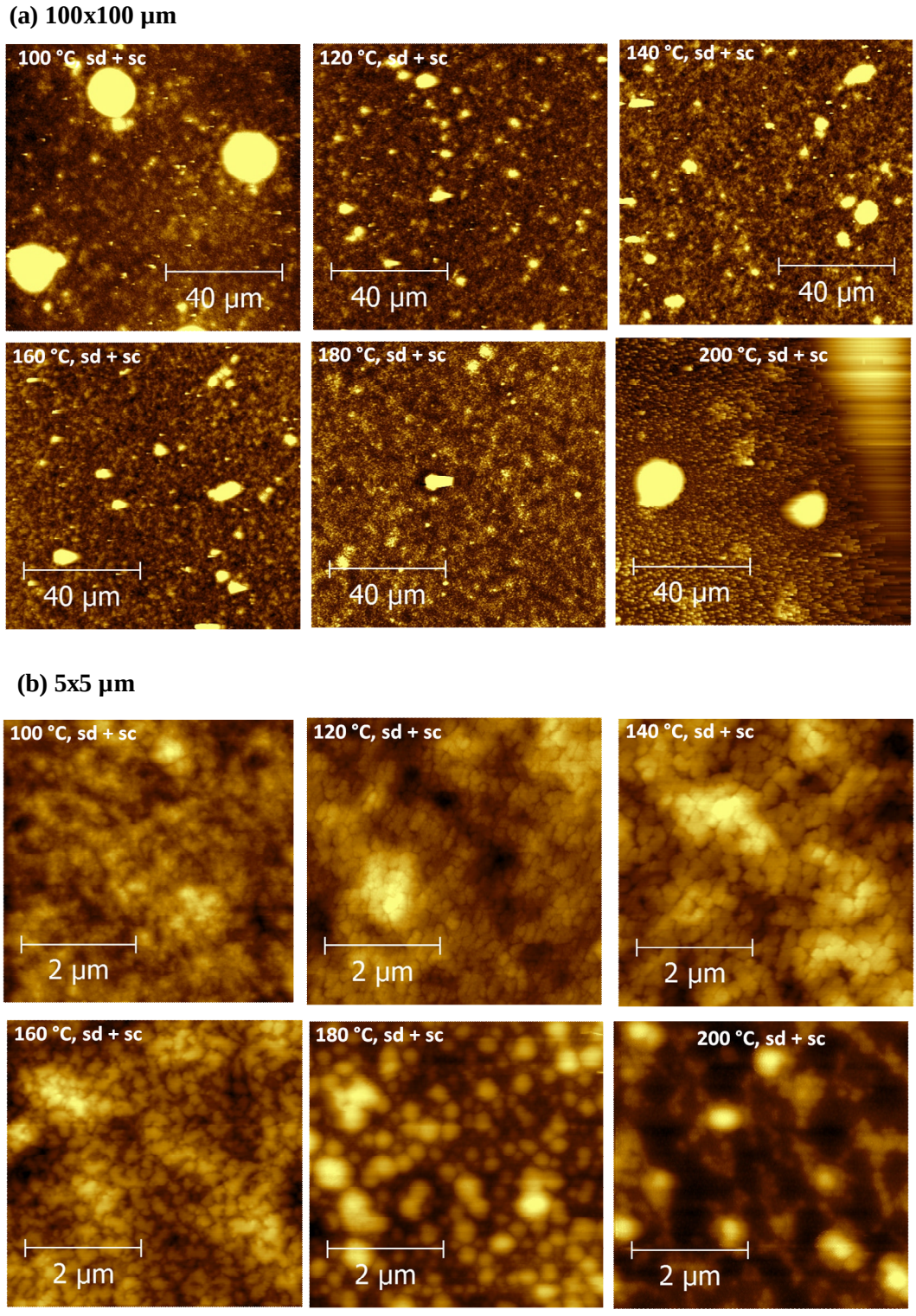

Figure 3-63. Tapping mode AFM images of slow dried and slow cooled devices. The z-scales are as follows (starting with lowest temperature): (a) 100x100 µm images: 200 nm, 130 nm, 100 nm, 100 nm, 150 nm, 230 nm. (b) 5x5 µm images: 70 nm, 80 nm, 50 nm, 60 nm, 110 nm, 150 nm.

3.7.4.2 Conclusion and Outlook

The aim of this work was to use phosphorescent emitters to increase the exciton diffusion range on the donor polymer. After investigating the host blend (PBTTT:bis-$PC_{61}BM$), a very interesting trend in V_{OC} was found. This blend is a prime example of how much the processing conditions can influence V_{OC}, which is often assumed to be only a parameter depending on the donor/acceptor materials (in case of pinning of the electrodes) or on the electrode work-functions (without pinning).

In the future one may try to explain the changes in V_{OC} as well as in J_{SC} and *FF* by investigating the morphology in more detail and it may be useful to determine the charge carrier recombination rates in the blends, similar to the work by Credgington et al..[198] Once the properties of the host blend are understood, the material system could then be used for similar experiments with triplet emitters. Note that the donor PBTTT is particularly interesting due to the extremely easy method to create bilayers with fullerenes, and the choice of bis-$PC_{61}BM$ will assure that no intercalation is occurring.

3.8 The Wider Picture

In this section I would like to move away from my own experimental results and focus on the general idea of using phosphorescent emitters in a donor/acceptor blend (or bilayer).

Although several reports have shown an improvement of device performance upon adding triplet emitters into SCs, it was not yet possible to improve the best performing devices (such as those containing an active layer of P3HT:$PC_{61}BM$) with their help. The problem is that many conditions and parameters must be fulfilled in order to achieve that. In the following I will list the requirements, most of which have already been discussed.

3.8.1 Requirements to Improve Exciton Dissociation via the Creation of Triplet Excitons via Phosphorescent Compounds

1. The entity that transfers the energy to the heterojunction in the pure host blend, i.e. in the absence of a phosphorescent guest, needs to be a singlet exciton (and not triplet excitons or already free polarons as partly in P3HT).

2. The triplet energy level of the polymer needs to lie above the CT level (to efficiently populate the CT level)[112] and the triplet energy of the guest needs to be higher than that of the host (to avoid triplets being trapped on the guest).

3. The mechanism to convert singlet to triplet exciton needs to work, i.e. either

    a. the remote heavy-atom effect improves the singlet to triplet conversion considerably (approach (a) on page 92), or

    b. the energy transfer (or the charge transfer of both electron and hole) from the host to the guest and the subsequent triplet back Dexter transfer to the host work efficiently.

4. The difference of the exciton diffusion length between singlets and triplets on the same material needs to be considerably large, so that the rising ratio of triplet excitons helps to dissociate more excitons. This condition actually includes that the product of triplet diffusivity and triplet lifetime is larger than the product of the singlet diffusivity and singlet lifetime. Whether this condition is fulfilled is not obvious because although it is widely accepted that triplet excitons have longer lifetimes, Dexter transfer is considered to be less efficient than Förster transfer (due to the required proximity between triplet donor and acceptor) and this may lead to a lower diffusivity.

5. When a third material is added to a host matrix consisting of a donor and an acceptor, most of the energy level configurations will result in charge trapping on the guest of at least one type of carrier. This problem can be avoided if the guest has a very high lying LUMO and a very deep HOMO or if the guest is only added to the donor material. In the latter case at least the LUMO of the guest is not important as long as no free polarons are created within the donor domains.

6. Intercalation between donor polymer and fullerene must not occur in the whole active layer as improving the exciton diffusion length would be meaningless.

7. The guest molecules should not aggregate in big clusters, and they should not localise themselves only *between* donor and acceptor domains.

8. The influence of the guest on charge transport needs to be reasonably small. Note that even if the energy levels are chosen wisely to avoid charge trapping, the presence of guest molecules in an otherwise rather crystalline region may already effect the mobility considerably. In a rather amorphous material such as MDMO-PPV this is less problematic.

3.8.2 Results in the Literature and Expected Improvement upon Singlet-Triplet Conversion

Several publications claim the increase of exciton harvesting by converting singlet to triplet excitons.[126-129,199-203] Apart from adding phosphorescent guests to the donor:acceptor blend or donor layer in case of bilayer devices, other methods have been used as well. Among them are the use of a magnetic field to induce ISC,[128] or the use of the phosphorescent material as the donor layer itself.[203]

Although bilayers fabricated via thermal evaporation serve as much better candidates for this kind of investigation than spin coated blends, only a few of these publications make use of them.[127,201,203] Thermally evaporated bilayers offer the advantage of a tight layer thickness control and enables the co-evaporation of the phosphorescent guest into the donor layer, hence circumventing the potential aggregation of the guest. Lee et al. for example claimed an improvement of J_{SC} of 40% using a PPV derivate as the host, PtOEP as the guest and C_{60} as the acceptor using thermal evaporation. Note that the polymer layer was not evaporated.

In some papers, the increase of J_{SC} in *blend* devices is so high that one may wonder whether such an increase can be the result of an effective increase of the exciton diffusion length alone. Arif et al.[199] for example claimed an improvement of almost 10 by adding trace amounts of Pt in a ladder-type poly(para-phenylene), and Schulz et al.[200] claimed an improvement of almost 10

by introducing a triplet forming Ir-complex into the polyfluorene-based polymer. As will be shown in the following, very high improvements of J_{SC} or IPCE are always possible as long as the starting morphology is sufficiently unoptimised for "standard" BHJ solar cells (too large domains) and the increase in exciton diffusion length upon singlet-triplet conversion is sufficiently large.

The highest possible improvement of J_{SC} by singlet-triplet conversion, assuming perfect distribution of the guest in the donor polymer and no negative effects on exciton dissociation or charge transport, is determined only by the morphology of the active layer, i.e. the distribution of donor and acceptor materials, and microcavity effects changing the absorption profile. In the following, the improvement of harvested excitons upon improving the exciton diffusion length is calculated in case of a sharp donor/acceptor bilayer.

3.8.2.1 Bilayers – 1D Random Walk with Absorbing Wall

In the case of a bilayer we may approximate the problem as a 1-dimensional (1D) random walk with an absorbing wall,[98,204] or more precisely as a 1D Wiener process with an absorbing wall. The convergence of a random walk toward the Wiener process is according to the central limit theorem, which tells us that after a large number of independent steps in the random walk, the walker's position is distributed according to a normal distribution

$$f(x, \mu, \sigma^2) = \frac{1}{\sqrt{2\pi\sigma^2}} e^{-\frac{(x-\mu)^2}{2\sigma^2}} \qquad \text{Eq. 3-37}$$

of total variance $\sigma^2 = (t/\delta t)\, \epsilon^2$, where x is the position of the walker, μ is the mean or expectation value, t is the time elapsed since the start of the random walk, ϵ is the size of a step of the random walk and δt is the time for a step. For a 1D random walk, the diffusion constant D can be calculated via $D = \epsilon^2/(2\,\delta t)$ and hence the variance

$$\sigma^2 = 2Dt\,. \qquad \text{Eq. 3-38}$$

For a 2D and 3D random walk, $\sigma^2 = 4Dt$ and $\sigma^2 = 6Dt$, respectively.

It was further found[98] that the fraction of a large number of particles (excitons) initially at $x = 0$ and which are deposited on the absorbing wall at distance d per unit time, at time t, is

$$q(D, d, t) = \frac{d}{t} \frac{1}{\sqrt{\pi 4Dt}} e^{-\frac{d^2}{4Dt}}\,. \qquad \text{Eq. 3-39}$$

The geometry of the model is illustrated in Figure 3-64.

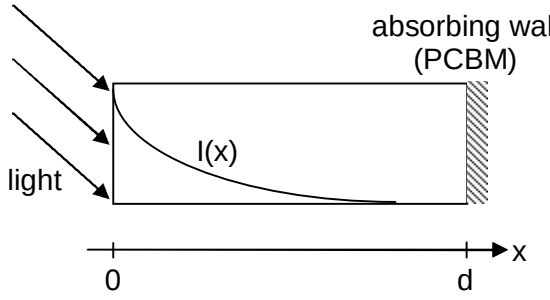

Figure 3-64. Geometry of the 1D random walk model. The light intensity *I*(*x*) follows the Beer-Lambert Law.

We further consider the probability of light absorption *a*(*x*) in the solar cell as a function of location *x* according to the Beer-Lambert Law

$$I(x) = I_0 e^{-\alpha x} , \qquad \text{Eq. 3-40}$$

where *I*(*x*) is the light intensity after absorption of a layer of thickness *x*, I_0 is the light intensity at $x = 0$, i.e. where the light enters the material, and α is the absorption coefficient. One finds that

$$\begin{aligned} a(x)dx &= \frac{1}{I_0} \cdot [-dI(x)] = -1 \cdot (-\alpha) \cdot e^{-\alpha x} dx = \alpha \cdot e^{-\alpha x} dx \\ &\rightarrow a(x) = \alpha \cdot e^{-\alpha x}. \end{aligned} \qquad \text{Eq. 3-41}$$

The function for *a*(*x*) obtained above satisfies $\int_0^\infty a(x)dx = 1$. The absorption coefficient was chosen so that 90% of incoming photons are absorbed after 100 nm, resulting in $\alpha = 2.3 \cdot 10^7$ m^{-1}. This is roughly the value for absorption of a P3HT film near its absorption maximum.[205]

If we assume that each absorbed photon generates exactly one exciton, we are ready to find the formula for the ratio *R* of the number of incoming photons over the number of excitons reaching the absorbing wall ($PC_{61}BM$):

$$R(d, D, \tau) = \int_0^d \left(a(x) \cdot \int_0^\tau q(D, d-x, t)dt \right) dx , \qquad \text{Eq. 3-42}$$

where τ is the lifetime of the exciton. Note that this ratio *R* is an upper limit for the IPCE. Eq. 3-42 cannot be integrated analytically, but it can be rewritten as

$$R(d,D,\tau) = \alpha \int_0^d e^{-\alpha x}\left[\mathrm{erf}\left(\frac{1}{2}\frac{d-x}{\sqrt{D\,\tau}}\right) - 1\right] dx\,, \qquad \text{Eq. 3-43}$$

where erf(y) is the error function defined as

$$\mathrm{erf}(y) = \frac{1}{\sqrt{\pi}} \int_0^y e^{-z^2}\, dz\,. \qquad \text{Eq. 3-44}$$

Note that Eq. 3-44 does not contain D or τ by themselves, only the product $D\,\tau$ occurs. We therefore see that it does not matter whether D is increased and τ constant or vice versa. Eq. 3-42 is visualised in Figure 3-65, where R is plotted as a function of the exciton diffusion length $L = \sqrt{D\,\tau}$.

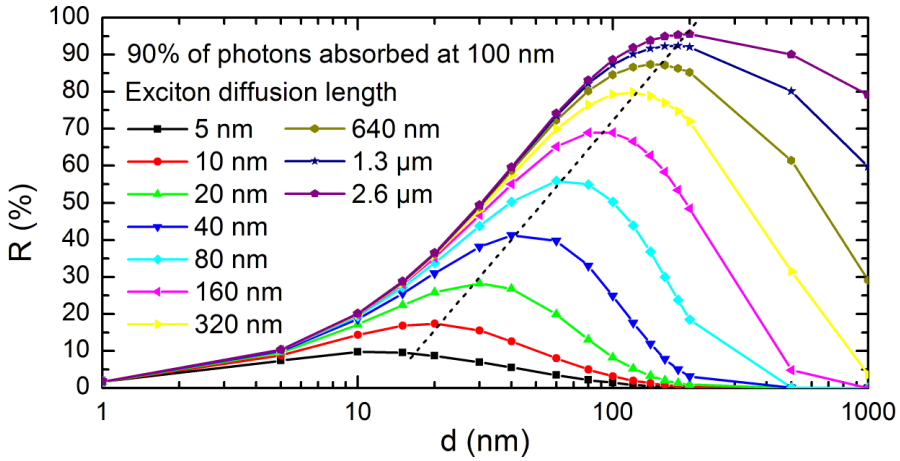

Figure 3-65. Shown is the R, i.e. the number of excitons reaching the $PC_{61}BM$ interface normalised by the number of incoming photons. R is shown as a function of donor layer thickness d with the exciton diffusion length as the parameter. The diffusion constant was assumed to be constant and the different values of the exciton diffusion lengths were obtained by assuming longer lifetimes. The black, straight, dashed line roughly goes through all the maximum values of R for the different exciton diffusion lengths.

First of all we note that for small layer thicknesses d, R is small due to the low number of absorbed photons. One can further see that for small layer thicknesses d < 5 nm, larger exciton diffusion lengths do not improve the ratio R of excitons reaching $PC_{61}BM$. For high thicknesses d, however, the relative increase in R upon changing the exciton diffusion length can be very large. For a 100 nm donor layer, a (singlet) exciton diffusion length of 5 nm and a (triplet) exciton diffusion length of 40 nm, R increases from 1.4% to 25%, i.e. it improves by a factor of ~ 18. We therefore see that in principle, when starting with a device that is very unoptimised for singlets due to too large domains, very high improvements are possible upon increasing the exciton diffusion length.

For the sake of completeness, the assumptions and short-comings of the above model are summarised here:

- Assumed was a random walk in one dimension.
- The assumption of a Wiener process requires small steps and a large number of steps. Considering an exciton "jump" of ~ 1 nm length, this is especially inaccurate for values of *d* smaller than ~ 10 nm.
- The model assumes an absorbing wall at one side, but not a reflecting boundary at the origin.
- Microcavity effects modulating the absorption profile are neglected.
- The reflection of light at the cathode was not considered. This effect helps absorbing more photons as light will travel through the material two times.

3.8.2.2 Blends – 1D Random Walk with Absorbing Shell

Replicating the model above for a BHJ morphology with a 3D random walk is mathematically more difficult. One may, however, approximate the problem by a 1D random walk with an average distance *d* to the absorbing wall. A distinct difference from the model above is that the absorption profile does not have to be taken into account because in the limit of small spheres (small compared to the active layer thickness), one can assume an averaged absorption probability across the whole sphere without introducing an error. We therefore obtain for R_{SS} (*R* for small spheres):

$$R_{SS}(d,D,\tau) = \int_0^\tau q(D,d-x,t)dt = \int_0^\tau \frac{d}{t}\frac{1}{\sqrt{\pi 4Dt}} e^{-\frac{d^2}{4Dt}} dt$$
$$R_{SS}(d,D,\tau) = 1 - \mathrm{erf}\left(\frac{1}{2}\frac{d}{\sqrt{D\,\tau}}\right) = 1 - \mathrm{erf}\left(\frac{1}{2}\frac{d}{L}\right) = R_{SS}^{L}(d)\,. \qquad \text{Eq. 3-45}$$

R_{SS} and *R* are plotted together for the same values of the parameter *L* in Figure 3-66. To better denote that *L* is the parameter and *d* is the variable, we may define $R^L_{SS}(d) = R_{SS}(d,D,\tau)$ and $R^L(d) = R(d,D,\tau)$. One can see that for small values of *d*, $R^L_{SS}(d)$ is much larger than $R^L(d)$. This is because for small values of *d*, the small number of overall absorbed photons reduce $R^L(d)$ considerably. Another interesting observation is that the intersection of $R^L(d)$ with $R^L_{SS}(d)$ occurs very close to the maximum of $R^L(d)$, which is denoted as a black dashed line in Figure 3-66.

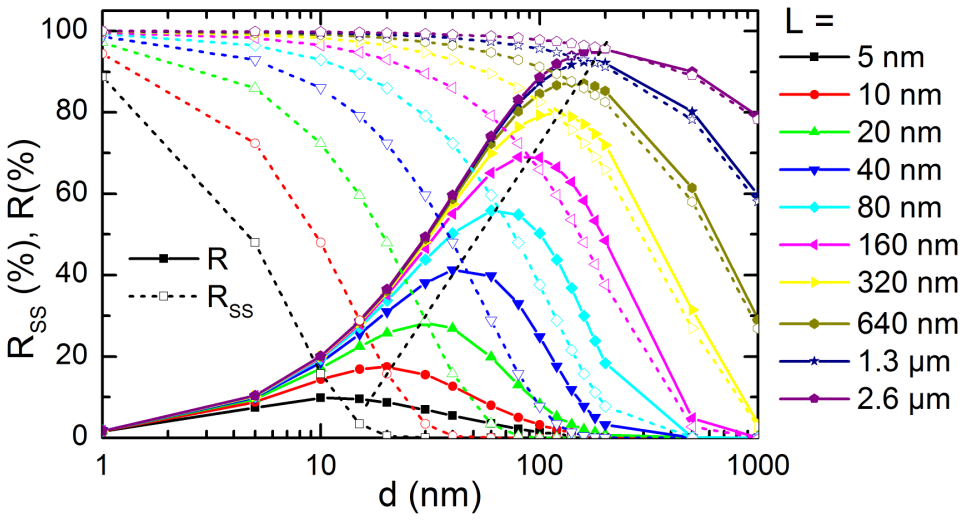

Figure 3-66. Visualisation of the ratio of excitons that can reach the interface for different exciton diffusion lengths *L* in case of a bilayer (*R*,solid lines with filled symbols) and in case of smaller spheres with an average distance *d* to the absorbing wall (R_{SS}, dashed curves with open symbols).

3.8.3 The Ultimate Solar Cell

It is certainly interesting to ask the question which materials or design concepts are the most promising ones to achieve the most efficient OSCs. We will assume in the following a single band gap material (i.e. no tandem cells). Without further restriction or consideration, the optimum band gap is then 1.4 eV, according to the Shockley-Queisser limit[3].

However, let us now also assume that two materials are needed, a donor D and acceptor A, at whose interface photogenerated excitons can be split effectively. Which energy level configurations would be optimum? On the one hand, lowering the absorber (donor D) band gap will improve the light harvesting at lower photon energies (see Figure 3-67) and hence lead to a higher possible J_{SC}. On the other hand will a reduced band gap at some point lead to a reduced effective band gap (E_{LUMO}(A) - E_{HOMO}(D)) which is proportional to V_{OC}. Hence the increase in J_{SC} by lowering the band gap will at some point be overcompensated by the reduction in V_{OC}.

In practice, the optimal band gap energy will depend on the restrictions placed on the energy needed to induce charge separation, the absorbing properties of the donor and restrictions on the acceptor used. In the case of an absorbing conjugated polymer in combination with $PC_{61}BM$, an optimal band gap of 1.3 to 1.9 eV is reported[206] for the absorbing conjugated polymer resulting in efficiencies of about 6%.[207] If we were allowed to freely chose the energy levels of A, which is a technological problem, the optimum band gap would be ~ 1.9 - 2.0 eV and efficiencies up to ~ 11% could be reached.[207]

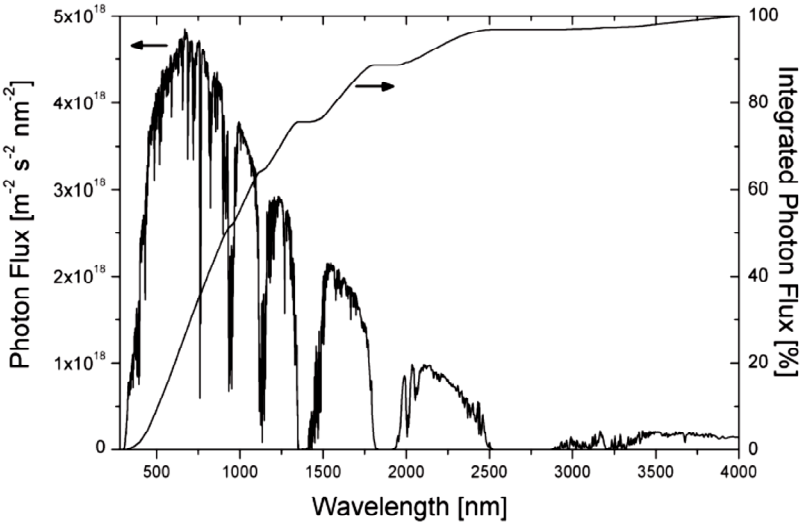

Figure 3-67. Photon flux according to the AM1.5 spectrum and integrated photon flux. Assuming all photons with an energy above the band gap of the absorber are absorbed, the integrated photon flux determines how much light is lost depending on the absorber band gap. However, lower band gap absorber materials will result in a small V_{OC}. Figure reprinted with permission from Kroon et al.,[206] Copyright (2008) Taylor & Francis.

Considering the ultimate SC morphology, in which exciton dissociation and charge collection both already work with 100% efficiency without the creation of mainly triplet excitons, as for example claimed by Park et al.[208], using triplet excitons is a loss mechanism. (Note that an IPCE curve is always a measure of the external quantum efficiency at low light intensities, at which the IPCE is usually measured. OSCs typically perform worse under higher light intensities so that the internal quantum efficiency under 1 Sun illumination is lower[209]). The use of triplets presents a loss mechanism because each photon loses an additional amount of energy, the exchange energy, which is ~ 0.7 eV[101] for many conjugated polymers. The optimum donor band gap would hence increase if triplets were used.

Nevertheless, the requirement of using BHJ architectures to effectively dissociate excitons in conventional state-of-the-art polymer-fullerene SCs is probably the major problem for efficient SC fabrication, because the huge influence of any parameter on the morphology makes it very difficult to obtain a morphology that allows efficiencies near 100% for both exciton harvesting and charge collection, if it can be reached at all. Note that also the problem of bimolecular charge recombination is bypassed by the use of bilayers.

The approach presented here may therefore circumvent the problem of morphology optimisation and decrease development costs of prototypes considerably by enabling the use of bilayers, which are much more easily reproduced and transferred from the lab scale to large-scale production.

3.9 Summary and Outlook

The aim of this work was to increase the number of triplet exciton to increase the effective exciton diffusion length in the active layer. To this end, two approaches have been proposed, one relying on Förster and back-Dexter transfer and the other one relying on the external heavy atom effect. To this end, different host-guest systems have been investigated.

3.9.1 P3HT- $PC_{61}BM$ with Cu-Complexes

Triplet emitting materials made from Cu complexes have been used with the aim of creating additional triplets inside P3HT to improve the efficiency of SCs comprising P3HT and $PC_{61}BM$ in the active layer. The Cu complexes used offer the advantage of Cu, which is more abundant and environmentally friendly, and has a high solubility in organic solvents. However, it turned out that the compounds act as hole traps in the used host. Also, as explained in the section 3.4.2 on page 108 about triplet states in P3HT, free charge carriers may be generated inside P3HT even without $PC_{61}BM$ in its proximity, so that the generation of triplet excitons may be of limited use or even counterproductive as triplet excitons have an even shorter lifetime than generated polarons.

3.9.2 MDMO-PPV:$PC_{61}BM$ with Ir-Complex

For that reason, I tried using other hosts, such as MDMO-PPV:$PC_{61}BM$ and also other triplet emitters, because the HOMO levels of the used Cu complexes are so high that hole trapping could occur for a range of host materials. It was claimed by Rand et al.[126] that an increase of J_{SC} upon increasing the exciton diffusion length was achieved upon doping this host blend with a phosphorescent guest, which seemed surprising knowing that intercalation is likely to occur for "normally treated" blends.

I achieved some positive results with respect to the aim of this work in the form of an increase of J_{SC} for "overannealed" blend devices and for bilayer devices, which is more plausible as intercalation is likely to be reduced in such systems. The bilayer devices also showed an increase in the MDMO-PPV IPCE peak as expected from an increase in the exciton diffusion length on the donor polymer. Photo-induced absorption measurements showed that the used Ir-complex attracts electrons from MDMO-PPV, leading to some deterioration of the charge transport, and that Dexter transfer from the guest to the donor is occurring.

3.9.3 P3HT:$PC_{61}BM$ Solar Cells with Ir-Complex Attached to P3HT

First results were obtained with a P3HT copolymer containing an Ir-complex and a polymer where P3HT is end-capped with an Ir-complex. Results show low conductivities compared to commercial P3HT as expected from the lower molecular weight and the absence of a high degree of regioregularity. Nevertheless, the copolymer precursor was improved upon addition of the guest. Some of the improvement comes from a larger film thickness of the final copolymer. However, the copolymer also showed PL quenching upon addition of the Ir-complex, indicating the possibility of an increased ISC rate on the host.

3.9.4 PBTTT:bis-$PC_{61}BM$

To avoid the problem of intercalation fully, PBTTT was used in combination with a large fullerene derivative that cannot fit into the side chains of PBTTT and hence prevents intercalation. We observed a strikingly clear trend in V_{OC} as a function of annealing temperature, which seems linked to the phase separation of the donor:acceptor blend. Adding a phosphorescent guest would be the next step.

3.9.5 P3HT:$PC_{61}BM$ Solar Cells Stirred in or Synthesised with $FeCl_3$

P3HT was synthesized with $FeCl_3$ (see appendix on page 208) to see whether Fe may bond to the polymer resulting in triplet exciton enhanced J_{SC}., similar to the claim of Arif et al..[199] However, due to the lack of regioregularity and crystallinity, currents were generally low and a reasonable comparison to purchased P3HT was not possible.

In another set of experiments, P3HT was stirred in an aqueous $FeCl_3$ solution in order to dope the polymer with Fe without reducing the crystallinity of the polymer[210] (see appendix page 210). The several hours long stirring in air did not deteriorate the polymer considerably, i.e. absorption peaks did not change their position and the conductivity in devices was still high. SCs made out of the doped material performed almost identical to the untreated polymer. More experiments need to be carried out using the doping of conjugated polymers with salts in order to establish whether this is a viable, more general strategy to dope donor materials with heavy atoms to increase the spin-orbit coupling and hence the number of triplet excitons under illumination.

3.9.6 The Wider Picture

I listed all the requirement needed to be fulfilled in order to improve the exciton diffusion length in OSCs by adding phosphorescent guests to the host. The literature claiming an increase in solar cell performance due to improved exciton harvesting was reviewed. Depending on the morphology and the change of exciton diffusion length via singlet-triplet conversion, very high improvements of J_{SC} and the IPCE are indeed possible as demonstrated with a 1D random walk model with an absorbing wall. The lack (in most publications) of a more direct proof of an increased ratio of triplet excitons in the active layer, for example via TA spectroscopy, is observed. It is also noted once again that the author found no publication where a high-performing solar cell (with a power conversion efficiency of ≥ 3 %) was improved by adding phosphorescent guests, demonstrating the complexities connected with this approach.

I also reviewed the properties of the ultimate single layer solar cell and came to the conclusion that if solar cells can be made to dissociate excitons and collect charges with 100% efficiency without using triplet excitons, the singlet to triplet conversion attempted in this work presents a loss mechanism in form of the (S_1-T_1) exchange energy. In this sense, the ultimate solar cell should be designed to avoid the creation of triplet excitons.

However, probably the major problem faced by the OSC community is precisely that obtaining a BHJ morphology that simultaneously optimises both exciton harvesting and charge transport is so difficult to achieve. The approach in this work may overcome this problem by enabling the use of bilayers, which help to avoid non-geminate bimolecular charge recombination and the problem of morphology optimisation.

4 Appendices

4.1 Towards Bilayer Devices

Bilayer devices offer the advantage of a better controlled morphology and, most importantly for the work here, a possibly fullerene free layer of donor polymer. In order to create bilayers, several attempts were undertaken, which will be briefly presented here.

4.1.1 Using a Bad Solvent for MDMO-PPV

One approach to achieve bilayers, i.e. to spin coat a material B on top of another material A, is by finding a solvent that dissolves A much less than B. One such suggested solvent was dichloromethane (DCM).

To find out how insoluble the polymer really is in DCM, I made solutions of MDMO-PPV in the good solvent chlorobenzene (CB) and spin coated it at different spin-speeds on spectrosil substrates. Then I spin coated DCM on top of the MDMO-PPV layer at 1800 rpm.

The result can be seen in Figure 4-1, where the absorption of the samples before and after spin coating (i.e. "rinsing") in DCM is shown for MDMO-PPV layers spin coated at 800, 1800 and 4000 rpm. Although DCM is indeed a bad solvent for MDMO-PPV, considerable amounts of material have been washed away. We therefore need to consider other methods to achieve bilayers.

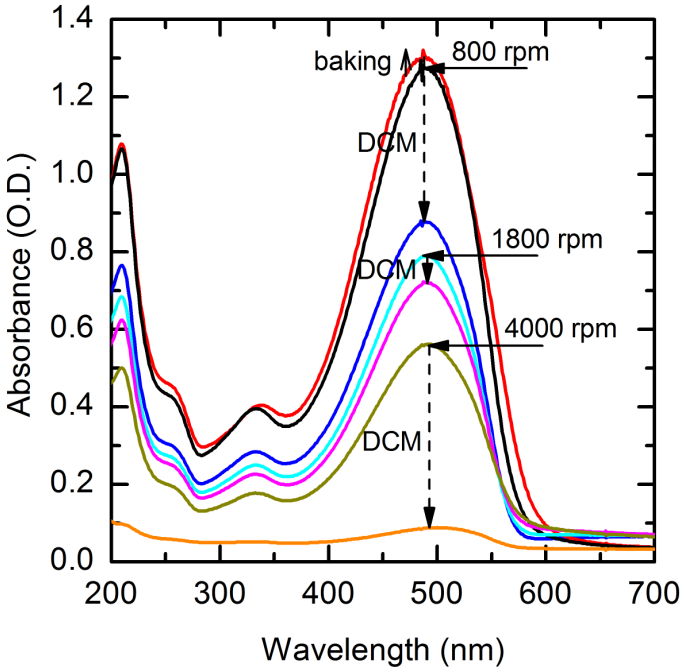

Figure 4-1. Solubility test of MDMO-PPV in dichloromethane (DCM). The sample spin coated at 800 rpm has been baked at 140 °C for 10 min prior to spin coating it with DCM. The other samples have not been baked. One can see a considerable loss in absorption upon spin coating DCM, indicating that a considerable amount of MDMO-PPV has been dissolved and removed.

4.1.2 MDMO-PPV/ Alq_3 Bilayer Devices

Another method of achieving bilayers is to move (partially) away from solution processing. One layer may be spin coated and the other evaporated on top. Searching for an electron transporting layer that may be evaporated on top of MDMO-PPV, tris(8-hydroxyquinolinato)aluminium (Alq_3, chemical structure can be seen in Figure 4-2b) made it into the final selection.

According to literature values for MDMO-PPV, its LUMO (2.8 eV) should lie slightly above that of the electron transporting material Alq_3 (3.0 eV) and its HOMO (5.3 eV) should lie as well above the HOMO of Alq_3 (5.7 eV). Alq_3 should hence form a type II heterojunction with MDMO-PPV potentially enabling exciton dissociation. The energy levels are shown in Figure 4-2. Note that now Ca has to be used instead of Al (to obtain an ohmic contact and pinning of the electrode work function to the LUMO of Alq_3).

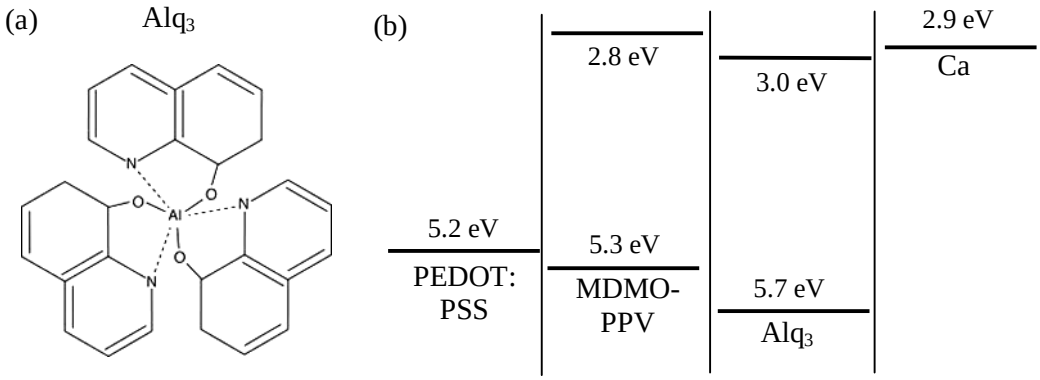

Figure 4-2. (a) Chemical structure of the electron transporting material Alq_3. (b) Work functions and HOMO/LUMO levels of the materials used during this experiment.

The JV curves of PEDOT:PSS/MDMO-PPV/Alq_3/Ca/Al devices are shown in Figure 4-3, presenting some interesting features. The devices seem to be ohmic (i.e. present a linear relationship between current and voltage) within the "usual" regime of 0 to 1.5 V (see right image in Figure 4-3). The diode behaviour, or rather, the more than linear increase in current, shows at voltages above ~ 3 V.

Within the equivalent SC circuit, the resistance in the low voltage regime (at V ~ 0) is a good approximation for the shunt resistance (R_{SH}) for small R_S. According to that approximation, R_{SH} would be about 10^4 Ω. (Pixel P2 (orange curve in Figure 4-3) even has a resistance of 10^6 Ω at $V = 0$). If everything else in these devices would work ideally, the high R_{SH} would actually help to achieve a high FF. However, we observe a virtually zero J_{SC} in the devices. This can have two causes. It either means (a) no current is generated in the cell in the first place or (b) the series resistance (R_S) is very high (possibly due to problems with the Ca evaporation or very low electron or hole mobilities). Note that the approximation for R_{SH} as the resistance at $V = 0$ breaks down for large values of R_S.

(a) The absence of considerable J_{SC} may indicate problems with exciton dissociation. Indeed, depending on the exact distribution of LUMO levels on MDMO-PPV, electrons may stay on the donor instead of transferring to Alq_3. The same is true for the HOMO levels. Assuming a lack of exciton dissociation is the cause for near zero J_{SC}, the values measured by Charlotte Fléchon (leading to virtually identical HOMO and LUMO levels on MDMO-PPV and Alq_3) are very reasonable.

(b) R_S (ideally zero) can be approximated as the resistance at a large forward bias. For all the devices, this value is large, around 0.4 kΩ. Such a high R_S can indeed reduce J_{SC} to very small values. Note that R_{SH} does not affect J_{SC}. Hence, if R_{SH} was large as well (ideally infinitely

large), V_{OC} would still be expected to show "normal values", i.e. those that are expected taking into account the effective band gap of the material system ($|E_{LUMO}$(acceptor) - E_{HOMO}(donor)|, around 2 V for MDMO-PPV/Alq_3). The orange curve in Figure 4-3 is special as it is the only curve that does not have a near zero V_{OC}. More precisely, whereas all the other devices have a V_{OC} of ~ 0.02 V, the orange curve has a V_{OC} of 1.17 V. The difference between the orange and the other curves may indeed result from a difference in R_{SH}. So in conclusion, all pixels seem to suffer from a large R_S and a small R_{SH}, except of the orange curve, which appears to have a much better (higher) R_{SH}.

Whether or not MDMO-PPV/Alq_3 is efficient regarding exciton dissociation remains uncertain at this point. Due to the very low SC performance of this material system, further investigations have not been carried out.

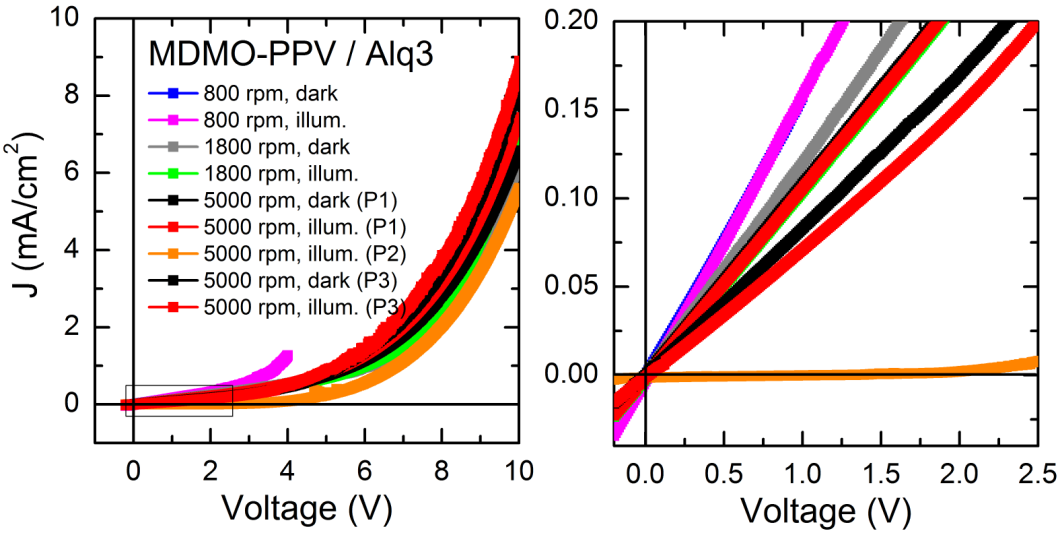

Figure 4-3. JV-curves of devices from Batch Ir35X. The spin-speed for the active polymer layer is indicated. Three pixels (P1, P2 and P3) are shown for the devices with the high spin-speed. Interestingly, there was only one device (P2), which, after driving it at voltages up to 10 V, showed a considerable open circuit voltage. More explanation in the text.

4.2 P3HT:PCBM Solar Cells with Cu-Complex C

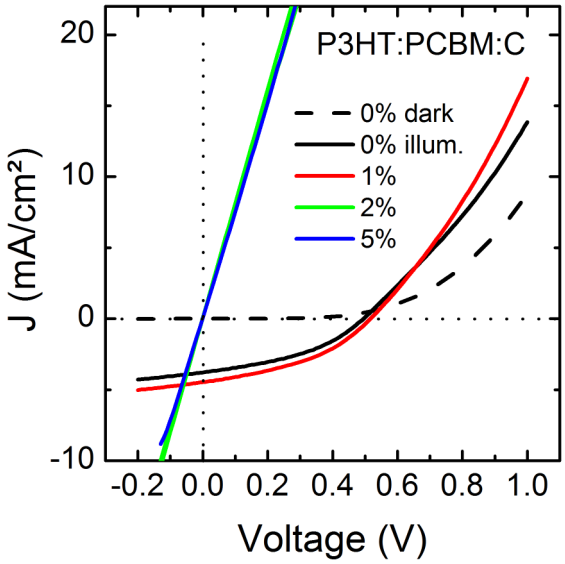

Figure 4-4. JV curves of devices with P3HT:PCBM solar cells with different amount of the Cu-complex C. The dashed line shows the dark JV curve. All other curves are taken under illumination. One can see a short-circuit like behaviour upon including 2% or more of the triplet emitter.

4.3 FET Characteristics of P3HT:PCBM Blends with Cu-Complex E

In the following the transfer (Figure 4-5) and output characteristics (Figure 4-6 and Figure 4-7) of FETs made with an active layer consisting of P3HT, PCBM and the Cu-complex E are presented. The shift of the threshold voltage (V_T) in Figure 4-5c points[211] towards an increase of the number of (donor-like) hole traps near the HOMO as more guest molecules are added. The shifts of V_T in Figure 4-5a and b may indicate a reduction of electron traps as more guest molecules are added.

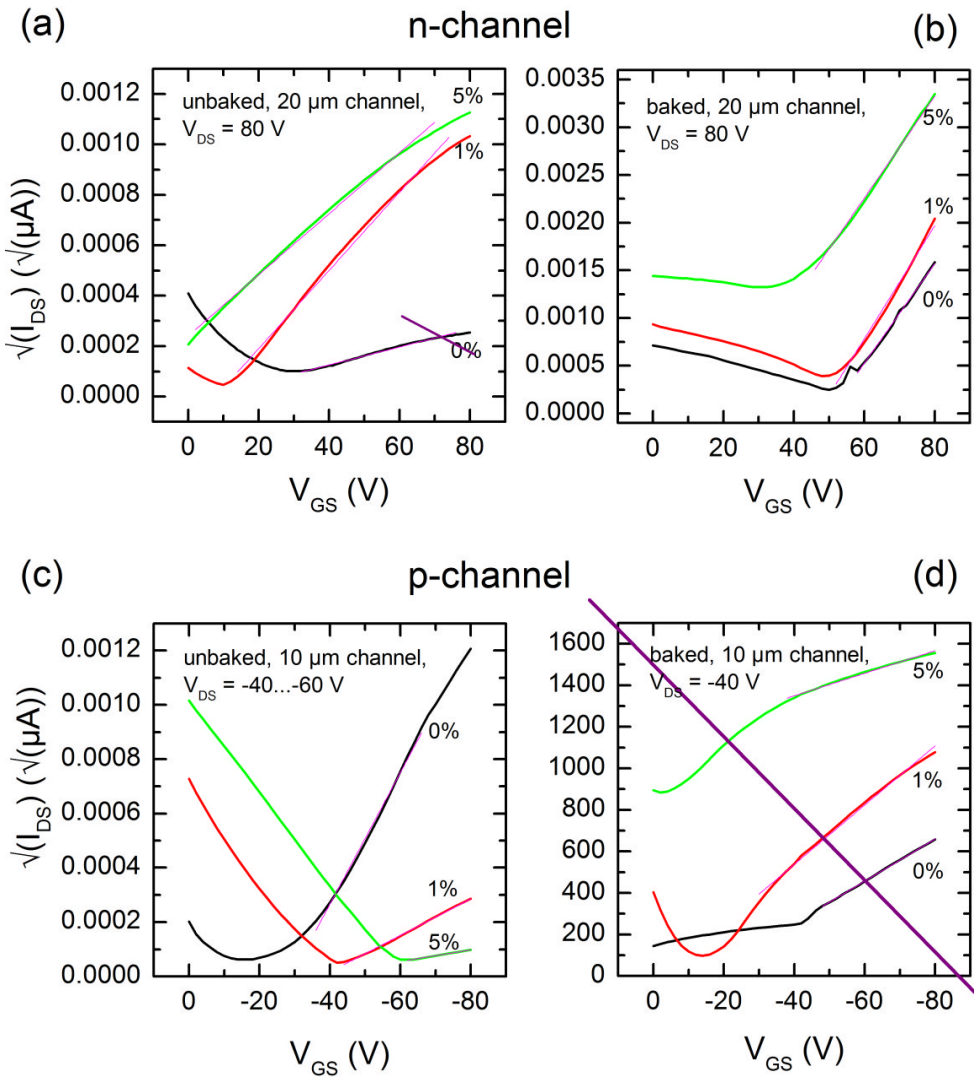

Figure 4-5. Transfer characteristics of FETs with an active layer blend made from P3HT, PCBM and the Cu-complex E with different concentrations of the Cu-complex (0, 1 and 5 wt%). Figure (a) and (b) were used to determine the electron mobility for the unbaked and baked devices. Figure (c) was used for the hole mobility for the unbaked devices. Due to lack of good output characteristics, no hole mobilities were extracted from (d) and from the 0% curve in (a).

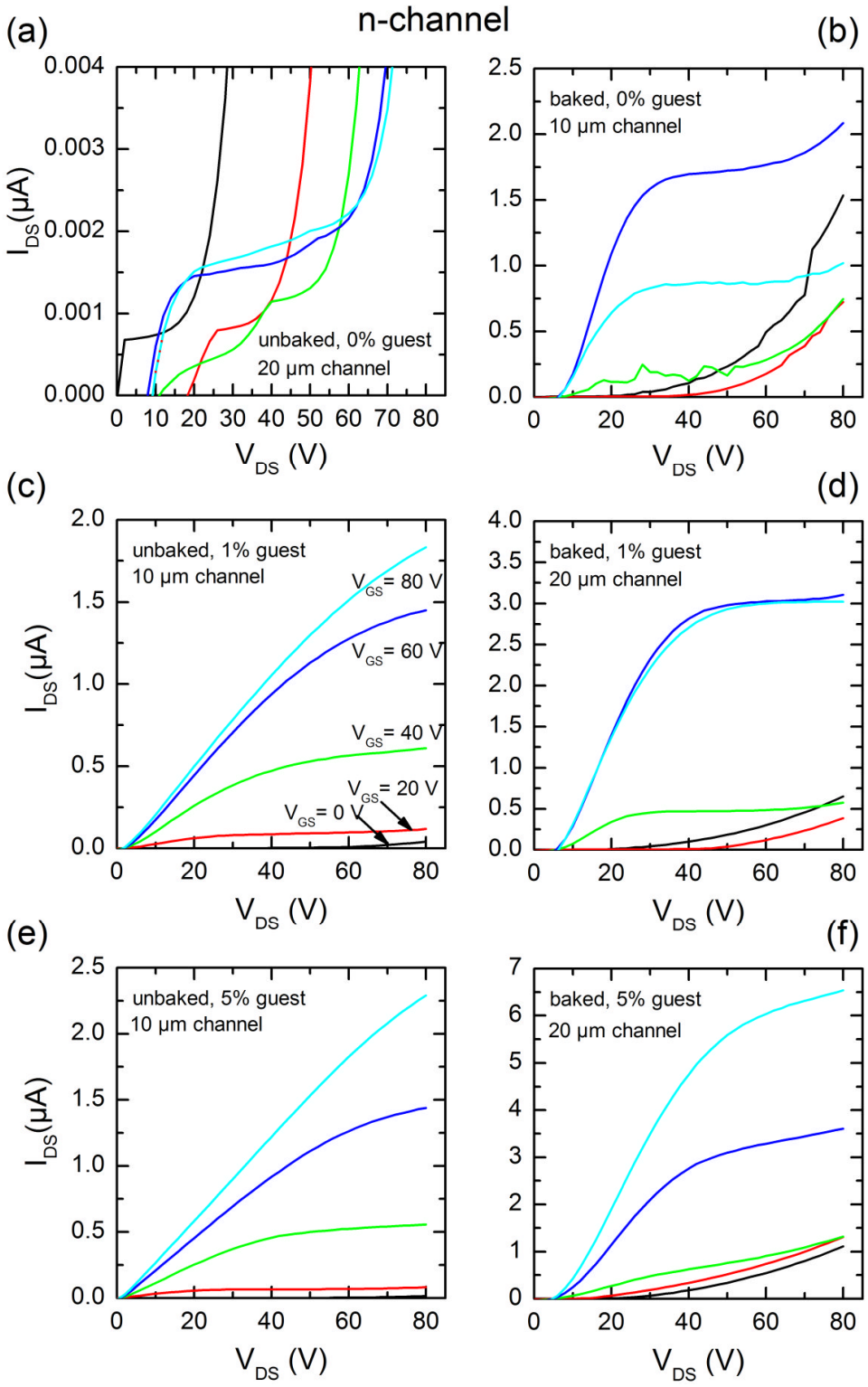

Figure 4-6. Output characteristics of FETs made of P3HT, PCBM and Cu-complex E. The curves demonstrate clear n-conduction enabling the extraction of electron mobilities for all tested guest concentrations (0, 1, 3%) and for both unbaked and baked devices.

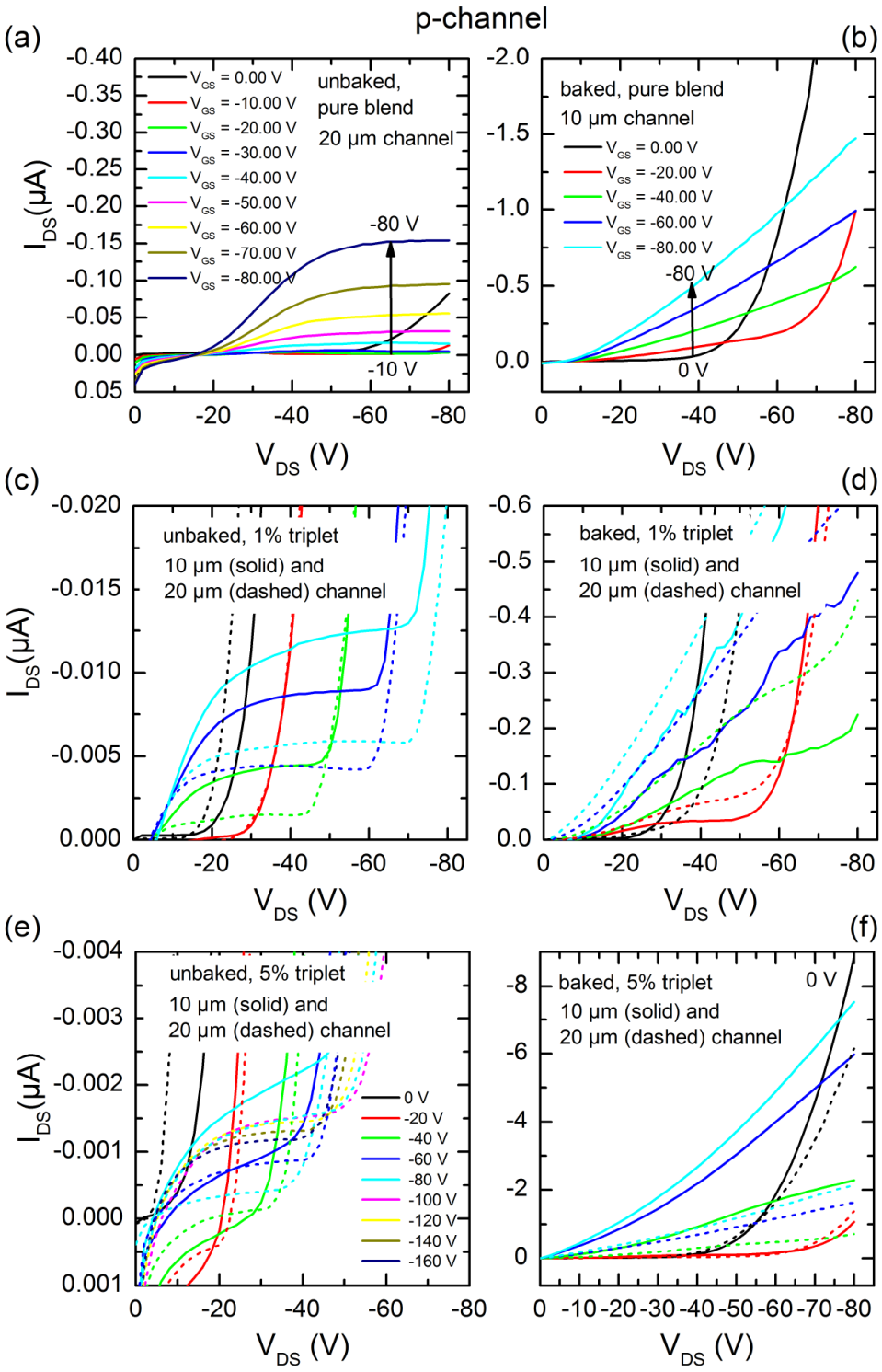

Figure 4-7. Output characteristics of FETs made of P3HT, PCBM and Cu-complex E. Only the unbaked devices (left) show clear p-conduction.

4.4 P3HT:PCBM Solar Cells Blended with Ir-Complex

According to the energy levels in Figure 3-31 (i.e. according to Charlotte Fléchon's measurements), blending P3HT with the Ir-compound should result in a type II heterojunction with holes transferring to the guest. However, no PL quenching is observed for P3HT upon adding the guest, indicating that no energy transfer or exciton dissociation occurs. (The PLQE was measured to be 3.0 % without and 4.1 % after addition of 5 wt% of the guest).

SCs consisting of blends of P3HT:PCBM in the active layer showed a reduction in performance upon adding the triplet, more precisely a reduction of *FF* and J_{SC} at all guest concentrations and a reduction of V_{OC} mainly at high guest concentrations (see Figure 4-8 and Figure 4-9).[viii] Mobility measurements on FETs (Figure 4-10), however, showed a reduction of electron mobilities when adding the triplet.[ix] As electron transport happens mainly via PCBM, this raises the question why SCs made out of MDMO-PPV and PCBM did not deteriorate in such a way when mixed with the Ir-compound.

It is well known, however, that mobilities as measured via FETs are different from those determined via investigating the JV curves. This has to do with (a) the direction of charge transport which is along the substrate plane in FETs but perpendicular to that that in SCs, and (b) it is not always clear which material is dominating the channel. PCBM may or may not preferentially aggregate at the channel depending on the polymer it is blended with.

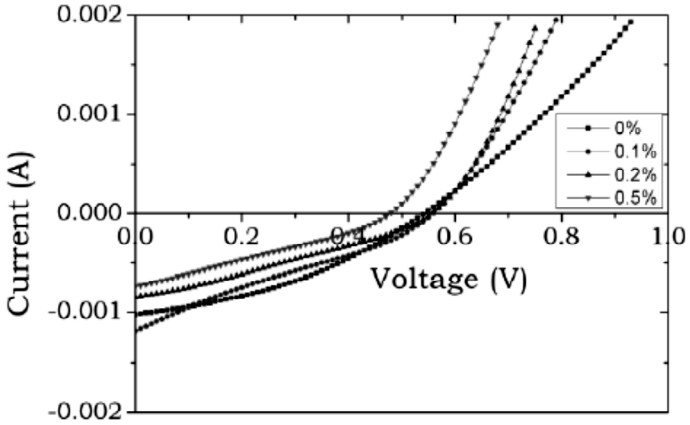

Figure 4-8. JV curves of P3HT:PCBM devices with different amounts of guest concentration. Figure taken from the literature.[212]

[viii] Solar cell devices with P3HT:PCBM and the guest ADS077RE have been fabricated and characterised by Shiv Kodam.
[ix] Mobility measurements of FETs with P3HT:PCBM and the guest ADS077RE were carried out by Giovanni Mattia Lazzerini.

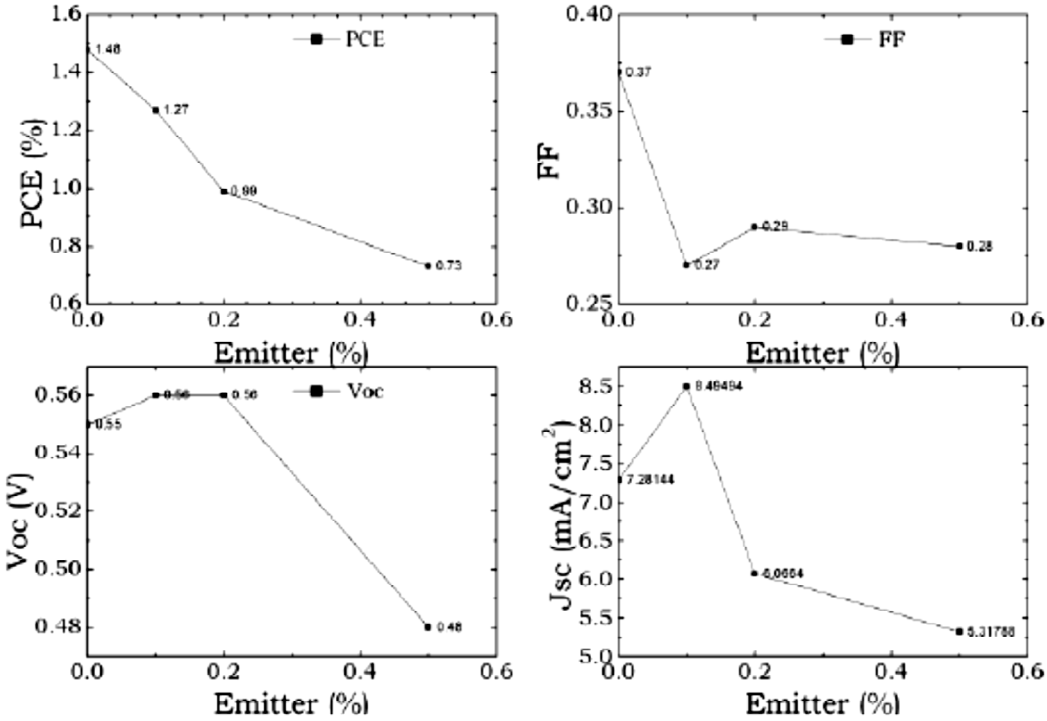

Figure 4-9. SC performance parameters corresponding to the curves shown in Figure 4-8. Figure taken from the literature.[212]

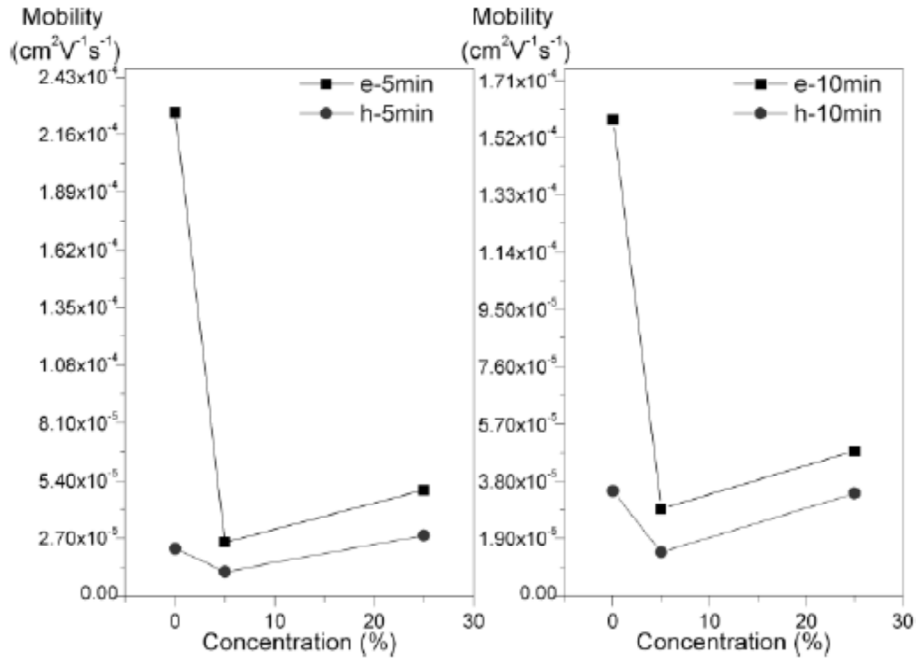

Figure 4-10. Mobility measurements of P3HT:PCBM FETs with different amount of guest concentrations after baking at 140 °C for (left) 5 min and (right) 10 min. Figure taken from the literature.[212]

4.5 P3HT:PCBM Solar Cells with P3HT Synthesized with $FeCl_3$

4.5.1 Motivation

It was claimed by Arif et al[199] that triplet enhanced ladder-type poly(para-phenylene) polymer with covalently bound trace amounts of Pd shows PCEs almost ten times greater than with the pristine ladder-type polymer. The enhanced IPCE was attributed to the presence of long-lived mobile triplet excitons.

A similar approach was attempted here, with P3HT as the donor and $FeCl_3$ as the catalyst in the synthesis. The polymer (from here on called P3HT-$FeCl_3$) was synthesized by Egle Sirtautaite-Sidlauskiene at the University of Nijmegen, Netherlands, in the group of Alan Rowan.

4.5.2 Results and Discussion

The device fabrication is identical to that described on page 110. The results are shown in Figure 4-11. Compared was P3HT synthesised by different companies (American Dye Source, ADS, and Lumtec) with P3HT-$FeCl_3$. Also, baked and unbaked samples are compared.

From the absorbance in (Figure 4-11a) we already see a large blue-shift of the P3HT-$FeCl_3$. indicating a lack of crystallinity. The PL (Figure 4-11b) was considerably less blue-shifted. The biggest problem of the P3HT-$FeCl_3$ is its low mobility due to the lack of crystallinity. J_{SC} (Figure 4-11c) is about an order of magnitude smaller than that achieved with the commercial materials.

4.5.3 Summary and Outlook

Due to the huge differences in crystallinity and mobility, a direct comparison between P3HT-$FeCl_3$ and the commercial materials is not reasonable. Note that using $FeCl_3$ in the synthesis was expected to lead to less regioregular P3HT (and generally more irreproducible results).

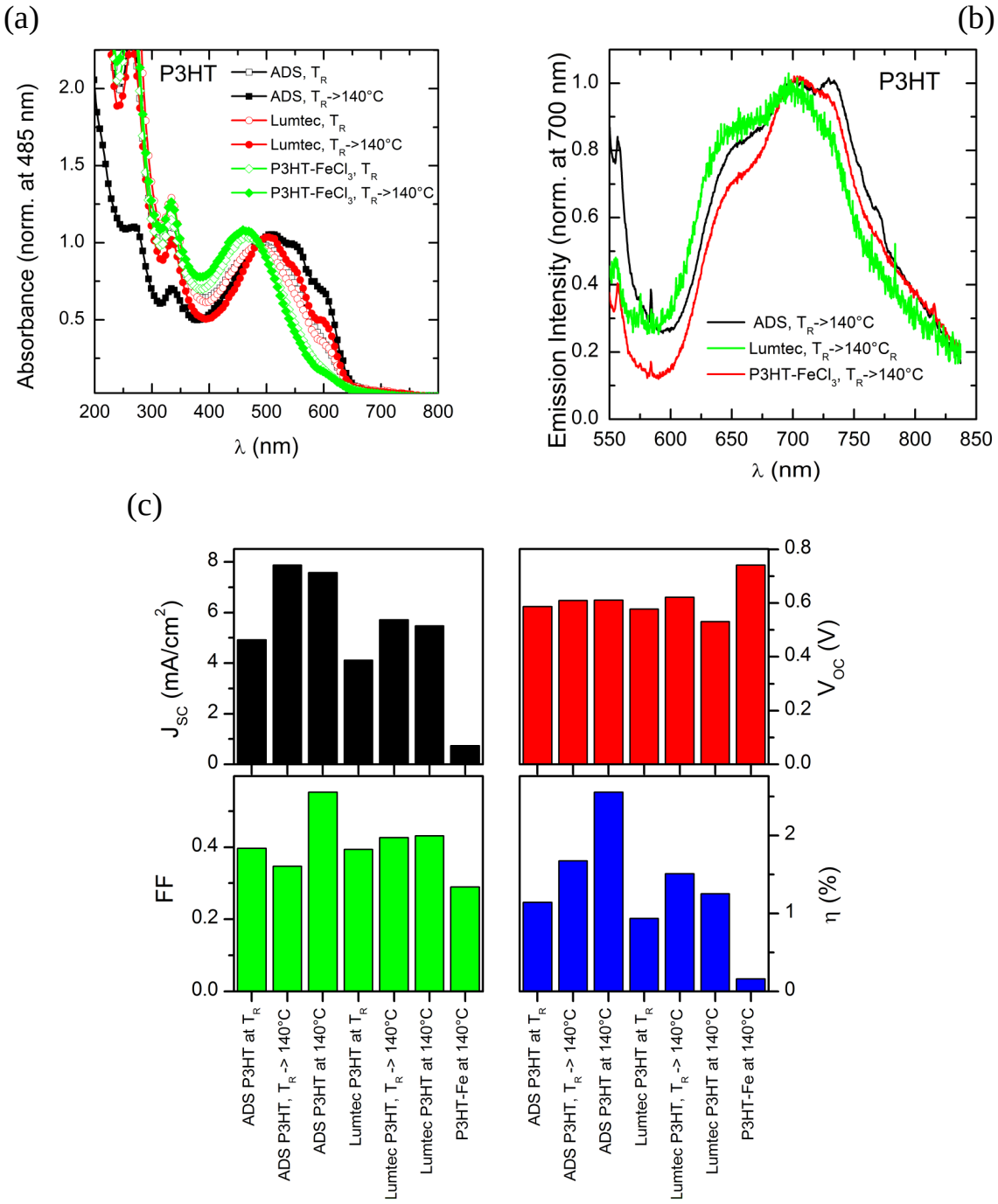

Figure 4-11. Absorbance (a) and emission spectra (b) of films of P3HT purchased from different companies (Lumtec and American Dye Source) and P3HT-$FeCl_3$, measured at room temperature in air. Solar cell performance parameters are shown in (c).

4.6 P3HT:PCBM Solar Cells with P3HT Stirred in $FeCl_3$

4.6.1 Motivation

There was an interesting paper by Kelkar et. al[210] regarding the doping of a polythiophene with $FeCl_3$. It was claimed that a complex formed between $FeCl_3$ and the polythiophene, that an increase in crystallinity takes place, and that this improved the thermal stability of the polymer. The proposed mechanism is the attachment of the Cl^- at the C=C bond of the polymer. Also, the S content seems to decrease upon increasing the doping duration, indicating that S is being replaced by Fe^+ during doping. This is hence a very interesting result with regards to the work in this dissertation, because we have seen that in most cases the guest will have a negative effect on charge transport in SCs, and this paper proposes the possibility of doping the polymer with a heavier atom without sacrificing mobility (as the crystallinity is claimed to improve).

4.6.2 Experiment

The aqueous $FeCl_3$ solution was prepared as 0.05 g/ml, i.e. 1 g $FeCl_3$ in 20 ml water. As the $FeCl_3$ comes as $FeCl_3$*6 H_2O, 1.67 g of this material was dissolved in 20 ml of water. The polymer was added to the solution and stirred in air at room temperature for 6 hours. Finally the polymer was rinsed in distilled water before storing it under nitrogen atmosphere.

4.6.3 Results and Discussion

The device fabrication is identical to that described on page 110.

The results are shown in Figure 4-12, where commercially available P3HT from ADS (black lines) is compared with the same polymer stirred in the aqueous $FeCl_3$ solution. Also compared are postannealed (after evaporation, filled symbols) with preannealed devices (after spin coating, open symbols).

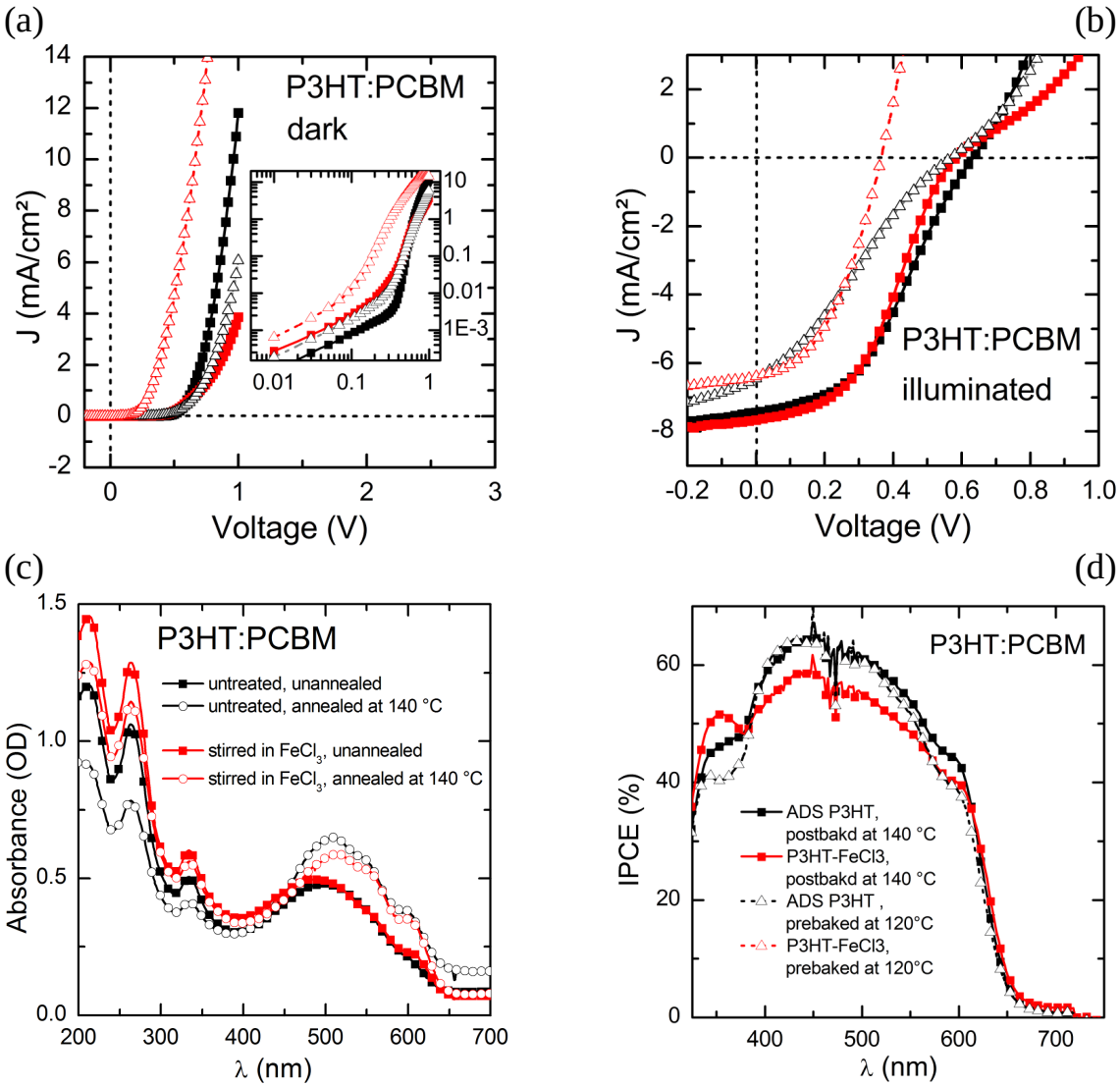

Figure 4-12. Results for P3HT:PCBM solar cells. Untreated commercial ADS P3HT is shown in black and ADS P3HT stirred in $FeCl_3$ is marked in red. Annealing is indicated by open symbols. Note that different samples were used for measurements of the absorbance (c) and the solar cell measurements (a, b, d).

The first noteworthy result is that stirring the polymer in water for several hours did not degrade it considerably. The dark curves are affected to some degree, showing higher leakage. Nevertheless, the doped postbaked device still works fairly well under illumination, showing only a small decrease in *FF* and V_{OC}. The prebaking affected both the undoped and doped devices negatively. The doped devices experienced a much larger loss in V_{OC} though.

From the absorption measurements of the unannealed samples we see that the vibronic shoulder at around 600 nm is more pronounced in the doped polymer than in the undoped one, but the main peak around 500 nm is actually slightly more in the blue for the doped polymer. Both

baked samples show a considerable vibronic shoulder and a similar main absorption peak wavelength. It hence cannot be easily concluded which material has the higher crystallinity.

The SC performance parameters are shown in Table 4-1. Regarding the postbaked devices we see a slightly higher J_{SC} for the doped polymer, but a lower V_{OC}. The FF remained constant. Note that the origin of the improvement of J_{SC} is not clear according to the IPCE spectra, which show an increase of the PCBM signal for the doped devices. For the prebaked devices we find a strong reduction in V_{OC}, which is partially compensated by an improved FF. J_{SC} is lower in the doped sample.

Table 4-1. Solar cell performance results. Pre-(post-) annealing means annealing before (after) cathode evaporation.

sample	annealing	J_{SC} (mA/cm²)	V_{OC} (V)	*FF*	η (%)
ADS-P3HT	140 °C postannealing	7.19	0.63	0.40	1.79
P3HT-$FeCl_3$	140 °C postannealing	7.45	0.58	0.41	1.78
ADS-P3HT	120 °C preannealing	7.06	0.57	0.28	1.11
P3HT-$FeCl_3$	120 °C preannealing	6.39	0.37	0.43	1.01

4.6.4 Conclusion and Outlook

The results presented above show that doping P3HT with different salts can lead to an improvement in J_{SC}. More experiments need to be done to obtain better statistics and to find out whether triplets are created upon the insertion of Fe into the polymer.

Bibliography

1 Sunpower. <http://us.sunpowercorp.com/about/newsroom/press-releases/?relID=125454> last visited on 12.12.2012.

2 Green, M. A. Third generation photovoltaics: solar cells for 2020 and beyond. *Physica E: Low-dimensional Systems and Nanostructures* **14**, 65-70, doi:10.1016/s1386-9477(02)00361-2 (2002).

3 Shockley, W. & Queisser, H. J. Detailed Balance Limit of Efficiency of p-n Junction Solar Cells *J. Appl. Phys.* **32**, doi:10.1063/1.1736034 (1961).

4 FirstSolar. <http://www.firstsolar.com/en/Innovation/Advanced-Thin-Film-Modules> last visited on 12.12.2012.

5 Kim, K., Liu, J., Namboothiry, M. A. G. & Carrolla, D. L. Roles of donor and acceptor nanodomains in 6% efficient thermally annealed polymer photovoltaics *Appl. Phys. Lett.* **90**, doi:10.1063/1.2730756 (2007).

6 Polyera. <http://www.polyera.com/newsflash/polyera-achieves-world-record-organic-solar-cell-performance> last visited on 12.12.2012.

7 Gao, F. *et al.* A new heteroleptic ruthenium sensitizer enhances the absorptivity of mesoporous titania film for a high efficiency dye-sensitized solar cell. *Chem. Commun.*, 2635-2637, doi:10.1039/B802909A (2008).

8 Heliatek. <http://www.heliatek.com/newscenter/latest_news/heliatek-erzielt-mit-107-effizienz-neuen-weltrekord-fur-seine-organische-tandemzelle/> last visited on 12.12.2012.

9 Masson, G., Latour, M. & Biancardi, D. Global Market Outlook For Photovoltaics until 2016. 74 (EPIA - European Photovoltaic Industry Association, 2012).

10 Sony. <http://pinktentacle.com/2007/05/flexible-full-color-organic-el-display/> last visited on 12.12.2012.

11 Sony. <http://www.ubergizmo.com/2011/05/sony-organic-tft-driven-flexible-e-paper/> last visited on 12.12.2012.

12 McNaught, A. D. & Wilkinson, A. (Blackwell Scientific Publications, Oxford, 1997).

13 Sonar, P., Foong, T. R. B., Singh, S. P., Li, Y. & Dodabalapur, A. A furan-containing conjugated polymer for high mobility ambipolar organic thin film transistors. *Chem. Commun.* **48**, 8383-8385, doi:10.1039/C2CC33093H (2012).

14 Jung, J. W., Liu, F., Russell, T. P. & Jo, W. H. A high mobility conjugated polymer based on dithienothiophene and diketopyrrolopyrrole for organic photovoltaics. *Energy & Environmental Science* **5**, 6857-6861, doi:10.1039/C2EE21149A (2012).

15 Wikipedia. <http://en.wikipedia.org/wiki/Conjugated_system> last visited on 12.12.2012.

16 Brütting, W. *Physics of Organic Semiconductors*. (Wiley-VCH, 2005).

17 Klauk, H. *Organic Electronics: Materials, Manufacturing and Applications*. (Wiley-VCH, 2006).

18 Pettersson, L. A. A., Roman, L. S. & Inganas, O. Modeling photocurrent action spectra of photovoltaic devices based on organic thin films. *J. Appl. Phys.* **86**, 487-496, doi:10.1063/1.370757 (1999).

19 Halls, J. J. M., Pichler, K., Friend, R. H., Moratti, S. C. & Holmes, A. B. Exciton diffusion and dissociation in a poly(p-phenylenevinylene)/C60 heterojunction photovoltaic cell. *Appl. Phys. Lett.* **68**, 3120–3122, doi:10.1063/1.115797 (1996).

20 Stübinger, T. & Brütting, W. Exciton diffusion and optical interference in organic donor-acceptor photovoltaic cells. *J. Appl. Phys.* **90**, 3632-3641, doi:10.1063/1.1394920 (2001).

21 Lakowicz, L. *Principles of Fluorescence Spectroscopy*. third edn, (Springer Science+Business Media,, 2006).

22 Dexter, D. L. A Theory of Sensitized Luminescence in Solids. *The Journal of Chemical Physics* **21**, 836-850, doi:10.1063/1.1699044 (1953).

23 Closs, G. L., Johnson, M. D., Miller, J. R. & Piotrowiak, P. A connection between intramolecular long-range electron, hole, and triplet energy transfers. *Journal of the American Chemical Society* **111**, 3751-3753, doi:10.1021/ja00192a044 (1989).

24 Marcus, R. A. On the Theory of Oxidation-Reduction Reactions Involving Electron Transfer. I *Journal of Chemical Physics* **24**, 966-978, doi:10.1063/1.1742723 (1956).

25 Baldo, M. A. & Forrest, S. R. Transient analysis of organic electrophosphorescence: I.Transient analysis of triplet energy transfer. *Phys. Rev. B* **62**, 10958-10966, doi:10.1103/PhysRevB.62.10958 (2000).

26 Karl, N. & Marktanner, J. Electron and Hole Mobilities in High Purity Anthracene Single Crystals. *Molecular Crystals and Liquid Crystals* **355**, doi:10.1080/10587250108023659 (2001).

27 Frenkel, J. On pre-breakdown phenomena in insulators and electronic semiconductors. *Physical Review* **54**, 647-648, doi:10.1103/PhysRev.54.647 (1938).

28 Dunlap, D. H., Parris, P. E. & Kenkre, V. M. Charge-Dipole Model for the Universal Field Dependence of Mobilities in Molecularly Doped Polymers. *Physical Review Letters* **77**, 542-545, doi:10.1103/PhysRevLett.77.542 (1996).

29 Bässler, H. Charge Transport in Disordered Organic Photoconductors a Monte Carlo Simulation Study. *physica status solidi (b)* **175**, 15-56, doi:10.1002/pssb.2221750102 (1993).

30 Gartstein, Y. N. & Conwell, E. M. High-field hopping mobility in molecular systems with spatially correlated energetic disorder. *Chemical Physics Letters* **245**, 351-358, doi:10.1016/0009-2614(95)01031-4 (1995).

31 Nicolai, H. T. *et al.* Unification of trap-limited electron transport in semiconducting polymers. *Nat Mater* **11**, 882-887, doi:10.1038/nmat3384 (2012).

32 Langevin, P. The recombination and mobilities of ions in gases. *Ann. Chim. Phys.* **28**, 433-530 (1903).

33 Deibel, C., Wagenpfahl, A. & Dyakonov, V. Origin of reduced polaron recombination in organic semiconductor devices. *Phys. Rev. B* **80**, 075203, doi:10.1103/PhysRevB.80.075203 (2009).

34 Juska, G., GeneviCius, K., Nekrasas, N., Sliauzys, G. & Osterbacka, R. Two dimensional Langevin recombination in regioregular poly(3-hexylthiophene). *Appl. Phys. Lett.* **95**, 013303-013303, doi:10.1063/1.3141513 (2009).

35 Koster, L. J. A., Mihailetchi, V. D., Ramaker, R. & Blom, P. W. M. Light intensity dependence of open-circuit voltage of polymer:fullerene solar cells. *Appl. Phys. Lett.* **86**, 123509-123503, doi:10.1063/1.1889240 (2005).

36 Ting, C.-J., Huang, M.-C., Tsai, H.-Y., Chou, C.-P. & Fu, C.-C. Low cost fabrication of the large-area anti-reflection films from polymer by nanoimprint/hot-embossing technology. *Nanotechnology* **19**, 205301, doi:10.1088/0957-4484/19/20/205301 (2008).

37 Heine, C. & Morf, R. H. Submicrometer gratings for solar energy applications. *Appl. Opt.* **34**, 2476-2482, doi:10.1364/AO.34.002476 (1995).

38 Nelson, J. Organic photovoltaic films. *Current Opinion in Solid State & Materials Science* **6**, 87-95, doi:10.1016/s1359-0286(02)00006-2 (2002).

39 Sun, S.-S. & Sariciftci, N. S. *Organic Photovoltaics: Mechanisms, Materials, and Devices*. (Boca Raton, FL: Raylor & Francis Group, LLC, , 2005).

40 Wagenpfahl, A., Rauh, D., Binder, M., Deibel, C. & Dyakonov, V. S-shaped current-voltage characteristics of organic solar devices. *Phys. Rev. B* **82**, doi:10.1103/PhysRevB.82.115306 (2010).

41 Wagenpfahl, A., Deibel, C. & Dyakonov, V. Organic Solar Cell Efficiencies Under the Aspect of Reduced Surface Recombination Velocities *Selected Topics in Quantum Electronics, IEEE Journal of* **16**, 1759-1763, doi:10.1109/JSTQE.2010.2042142 (2010).

42 Kraabel, B. *et al.* Subpicosecond photoinduced electron transfer from conjugated polymers to functionalized fullerenes *The Journal of Chemical Physics* **104**, 4267–4273, doi:10.1063/1.471154 (1996).

43 Burroughes, J. H. *et al.* Light-Emitting-Diodes Based On Conjugated Polymers. *Nature* **347**, 539-541, doi:10.1038/347539a0 (1990).

44 Huang, Z. H., Yang, J. H., Chen, L. C. & et, a. Study on EL emission region of polymer thin film in PPV LED. *Synthetic Met.* **91**, 1-3, doi:10.1016/S0379-6779(97)04041-1 (1997).

45 McCulloch, I. *et al.* Liquid-crystalline semiconducting polymers with high charge-carrier mobility. *Nature Materials* **5**, 328-333, doi:10.1038/nmat1612 (2006).

46 Sirringhaus, H. *et al.* High-resolution inkjet printing of all-polymer transistor circuits. *Science* **290**, 2123-2126, doi:10.1557/mrs2001.127 (2000).

47 Halls, J. J. M. *et al.* Efficient photodiodes from interpenetrating polymer networks. *Nature* **376**, 498-500, doi:10.1038/376498a0 (1995).

48 Sariciftci, N. S., Smilowitz, L., Heeger, A. J. & Wudl, F. Photoinduced Electron-Transfer From A Conducting Polymer To Buckminsterfullerene. *Science* **258**, 1474-1476, doi:10.1126/science.258.5087.1474 (1992).

49 Chasteen, S. V., Sholin, V., Carter, S. A. & Rumbles, G. Towards optimization of device performance in conjugated polymer photovoltaics: Charge generation, transfer and transport in poly(p-phenylene-vinylene) polymer heterojunctions. *Solar Energy Materials \& Solar Cells* **92**, 651-659 (2008).

50 Vieu, C. *et al.* Electron beam lithography: resolution limits and applications. *Appl. Surf. Sci., Surf. Sci. in Micro & Nanotechnol.* **164**, 111-117, doi:10.1016/S0169-4332(00)00352-4 (2000).

51 Grigorescu, A. E. & Hagen, C. W. Resists for sub-20-nm electron beam lithography with a focus on HSQ: state of the art *Nanotechnology* **20**, doi:10.1088/0957-4484/20/29/292001 (2009).

52 Schäffer, E., Harkema, S., Roerdink, M., Blossey, R. & Steiner, U. Thermomechanical lithography: pattern replication using a temperature gradient driven instability. *Adv. Mater.* **15**, 514-517, doi:10.1002/adma.200390119 (2003).

53 Dürig, U. *et al.* Millipede-an AFM data storage system at the frontier of nanotribology. *Tribol. Lett.* **9**, 25-32 (2000).

54 Gotsmann, B., Duerig, U., Frommer, J. & Hawker, C. J. Exploiting chemical switching in a Diels-Alder polymer for nanoscale probe lithography and data storage. *Advanced Functional Materials* **16**, 1499-1505 (2006).

55 Wong, A. K.-K. *Resolution enhancement techniques in optical lithography*. (SPIE - The International Society for Optical Engineering, 2001).

56 Betzig, E. & Trautman, J. K. Near-Field Optics: Microscopy, Spectroscopy, and Surface Modification Beyond the Diffraction Limit. *Science* **257**, 189-195, doi:10.1126/science.257.5067.189 (1992).

57 Riehn, R., Charas, A., Morgado, J. & Cacialli, F. Near-field optical lithography of a conjugated polymer. *Applied Physics Letters* **82 (4)**, 526-528 (2003).

58 Ghislain, L. P. *et al.* Near-field photolithography with a solid immersion lens. *Appl. Phys. Lett.* **74**, doi:10.1063/1.123168 (1999).

59 Credgington, D. *et al.* High-Resolution Scanning Near-Field Optical Lithography of Conjugated Polymers. *Adv. Funct. Mater.* **20**, 2842-2847, doi:10.1002/adfm.201000202 (2010).

60 Chou, S. Y., Krauss, P. R. & Renstrom, P. J. Nanoimprint lithography. *J. of Vac. Sci. & Technol. B* **14**, doi:10.1116/1.588605 (1996).

61 Chou, S. Y., Keimel, C. & Gu, J. Ultrafast and direct imprint of nanostructures in silicon. *Nature* **417**, 835-837, doi:10.1038/nature00792 (2002).

62 Fenwick, O. *et al.* Thermochemical nanopatterning of organic semiconductors. *Nat. Nanotechnol.* **4**, 664-668, doi:10.1038/nnano.2009.254 (2009).

63 Basu, A. S., McNamara, S. & Gianchandani, Y. B. Scanning thermal lithography: Maskless, submicron thermochemical patterning of photoresist by ultracompliant probes. *Journal Of Vacuum Science & Technology* **B 22**, 3217-3220 (2004).

64 Szoszkiewicz, R. *et al.* High-Speed, Sub-15 nm Feature Size Thermochemical Nanolithography. *Nano Lett.* **7**, 1064-1069, doi:10.1021/nl070300f (2007).

65 Wei, Z. *et al.* Nanoscale Tunable Reduction of Graphene Oxide for Graphene Electronics. *Science* **328**, 1373 - 1376, doi:10.1126/science.1188119 (2010).

66 Pires, D. *et al.* Nanoscale Three-Dimensional Patterning of Molecular Resists by Scanning Probes. *Science* **328**, 732 - 735 (2010).

67 Doi, Y. *et al.* Nanopatterning of polyfluorene derivative using electron-beam lithography. *J. of Vac. Sci. & Technol. B* **23**, 2051, doi:10.1116/1.2050655 (2005).

68 Tilke, A. *et al.* Low-energy electron-beam lithography using calixarene. *Journal of Vacuum Science Technology B* **17**, 1594-1597 (1999).

69 Binnig, G., Quate, C. F. & Gerber, C. Atomic Force Microscope. *Physical Review Letters* **56**, 930-933, doi:10.1103/PhysRevLett.56.930 (1986).

70 Gmelin, E., Fischer, R. & Stitzinger, R. Sub-micrometer thermal physics“ An overview on SThM techniques. *Thermochim. Acta* **310**, 1-17, doi:10.1016/S0040-6031(97)00379-1 (1998).

71 Majumdar, A. Scanning Thermal Microscopy. *Annual Review of Materials Science* **29**, 505-585, doi:10.1146/annurev.matsci.29.1.505 (1999).

72 Fischer, H. Calibration of micro-thermal analysis for the detection of glass transition temperatures and melting points. *Journal of Thermal Analysis and Calorimetry* **92**, 625-630, doi:10.1007/s10973-007-8554-1 (2008).

73 Tillman, M. S., Takatoya, T., Hayes, B. S. & Seferis, J. C. Influence of Polymer Specimen Structure on The Reproducibility of Micro-thermomechanical Transitions. *Journal of Thermal Analysis and Calorimetry* **62**, 599-608, doi:10.1023/a:1012085020210 (2000).

74 Tolk, M., Fenwick, O. & Cacialli, F. *Nanoscale Patterning of Conjugated Polymers* MSc Nanotechnology thesis, University College London, (2009).

75 Reading, M. *et al.* Micro-thermal analysis of polymers: Current capabilities and future prospects. *Macromol. Symp.* **167**, 45-62 (2001).

76 Gorbunov, V. V., Fuchigami, N., Hazeland, J. L. & Tsukruk, V. V. Probing surface microthermal properties by scanning thermal microscopy. *Langmuir* **15**, 8340-8343, doi:10.1021/la990913a (1999).

77 Tolk, M., Fenwick, O., Ahmad, S. & Cacialli, F. The influence of the substrate thermal conductivity on scanning thermochemical lithography. *J. Appl. Phys.* **111**, 124317-124318, doi:10.1063/1.4729809 (2012).

78 Takashi, Y. *et al.* Analysis on thermal properties of tin doped indium oxide films by picosecond thermoreflectance measurement. *J. of Vac. Sci. & Technol. A* **23**, 1180-1186, doi:10.1116/1.1872014 (2005).

79 Schlott, M., Dauth, W., Kutzner, M., Gehman, B. & Vahlstrom, S. (2001).

80 Damon, D. H. Thermal Conductivity of Vitreous Silica at Low Temperatures. *Physical Review B (Condensed Matter and Materials Physics)* **B**, 5860-5865 (1973).

81 Chen, G. & Hui, P. Thermal conductivities of evaporated gold films on silicon and glass. *Appl. Phys. Lett.* **74**, 2942-2945, doi:10.1063/1.123973 (1999).

82 Morgado, J., Cacialli, F., Gruner, J., Greenham, N. C. & Friend, R. H. Luminescence properties of poly(p-phenylenevinylene): role of the conversion temperature on the photoluminescence and electroluminescence efficiencies. *J. Appl. Phys.* **85**, 1784-1791, doi:10.1063/1.369177 (1999).

83 Okuzaki, H., Ikeda, N., Kubota, I. & Kunugi, T. Mechanical properties and structure of poly(p-phenylenevinylene) films prepared by the zone-reaction method. *Macromolecules* **32**, 5606-5612, doi:10.1021/ma9817875 (1999).

84 Shah, H. V. & Arbuckle, G. A. A comprehensive analysis of the thermal elimination reaction in a poly(p-phenylene vinylene) precursor. *Macromolecules* **32 (5)**, 1413-1423, doi:10.1021/ma981108q (1999).

85 Jin, J., Manoharan, M. P., Wang, Q. & Haque, M. A. In-plane thermal conductivity of nanoscale polyaniline thin films *Appl. Phys. Lett.* **95**, 033113-033115, doi:10.1063/1.3184786 (2009).

86 Lu, B.-Y. *et al.* Thermoelectric Performances of Free-Standing Polythiophene and Poly(3-Methylthiophene) Nanofilms *Chinese Physical Letters* **27**, 057201, doi:10.1088/0256-307X/27/5/057201 (2010).

87 Hiroshige, Y., Ookawa, M. & Toshimab, N. Thermoelectric figure-of-merit of iodine-doped copolymer of phenylenevinylene with dialkoxyphenylenevinylene *Synthetic Met.* **157**, 467-474, doi:10.1016/j.synthmet.2007.05.003 (2007).

88 Milliron, D. J., Hill, I. G., Shen, C., Kahn, A. & Schwartz, J. Surface oxidation activates indium tin oxide for hole injection *J. Appl. Phys.* **87**, 572-576, doi:10.1063/1.371901 (2000).

89 Kim, J.-S., Cacialli, F. & Friend, R. Surface conditioning of indium-tin oxide anodes for organic light-emitting diodes. *Thin Solid Films* **445**, 358-366 (2003).

90 Morgado, J., Thomas, D. S., Friend, R. H. & Cacialli., F. Role of Indium Chloride on the Luminescence Properties of PPV. *Synthetic Met.* **111**, 549-552, doi:10.1016/S0379-6779(99)00417-8 (2000).

91 Stevenson, R. & Richards, D. The use of a near-field probe for the study of semiconductor heterostructures. *Semiconductor Science and Technology* **13**, 882-886, doi:10.1088/0268-1242/13/8/009 (1998).

92 Cotton, D. V., Fell, C. J., Belcher, W. J. & Dastoor, P. C. The origin of fine structure in near-field scanning optical lithography of an electroactive polymer. *J. Phys. D: Appl. Phys.* **41**, 195107-195115, doi:10.1088/0022-3727/41/19/195107 (2008).

93 Hung, M. T., Kim, J. & Ju, Y. S. Exploration of Thermolithography for Micro- and Nanomanufacturing. *Applied Physics Letters* **88**, 123110 (2006).

94 Anderson, A. *et al.* Chemical interactions at polymer interfaces: poly(p-xylelene-alpha-tetrahydrothiophene-bromide, chloride) on indium-tin oxide. *Synthetic Met.* **10**, 13-17, doi:10.1016/S0379-6779(99)00055-7 (1999).

95 Vettiger, P. *et al.* The "millipede" - nanotechnology entering data storage *IEEE transactions on nanotechnology* **1**, 39-55, doi:10.1109/TNANO.2002.1005425 (2002).

96 Segal, M., Baldo, M. A., Holmes, R. J., Forrest, S. R. & Soos, Z. G. Excitonic singlet-triplet ratios in molecular and polymeric organic materials. *Physical Review B* **68**, 075211 (2003).

97 Peumans, P., Yakimov, A. & Forrest, S. R. Small molecular weight organic thin-film photodetectors and solar cells. *J. Appl. Phys.* **93**, 3693, doi:10.1063/1.1534621 (2003).

98 Samiullah, M., Moghe, D., Scherf, U. & Guha, S. Diffusion length of triplet excitons in organic semiconductors. *Phys. Rev. B* **82**, doi:10.1103/PhysRevB.82.205211 (2010).

99 Baldo, M. A., Thompson, M. E. & Forrest, S. R. High-efficiency fluorescent organic light-emitting devices using a phosphorescent sensitizer. *Nature* **403**, 750-753, doi:10.1038/35001541 (2000).

100 Rohatgi-Mukherjee, K. K. *Fundamentals of Photochemistry*. (New Age International (P) Ltd., 2006).

101 Köhler, A. *et al.* The singlet-triplet energy gap in organic and Pt-containing phenylene ethynylene polymers and monomers. *Journal of Chemical Physics* **116**, 9457-9463, doi:10.1063/1.1473194 (2002).

102 Deibel, C., Strobel, T. & Dyakonov, V. Role of the Charge Transfer State in Organic Donor–Acceptor Solar Cells. *Adv. Mater.* **22**, 4097-4111, doi:10.1002/adma.201000376 (2010).

103 Bakulin, A. A. *et al.* The Role of Driving Energy and Delocalized States for Charge Separation in Organic Semiconductors. *Science*, doi:10.1126/science.1217745 (2012).

104 Kasha, M. Collisional Perturbation of Spin-Orbital Coupling and the Mechanism of Fluorescence Quenching. A Visual Demonstration of the Perturbation. *The Journal of Chemical Physics* **20**, 71-74, doi:10.1063/1.1700199 (1952).

105 Basu, G., Kubasik, M., Anglos, D. & Kuki, A. Spin-forbidden excitation transfer and heavy-atom induced intersystem crossing in linear and cyclic peptides. *The Journal of Physical Chemistry* **97**, 3956-3967, doi:10.1021/j100118a006 (1993).

106 Turro, N. J., Kavarnos, G. J., Cole, T., Scribe, P. & Dalton, J. C. Molecular photochemistry. XXXIX. External heavy-atom-induced spin-obital coupling. Spectroscopic study of naphthonorbornanes. *Journal of the American Chemical Society* **93**, 1032-1034, doi:10.1021/ja00733a045 (1971).

107 Romanova, Z. S., Deshayes, K. & Piotrowiak, P. Remote Intermolecular "Heavy-Atom Effect": Spin−Orbit Coupling Across the Wall of a Hemicarcerand. *Journal of the American Chemical Society* **123**, 2444-2445, doi:10.1021/ja002612p (2001).

108 Robinson, G. W. Intensity Enhancement of Forbidden Electronic Transitions by Weak Intermolecular Interactions. *The Journal of Chemical Physics* **46**, 572-585, doi:10.1063/1.1840705 (1967).

109 Petelenz, P. & Fünfschilling, J. Resonantly enhanced external heavy atom effect in organic glasses. *Chemical Physics* **145**, 333-342, doi:10.1016/0301-0104(90)87042-a (1990).

110 Wilson, J. S. *et al.* The Energy Gap Law for Triplet States in Pt-Containing Conjugated Polymers and Monomers. *Journal of the American Chemical Society* **123**, 9412-9417, doi:10.1021/ja010986s (2001).

111 Robinson, G. & Frosch, R. Electronic Excitation Transfer and Relaxation *Journal of Chemical Physics* **38**, 1187, doi:10.1063/1.1733823 (1963).

112 Veldman, D., Meskers, S. C. J. & Janssen, R. A. J. The Energy of Charge-Transfer States in Electron Donor–Acceptor Blends: Insight into the Energy Losses in Organic Solar Cells. *Adv. Funct. Mater.* **19**, 1939–1948, doi:10.1002/adfm.200900090 (2009).

113 Yang, K., Arif, M., Förster, M., Scherf, U. & Guha, S. Triplet excitons in a ladder-type conjugated polymer: Application in solar cells. *Synthetic Met.* **159**, 2338-2341, doi:10.1016/j.synthmet.2009.07.041 (2009).

114 Guo, F., Kim, Y.-G., Reynolds, J. R. & Schanze, K. S. Platinum–acetylide polymer based solar cells: involvement of the triplet state for energy conversion. *Chem. Commun.*, 1887-1889, doi:10.1039/b516086c) (2006).

115 Goutermann, M. & Holten, D. Electron Transfer from Photoexcited Singlet and Triplet Bacteriopheophytin II. Theoretical. *Photochem.Photobiol.* **25**, doi:10.1111/j.1751-1097.1977.tb07427.x (1977).

116 McNeill, C. R., Westenhoff, S., Groves, C., Friend, R. H. & Greenham, N. C. Influence of nanoscale phase separation on the charge generation dynamics and photovoltaic performance of conjugated polymer blends: Balancing charge generation and separation. *The Journal of Physical Chemistry C* **111**, 19153–19160, doi:10.1021/jp075904m (2007).

117 Yin, C., Kietzke, T., Neher, D. & Horhold, H. H. Photovoltaic properties and exciplex emission of polyphenylenevinylenebased blend solar cells. *Appl. Phys. Lett.* **90**, doi:10.1063/1.2710474 (2007).

118 Gonzalez-Rabade, A., Morteani, A. C. & Friend, R. H. Correlation of Heterojunction Luminescence Quenching and Photocurrent in Polymer-Blend Photovoltaic Diodes. *Adv. Mater.* **21**, 3924, doi:10.1002/adma.200901114 (2009).

119 Veldman, D. *et al.* Compositional and electric field dependence of the dissociation of charge transfer excitons in alternating polyfluorene copolymer/fullerene blends. *Journal of the American Chemical Society* **130**, 7721–7735, doi:10.1021/ja8012598 (2008).

120 Marsh, R. A., Hodgkiss, J. M. & Friend, R. H. Direct measurement of field-assisted charge separation in polymer:fullerene photovoltaic devices. In preparation for publication. *Adv. Mater.* **22**, 3672-3676, doi:10.1002/adma.201001010 (2010).

121 Mihailetchi, V. D., Koster, L. J. A., Hummelen, J. C. & Blom, P. W. M. Photocurrent generation in polymer-fullerene bulk heterojunctions. *Physical Review Letters* **93**, doi:10.1103/PhysRevLett.93.216601 (2004).

122 Shuttle, C. G. *et al.* Bimolecular recombination losses in polythiophene: Fullerene solar cells. *Phys. Rev. B* **78**, doi:10.1103/PhysRevB.78.113201 (2008).

123 Maturova, K., van Bavel, S. S., Wienk, M. M., Janssen, R. A. J. & Kemerink, M. Morphological Device Model for Organic Bulk Heterojunction Solar Cells. *Nano Lett.* **9**, 3032-3037, doi:10.1021/nl901511a (2009).

124 Ohkita, H. *et al.* Charge carrier formation in polythiophene/fullerene blend films studied by transient absorption spectroscopy. *Journal of the American Chemical Society* **130**, 3030–3042, doi:10.1021/ja076568q (2008).

125 Hedley, G. J., Ruseckas, A. & Samuel, I. D. W. Ultrafast luminescence in Ir(ppy)3. *Chemical Physics Letters* **450**, 292-296, doi:10.1016/j.cplett.2007.11.028 (2008).

126 Rand, B. P. *et al.* Photocurrent enhancement in polymer:fullerene bulk heterojunction solar cells doped with a phosphorescent molecule. *Appl. Phys. Lett.* **95**, doi:10.1063/1.3257383 (2009).

127 Luhman, W. A. & Holmes, R. J. Enhanced exciton diffusion in an organic photovoltaic cell by energy transfer using a phosphorescent sensitizer. *Appl. Phys. Lett.* **94**, 153304-153303, doi:10.1063/1.3120566 (2009).

128 Xu, Z. & Hu, B. Photovoltaic Processes of Singlet and Triplet Excited States in Organic Solar Cells. *Adv. Funct. Mater.* **18**, 2611 - 2617, doi:10.1002/adfm.200800331 (2008).

129 Winroth, G., Podobinski, D. & Cacialli, F. Dopant optimization for triplet harvesting in polymer photovoltaics. *J. Appl. Phys.* **110**, 124504, doi:10.1063/1.3665688 (2011).

130 Kim, M.-S., Kim, B.-G. & Kim, J. Effective Variables To Control the Fill Factor of Organic Photovoltaic Cells. *ACS Applied Materials & Interfaces* **1**, 1264-1269, doi:10.1021/am900155y (2009).

131 Gupta, D., Bag, M. & Narayan, K. S. Correlating reduced fill factor in polymer solar cells to contact effects. *Appl. Phys. Lett.* **92**, 093301, doi:10.1063/1.2841062 (2008).

132 Mauer, R., Howard, I. A. & Laquai, F. Effect of Nongeminate Recombination on Fill Factor in Polythiophene/Methanofullerene Organic Solar Cells. *The Journal of Physical Chemistry Letters* **1**, 3500-3505, doi:10.1021/jz101458y (2010).

133 Liu, J., Shi, Y. & Yang, Y. Solvation-Induced Morphology Effects on the Performance of Polymer-Based Photovoltaic Devices. *Adv. Funct. Mater.* **11**, doi:10.1063/1.1620683 (2001).

134 Ramsdale, C. M. *et al.* The origin of the open-circuit voltage in polyfluorene-based photovoltaic devices *J. Appl. Phys.* **92**, doi:10.1063/1.1506385 (2002).

135 Mihailetchi, V. D., Blom, P. W. M., Hummelen, J. C. & Rispens, M. T. Cathode dependence of the open-circuit voltage of polymer:fullerene bulk heterojunction solar cells. *J. Appl. Phys.* **94**, doi:10.1063/1.1620683 (2003).

136 Blom, P. W., Jong, M. J. M. d. & Vleggaar, J. J. M. Electron and hole transport in poly(p-phenylene vinylene) devices *Applied Physics Letters* **68**, doi:10.1063/1.116583 (1996).

137 Blom, P. W. M., Jong, M. J. M. d. & Munster, M. G. v. Electric-field and temperature dependence of the hole mobility in poly p-phenylene vinylene . *Physical Review B* **55**, R656 (1997).

138 Burrows, P. E. *et al.* Relationship between electroluminescence and current transport in organic heterojunction light-emitting devices. *J. Appl. Phys.* **79**, doi:10.1063/1.362350 (1996).

139 Lampert, M. A. & Mark, P. *Current Injection in Solids*. (Academic, 1970).

140 Rose, A. Space-Charge-Limited Currents in Solids. *Physical Review* **97**, 1538–1544, doi:10.1103/PhysRev.97.1538 (1955).

141 Bonham, J. S. & Jarvis, D. H. A new approach to space-charge-limited cunduction theory. *Australian Journal of Chemistry* **30**, doi:10.1071/CH9770705 (1977).

142 Schafferhans, J., Baumann, A., Wagenpfahl, A., Deibel, C. & Dyakonov, V. Oxygen doping of P3HT:PCBM blends: Influence on trap states, charge carrier mobility and solar cell performance *Organic Electronics* **11**, 1693-1700, doi:10.1016/j.orgel.2010.07.016 (2010).

143 Mandoc, M. M., Koster, L. J. A. & Blom, P. W. M. Optimum charge carrier mobility in organic solar cells. *Appl. Phys. Lett.* **90**, 133504-133503, doi:10.1063/1.2711534 (2007).

144 Deibel, C., Wagenpfahl, A. & Dyakonov, V. Influence of charge carrier mobility on the performance of organic solar cells. *physica status solidi (RRL) – Rapid Research Letters* **2**, 175-177, doi:10.1002/pssr.200802110 (2008).

145 Blakesley, J. C. & Neher, D. Relationship between energetic disorder and open-circuit voltage in bulk heterojunction organic solar cells. *Phys. Rev. B* **84**, 075210, doi:10.1103/PhysRevB.84.075210 (2011).

146 Deibel, C. <http://de.slideshare.net/disorderedmatter/20110725-deibel-spie-san-diego> last visited on 12.12.2012.

147 de Mello, J. C., Wittmann, H. F. & Friend, R. H. An improved experimental determination of external photoluminescence quantum efficiency. *Adv. Mater.* **9**, 230-232, doi:10.1002/adma.19970090308 (1997).

148 Hwang, I.-W., Moses, D. & Heeger, A. J. Photoinduced carrier generation in P3HT/PCBM bulk heterojunction materials. *The journal of physical chemistry C* **112**, 4350-4354, doi:10.1021/jp075565x (2008).

149 Choulis, S. A. *et al.* High ambipolar and balanced carrier mobility in regioregular poly(3-hexylthiophene). *Appl. Phys. Lett.* **85**, 3890-3892, doi:10.1063/1.1805175 (2004).

150 Bavel, S. S. v., Sourty, E., With, G. d. & Loos, J. Three-Dimensional Nanoscale Organization of Bulk Heterojunction Polymer Solar Cells. *Nano Lett.* **9**, 507-513, doi:10.1021/nl8014022 (2008).

151 Kutal, C. Spectroscopic and photochemical properties of d10 metal complexes. *Coordination Chemistry Reviews* **99**, 213-252 (1990).

152 McMillin, D. R., Kirchhoff, J. R. & Goodwin, K. V. Exciplex quenching of photo-excited copper complexes. *Coordination Chemistry Reviews* **65**, 83-92 (1985).

153 Cuttell, D. G., Kuang, S. M., Fanwick, P. E., McMillin, D. R. & Walton, R. A. Simple Cu(I) Complexes with Unprecedented Excited-State Lifetimes. *Journal of the American Chemical Society* **124**, 6-7, doi:10.1021/ja012247h (2002).

154 Zhang, Q. *et al.* Highly Efficient Green Phosphorescent Organic Light-Emitting Diodes based on CuI complexes. *Adv. Mater.* **16**, 432-436, doi:10.1002/adma.200306414 (2004).

155 Chu, C.-W., Shrotriya, V., Li, G. & Yang, Y. Tuning acceptor energy level for efficient charge collection in copper-phthalocyanine-based organic solar cells. *Appl. Phys. Lett.* **88**, 153504-153503, doi:10.1063/1.2194207 (2006).

156 Kim, Y. *et al.* Composition and annealing effects in polythiophene/fullerene solar cells. *Journal of Materials Science* **40**, 1371-1376, doi:10.1007/s10853-005-0568-0 (2005).

157 Kalita, G., Masahiro, M., Koichi, W. & Umeno, M. Nanostructured morphology of P3HT:PCBM bulk heterojunction solar cells. *Solid-State Electronics* **54**, 447-451, doi:10.1016/j.sse.2009.11.010 (2010).

158 Kim, K., Liu, J., Namboothiry, M. A. G. & Carrolla, D. L. Roles of donor and acceptor nanodomains in 6% efficient thermally annealed polymer photovoltaics *Applied Physics Letters* **90**, doi:10.1063/1.2730756 (2007).

159 Padinger, F., Rittberger, R. S. & Sariciftci, N. S. Effects of Postproduction Treatment on Plastic Solar Cells. *Adv. Funct. Mater.* **13**, 85-88, doi:10.1002/adfm.200390011 (2003).

160 Janssen, R. A. J., Smilowitz, L., Sariciftci, N. S. & Moses, D. Triplet-state photoexcitations of oligothiophene films and solutions. *The Journal of Chemical Physics* **101**, 1787-1798, doi:10.1063/1.467757 (1994).

161 Kraabel, B., Moses, D. & Heeger, A. J. Direct observation of the intersystem crossing in poly(3-octylthiophene). *The Journal of Chemical Physics* **103**, 5102-5108, doi:10.1063/1.470597 (1995).

162 Jiang, X. M. *et al.* Spectroscopic Studies of Photoexcitations in Regioregular and Regiorandom Polythiophene Films. *Adv. Funct. Mater.* **12**, 593, doi:10.1002/1616-3028(20020916)12:9<587::AID-ADFM587>3.0.CO;2-T (2002).

163 Korovyanko, O. J., sterbacka, R. Ö., Jiang, X. M., Vardeny, Z. V. & Janssen, R. A. J. Photoexcitation dynamics in regioregular and regiorandom polythiophene films. *Phys. Rev. B* **64**, 235122, doi:10.1103/PhysRevB.64.235122 (2001).

164 Grancini, G. *et al.* Transient Absorption Imaging of P3HT:PCBM Photovoltaic Blend: Evidence For Interfacial Charge Transfer State. *The Journal of Physical Chemistry Letters* **2**, 1099-1105, doi:10.1021/jz200389b (2011).

165 Li, K. *et al.* Determination of free polaron lifetime in organic bulk heterojunction solar cells by transient time analysis. *J. Appl. Phys.* **108**, 084511, doi:10.1063/1.3493114 (2010).

166 Garcia-Belmonte, G. *et al.* Charge carrier mobility and lifetime of organic bulk heterojunctions analyzed by impedance spectroscopy. *Organic Electronics* **9**, 847-851, doi:10.1016/j.orgel.2008.06.007 (2008).

167 Brown, T. M. *et al.* Time dependence and freezing-in of the electrode oxygenplasma-induced work function enhancement in polymer semiconductor heterostructures. *Organic Electronics* **12**, 623-633, doi:10.1016/j.orgel.2011.01.015 (2011).

168 Kumar, A., Sista, S. & Yang, Y. Dipole induced anomalous S-shape I-V curves in polymer solar cells. *J. Appl. Phys.* **105**, 094512-094516, doi:10.1063/1.3117513 (2009).

169 Köntges, M. *et al.* Light induced changes in the electrical behavior of CdTe and Cu(In,Ga)Se2 solar cells. *Thin Solid Films* **403–404**, 280-286, doi:10.1016/S0040-6090(01)01507-3 (2002).

170 Tress, W. *et al.* Imbalanced mobilities causing S-shaped IV curves in planar heterojunction organic solar cells. *Appl. Phys. Lett.* **98**, 063301-063303, doi:10.1063/1.3553764 (2011).

171 Jo, J., Kim, S.-S., Na, S.-I., Yu, B.-K. & Kim, D.-Y. Time-Dependent Morphology Evolution by Annealing Processes on Polymer:Fullerene Blend Solar Cells. *Adv. Funct. Mater.* **19**, 866-874, doi:10.1002/adfm.200800968 (2009).

172 Chirvase, D., Parisi, J., Hummelen, J. C. & Dyakonov, V. Influence of nanomorphology on the photovoltai action of polymer-fullerene composites. *Nanotechnology* **15**, 1317-1323, doi:10.1088/0957-4484/15/9/035 (2004).

173 Ayzner, A. L., Tassone, C. J., Tolbert, S. H. & Schwartz, B. J. Reappraising the Need for Bulk Heterojunctions in Polymer−Fullerene Photovoltaics: The Role of Carrier Transport in All-Solution-Processed P3HT/PCBM Bilayer Solar Cells. *The Journal of Physical Chemistry C* **113**, 20050-20060, doi:10.1021/jp9050897 (2009).

174 Nalwa, K. S., Mahadevapuram, R. C. & Chaudhary, S. Growth rate dependent trap density in polythiophene-fullerene solar cells and its implications *Appl. Phys. Lett.* **98**, doi:10.1063/1.3560483 (2011).

175 Schafferhans, J., Baumann, A., Deibel, C. & Dyakonov, V. Trap distribution and the impact of oxygen-induced traps on the chargetransport in poly(3-hexylthiophene). *Appl. Phys. Lett.* **93**, doi:10.1063/1.2978237 (2008).

176 Arkhipov, V. I., Emelianova, E. V., Heremans, P. & Bässler, H. Analytic model of carrier mobility in doped disordered organic semiconductors. *Phys. Rev. B* **72**, doi:10.1103/PhysRevB.72.235202 (2005).

177 Peet, J., Tamayo, A. B., Dang, X.-D., Seo, J. H. & Nguyen, T.-Q. Small molecule sensitizers for near-infrared absorption in polymer bulk heterojunction solar cells *Appl. Phys. Lett.* **93**, 163306, doi:10.1063/1.3001802 (2008).

178 Veenstra, S. C. *et al.* Photovoltaic Properties of a Conjugated Polymer Blend of MDMO−PPV and PCNEPV. *Chemistry of Materials* **16**, 2503-2508, doi:10.1021/cm049917d (2004).

179 Hedley, G. J., Ruseckas, A. & Samuel, I. D. W. Vibrational Energy Flow Controls Internal Conversion in a Transition Metal Complex. *The Journal Of Physical Chemistry A* **114**, 8961-8968, doi:10.1021/jp101087v (2010).

180 Offermans, T., van Hal, P. A., Meskers, S. C. J., Koetse, M. M. & Janssen, R. A. J. Exciplex dynamics in a blend of pi-conjugated polymers with electron donating and accepting properties: MDMO-PPV and PCNEPV. *Phys. Rev. B* **72**, 045213, doi:10.1103/PhysRevB.72.045213 (2005).

181 S.-H. Khong *et al.* General Photo-Patterning of Polyelectrolyte Thin Films via Efficient Ionic Bis(Fluorinated Phenyl Azide) Photo-Crosslinkers and their Post-Deposition Modification. *Adv. Funct. Mater.* **17**, 2490, doi:10.1002/adfm.200600506 (2007).

182 Scully, S. R. & McGehee, M. D. Effects of optical interference and energy transfer on exciton diffusion length measurements in organic semiconductors. *J. Appl. Phys.* **100**, 034907-034905, doi:10.1063/1.2226687 (2006).

183 Nogueira, A. F. *et al.* Charge Recombination in Conjugated Polymer/Fullerene Blended Films Studied by Transient Absorption Spectroscopy. *The Journal of Physical Chemistry B* **107**, 1567-1573, doi:10.1021/jp027101z (2003).

184 Hallermann, M. *et al.* Charge Transfer Excitons in Polymer/Fullerene Blends: The Role of Morphology and Polymer Chain Conformation. *Adv. Funct. Mater.* **19**, 3662-3668, doi:10.1002/adfm.200901398 (2009).

185 Mayer, A. C. *et al.* Bimolecular Crystals of Fullerenes in Conjugated Polymers and the Implications of Molecular Mixing for Solar Cells. *Adv. Funct. Mater.* **19**, 1173-1179, doi:10.1002/adfm.200801684 (2009).

186 Cates, N. C., Gysel, R., Dahl, J. E. P., Sellinger, A. & McGehee, M. D. Effects of Intercalation on the Hole Mobility of Amorphous Semiconducting Polymer Blends. *Chemistry of Materials* **22**, 3543-3548, doi:10.1021/cm1008619 (2010).

187 Hoppe, H. *et al.* Nanoscale Morphology of Conjugated Polymer/Fullerene-Based Bulk-Heterojunction Solar Cells. *Adv. Funct. Mater.* **14**, 1005-1011, doi:10.1002/adfm.200305026 (2004).

188 Brabec, C. J. *et al.* Tracing photoinduced electron transfer process in conjugated polymer/fullerene bulk heterojunctions in real time. *Chemical Physics Letters* **340**, 232-236, doi:10.1016/S0009-2614(01)00431-6 (2001).

189 Greenham, N. C. *et al.* Measurement of absolute photoluminescence quantum efficiencies in conjugated polymers. *Chemical Physics Letters* **241**, 89-96, doi:10.1016/0009-2614(95)00584-q (1995).

190 Samal, G. S., Tripathi, A. K., Biswas, A. K., Singh, S. & Mohapatra, Y. N. Photoluminescence quantum efficiency (PLQE) and PL decay characteristics of polymeric light emitting materials. *Synthetic Met.* **155**, 344-348, doi:10.1016/j.synthmet.2005.09.010 (2005).

191 Mozer, A. J. *et al.* Charge carrier mobility in regioregular poly(3-hexylthiophene) probed by transient conductivity techniques: A comparative study. *Phys. Rev. B* **71**, doi:10.1103/PhysRevB.71.035214 (2005).

192 Muller, J. G. *et al.* Ultrafast dynamics of charge carrier photogeneration and geminate recombination in conjugated polymer : fullerene solar cells. *Phys. Rev. B* **72**, doi:10.1103/PhysRevB.72.195208 (2005).

193 Rance, W. L. *et al.* Photoinduced carrier generation and decay dynamics in intercalated and non-intercalated polymer:fullerene bulk heterojunctions. *ACS Nano* **5**, 5635-5646, doi:10.1021/nn201251v (2011).

194 Cates, N. C. *et al.* Tuning the Properties of Polymer Bulk Heterojunction Solar Cells by Adjusting Fullerene Size to Control Intercalation. *Nano Lett.* **9**, 4153-4157, doi:10.1021/nl9023808 (2009).

195 Kim, C.-H., Song, M., Jin, S.-H. & Lee, J. W. High Open-Circuit Voltage of Organic Bulk Heterojunction Solar Cells Base on Poly(3-hexylthiophene): Fullerene Derivatives. *Molecular Crystals and Liquid Crystals* **538**, 216-222, doi:10.1080/15421406.2011.564059 (2011).

196 Namdas, E. B. *et al.* Phosphorescent Light-Emitting Transistors: Harvesting Triplet Excitons. *Adv. Mater.* **21**, 4957-4961, doi:10.1002/adma.200900919 (2009).

197 Li, G. *et al.* High-efficiency solution processable polymer photovoltaic cells by self-organization of polymer blends. *Nature Materials* **4**, 864-868, doi:10.1038/nmat1500 (2005).

198 Credgington, D., Hamilton, R., Atienzar, P., Nelson, J. & Durrant, J. R. Non-Geminate Recombination as the Primary Determinant of Open-Circuit Voltage in Polythiophene:Fullerene Blend Solar Cells: an Analysis of the Influence of Device Processing Conditions. *Adv. Funct. Mater.* **21**, 2744-2753, doi:10.1002/adfm.201100225 (2011).

199 Arif, M. *et al.* Harvesting triplet excitons for application in polymer solar cells. *Appl. Phys. Lett.* **94**, doi:10.1063/1.3082081 (2009).

200 Schulz, G. L. & Holdcroft, S. Conjugated Polymers Bearing Iridium Complexes for Triplet Photovoltaic Devices. *Chemistry of Materials* **20**, 5351-5355, doi:10.1021/cm800955f (2008).

201 Lee, C.-L., Hwang, I.-W., Byeon, C. C., Kim, B. H. & Greenham, N. C. Triplet Exciton and Polaron Dynamics in Phosphorescent Dye Blended Polymer Photovoltaic Devices. *Adv. Funct. Mater.* **20**, 2945-2950, doi:10.1002/adfm.201000763 (2010).

202 Shakya, P. *et al.* The effect of applied magnetic field on photocurrent generation in poly-3-hexylthiophene:[6,6]-phenyl C61-butyric acid methyl ester photovoltaic devices. *Journal of Physics-Condensed Matter* **20**, doi:10.1088/0953-8984/20/45/452203 (2008).

203 Shao, Y. & Yang, Y. Efficient Organic Heterojunction Photovoltaic Cells Based on Triplet Materials. *Adv. Mater.* **17**, 2841-2844, doi:10.1002/adma.200501297 (2005).

204 Chandrasekhar, S. Stochastic Problems in Physics and Astronomy. *Reviews of Modern Physics* **15**, doi:10.1103/RevModPhys.15.1 (1943).

205 Kim, Y. *et al.* A strong regioregularity effect in self-organizing conjugated polymer films and high-efficiency polythiophene:fullerene solar cells. *Nat Mater* **5**, 197-203, doi:10.1038/nmat1574 (2006).

206 Kroon, R., Lenes, M., Hummelen, J. C., Blom, P. W. M. & Boer, B. d. Small Bandgap Polymers for Organic Solar Cells. *Polymer Review* **48**, 531-582, doi:10.1080/15583720802231833 (2008).

207 Koster, L. J. A., Mihailetchi, V. D. & Blom, P. W. M. Ultimate efficiency of polymer/fullerene bulk heterojunction solar cells. *Appl. Phys. Lett.* **88**, doi:10.1063/1.2181635 (2006).

208 Park, S. H. *et al.* Bulk heterojunction solar cells with internal quantum efficiency approaching 100%. *Nat Photon* **3**, 297-302, doi:10.1038/nphoton.2009.69 (2009).

209 Koster, L. J. A., Mihailetchi, V. D., Xie, H. & Blom, P. W. M. Origin of the light intensity dependence of the short-circuit current of polymer/fullerene solar cells. *Appl. Phys. Lett.* **87**, 203502-203503, doi:10.1063/1.2130396 (2005).

210 Kelkar, D. & Chourasia, A. Structural properties of polythiophene doped with FeCl3. *Chemistry & Chemical Technology* **5**, 309-315 (2011).

211 Scheinert, S., Pernstich, K. P., Batlogg, B. & Paasch, G. Determination of trap distributions from current characteristics of pentacene field-effect transistors with surface modified gate oxide. *J. Appl. Phys.* **102**, 104503, doi:10.1063/1.2803742 (2007).

212 Kodam, S. *Investigating the effect on the device performance of organic photovoltaic cells when doped with an electrophosphorescent dopant* Master of Science in Nanotechnology thesis, University College London, (2011).